
The University Of Sheffield.

# SOUND PROPAGATION IN AIR-FILLED PIPES WITH INHOMOGENEITIES

Jevgenija Prisutova

Submitted for the degree of Doctor of Philosophy

Department of Mechanical Engineering

University of Sheffield

October 2015

## Abstract

This work is concerned with sound propagation, reflection and absorption in air-filled pipes with inhomogeneities such as an open end, lateral connection, cross-sectional change or porous termination. The focus in this study is made on the sound intensity which is a vector quantity. Because the sound intensity is treated as a complex vector, it gives more information about the local net transport of energy (real part) and local oscillatory transport of energy (imaginary part) and its direction. This provides a possibility to obtain more information on the nature of inhomogeneities in the pipe and their extent. An attempt is made to study the sound intensity in a pipe transmitted through higher-order modes. The results of this work are applied to measure the acoustical properties of porous media and living plants. It is shown that the frequency range of the standard ISO 10534-2 method can be extended significantly to measure the absorption and reflection from a large, inhomogeneous material specimen such as a living plant. The presented experimental data are supported by the hybrid numerical method which is based on the normal modal decomposition and finite element modelling, analytical methods which are based on normal mode decomposition alone and models for the acoustical properties of porous media. It is shown that accurate measurements of the sound intensity in a pipe are problematic. Therefore, this work presents experimental and theoretical evidence together with a sensitivity analysis and discussion on the applicability of this technology for the characterisation of conditions in air-filled pipes.

# Acknowledgements

First of all, I would like to say how grateful and indebted I am to my PhD supervisor, Professor Kirill Horoshenkov. His outstanding knowledge of the subject, academic and moral support and patience helped me to overcome all encountered difficulties and made this work possible. I would also like to thank my second supervisor, Professor Simon Tait for his helpfulness.

It is my pleasure to express my gratitude to the technical staff in the Acoustics and Hydraulics laboratories at the Universities of Bradford and Sheffield, especially Mr Nigel Smith, whose extraordinary assistance in setting up the experiments is greatly appreciated. Furthermore, I would like to thank the Acoustics Research Group for supporting me and sharing with me happy years of my PhD. I am grateful to Dr Andy Nichols, Mr Giulio Dolcetti and Dr Michael Pelegrinis for their help in planning and conducting the experimental work, and to Dr Anton Krynkin for his theoretical advice. I would also like to mention Mr Andy Birch, Mr Darren Sugden and Mrs Lindsay Fox, whose willingness to help with planning and organising my conference trips and secondments is very important.

I would like to thank Dr Wenbo Duan and Dr Ray Kirby for their theoretical assistance on the subject of complex sound intensity, as well as for kindly providing me with the requested numerical data. I am also extremely grateful to Dr Jean-Philippe Groby and Dr Bruno Brouard for their advice on the acoustics of porous media, and their help in

setting up the experiments, getting hold of plants specimens and analysing the measured data.

Last but not least, I would like to express my deepest appreciation to my parents and my brother, who supported me through thick and thin and always had faith in me. I would like to thank my closest friends for their loyalty and encouraging me in difficult times. Finally, I am truly grateful to my boyfriend Ryan for his love and support, standing by me through the good and bad times and being patient and understanding while I was writing this thesis.

# List of publications

## Journal papers

1. Prisutova, J., Horoshenkov, K., Groby, J.-P., Brouard, B. (2014) A method to determine the acoustic reflection and absorption coefficients of porous media by using modal dispersion in a waveguide. *Journal of the Acoustical Society of America* 136(6) 2947-2958.

2. Duan, W., Kirby, R., Prisutova, J., Horoshenkov, K. (2015) On the use of power reflection ratio and phase change to determine the geometry of a blockage in a pipe. *Applied Acoustics* 87 190-197.

3. Duan, W., Kirby, R., Prisutova, J., Horoshenkov, K. (2013) The measurement and prediction of complex acoustic intensity in an acoustic waveguide. *Journal of the Acoustical Society of America* 134(5) 3674-3685.

## Conference papers

1. Prisutova, J., Horoshenkov, K., Groby, J.-P., Brouard, B. (2014) The frequency and angular dependence of the absorption coefficient of common types of living plants. Proceedings of the 43rd International Congress on Noise Control Engineering. *Internoise 2014*, Melbourne, Australia, 2014.

2. Brouard, B., Prisutova, J., Groby, J.-P., Horoshenkov, K. (2014) Détermination de coefficients d'absorption et de réflexion de matériaux au delà de la fréquence de coupure du tube à impédance. Proceedings of the 12th Congrès Français d'Acoustique. *CFA 2014*, Poitiers, France, 2014.

3. Prisutova, J., Horoshenkov, K., Duan, W., Kirby, R. (2014) An acoustic method of blockage characterisation in a pipe based on the cross-sectional mode analysis. Proceedings of the 21st International Congress of Sound and Vibration. *ICSV21*, Beijing, China, 2014.

4. Prisutova, J., Horoshenkov, K., Groby, J.-P., Brouard, B. (2014) Laboratory measurement of the acoustic absorption coefficient of living plants via modal dispersion. Proceedings of the 21st International Congress of Sound and Vibration. *ICSV21*, Beijing, China, 2014.

5. Prisutova, J., Horoshenkov, K., Groby, J.-P., Brouard, B. (2013) Laboratory measurement of the acoustic absorption coefficient based on the modal dispersion. Proceedings of the 166th Meeting of the Acoustical Society of America. *ASA 2013*, San Francisco, USA, 2013.

6. Duan, W., Prisutova, J., Horoshenkov, K., Kirby, R. (2012) A comparison between measured and predicted complex intensity in a flanged cylindrical pipe. Proceedings of Acoustics 2012. *Acoustics 2012*, Nantes, France, 2012.

7. Prisutova, J., Horoshenkov, K. (2012) The measurement of complex intensity near the open end of a flanged cylindrical pipe. Proceedings of Acoustics 2012. *Acoustics 2012*, Nantes, France, 2012.

8. Horoshenkov, K., Prisutova, J., Kirby, R., Duan, W. (2011) On the variation of the acoustic intensity vector near an open end of a pipe. Proceedings of Forum Acusticum 2011. *Forum Acousticum 2011*, Aalborg, Denmark, 2011.

9. Prisutova, J., Horoshenkov, K. (2010) A method to calculate the acoustic intensity near an open end of a flanged round pipe. Proceedings of 20th International Congress on Acoustics 2010. *ICA 2010*, Sydney, Australia, 2010.

# Contents

# List of Figures

# List of Tables

# Nomenclature

| Symbol | Definition | Units |
|---|---|---|
| $a$ | width of the tube cross-section | [m] |
| $a_{mn}$ | absolute values of forward waves | [−] |
| $A_0$ | amplitude of Gaussian pulse | [−] |
| $A_{mn}$ | modal excitation coefficients in incident sound wave | [−] |
| $A_n$ | modal amplitude | [−] |
| $A_v$ | leaf area per unit volume | [$m^3$] |
| $b_{mn}$ | absolute values of backward waves | [−] |
| $B_n$ | modal amplitude | [−] |
| $c$ | velocity of ultrasonic beam | [m/s] |
| $c_0$ | speed of sound in air | [m/s] |
| $c_{0,i}$ | speed of sound at the $i-$th location | [m/s] |
| $\tilde{c}_{eq}$ | complex sound speed of equivalent fluid | [m/s] |
| $c'$ | speed of sound in porous material | [m/s] |
| $C_{1u}$ | phase cornerfrequency | [Hz] |
| $C_{2u}$ | phase cornerfrequency | [Hz] |
| $C_{3u}$ | phase cornerfrequency | [Hz] |
| $C_{4u}$ | phase cornerfrequency | [Hz] |
| $C_n$ | modal amplitude | [−] |
| $d_s$ | material sample thickness | [m] |
| $e(\omega)$ | artificially added measurement error | [Pa] |

| | | |
|---|---|---|
| $e_{pp}$ | p-p intensity measurements error | [−] |
| $e_{pu}$ | p-u intensity measurements error | [−] |
| $E_{mn}$ | modal energy flux through cross-section of impedance tube | [W] |
| $E_{mn}^{(i)}$ | modal energy flux incident on material sample in impedance tube | [W] |
| $E_{mn}^{(r)}$ | modal energy flux reflected from material sample in impedance tube | [W] |
| $E^{(i)}$ | total energy flux incident on material sample in impedance tube | [W] |
| $E^{(r)}$ | total energy flux reflected from material sample in impedance tube | [W] |
| $f$ | sound frequency | [Hz] |
| $f_0$ | initial frequency of sine chirp | [Hz] |
| $f_{c1u}$ | sensitivity cornerfrequency | [Hz] |
| $f_{c2u}$ | sensitivity cornerfrequency | [Hz] |
| $f_{c3u}$ | sensitivity cornerfrequency | [Hz] |
| $f_{c4u}$ | sensitivity cornerfrequency | [Hz] |
| $f_{mn}$ | cut-on frequency [Hz] | |
| $f_s$ | sampling frequency | [Hz] |
| $F$ | cost function | [−] |
| $F(\omega)$ | viscosity correction function | [−] |
| $F_1$ | time harmonic sound source in region $R_1$ | [−] |
| $h_f$ | mean thickness of single leaf | [m] |
| $h_p$ | estimated thickness of plant layer | [m] |
| $h_{\sigma n}^{(2)}$ | spherical Hankel function of the second kind | [−] |
| $\mathbf{I}(\omega)$ | non-instantaneous active intensity | [W/m$^2$] |
| $\mathbf{I}(t)$ | instantaneous active intensity | [W/m$^2$] |
| $\bar{I}$ | time-averaged sound intensity | [W/m$^2$] |

| | | |
|---|---|---|
| $I_i$ | total intensity incident on material sample in impedance tube | [W/m$^2$] |
| $I_j(t)$ | instantaneous intensity in $j$ direction | [W/m$^2$] |
| $I_{mn}$ | modal instantaneous intensity through cross-section of impedance tube | [W/m$^2$] |
| $\tilde{I_{mn}}$ | modal time-averaged intensity through cross-section of impedance tube | [W/m$^2$] |
| $I_r$ | total intensity reflected from material sample in impedance tube | [W/m$^2$] |
| $\mathbf{I}_{rad}(t)$ | instantaneous radiating intensity | [W/m$^2$] |
| $\tilde{I}_{z,a}$ | time-averaged active axial intensity | [W/m$^2$] |
| $\tilde{I}_{z,re}$ | time-averaged reactive axial intensity | [W/m$^2$] |
| $I^m$ | measured intensity | [W/m$^2$] |
| $I^{pr}$ | predicted intensity | [W/m$^2$] |
| $\mathbf{J}(\omega)$ | non-instantaneous reactive intensity | [W/m$^2$] |
| $\mathbf{J}(t)$ | instantaneous reactive intensity | [W/m$^2$] |
| $J_m$ | Bessel function of the first kind and of the $m$-th order | [−] |
| $\mathbf{J}_{osc}(t)$ | instantaneous oscillating intensity | [W/m$^2$] |
| $K$ | wavenumber in frequency-wavenumber spectra | [m$^{-1}$] |
| $k_c$ | complex characteristic wavenumber | [m$^{-1}$] |
| $k_{mn}$ | modal wavenumber | [m$^{-1}$] |
| $\tilde{K}_{eq}$ | equivalent fluid bulk modulus | [Pa] |
| $K_{max}$ | maximum value of wavenumber in wavenumber spectra | [m$^{-1}$] |
| $K_{min}$ | minimum value of wavenumber in wavenumber spectra | [m$^{-1}$] |
| $L_1$ | axial length of region $R_1$ | [m] |
| $L_2$ | axial length of region $R_2$ | [m] |
| $L_3$ | boundary between modal representation and finite element discretisation in pipe | [m] |
| $m$ | mode number | [−] |

| | | |
|---|---|---|
| $m_2$ | the number of modes in region $R_2$ | [−] |
| $m_4$ | the number of modes in region $R_4$ | [−] |
| $n$ | mode number | [−] |
| $n_0$ | initial sampling position of impulse response maximum | [−] |
| $n_1$ | and $n_3$ are the number of nodes in regions $R_1$ and $R_3$ | [−] |
| $n_1$ | in the number of nodes in region $R_1$ | [−] |
| $n_3$ | in the number of nodes in region $R_3$ | [−] |
| $n_f$ | number of leaves on a plant | [−] |
| $n_i$ | $i-$th sampling position of the impulse response maximum | [−] |
| $\mathbf{n_A}$ | outward unit normal vector over surface $\Gamma_A$ | [−] |
| $\mathbf{N}$ | trial (shape) function | [−] |
| $N_{1_j}$ | global trial (shape) function for mesh in region $R_1$ | [−] |
| $N_{3_j}$ | global trial (shape) function for mesh in region $R_3$ | [−] |
| $N_{Pr}$ | Prandtl number | [−] |
| $\tilde{(}p)$ | wavenumber-frequency pressure spectrum | [Pa] |
| $p(t)$ | instantaneous sound pressure | [Pa] |
| $p^-_{rms}$ | mean square pressure in backward direction | [Pa] |
| $p^+_{rms}$ | mean square pressure in forward direction | [Pa] |
| $p_{1_j}$ | values of sound pressure at nodes $j$ in region $R_1$ | [Pa] |
| $p_{3_j}$ | values of sound pressure at nodes $j$ in region $R_3$ | [Pa] |
| $p_{b,r}$ | frequency-wavenumber spectrum measured in front of blockage | [Pa] |
| $p_{b,tr}$ | frequency-wavenumber spectrum measured behind blockage | [Pa] |
| $p_e$ | frequency-wavenumber spectrum measured in empty pipe | [Pa] |
| $p_1$ | sound pressure in region $R_1$ | [Pa] |
| $p_2$ | sound pressure in region $R_2$ | [Pa] |
| $p_3$ | sound pressure in region $R_3$ | [Pa] |
| $p_4$ | sound pressure in region $R_4$ | [Pa] |

| | | |
|---|---|---|
| $p_e$ | frequency-position spectrum of sound pressure with added error | [Pa] |
| $\tilde{p}_e$ | frequency-wavenumber spectrum of sound pressure with added error | [Pa] |
| $p_f$ | number of pixels in single leaf | [−] |
| $p_m$ | frequency-position spectrum of measured sound pressure | [Pa] |
| $\tilde{(p_m)}$ | frequency-wavenumber spectrum of measured sound pressure | [Pa] |
| $p_{m_1}$ | sound pressure recorded with first microphone | [Pa] |
| $p_{m_1}$ | sound pressure recorded with second microphone | [Pa] |
| $p_s$ | number of pixels in reference square | [−] |
| $p_-$ | amplitude of backward-travelling sound pressure wave | [Pa] |
| $p_+$ | amplitude of forward-travelling sound pressure wave | [Pa] |
| $P_0$ | air equilibrium pressure | [Pa] |
| $r$ | radial coordinate | [m] |
| $r_0$ | monopole sound source radial coordinate | [m] |
| $R$ | outer radius of finite element mesh in Region $R_3$ | [m] |
| $R_{00}$ | plane wave reflection coefficient | [−] |
| $R_1$ | region 1 in open-ended pipe | [−] |
| $R_2$ | region 2 in open-ended pipe | [−] |
| $R_3$ | region 3 in open-ended pipe | [−] |
| $R_4$ | region 4 in open-ended pipe | [−] |
| $R_{int}$ | reflection coefficient (integral method) | [−] |
| $R_{max}$ | reflection coefficient (maximum amplitude method) | [−] |
| $R_{mn}$ | modal reflection coefficient | [−] |
| $R_{mn}^{(\mathrm{m})}$ | measured modal reflection coefficient | [−] |
| $R_{mn}^{pred}$ | modal reflection coefficient calculated exactly | [−] |
| $R_{mn}^{sim}$ | modal reflection coefficient with simulated error | [−] |

| | | |
|---|---|---|
| $R_{mnl}$ | generalised modal reflection coefficients | [−] |
| $R_{theo}$ | predicted modal reflection coefficient | [−] |
| $s$ | standing wave ratio | [−] |
| $s(t)$ | sine chirp function | [Pa] |
| $s_f$ | mean area of single leaf | [$m^2$] |
| $s_p$ | total area of leaves on plant | [$m^2$] |
| $s_s$ | area of reference square | [$m^2$] |
| $S$ | cross-sectional area of duct | [$m^2$] |
| $S_{pu}$ | pressure and velocity cross-spectrum | [$W/m^2$] |
| $S_u$ | particle velocity sensitivity of Microflown | [mV/Pa] |
| $t$ | time | [s] |
| $t_0$ | delay in Gaussian pulse function | [s] |
| $T$ | total duration of signal | [s] |
| $u$ | instantaneous sound velocity | [m/s] |
| $\tilde{u}$ | frequency spectrum of sound velocity | [m/s] |
| $\mathbf{u}_{eq}$ | fluid displacement | [m] |
| $u_j(t)$ | instantaneous velocity in $j$ direction | [m/s] |
| $u_z$ | axial velocity | [m/s] |
| $u_z^*$ | complex conjugate of axial velocity | [m/s] |
| $v(t)$ | Gaussian pulse function | [Pa] |
| $\mathbf{v}$ | velocity of fluid particles at high frequencies | [m/s] |
| $\mathbf{v}_{eq}$ | fluid velocity | [m/s] |
| $V$ | homogeneisation volume | [$m^3$] |
| $V_{air}$ | volume occupied by air in pores | [$m^3$] |
| $V_f$ | volume of plant foliage | [$m^3$] |
| $V_p$ | equivalent volume occupied by plant | [$m^3$] |
| $V_{total}$ | total volume occupied by porous material | [$m^3$] |
| $w_f$ | mean weight of single leaf | [g] |

| | | |
|---|---|---|
| $w_p$ | total weight of leaves/stems | [g] |
| $x$ | cross-sectional coordinate | [m] |
| $x_m$ | cross-sectional microphone position | [m] |
| $y$ | cross-sectional coordinate | [m] |
| $y_m$ | cross-sectional microphone position | [m] |
| $z$ | axial coordinate | [m] |
| $z_0$ | monopole sound source axial coordinate | [m] |
| $z_1$ | initial microphone coordinate | [m] |
| $z_2$ | final microphone coordinate | [m] |
| $z_i$ | $i-$th axial location of probe, | [m] |
| $Z_a$ | acoustic impedance of pipe | [Pa s/m$^3$] |
| $Z_c$ | complex characteristic impedance | [Pa s/m] |
| $Z_{eq}$ | characteristic impedance of equivalent fluid | [Pa s/m] |
| $Z_i$ | specific acoustic impedance of pipe | [Pa s/m] |
| $Z_m$ | mechanical acoustic impedance of pipe | [Pa s m] |
| $Z_{mnl}$ | generalised radiation impedances | [Pa s/m] |
| $Z_s$ | surface impedance | [Pa s/m] |
| $\alpha_{00}$ | plane wave absorption coefficient | [−] |
| $\alpha_{amp}$ | absorption coefficient (amplitude method) | [−] |
| $\alpha_{int}$ | absorption coefficient (intensity method) | [−] |
| $\alpha_{mn}$ | zeros of $\partial J_m/\partial n$ | [−] |
| $\alpha_\infty$ | tortuosity | [−] |
| $\beta$ | Gaussian pulse width | [−] |
| $\gamma$ | specific heat ratio of air | [−] |
| $\gamma_{mn}$ | wavenumbers corresponding to zeros of $J'_m$ | [−] |
| $\Gamma_1$ | total outer surface of region $R_1$ | [−] |
| $\Gamma_\mathrm{A}$ | surface separating regions $R_1$ and $R_2$ | [−] |
| $\Gamma_\mathrm{B}$ | surface separating regions $R_2$ and $R_3$ | [−] |

| | | |
|---|---|---|
| $\Gamma_C$ | surface separating regions $R_3$ and $R_4$ | [−] |
| $\delta(x)$ | Dirac delta-function | [−] |
| $\delta_{eq}$ | equivalent fluid wavenumber | [$m^{-1}$] |
| $\Delta$ | spacing between two microphone positions | [m] |
| $\Delta F$ | swept frequency range | [Hz] |
| $\Delta\Omega$ | swept frequency range | [Hz] |
| $\epsilon$ | error between measured and predicted data | [−] |
| $\epsilon_I$ | error between measured and predicted intensities | [−] |
| $\epsilon_{\mathrm{Im}}$ | error between measured and predicted imaginary parts of modal reflection coefficient | [−] |
| $\epsilon_{\mathrm{Re}}$ | error between measured and predicted real parts of modal reflection coefficient | [−] |
| $\epsilon_{\alpha_{total}}$ | error between measured and predicted absorption coefficient | [−] |
| $\zeta$ | normalised acoustic impedance of pipe | [−] |
| $\eta$ | viscosity of air | [Pa s] |
| $\theta$ | circumferential coordinate | [rad] |
| $\theta_0$ | monopole sound source circumferential coordinate | [rad] |
| $\theta_f$ | dominant angle of leaf orientation | [degrees] |
| $\theta_{mn}$ | angle of sound incidence in air | [rad] |
| $\theta_p$ | angle between axes of pores and surface normal | [rad] |
| $\theta_t$ | refraction angle in porous material | [rad] |
| $\Lambda$ | viscous characteristic length | [m] |
| $\Lambda'$ | thermal characteristic length | [m] |
| $\rho_0$ | density of air | [$kg/m^3$] |
| $\tilde{\rho}_{eq}$ | equivalent fluid density | [$kg/m^3$] |
| $\sigma$ | flow resistivity | [$N\,s/m^4$] |
| $\sigma_n$ | order of Hankel function | [−] |
| $\tau$ | transmission coefficient | [−] |

| | | |
|---|---|---|
| $\tau_{int}$ | transmission coefficient (integral method) | [−] |
| $\tau_{max}$ | transmission coefficient (maximum amplitude method) | [−] |
| $\Upsilon(r)$ | radial component of sound pressure field in region $R_4$ | [−] |
| $\phi$ | open porosity | [−] |
| $\phi_{mn}$ | phases of forward waves | [rad] |
| $\phi_u$ | phase sensitivity of Microflown | [degrees] |
| $\Phi_n(r,\theta)$ | eigenfunctions in region $R_2$ | [−] |
| $\psi_{mn}$ | phases of backward waves | [rad] |
| $\Psi_{mn}$ | eigen function of impedance tube | [−] |
| $\Psi(\theta,\phi)$ | transverse component of sound pressure field in region $R_4$ | [−] |
| $\omega$ | angular frequency | [Hz] |
| $\omega_0$ | initial frequency of sine chirp | [Hz] |
| $\mathbf{\Omega_1}$ | volume of region $R_1$ | [$m^3$] |

# Chapter 1

# Introduction

## 1.1 General background

Over the past years, the problem of sound pressure distribution in different kinds of pipes has been extensively studied, employing a range of methods. These are analytical, numerical and hybrid methods. These studies contribute to a better understanding of reflection, transmission and scattering processes occurring in a pipe, and have practical engineering applications, such as examination of the conditions of underground and ventilation pipelines, non-destructive testing and analysis of porous media and other materials properties. An overwhelming majority of these methods are confined to sound pressure analysis. However, there are applications for which the knowledge of scalar sound pressure is insufficient and there is a need to analyse the sound intensity vector field. Sound intensity has been long used for description of the sound energy flow in noise control applications, but it is usually treated as a real quantity by taking the time average of the instantaneous sound intensity. This approach works well if both

the sound pressure and sound velocity are in phase with each other, as it happens in a free field. But this method would not work for those fields where the sound pressure and sound velocity are out of phase. For such conditions one needs to treat sound intensity as a complex quantity, where the real part would represent the net energy transport and the imaginary part the oscillatory energy flow. However, this approach might be challenging, because the use of the complex sound intensity to describe sound propagation in ducts is complicated. The cause for this might be the rapid fluctuations of sound intensity vector which makes the measurement and prediction of this quantity in a duct rather problematic. As a result, a bulk of previous studies on sound intensity has been confined to unguided medium with main application to sound power measurement and noise control.

In many studies of sound propagation in pipes it is common to limit the frequency range to that of the plane wave regime (eg. Amir et al., 1995; Sharp and Campbell, 1997; de Salis and Oldham, 1999). This approach is suitable for the majority of current applications, but in some cases, such as material testing and damage detection, using the higher frequencies in the modal regime may be beneficial. The procedure for the determination of the plane wave acoustic absorption coefficient of a material is detailed in standards ISO 10534-2 (1998). However, the high frequency limit for this regime is restricted by cross-sectional dimensions of a pipe. As a result, there is often a conflict between the high frequency limit which needs to be achieved and the size of the samples which the pipe is able to accommodate in order to determine the acoustical absorbing properties for a representative area of the material specimen. Several studies have rather successfully been carried out in order to overcome this issue, but their results may still be subject to poor signal-to-noise ratio, phase mismatch and calibration problems.

Therefore, the purpose of this research is to investigate the complex sound intensity distribution in waveguides with different boundary conditions and at frequencies at which several higher order modes can be excited. This includes the problem of an open end

of a pipe, blockage detection and porous media characterisation by analysing the reflected and transmitted sound intensity fields. This will be achieved by undertaking the experimental measurements and comparing the obtained data against the predictions generated by the numerical model and thus gaining fundamental understanding of instantaneous and time-averaged complex intensity scattered by inhomogeneities in pipes. Additionally, an alternative method for measuring the reflection and absorption coefficient of a relatively large specimen of porous media and living plants in an acoustic waveguide will be presented. It is based on applying the two-dimensional Fourier transform to sound pressure data, collected with a simulated microphone array. The results of this project can help to improve the quality of acoustic instruments which have been developed for the inspection of the underground pipes (Acoustic Sensing, 2015). These instruments analyse the acoustic intensity vector recorded in the pipe. If the sensor is placed at a position where the intensity distribution is complex because of the presence of standing waves or higher order modes propagating in different directions, then the analysis of the recorded data becomes a challenging task. In order to resolve it, one needs to be aware of the distribution of the acoustic intensity to compensate for this effect.

## 1.2 Aims and objectives

The aim of this research is to gain a fundamental understanding of complex intensity field distribution in an acoustic, air-filled waveguide. The obtained knowledge can then be used to develop a fast and efficient acoustic detection system to characterise the reflections from inhomogeneities in an air-filled waveguide. To fulfil this aim, the 8 specific objectives were set. These objectives are listed in Table 1.1.

| No. | Objectives |
|---|---|
| 1 | Develop a new experimental facility for studying sound propagation in modal regimes in pipes |
| 2 | Identify and use a suitable mathematical model for the prediction of sound intensity in pipes |
| 3 | Carry out a series of experiments to validate this model |
| 4 | Use the experimental facility and the numerical model for studying the complex flow of acoustic energy in pipes with inhomogeneities and near the open ends |
| 5 | Use the numerical model and experimental facility to understand better the behaviour of the 3-component vector of the sound intensity in a pipe before and after an inhomogeneity |
| 6 | Develop and validate a method to determine modal reflection coefficients of porous materials at normal and oblique incidence |
| 7 | Apply the new method to study the acoustical properties of living plants and use these data to validate the equivalent fluid model |
| 8 | Use the above results to propose a practical method for characterisation of inhomogeneities and materials in pipes based on acoustic data |

Table 1.1: Objectives of the project

## 1.3 Report structure

This thesis is organised in the following manner. Chapter 2 gives coverage of the literature review. Basic concepts of the sound field in a waveguide are presented, together with the sound intensity and methods of its measurement, as well as the existing work on the acoustic pulse reflectometry, porous media and living plants acoustics.

Chapter 3 gives an insight into complex sound intensity theory, the methods of separation of its real and imaginary components and its validation against experimental data.

Chapter 4 presents an application of complex sound intensity data to blockage detection and its reflection and transmission coefficients determination. The adopted experimen-

tal setup is described, and results obtained with it are compared to theoretical predictions.

Chapter 5 describes a method to obtain modal reflection and absorption coefficients of porous materials in a waveguide. The theoretical framework for the developed method is presented, and the adopted experimental setups are described. The modal reflection and total absorption coefficients are shown for several different materials and the quality of obtained results is analysed.

Chapter 6 details the application of the proposed method to obtain the reflection and absorption coefficients to living plants. It introduces criteria for choice of living plants suitable for enhanced sound absorption and examines the approach of linking the morphological parameters of plants with non-acoustical characteristics, such as porosity, flow resistivity and other.

Chapter 7 presents a sensitivity analysis. It offers the comparison between the predicted data and the data simulated to include an artificially introduced phase and a random and constant positioning errors. Furthermore, it examines the influence of the measurement step and window length and shape on the accuracy of the measured data. Finally, it studies how the loudspeaker positioning affects the sound field distribution in a waveguide.

Chapter 8 reviews the achievements and limitations of the conducted research, as well as the future work and recommendations.

Each chapter is concluded with a section summarising the contents of the chapter.

# Chapter 2

# Literature review

The fundamentals of the sound intensity theory are presented in this chapter to give a reader a brief introduction into the underpinning physics. The published papers on the sound propagation in air-filled cylindrical flanged / unflanged pipes are reviewed, as well as the previous work on the sound propagation in the presence of living plants.

## 2.1 Sound field in a duct

Duct acoustics is a branch of acoustics which deals with sound propagation in ducts and waveguides, which is of practical concern in many areas of engineering, such as noise reduction of ventilating and air-conditioning systems, silencers for combustion engines, use of impedance tubes for testing of acoustic properties of materials and similar applications.

A plane wave is the most basic case when a harmonic disturbance in a duct propagates along its axis at the sound speed $c_0$. Linearity condition suggests that any harmonic dis-

turbance occurring at frequency $\omega$ will generate the sound field where the sound pressure $p$ will also vary sinusoidally with time and at frequency $\omega$, and velocity changes and perturbations of density and temperature will have the same frequency. Sound pressure field will then be the product of the complex vibration amplitude and complex factor $e^{i\omega t}$, which takes time into account. It follows that any linear quantity in such sound field can be defined as its real part, so the actual sound pressure is the real part of the complex sound pressure field (Jacobsen, 2010):

$$p = \mathrm{Re}\{\tilde{p}\} = \mathrm{Re}\{|\tilde{p}|e^{i(\omega t+\varphi)}\} = |\tilde{p}|\cos(\omega t + \varphi), \tag{2.1.1}$$

where the tilde above the sound pressure $p$ denotes its complex nature, $i = \sqrt{-1}$ and $\varphi$ is the phase of the complex sound pressure at $t = 0$ moment of time. When the factor $e^{i\omega t}$ is present in the equation, the derivative operator $\dfrac{\partial}{\partial t}$ can be replaced with $i\omega$ and $\dfrac{\partial^2}{\partial t^2}$ with $-\omega^2$. So the linearised wave equation

$$\nabla^2\tilde{p} - \frac{1}{c^2}\frac{\partial^2\tilde{p}}{\partial t^2} = 0 \tag{2.1.2}$$

becomes

$$\nabla^2\tilde{p} + \left(\frac{\omega}{c_0}\right)^2\tilde{p} = \nabla^2\tilde{p} + k^2\tilde{p} = 0, \tag{2.1.3}$$

which is called the Helmholtz equation and where $k$ is a wavenumber. The general solution to this equation for a given frequency $\omega$ is

$$\tilde{p} = p_+e^{i(\omega t-kz)} + p_-e^{i(\omega t+kz)}, \tag{2.1.4}$$

where $p_+$ and $p_-$ are complex quantities representing the waves travelling in the duct forward and backward, respectively, and $z$ is the direction of the axis of the duct.

If the sound wave is propagating from the source at $z < 0$ along the duct, terminated at one end with the surface, as shown in Figure 2.1, then the right-hand side of Equation

(2.1.4) can be considered as a superposition of a wave travelling forward and a wave travelling backward.

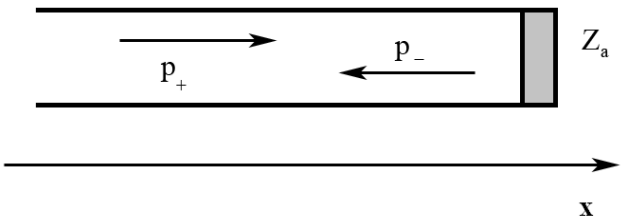


Figure 2.1: Incident and reflected sound wave in a closed pipe

$Z_a$ is the acoustic impedance of the pipe and it will be described later.

$p_+$ is always equal or greater than $p_-$ and their ratio is the reflection coefficient, which depends on the acoustic properties of the surface:

$$R = \frac{p_-}{p_+}. \tag{2.1.5}$$

Equation (2.1.4) can now be rewritten as follows:

$$\tilde{p} = p_+ \left( e^{i(\omega t - kz)} + R e^{i(\omega t + kz)} \right), \tag{2.1.6}$$

which reveals the dependence of the sound pressure amplitude on the position. The maximum value the acoustic pressure can reach occurs in the case of constructive interference, i.e. when the incident and the reflected waves are in phase:

$$p_{max} = |p_+|(1 + |R|), \tag{2.1.7}$$

and the minimum value occurs in case of destructive interference, when the incident

and the reflected waves of the sound pressure are out of phase:

$$p_{min} = |p_+|(1 - |R|), \tag{2.1.8}$$

and their ratio is the standing wave ratio:

$$s = \frac{p_{max}}{p_{min}} = \frac{1 + |R|}{1 - |R|}. \tag{2.1.9}$$

The acoustic velocity is the spatial derivative of the sound pressure:

$$\tilde{u_z} = -\frac{1}{i\omega\rho_0}\frac{\partial\tilde{p}}{\partial z} = \frac{1}{\rho_0 c_0}\left(p_+ e^{i(\omega t - kz)} + p_- e^{i(\omega t + kz)}\right), \tag{2.1.10}$$

where the quantity $\rho_0 c_0$ is called the characteristic impedance of medium, and the acoustic impedance of the pipe is

$$Z_a = \frac{\tilde{p}}{S\,\tilde{u}} = \frac{\rho_0 c_0}{S}\left(\frac{e^{-ikz} + Re^{ikz}}{e^{-ikz} - Re^{ikz}}\right) = \frac{\rho_0 c_0}{S}\left(\frac{(1 + R)}{(1 - R)}\right)_{z=0}, \tag{2.1.11}$$

where the term $S\,\tilde{u}$ is sometimes referred to as the volume velocity and $S$ is the cross-sectional area of the duct. The specific acoustic impedance is the ratio of the sound pressure and the normal sound velocity:

$$Z_i = \frac{\tilde{p}}{\tilde{u}_z} = \rho_0 c_0 \frac{e^{-ikz} + Re^{ikz}}{e^{-ikz} - Re^{ikz}} = Z_a S. \tag{2.1.12}$$

It is related to the mechanical impedance for the unit area, where the mechanical impedance is the ratio of the force, driving the particles inside the waveguide, and the sound velocity:

$$Z_m = \frac{\tilde{p}S}{\tilde{u}_z} = S\rho_0 c_0 \frac{e^{-ikz} + Re^{ikz}}{e^{-ikz} - Re^{ikz}} = Z_a S^2. \tag{2.1.13}$$

From Equations (2.1.11), (2.1.12) and (2.1.13) it is easy to observe that all three types of acoustic impedances are related to each other. Most commonly, the dimensionless,

normalised acoustic impedance, expressed in $\rho_0 c_0$ units, is used:

$$\zeta = \frac{Z_i}{\rho_0 c_0}, \tag{2.1.14}$$

which describes the ratio of the specific acoustic impedance to the characteristic acoustic impedance of fluid. The reflection coefficient $R$ can also be expressed in terms of the acoustic impedance:

$$R = \frac{Z_a - {}^{\rho_0 c_0}/_S}{Z_a + {}^{\rho_0 c_0}/_S}. \tag{2.1.15}$$

Equation (2.1.15) shows the relation between the acoustic impedance, the characteristic impedance of the tube $\frac{\rho_0 c_0}{S}$ and the boundary conditions of the pipe. The value of the reflection coefficient $R$ can vary from 1 to -1. If $|Z_a| \gg \frac{\rho_0 c_0}{S}$, then the reflection coefficient $R \simeq 1$, which means that the sound pressure and sound velocity are in phase and the reflection is from the rigid boundary. If $|Z_a| = \frac{\rho_0 c_0}{S}$, then $R = 0$ and no reflection is taking place. If $|Z_a| \ll \frac{\rho_0 c_0}{S}$, then the reflection coefficient $R \simeq -1$, which implies that the sound pressure and velocity are out of phase. This is true in case of the open-ended pipe at low frequencies, which will be shown later.

If the pipe with the open end is considered, its terminating acoustic impedance is in fact the radiation impedance of the piston installed at the end of the pipe. If the pipe is flanged, then its acoustic impedance is the impedance of the piston put in a rigid baffle.

The transmission coefficient, which is the quantity opposite to the reflection coefficient, is then expressed in a following way:

$$\tau = \frac{p_t}{p_+} = 1 + R, \tag{2.1.16}$$

which shows the ratio of the transmitted power to the incident power.

## 2.2 Sound intensity

The instantaneous sound intensity, which is a product of the sound pressure and the particle velocity in a three dimensional space, can be presented in a following way:

$$\mathbf{I}(t) = p\,\mathbf{u}. \tag{2.2.1}$$

where $\mathbf{u}$ is the particle velocity vector. For a one dimensional plane wave in a narrow pipe, the relationship between the instantaneous pressure and the instantaneous velocity is expressed as follows:

$$u^+ = \frac{p^+}{(\rho_0\, c_0)}, \quad u^- = -\frac{p^-}{\rho_0\, c_0}, \tag{2.2.2}$$

where + and − signs in superscripts refer to the waves propagating forward and backwards in $x$-direction, and the dependence on $z$ and $t$ is implicit. Then, the instantaneous sound intensity is given by

$$I(t) = \frac{(p^+)^2 - (p^-)^2}{\rho_0\, c_0}, \tag{2.2.3}$$

and the time-averaged, or mean intensity -

$$\bar{I} = \frac{(p^+_{rms})^2 - (p^-_{rms})^2}{\rho_0\, c_0}, \tag{2.2.4}$$

where $p^+_{rms}$ and $p^-_{rms}$ are mean square pressures in the forward and backwards directions, respectively. It follows, that if the mean intensity is zero at any point in the sound field, it will be zero everywhere, as mean square pressures do not depend on a position. However, the instantaneous intensity at any point of the field can fluctuate about the zero mean value, implying that the instant flow of energy in a local region can change the direction and magnitude, as the magnitudes of the instantaneous velocity and pressure can fluctuate. Because the potential energy is proportional to the square of the sound pressure, and the kinetic energy is proportional to the square of the particle velocity, there is a continuous exchange between these two keeping the total energy in the pipe

constant in the absence of any losses. The type of this exchange can depend on the nature of a propagating wave. If a pure progressive wave is considered, i.e. a propagating wave transferring energy through the medium, then the maxima of the sound pressure coincide with those of the potential energy, and their spatial distributions are concentrated in clusters. Then the intensity at any point in space varies with time, but is never negative, which results in no intensity oscillations taking place. However, if a pure standing wave is considered, i.e. the wave pattern remaining in a constant position due to the interference of two waves travelling in opposite directions with no net transfer of energy, then the flow is purely oscillatory, indicating alternating concentrations of kinetic and potential energies.

According to Fahy (1995), in the time-stationary fields the instantaneous sound intensity can be divided into two parts: active intensity and reactive intensity. This distinction is used to distinguish between the sound fields with different characteristics. For example, in a plane wave field or in a far field the sound pressure and the particle velocity are in phase which each other, which is a characteristic of an active sound field. In the other types of field, such as a near field, the pressure and the velocity are in quadrature, or $90^{\circ}$ out of phase, which is common for a reactive sound field. The active component represents the net energy transport and the reactive component represents the oscillatory transport of the energy. The time-averaged value of the former component is non-zero, whereas the same of the latter is equal to zero. There are no physical sound fields which would be purely reactive, such as pure standing wave field or pure diffuse field - some amount of the mechanical energy is transformed into heat, which creates a flow of the energy from the region where it is generated to the one where it is dissipated. Although the active sound intensity measurement is more widespread and has more applications (such as sound power determination and location of noise generating regions), the reactive sound intensity is also of use (e.g. the analysis of scattering in monochromatic sound fields).

According to Jacobsen (1991), in a non-monochromatic sound field it is preferable to use the narrow band source to be able to represent the complex instantaneous intensity using the method suggested by Heyser (1986). This approach may cause certain challenges, so it may be sensible to simplify the problem and use a monochromatic representation of the sound field, i.e. use a sine wave excitation. For a monochromatic sound field, the real part is normally called the instantaneous active intensity and the imaginary part the instantaneous reactive intensity (Fahy, 1995). On the other hand, in the case of a stationary sound field, it is common to take a time average of the instantaneous intensity and treating this intensity as a real quantity. Here the real part is often called the active or mean active intensity (Fahy, 1995), so that it corresponds to the terminology used for the instantaneous active intensity discussed previously. This definition works well for the real part of the instantaneous complex intensity. However, if the time average of the imaginary part of the instantaneous intensity is taken, then this will give zero. To address this, Fahy (1995) uses the amplitude of the imaginary part of the instantaneous intensity and defines this as the reactive intensity. Thus for instantaneous complex intensity, Fahy adopts the terminology of instantaneous active and instantaneous reactive intensity, and for non-instantaneous intensity, active and reactive intensity. In view of the simplicity of this approach, the terminology of Fahy is also adopted here.

Two techniques for calculating of the instantaneous complex intensity are investigated here. The first technique is the aforementioned method by Heyser (1986). He defines the instantaneous active $\mathbf{I}(t)$ and reactive $\mathbf{J}(t)$ intensities as

$$\mathbf{I}(t) = \frac{1}{2} p\mathbf{u} + \frac{1}{2}\hat{p}\hat{\mathbf{u}} \tag{2.2.5}$$

and

$$\mathbf{J}(t) = \frac{1}{2}\hat{p}\mathbf{u} - \frac{1}{2} p\hat{\mathbf{u}}, \tag{2.2.6}$$

respectively. Here, $t$ is time, and $p$ and $\mathbf{u}$ are the time history values of pressure and

velocity, respectively, with ˆ denoting the Hilbert transform. The second technique was introduced by Schiffrer and Stanzial (1994), Stanzial et al. (1996), and Stanzial and Prodi (1997), who define radiating and oscillating components of instantaneous intensity so that

$$\mathbf{I}_{rad}(t) = \frac{p^2 \langle p\mathbf{u} \rangle}{\langle p^2 \rangle} \tag{2.2.7}$$

and

$$\mathbf{J}_{osc}(t) = \frac{\langle p^2 \rangle p\mathbf{u} - p^2 \langle p\mathbf{u} \rangle}{\langle p^2 \rangle}, \tag{2.2.8}$$

respectively, and $\langle \cdot \rangle$ denotes the time average. This method introduces the time averaging, which does not appear in the method described by Heyser (1986). It is not an issue for time stationary problems, but for transient problems the result will depend on the choice of the time window chosen for the averaging procedure. Stanzial and Prodi (1997) suggested that their method can be applied to transient problems if the analysis is limited to narrow band signals. However, the latter method must be used with care for the analysis of transient problems, as the outcome will strongly depend on the choice of the window selected for time averaging and filtering method (see Duan et al., 2013). If multiple signals are present within the window and they do not overlap, this may cause interference and distorted values of complex intensity. Furthermore, the radiation of sound from the complex noise sources should be studied with caution.

Nonetheless, if used carefully, then both methods are of use in the analysis of instantaneous intensity. It is still possible to use these definitions for a stationary monochromatic field by taking a time average of the instantaneous intensity, however, to compute non-instantaneous, frequency dependent active and reactive intensity, it is usual practice to use the cross-spectrum between the measured sound pressure and particle velocity:

$$\mathbf{I}(\omega) = \mathrm{Re}[S_{pu}(\omega)] \tag{2.2.9}$$

and

$$\mathbf{J}(\omega) = -\mathrm{Im}[S_{pu}(\omega)], \tag{2.2.10}$$

which are active and reactive intensities in a time stationary sound field, respectively. $S_{pu}(\omega)$ denotes the cross-spectrum for $\omega \geq 0$, and the minus sign in Equation (2.2.10) refers to the reactive intensity pointing in the direction of decreasing pressure.

For theoretical predictions of non-instantaneous active and reactive intensity, the following expressions were used, respectively (Duan et al., 2013):

$$\mathbf{I}(\omega) = 0.5\mathrm{Re}\{p\mathbf{u}^*\} \tag{2.2.11}$$

and

$$\mathbf{J}(\omega) = 0.5\mathrm{Im}\{p\mathbf{u}^*\}. \tag{2.2.12}$$

## 2.3 Sound intensity measurements

Measurements of the acoustic intensity field are far more complicated than measurements of the acoustic pressure. As described above, the acoustic intensity is a product of acoustic pressure and acoustic velocity. According to Fahy (1995), the latter two quantities are both functions of the velocity potential of the field, but the relationship between them depends on the acoustic field and is not single-valued. Therefore, two transducers are required to determine the acoustic intensity. Currently, only two methods of acoustic intensity measurement are available. One of them employs a matched pair of microphones and it is called 'p-p' method. The other, relatively new method relies on a microphone combined with a particle velocity sensor. Both methods have their advantages and disadvantages. Background noise reduces the accuracy of 'p-p' probe, but has no influence on 'p-u' probe, and reactive sound fields increase 'p-u' probe phase mismatch, but do not affect 'p-p' probe (Jacobsen, 2005).

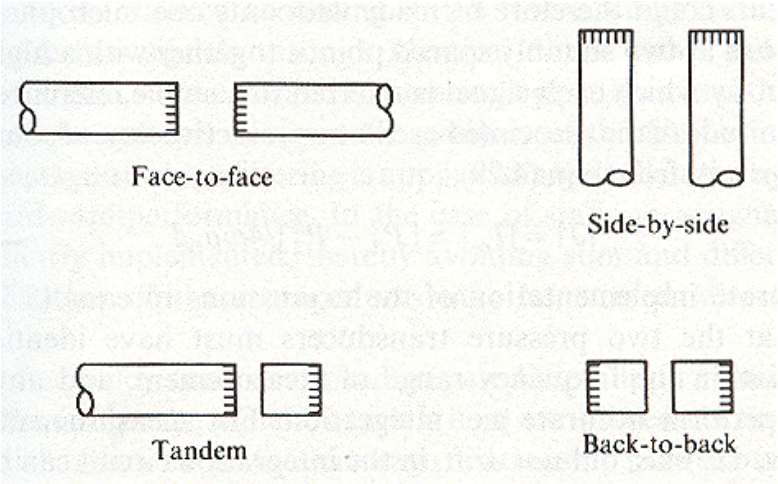


Figure 2.2: Schematic p-p intensity probe configurations (Fahy, 1995).

### 2.3.1 The 'p-p' principle

This method uses two identical pressure microphones, placed closely together, so that the distance between the microphones is much smaller that the acoustic wavelength. There are different types of microphones' configurations, some of which are shown in Figure 2.2.

In a sound field with small amplitude variations the acoustic velocity can be expressed as

$$u_n(t) = -\frac{1}{\rho_0}\int_{-\infty}^{t}\left(\frac{dp(\tau)}{d\mathbf{n}}\right)\Delta\tau, \tag{2.3.1}$$

where **n** is the normal in the direction perpendicular to the microphone plane, and approximated as

$$u_n(t) \approx -\frac{1}{\rho_0\Delta}\int_{-\infty}^{t}\left[p_{m_1}(\tau) - p_{m_2}(\tau)\right]\Delta\tau, \tag{2.3.2}$$

where $\Delta$ is the distance between the microphones. The acoustic pressure at $\frac{\Delta}{2}$ can be approximated as

$$p(t) \approx \frac{1}{2}[p_{m_1}(t) + p_{m_2}(t)], \tag{2.3.3}$$

so the acoustic intensity becomes

$$I_n(t) \approx \frac{1}{2\rho_0\Delta}[p_{m_1}(t) + p_{m_2}(t)] \int_{-\infty}^{t} [p_{m_1}(\tau) - p_{m_2}(\tau)]\,\Delta\tau. \tag{2.3.4}$$

The error, associated with this principle of intensity measurements in a plane wave interference field is equal to

$$e_{pp}(I) = \frac{I_e - I}{I} \approx -\frac{2}{3}(kh)^2 + \frac{2}{15}(kh)^4, \tag{2.3.5}$$

where $h$ is half the separation distance between two microphones, and $e(I) < 5\%$ for $2kh < 0.55$. The current manufacturers of the intensity probes, based on 'p-p' principle, include such companies as Danish-based Brüel and Kjær and G.R.A.S.

### 2.3.2 The 'p-u' principle

In this method, described by Fahy (1995, pp. 90-91), two parallel ultrasonic beams, directed oppositely, are affected by air movement of sound wave propagation. This results in a phase difference upon arrival to a respective receiver. If the transit times are $t^+ = \frac{\Delta}{c+u}$ and $t^- = \frac{\Delta}{c-u}$, where $\Delta$ is the distance between the transducers (approximately 28 mm), $c$ and $u$ are the velocities of ultrasonic beam and particles, respectively, this will result in following phase difference:

$$\delta\varphi = \omega_u \Delta \left[\frac{1}{c-u} - \frac{1}{c+u}\right] \approx \frac{2\,\omega_u\,du}{c^2}, \tag{2.3.6}$$

where $\omega_u$ is the ultrasonic frequency. Then the phase difference is transformed into the electrical analogue of $u$. The error of 'p-u' measurements can be quantified in a following way, assuming perfect transduction by the associated pressure transducer:

$$e_{pu}(I) = \frac{1}{2}\left(\frac{c^2}{2\Delta}\frac{T^- - T^+}{u(T^+/2, \Delta/2)} - 1\right), \tag{2.3.7}$$

where $T^+$ and $T^-$ are signal transit times in positive and negative directions, respectively.

The limitation of this probe is its inability to perform in conditions when any non-acoustical flow is present, such as wind. Furthermore, as it measured the particle velocity only in one direction at a time, it is impossible to get a full instantaneous intensity vector. However, if the information on the mean intensity is sufficient, three sequential measurements can be performed and their results combined. The only manufacturer of the intensity probes based on the 'p-u' principle is the company called Norwegian Electronics, but due to more accurate and smaller probes becoming commercially available, its production has been discontinued.

### 2.3.3 Microflown

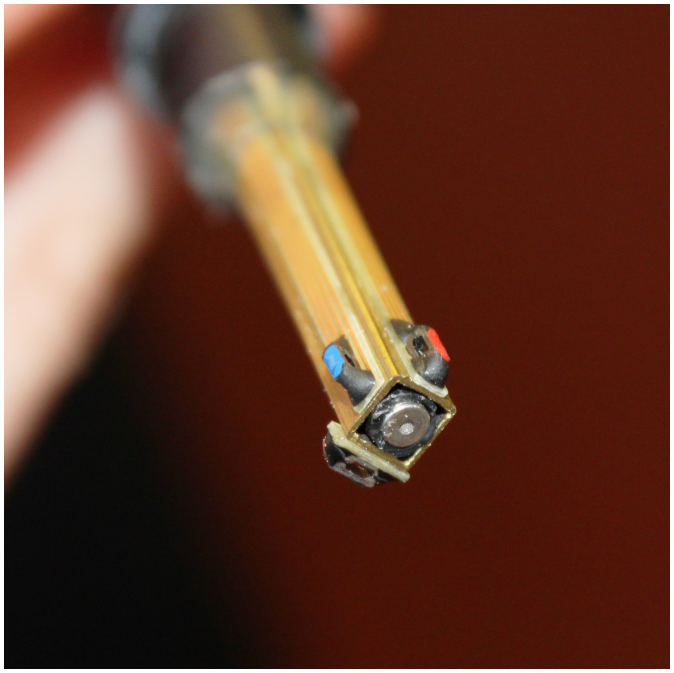

Figure 2.3: Close-up of Microflown velocity sensors situated at the sides of the probe - radial blue, circumferential red, axial green (on the opposite side of the red sensor), and a microphone at the top of the probe.

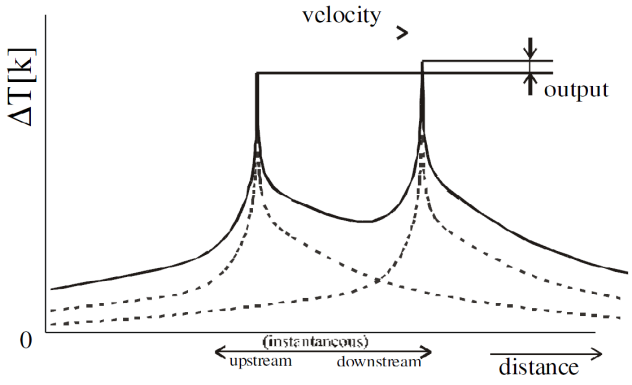


Figure 2.4: Temperature distribution due to the convection between two wires, (De Bree, 2004).

Microflown is an acoustic probe, based on the 'p-u' principle, but it uses a different approach to the velocity measurement than the one described above (de Bree, 2007). It was invented at the University of Twente, Netherlands, in 1994, and was firstly used for the analysis of the noise-related problems, but later it was discovered that it can deliver intensity data of a higher quality that traditionally used 'p-p' sensors. It consists of a standard microphone and another velocity sensor which is two tiny platinum wires, separated by approximately 100 μm. Overall, the sensor is 1 mm wide, 2 mm long and 300 μm thick. The wires themselves are 200 nm thin and 10 μm wide. They are heated to the operational temperature of about 200°C. Particle velocity alters the temperatures of both wires, and the upstream wire is heated less than the downstream due to the convective heat transfer. So the temperature difference occurs (see Figure 2.4), causing the change in the electrical resistance and a voltage difference. This difference is proportional to the velocity of the flow, and is also directional, so it is possible to determine the direction of the sound wave movement. This velocity probe seems to use a similar principle to hot wire probes used in wind tunnels in the 1960's and 70's and still made by companies such as Dantec Dynamics.

The frequency response of the sensor is flat only in the region between 100 Hz and 1 kHz. At the lower frequencies the sensitivity is believed to be increasing due to

the thermal boundary layer on the wires. At the higher frequencies the sensitivity is decreased because of the diffusion effects. To correct the frequency response, electric signal conditioning is used, which modifies the amplitude and the phase response to make them flat. The Microflown conditioning amplifier has two data recording modes: corrected and uncorrected. In the uncorrected mode, the particle velocity sensitivity and the phase can be estimated using the following formulae:

$$S_u\,[\text{mV/Pa}] = \frac{S_u@250\text{ Hz}}{\sqrt{1+\frac{f_{c1u}^2}{f^2}}\sqrt{1+\frac{f^2}{f_{c2u}^2}}\sqrt{1+\frac{f^2}{f_{c3u}^2}}\sqrt{1+\frac{f_{c4u}^2}{f^2}}}, \tag{2.3.8}$$

$$\phi_u\,[\text{deg}] = \arctan\frac{C_{1u}}{f} - \arctan\frac{f}{C_{2u}} - \arctan\frac{f}{C_{3u}} + \arctan\frac{C_{4u}}{f}, \tag{2.3.9}$$

and for the corrected mode:

$$S_u\,[\text{mV/Pa}] = \frac{S_u@250\text{ Hz}}{\sqrt{1+\frac{f_{c1u}^2}{f^2}}\sqrt{1+\frac{f_{c4u}^2}{f^2}}}, \tag{2.3.10}$$

$$\phi_u\,[\text{deg}] = \arctan\frac{C_{1u}}{f} + \arctan\frac{C_{4u}}{f}, \tag{2.3.11}$$

where $S_u@250$ Hz is the sensitivity at 250 Hz, $f_{c1u}, f_{c2u}, f_{c3u}, f_{c4u}$ are sensitivity corner-frequencies, $C_{1u}, C_{2u}, C_{3u}, C_{4u}$ are phase cornerfrequencies, $f$ is the frequency of interest, and a cornerfrequency is a frequency at which the frequency response decays 3dB. These formulae are given in a conditioning report, which is provided with every Microflown probe. Therefore, it is possible to correct the sensitivity and phase mismatch of the recorded signal.

There are several commercially available Microflown products, such as Scanning Probe, which consists of a single Microflown sensor; 1/2" PU and 1/2" mini PU probes, which consist of a small pressure element, a velocity sensor, are packaged in a special case which has a gain of 15 dB, with the latter being smaller in size; the PU match being the smallest 'p-u' probe and the USP, which consists of a pressure microphone and three

orthogonally placed velocity sensors and which is depicted in Figure 2.3. The latter has been used for several measurements described in this thesis. Its advantages are its size, which is approximately 5x5x5 $mm^3$ without a cap, whole audible frequency bandwidth, measurements in the near and reactive fields and the need of only four channels for a full three-dimensional sound field description.

## 2.4 Models for sound propagation in a pipe

One old problem which continues to attract the attention is the problem of sound propagation in a pipe with a discontinuity. The most simple discontinuity is the end of an open pipe with or without a flange. The problem of the acoustic pressure distribution in flanged and unflanged circular pipes is not new and it has been studied intensively. The initial studies go back to Lord Rayleigh (1896), who investigated the wave motion in open-ended pipes and made the first approximate calculations of the correction for an open end.

Levine and Schwinger (1948) used the Green's function to formulate a problem. They derived the integral equation resembling Wiener-Hopf integral and solved it using the Fourier transform method. However, their solution was for an unflanged pipe only, as the presence of an infinite flange on an open end of the pipe would require the additional term in the Green's function, representing the image effect of the flange, which considerably complicates the solution. Furthermore, the solution included the fundamental mode only and did not take into account the effect of higher order modes.

Nomura et al. (1960) solved the radiation problem for the pipe with the infinite flange for $\gamma = ka < 3.8317$, making use of Weber-Schafheitlin integrals and Jacobi polynomials. They derived two infinite sets of equations, one for the outside and one for the inside region, solved them numerically and connected the solutions at the boundary

Felsen and Yee (1968) calculated the modal reflection and coupling coefficients for both flanged and unflanged semi-infinite pipes using the ray tracing method. The incident mode was decomposed into the local plane waves colliding with the edge of the pipe mouth and the discontinuity on the mouth was treated as an equivalent nonisotropic ring source, whose radiation back into the pipe is regarded as the reflected waves. These waves were then converted to the modal form to derive the modal reflection coefficients. Although the solution for the low-frequency regime is not straightforward when applying this method, the authors succeeded in modifying the suggested algorithm to accommodate all frequencies.

A solution for the two-dimensional case of sound propagation inside an open-ended flanged pipe was proposed by Shenderov (1972). He uses the modal expansion of the velocity potential inside a pipe, and solves the equation for the unknown modal reflection coefficients using a change of variables and Dirichlet double integral substitution formula. The results of his method are compared with the three-dimensional models in the subsequent chapter of this thesis.

Zorumski (1973) extended the Morse's equation (1949) for the radiation impedance of a vibrating rigid piston to calculate the generalised radiation impedances $Z_{mnl}$ for all modes in circular and annular waveguides with the infinite flange on an end of a waveguide. The equation for $Z_{mnl}$ was simplified to a single infinite integral and then was used to derive an infinite matrix equation, which related the generalised radiation impedances to the generalised mode reflection coefficients $R_{mnl}$. The possible singularity was treated using the Sonine's infinite integral and Neumann's addition theorem.

Norris and Sheng (1989) have also represented the acoustic potential in the pipe as the modal series. They solve the problem in a way similar to Nomura, but the novelty of their method is the fact that they are treating a flanged pipe as a rigid half-space with infinitely deep holes.

Silva et al. (2009) used the results of Levine and Schwinger for the unflanged case and the results of Zorumski for the case of infinite flange and derived the approximation formulae for the reflection coefficients by numerical and analytical fitting. They ensured that all the basic mathematical and physical principles, like causality and hermitian symmetry, were met and presented three models for the reflection coefficient calculation, which are shown in Figure 2.5 [see Equations (15), (16) and (21) in the original paper].

| Model | Unflanged case $\beta = 1/2,\ \eta = 0.6133$ | Flanged case $\beta = 1,\ \eta = 0.8216$ |
|---|---|---|
| $\mathcal{R}(\omega) = -\left(1 - \frac{jka}{\alpha}\right)^{-(\nu+1)}$<br>$r(t) = -A\left(\frac{ct}{a}\right)^{\nu} \exp\left(-\alpha\frac{ct}{a}\right)$ | $\alpha = 1.2266$<br>$\nu = 0.504$<br>$A = 1.534\ \frac{c}{a}$ | $\alpha = 0.8216$<br>$\nu = 0.350$<br>$A = 0.861\ \frac{c}{a}$ |
| $\mathcal{R}(\omega) = -\frac{1-n_1 jka}{1-d_1 jka+d_2(jka)^2}$ | $n_1 = 0.167$<br>$d_1 = 1.393,$<br>$d_2 = 0.457$ | $n_1 = 0.182$<br>$d_1 = 1.825,$<br>$d_2 = 0.649$ |
| $\lvert\mathcal{R}\rvert = \frac{1+a_1(ka)^2}{1+(\beta+a_1)(ka)^2+a_2(ka)^4+a_3(ka)^6},$<br>$\frac{L}{a} = \eta\frac{1+b_1(ka)^2}{1+b_2(ka)^2+b_3(ka)^4+b_4(ka)^6},$<br>non causal | $a_1 = 0.800$<br>$a_2 = 0.266$<br>$a_3 = 0.0263$<br>$b_1 = 0.0599$<br>$b_2 = 0.238$<br>$b_3 = -0.0153$<br>$b_4 = 0.00150$ | $a_1 = 0.730$<br>$a_2 = 0.372$<br>$a_3 = 0.0231$<br>$b_1 = 0.244$<br>$b_2 = 0.723$<br>$b_3 = -0.0198$<br>$b_4 = 0.00366$ |

Figure 2.5: Results of approximate radiation models (Silva, 2009).

### 2.4.1 Hybrid FEM model

A suitable theory that was used to predict the sound field distribution at the end of an open-ended flanged pipe was proposed by Duan et al. (2013). It is a hybrid model, originally developed by Kirby (2008), and applied to study the sound propagation in ventilation ducts (Duan and Kirby, 2012). It makes use of the modal decomposition approach for uniform and rather simple regions in the pipe, where the sound field distribution is rather simple, but employs finite element modelling for regions such as a

geometrical discontinuity, point source or wall impedance change. This model is used for the theoretical predictions of the sound intensity distribution in waveguides in this thesis.

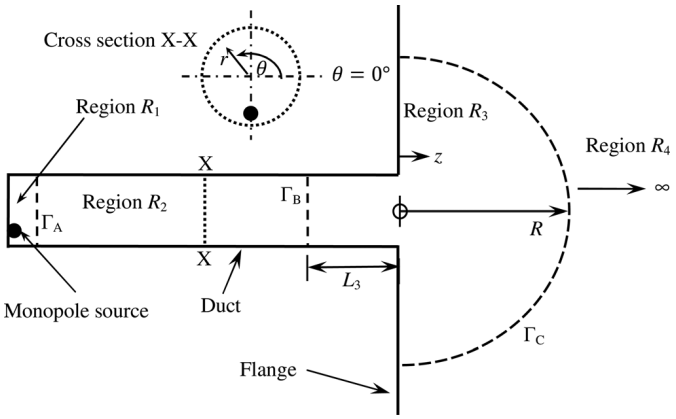


Figure 2.6: Schematic drawing of a pipe (Duan *et al.*, 2013).

Figure 2.6 schematically shows the problem which is modelled here. Sound propagation in region $R_q$ ($q = 1, 2, 3$, and 4) is governed by the following acoustic wave equation:

$$\frac{1}{c_0^2}\frac{\partial^2 p_q}{\partial t^2} - \nabla^2 p_q = F_1, \tag{2.4.1}$$

where $c_0$ is the speed of sound, $p_q$ is the acoustic pressure, $t$ is time, and $F_1$ is assumed to be a time harmonic sound source in region $R_1$, given as

$$F_1 = \delta(r - r_0)\,\delta(\theta - \theta_0)\,\delta(z - z_0)\,e^{i\omega t}, \tag{2.4.2}$$

for a cylindrical coordinate system $(r, \theta, z)$, with $(r_0, \theta_0, z_0)$ denoting the location of the monopole sound source, and $\delta(x)$ is the Dirac delta-function.

A finite element discretisation is used for regions $R_1$ and $R_3$, so that the pressure $p = \mathbf{Np}$, where $\mathbf{N}$ and $\mathbf{p}$ are row and column vectors, respectively, and these hold the global trial (or shape) functions and the unknown acoustic pressures. After applying the Galerkin

method, the governing equation in region $R_1$ can be written as

$$\int_{\mathbf{\Omega_1}} \left[\nabla \mathbf{N_1}^T \nabla \mathbf{N_1} - k_1^2 \mathbf{N_1}^T \mathbf{N_1}\right] d\mathbf{\Omega_1}\, \mathbf{p_1} = \int_{\mathbf{\Gamma_A}} \mathbf{N_1}^T \nabla p_1 \cdot \mathbf{n}_A \, d\Gamma_1 + \int_{\mathbf{\Omega_1}} \mathbf{N_1}^T F_1 \, d\mathbf{\Omega_1} \tag{2.4.3}$$

with

$$\int_{\mathbf{\Omega_1}} \mathbf{N_1}^T F_1 \, d\mathbf{\Omega_1} = \mathbf{N_1}^T (r_0, \theta_0, z_0). \tag{2.4.4}$$

Here, $\mathbf{\Omega_1}$ denotes the volume of region $R_1$, $\Gamma_1$ is its total outer surface, and $\mathbf{n_A}$ is the outward unit normal vector over surface $\Gamma_A$; the surfaces of region $R_1$ that do not lie on $\Gamma_A$ are assumed to be hard walled so the integral over these surfaces in Equation (2.4.3) is zero.

For region $R_3$, the acoustic pressure is approximated in a similar way as described previously:

$$p_3(x, y, z) = \sum_{j=1}^{n_3} N_{3_j} \, p_{3_j} = \mathbf{N_3}\, \mathbf{p_3}, \tag{2.4.5}$$

where $N_{3_j}$ is a global trial (shape) function for the mesh in region $R_3$, $p_{3_j}$ are values of sound pressure at nodes $j$, $n_3$ in the number of nodes in region $R_3$, and $\mathbf{N_3}$ and $\mathbf{p_3}$, are row and column vectors, respectively. After applying Galerkin method, the governing equation for region $R_3$ is

$$\int_{\mathbf{\Omega_3}} \left[\nabla \mathbf{N_3^T} \nabla \mathbf{N_3} - k_3^2 \mathbf{N_3^T} \mathbf{N_3}\right] d\mathbf{\Omega_3}\, \mathbf{p_3} = \int_{\Gamma_3} \mathbf{N_3^T} \nabla p_3 \cdot \mathbf{n}_3 \, d\Gamma_3, \tag{2.4.6}$$

where $\mathbf{n}_3$ is the outward unit normal vector to $R_3$.

The pressure in regions $R_2$ and $R_4$ is expanded over a series of eigenmodes to give

$$p_2(r, \theta, z) = \sum_{n=0}^{\infty} A_n \, \Phi_n(r, \theta) \, e^{-ik\lambda_n z} + \sum_{n=0}^{\infty} B_n \, \Phi_n(r, \theta) \, e^{ik\lambda_n z} \tag{2.4.7}$$

and

$$p_4(r,\theta,z) = \sum_{n=0}^{\infty} C_n\, \Upsilon(r)\, \Psi_n(\theta,\phi), \tag{2.4.8}$$

respectively. Here, $A_n$, $B_n$ and $C_n$ are modal amplitudes. The dimensionless wavenumber in region $R_2$ is given by $\lambda_n$, and the eigenfunctions in regions $R_2$ and $R_4$ are given by $\Phi_n(r,\theta)$ and $\Psi_n(\theta,\phi)$, respectively. In region $R_4$, the sound pressure field is separated into a radial component $\Upsilon(r)$ and a transverse component $\Psi(\theta,\phi)$. Substituting Equation (2.4.8) in the governing equation (2.4.1) yields, after separating variables and re-arranging:

$$\frac{1}{\Upsilon_n(r)}\left[r^2\frac{\partial^2\Upsilon_n(r)}{\partial r^2} + 2\,r\,\frac{\partial\Upsilon_n(r)}{\partial r}\right] + k_4^2\,r^2 = -\frac{1}{\Psi_n(\theta,\phi)}\,\nabla^2_{\theta\phi}\,\Psi_n(\theta,\phi), \tag{2.4.9}$$

where the operator $\nabla^2_{\theta\phi} = (1/\sin\theta)\,(\partial/\partial\theta)\,(\sin\theta\,(\partial/\partial\theta)) + (1/\sin\theta)\,(\partial^2/\partial\phi^2)$. Separation of variables in Equation (2.4.9) means that both sides of it must be equal to some constant on the right-hand side of Equation (2.4.9), then $\Psi(\theta,\phi)$ must satisfy:

$$\nabla^2_{\theta\phi}\Psi_n(\theta,\phi) + s_n^2\,\Psi_n(\theta,\phi) = 0. \tag{2.4.10}$$

In the same manner, the left-hand side of Equation (2.4.9) can be substituted with $\sigma_n(\sigma_n+1) = s_n^2$, and then

$$\zeta^2\,\frac{\partial^2\Upsilon_n(r)}{\partial\zeta^2} + 2\,\zeta\,\frac{\partial\Upsilon_n(r)}{\partial\zeta} + \left[\zeta^2 - \sigma_n(\sigma_n+1)\right]\Upsilon_n(r) = 0 \tag{2.4.11}$$

with $\zeta = k_4\,r$, and $k_4$ is the wavenumber in region $R_4$. Then

$$s_n^2 = \sigma_n(\sigma_n+1). \tag{2.4.12}$$

Equation (2.4.11) can be solved analytically, yielding

$$\Upsilon_n(r) = h^{(2)}_{\sigma n}(k_4 r), \tag{2.4.13}$$

where $h^{(2)}_{\sigma n}$ is spherical Hankel function of the second kind, of order $\sigma_n$, which is a well-known solution for spherical harmonics. For sound radiation from a sphere Hankel functions are of integer order, with $\sigma_n = 0, 1, 2, 3$. However, a truncated sphere is used in the this study, so that the order of Hankel function is no longer integer except for the fundamental mode, where $\sigma_n = 0$.

The hybrid method proceeds by enforcing continuity of the acoustic pressure and normal velocity over the surfaces $\Gamma_A$, $\Gamma_B$ and $\Gamma_C$, and these conditions are enforced here using mode matching procedure (Kirby, 2008). The final system of equations is written in the matrix form to give

$$\begin{bmatrix} \mathbf{R_{12}} & \mathbf{R_{13}} \\ \mathbf{R_{31}} & \mathbf{R_{34}} \end{bmatrix} \begin{bmatrix} \mathbf{T_{12}} \\ \mathbf{T_{34}} \end{bmatrix} = \begin{bmatrix} \mathbf{F_1} \\ \mathbf{0} \end{bmatrix} \tag{2.4.14}$$

Equation (2.4.14) forms a set of $n_t = n_1 + 2m_2 + n_3 + m_4$ linear equations, where $n_1$ and $n_3$ are the number of nodes in regions $R_1$ and $R_3$, and $m_2$ and $m_4$ are the number of modes in regions $R_2$ and $R_4$, respectively. The terms of Equation (2.4.14) are defined in the original papers by Kirby (2008) and Duan et al. (2013).

Here, the outer radius of the finite element mesh in Region $R_3$ is $R$. If only one plane wave propagates, the problem is reduced to two dimensions only. However, above the first cut-on frequency the problem is no longer axisymmetric, and a three dimensional model is required. A very fine mesh must be used in regions $R_1$ and $R_3$ to ensure a good accuracy of the predictions. For the two dimensional model, a minimum of 45 nodes per wavelength is recommended to use (Duan et al., 2013). For the three-dimensional model the mesh within $R_3$ is optimised, so it is finer on surfaces $\Gamma_B$ and $\Gamma_C$, but coarser inside these regions for computational efficiency. Here, at least 27 nodes per wavelength are present on the surfaces $\Gamma_B$ and $\Gamma_C$, and 11 nodes per wavelength within the volume of the regions. 40 and 60 modes are used in Region $R_2$ for two dimensional and three dimensional models, respectively, while 80 and 120 modes were employed in Region $R_4$.

## 2.5 Acoustics pulse reflectometry

Acoustic methods have been used extensively to test the conditions of a pipe and locate blockages, cracks or other inhomogeneities. The primary application of these methods is linked to the quality inspection of pipes in chemical engineering, oil, gas and water industries and musical instruments. These methods are attractive as they offer a fast and non-destructive means for locating inhomogeneities or determining the geometry of a remote section of a pipeline. Many of the methods are based on the acoustic pulse reflectometry, the original application of which was seismological, to observe the stratifications in the earth's crust. The crust is made up of several layers of different rock, so when a pressure wave penetrates these layers, reflections occur due to impedance differences between the layers and they are recorded at the surface. An impulsive pressure wave is used as a source of sound excitation, produced by a dynamite explosion, or similar. Due to the impulsive nature of the excitation signal, the recorded signal is called the input impulse response. Ware and Aki (1969) were the first to calculate the reflection coefficients of different layers from the input impulse response. Their method assumes no losses during the propagation. Once the boundary reflection coefficients and surface impedances of the rock are known, the impedances of the deeper layers of the rock can be obtained. This phenomenon is similar to that when the pulse reflects from any impedance discontinuity in the pipe, and several reflections are combined into one impulse response. This allows the determination of the pipe geometry and detection of leaks, blockages and other discontinuities.

One of the first works on the blockage detection in pipes was by Antonopoulos-Domis (1980). He found that the first two resonant frequencies of the pipe depend on the location of the blockage and employed the eigen-frequency shift analysis to detect the blockage in the cooling system wrapper of sodium-cooled fast nuclear reactors. However, his method cannot identify the size and the location of the blockage.

It was subsequently found by Wu and Fricke (1990) that the eigen-frequency shift is uniquely related to the location of the blockage, and the amplitude of this shift depends on the blockage size. Although their method delivers very accurate results, it is inapplicable for a majority of measurements. It requires two separate tests to be performed, with and without the blockage in the pipe, and with different boundary conditions at the pipe termination, where each of the tests asks for at least on end of the pipe to be closed with a perfectly rigid termination.

Based on the work of Wu and Fricke, de Salis and Oldham (1999) introduced a method to recover the blockage area under one set of pipe termination boundary conditions. It relies on the measurement of resonance and anti-resonance frequencies. The authors made use of a deterministic maximum length sequence to drive the loudspeaker, in order to minimise the problem of the anti-resonance frequencies, corresponding to pressure minima, being affected by background noise. It was shown later by the same authors (2001) that it is possible to omit the measurements in the duct without the blockage.

Recently, Duan et al. (2015) suggested a method to obtain both the length and cross-sectional area of a blockage using a single microphone to capture the incident and reflected pulses. The amplitude and phase change between the incident and reflected signals were substituted into two independent equations which in turn recover the length and cross-sectional area of the blockage. Although the measurements are limited to the plane wave regime, a relatively large number of blockage types can be recovered.

A substantial amount of research was performed in the musical acoustics area. Reconstructions of the bores of various brass instruments were presented by Smith (1988), Watson and Bowsher (1987, 1988) and Watson (1989), using the input impulse responses measured with a pulse reflectometer. The cylindrical symmetry was assumed in their works. Later, Amir et al. (1995) presented a layer-peeling method, which included the effect of losses.

## 2.6 Sound propagation in porous media

### 2.6.1 Porous materials

Porous materials play a significant role in everyday life. Their physical properties are of interest in geophysics, aero and civil engineering, medicine and other science and engineering disciplines. Hence, it is important to have robust analytical and numerical methods which are capable of predicting their behaviour in real-life applications. In acoustics, porous materials are used mainly for noise abatement. In these applications porous materials are able to convert a considerable amount of mechanical energy of vibration or incident sound wave into heat. This is achieved through the viscous, inertial and thermal energy dissipation in the material pores and through the inherent mechanical damping in the material frame.

Porous materials are heterogeneous structures, which consist of a solid skeleton (solid phase) and a network of interconnected pores, saturated by a fluid, usually air or water (fluid phase). Generally, the volume occupied by air in acoustic porous media is higher than 90%, which means that the density of a porous material is more than 10 times smaller than that of the skeleton, making the material lightweight and dissipative, which is of a great advantage in engineering applications. The skeleton may be either continuous, as in foams or ceramics, or non-continuous, as in fibrous or granular materials. The process of energy dissipation by porous materials is governed by three separate mechanisms. The first one is structural losses, which are attributed to the vibration of the skeleton. At the molecular level, this mechanism is caused by the rotation of molecules with respect to one another, which decreases the initial energy gained by the material. The second mechanism is associated with the heat transfer between the areas occupied by the pores and solid skeleton. The thermal conductivity of air is usually much smaller than that of the skeleton material, which causes the diffusion and the heat exchange between the two phases. Finally, the third mechanism is connected to

the viscous losses. The viscous losses in porous materials are caused by the movement of viscous fluid layers with respect to one another, which generates dissipation. A viscous boundary layer is formed. If the thickness of the viscous boundary layer is much smaller in comparison to the side of the pore, then the viscous effects can be neglected, whereas if they are of the same order of magnitude, the viscous effects have to be taken into account.

There are several non-acoustical parameters of a porous medium which values determine its acoustical properties. The first macroscopic parameter is the open porosity, which is usually denoted by $\phi$. It is the dimensionless ratio of the volume of air contained in a porous material sample to the total volume of that sample:

$$\phi = \frac{V_{air}}{V_{total}}, \tag{2.6.1}$$

where $V_{air}$ is the volume occupied by the air in pores, and $V_{total}$ is the total volume occupied by the porous material. It should be noted that only the air contained in open pores counts towards the open porosity. A material is acoustically non-porous if its pores are closed. The porosity of good quality sound absorbing materials is usually above 0.9.

The flow resistivity $\sigma$ is another macroscopic parameter, defining the resistance to move air through a material sample of the thickness $d_s$:

$$\sigma = \frac{P_2 - P_1}{Q\, d_s}, \tag{2.6.2}$$

where $P_2 - P_1$ is the pressure difference across the thickness of the sample and $Q$ is the airflow per unit surface. The unit of the flow resistivity is $N\, m^{-4} s$.

Another macroscopic parameter is the tortuosity $\alpha_\infty$. Johnson et al. (1987) describe it as a “measure of a disorder in a material system”. Its mathematical definition is given

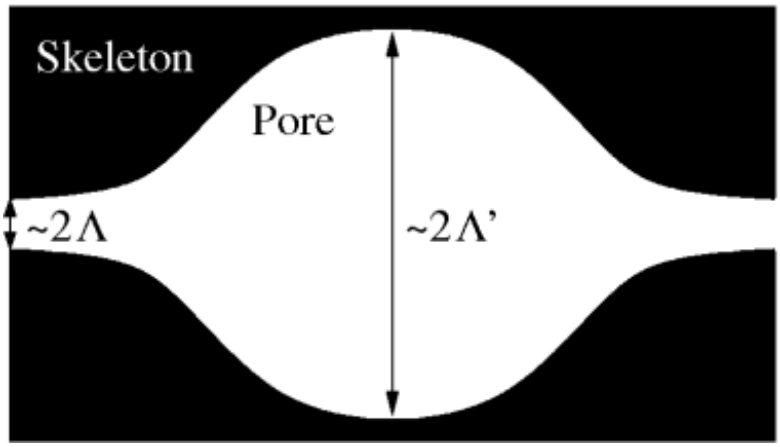


Figure 2.7: A schematic representation of a pore. The thermal characteristic length, controlling the thermal effects at medium and high acoustical frequencies is related to the size of the pores whereas the viscous characteristic length, controlling the viscous effects at medium and high acoustical frequencies is related to the size of the interconnection between two pores (Matelys, 2014).

by

$$\alpha_\infty = \frac{\frac{1}{V}\int_V v^2 dV}{\left(\frac{1}{V}\int_V \mathbf{v} dV\right)^2}, \tag{2.6.3}$$

where $V$ is the homogeneisation volume and $\mathbf{v}$ is the velocity of the fluid particles at high frequencies, where the viscous boundary layer is much smaller compared to the characteristic size of the pores. The tortuosity can also be described as a factor of the structure shape and expressed as (Zwikker and Kosten, 1949):

$$\alpha_\infty = \frac{1}{\cos^2 \theta_p}, \tag{2.6.4}$$

where $\theta_p$ is an angle between the axes of the pores and the surface normal.

Another parameters are the viscous (Johnson et al., 1987) and thermal (Champoux and Allard, 1991) characteristic lengths. These parameters describe the thermal and viscous effects in a porous material and relate to the geometry of a pore (see Figure 2.7).

To express the wave equation for porous media, it is assumed to be an equivalent fluid with complex and frequency-dependent parameters. It is achieved by combining the

equation of motion:

$$i\omega\tilde{\rho}_{eq}\mathbf{v}_{eq} = -\nabla p, \tag{2.6.5}$$

and constitutive law:

$$p = -\tilde{K}_{eq}\nabla.\mathbf{u}_{eq}, \tag{2.6.6}$$

where $\mathbf{v}_{eq} = i\omega\,\mathbf{u}_{eq}$ is the fluid velocity, $\mathbf{u}_{eq}$ is the fluid displacement, $\tilde{\rho}_{eq}$ is the equivalent fluid density and $\tilde{K}_{eq}$ is the equivalent fluid bulk modulus. Then the wave propagation equation is defined in a similar way to Helmholtz equation:

$$\nabla^2 p + \delta_{eq}^2 p = 0, \tag{2.6.7}$$

with $\delta_{eq}$ being the equivalent fluid wavenumber. It can be expressed as follows:

$$\delta_{eq} = \omega\sqrt{\frac{\tilde{\rho}_{eq}}{\tilde{K}_{eq}}}. \tag{2.6.8}$$

The characteristic impedance and the complex sound speed of the equivalent fluid are then presented in the following way, respectively:

$$Z_{eq} = \tilde{\rho}_{eq}\tilde{c}_{eq} = \sqrt{\tilde{K}_{eq}\tilde{\rho}_{eq}} \tag{2.6.9}$$

and

$$\tilde{c}_{eq} = \sqrt{\frac{\tilde{K}_{eq}}{\tilde{\rho}_{eq}}}. \tag{2.6.10}$$

In order to predict the acoustical behaviour of porous media, numerous equivalent fluid models were proposed, and each of them offers different expressions for the equivalent fluid density and compressibility. The model which is used in this work for the majority of theoretical predictions of the acoustical properties of porous materials is the five-parameter Johnson-Champoux-Allard model (Champoux and Allard, 1991). It presents

the expression for the equivalent fluid density in the following form:

$$\tilde{\rho}_{eq}(\omega) = \rho_0 \alpha_\infty \left[ 1 + \frac{\sigma\phi}{i\alpha_\infty \rho_0 \omega} \left( 1 + \frac{4i\alpha_\infty^2 \eta \rho_0 \omega}{\sigma^2 \Lambda^2 \phi^2} \right)^{1/2} \right], \tag{2.6.11}$$

and the equivalent fluid compressibility

$$\tilde{K}_{eq}(\omega) = \gamma P_0 \left( \gamma - \frac{(\gamma - 1)}{\left[ 1 + \frac{\sigma\phi}{i\alpha_\infty \rho_0 N_{Pr} \omega} \left( 1 + \frac{4i\alpha_\infty^2 \eta \rho_0 N_{Pr} \omega}{\sigma^2 \Lambda^2 \phi^2} \right)^{1/2} \right]} \right)^{-1}, \tag{2.6.12}$$

where $\eta$ is the viscosity of air, $\gamma$ is the specific heat ratio of air, $P_0$ is the air equilibrium pressure, $\rho_0$ is the density of air, $N_{Pr}$ is the Prandtl number, and $\Lambda$ and $\Lambda'$ are viscous and thermal characteristic lengths.

Some porous materials are heterogeneous, with the varying size of pores. It was found that the acoustic effectiveness of a material can be largely determined by its pore size distribution (Horoshenkov et al., 2004). This parameter can be directly measured using a water suction method (Leclaire et al., 1998) and then used to obtain a log-normal probability density function, which, together with porosity, tortuosity and flow resistivity can be substituted into expressions for the characteristic impedance and the propagation constant. In this case, Pade approximation model can be used to predict the acoustic behaviour of the material. The dynamic density and complex compressibility can be expressed as follows (Horoshenkov et al., 1998):

$$\tilde{\rho}_{eq}(\omega) = \frac{\alpha_\infty}{\phi} \left( \rho_0 - \frac{\phi\sigma}{i\omega\alpha_\infty} F(\omega) \right) \tag{2.6.13}$$

and

$$\tilde{K}_{eq}(\omega) = \frac{\phi}{\gamma P_0} \left( \gamma - \frac{\gamma - 1}{1 - \frac{\phi\sigma}{i\omega\alpha_\infty \rho_0 N_{Pr}} F(\omega N_{Pr})} \right), \tag{2.6.14}$$

where $N_{Pr} \cong 0.709$ is the Prandtl number for air and $F(\omega)$ is the viscosity correction function originally introduced by Biot (1956). In the case of the materials with the log-normal pore size distribution, this function can be given by a simple polynomial ratio

(Horoshenkov et al., 1998):

$$F(\varepsilon) \cong \bar{F}(\varepsilon)\frac{1 + a_1\varepsilon + a_2\varepsilon^2}{1 + b_1\varepsilon}. \tag{2.6.15}$$

Here, $a_1$, $a_2$ and $b_1$ are real coefficients which depend on the pore geometry. The frequency-dependent parameter $\varepsilon$ can be expressed as follows:

$$\varepsilon = \left(\frac{-i\omega\alpha_\infty\rho_0}{\sigma\phi}\right)^{1/2} \tag{2.6.16}$$

and represents the ratio of the mean pore radius to the viscous boundary layer thickness.

In some cases, e.g. when it is necessary to model the acoustical properties of living plants, it is sufficient to use semi-empirical models which depend on a fewer parameters. One particular model adopted for this work is the Miki model (1990). This model depends on the porosity, tortuosity and flow resistivity which are used to predict the complex characteristic impedance and wavenumber in a porous medium using the following empirical formulae:

$$Z_c = \rho_0 c_0\left[1 + 5.50\left(10^3 X\right)^{-0.632} - 8.43i\left(10^3 X\right)^{-0.632}\right], \tag{2.6.17}$$

$$k_c = \frac{\omega}{c_0}\left[1 + 7.81\left(10^3 X\right)^{-0.618} - 11.41i\left(10^3 X\right)^{-0.618}\right], \tag{2.6.18}$$

where $X = f/\sigma$ and $f$ being the frequency of sound in Hertz.

The following formulae were used in this work to calculate the surface impedance and the modal reflection coefficients at oblique angles of incidence:

$$Z_s(\omega) = -i\frac{Z_c\,(\omega)}{\cos\theta_t(\omega)}\cot\left(k_c(\omega)\cos\theta_t(\omega)\,d_s\right), \tag{2.6.19}$$

$$Z_c(\omega) = \sqrt{\tilde{\rho}_{eq}(\omega)\tilde{K}_{eq}(\omega)}, \quad k_c(\omega) = \omega\sqrt{\frac{\tilde{\rho}_{eq}(\omega)}{\tilde{K}_{eq}(\omega)}}, \tag{2.6.20}$$

$$R_{mn}(\omega) = \frac{Z_s(\omega)\cos\theta_{mn} - \rho_0 c_0}{Z_s(\omega)\cos\theta_{mn} + \rho_0 c_0}, \tag{2.6.21}$$

where

$$\frac{\sin\theta_{mn}(\omega)}{c_0} = \frac{\sin\theta_t(\omega)}{c'(\omega)}, \tag{2.6.22}$$

$d_s$ is the material sample thickness, $\theta_{mn}$ and $c_0$ are the angle of incidence and the speed of sound in air, respectively, and $\theta_t$ and $c'$ are the refraction angle and the speed of sound in the porous material, respectively. Equation (2.6.22) is the classical form of Snell's law of refraction (Allard, 2009).

### 2.6.2 Porous material absorption measurement techniques

Impedance tube measurements are used extensively for acoustic material characterisation. The procedure for the determination of the plane wave, normal incidence acoustic absorption coefficient of a material is detailed in ISO 10534-2 (1998). However, this procedure bounds the adopted frequency range, which depends on the size of the sample. As a result, there is a conflict between the highest frequency which can be attained with this method and the size of the samples which the tube is able to accommodate in order to determine the acoustical absorbing properties for a representative area of the material specimen.

Several efforts have been made in the past to overcome this problem. Coulon et al. (2012) used an impedance tube coupled with a horn to increase the area of the sample which can be tested under the plane wave regime. This method is believed to work well provided there is little or no scattering of the incident plant wave into higher order modes.

Akoum and Ville (1998) and Schultz et al. (2006) have been the first to propose multimodal decomposition methods which can be used to extend the frequency range of

an impedance tube to enable to measure the reflection and absorption properties of relatively large material specimens beyond the maximum frequency of the plane wave regime in an acoustic waveguide. However, these studies are based on the use of a number of microphone pairs installed at several cross-sectional positions near the terminated end of the waveguide. It can be argued that the use of several microphones increases the probability of a phase mismatch and can be time-consuming in terms of calibration. Additionally, the proximity of these microphones to the acoustic termination can result in a poor signal-to-noise ratio, problems associated with the standing waves in the tube and from the influence of the evanescent modes near the tube termination.

Out-of-tube methods of the reflection and absorption measurements at oblique incidence also exist, as it was detailed by Tamura (1990, 1995). In these papers, the numerical method to measure the reflection coefficient at the range of angles is described and its predictions are compared to experimentally obtained results for two types of material. One can assume the theoretical underpinning of the Tamura's method allows to suggest that this method can be more stable than the one described in this study, as it does not employ numerical fitting and function minimisation. However, the method by Tamura predicts the total reflection coefficient instead of modal reflection coefficient, which might be of interest in some cases. The experimental setup detailed in Tamura's paper is also not easy to run, as it requires an anechoic chamber to control the unwanted reflections, a relatively large material sample and a much larger number of measurement positions (over 200 positions according to Tamura (1995)). The authors in the Tamura's paper do not provide any data for the acoustical properties of the tested materials below 500 Hz. This might lead to a conclusion that this method suffers from a typical limitation of those methods which require the compensation for the edge diffraction effect.

Another out-of tube method was presented by Minten et al. (1988). In this work, a two-microphone technique is employed to determine the specific acoustic impedance, which

can later be used to calculate such acoustical characteristics of an absorbing sample as the reflection and absorption coefficients. The measurements are performed at a range of angles. The authors also consider two most common two-microphone measurements errors, i.e. the error due to the finite distance approximation and the error as a result of a systematic phase error between measurement channels, and take these errors into account when calculating the absorption coefficient. However, this method may suffer from the same issues as the one by Tamura (1995) - it requires an anechoic chamber to run it and it only predicts the total reflection and absorption coefficient, as opposed to modal reflection coefficients. Finally, the authors did not provide the data for the measurements at high angles of incidence for frequencies below 500 Hz because of the phase error being of the same order of magnitude as the measured phase.

## 2.7 Sound absorption by living plants

In the recent years, noise reduction using sustainable means, such as green walls and barriers has become increasingly popular. However, there have been almost no controlled experiments on the sound absorption by living plants. Some work has been done on the sound absorption by plant leaves in the free-field conditions. Martens (1981) estimated the sound absorption by leaves by studying four types of plants (privet, birch, oak and hazel) in the laboratory conditions and measuring their leaves' vibration velocity using the laser vibrometry technique. They found out that it varies considerably with the frequency of sound and the orientation of leaf with respect to the source of sound. Also, the measured vibration velocities were much smaller than those of air particles, meaning that only a fraction of the sound energy will cause a leaf to vibrate, and the remaining energy will be reflected or diffracted by the leaf. However, although the total amount of leaves is large and their overall contribution to the sound energy absorption may be rather significant, it is still to be estimated how large is the fraction of the energy

which is absorbed by the leaf rather than due to the ground effect and the thermoviscous absorption in boundary layers.

Wong et al. (2010) conducted the experiments with different vertical greenery systems, both in field conditions and in a reverberation room. For the field experiments, eight vertical greenery systems situated in HortPark in Singapore were used to determine the insertion loss, i.e. the attenuation of noise due to the introduction of greenery systems between a source and a receiver. They concluded that these systems have a positive effect on the noise abatement, up to 8.8 dB for some vertical systems, which is caused by the soil absorption at low to medium frequencies and by the leaf scattering at higher frequencies. The vertical greenery systems were also tested in controlled conditions in a reverberation room. It was found that there is a strong positive correlation between the systems being present and the enhanced sound absorption, which increased with greater greenery coverage.

The experiments on the sound transmission through foliage and its dependence on a plant geometry were first performed by Aylor (1972). He used dense reeds growing in water to account for the effect of the ground attenuation and estimated the relationship between leaf area density, breadth of canopy, leaf width and frequency. It was established that for effective sound absorption, vegetation has to be dense and have wide leaves, but its depth does not play a major role in noise attenuation.

Some research was done in the area of the sound propagation through trees. Martens (1980) performed the experiments on four model forests in an anechoic chamber. Based on his results, it becomes clear that foliage has a strong positive effect on sound absorption, acting as noise amplifier in low to medium frequency band and as a noise filter in higher frequency band. The quality of the filter enhances with an increase in the leaf size and in the total volume of biomass. Additionally, it was found that the filter does not attenuate the traffic noise spectrum, however, it changes its pitch which is useful for urban noise abatement.

Burns (1979) measured the sound absorption by pine trees in a controlled conditions in a reverberant chamber. The purpose of his research was to determine the mechanism of absorption in forests, previously studied by Aylor (1972) and Embleton (1963) who claim that the mid-frequency absorption in forests was due to the soil absorption. The results of Burns were consistent with those of the latter two, however, he could neither prove or disprove the statement that the high-frequency absorption is due to the scattering from boughs.

Finally, some more recent research was to measure directly the sound absorption by plants in an impedance tube in a plane wave regime by Horoshenkov (2013). In this work the authors were treating living plants as porous media. Such plant geometry data as the angle of leaf orientation and leaf area density were linked to non-acoustical parameters, such as the tortuosity and flow resistivity via the optimisation analysis. These are later substituted into an equivalent fluid model for acoustical behaviour predictions. The influence of two types of soil on sound absorption by living plants was also analysed. This research proved that plants significantly enhance the sound absorption of soil and that plants morphological characteristics can be used to predict their acoustical performance.

## 2.8 Summary

This chapter summarises the research which has been performed in the area of sound propagation in pipes, sound intensity and its measurements, acoustics of porous media and living plants and methods of measurement of their sound absorption properties. The sections on the sound field in a pipe and the sound intensity provide a substantial basis for the complex sound intensity measurements in a waveguide and for the subsequent data analysis. In addition, no published work has been found on the complex sound intensity measurements in a waveguide above the first cut-on frequency, so the

measurements and models presented in this thesis cover the existing gap in the literature. The section on the acoustic pulse reflectometry reviews the existing methods and applications, and serves as a basis for the sound intensity measurements for blockage characterisation, presented in this thesis. The section on the porous media discusses the basic principles of porous media acoustics, as well as the existing models used for porous media characterisation, some of which are used in this thesis for the experimental data validation. Moreover, this section provides the overview of the existing methods of measuring the absorption by porous materials, and there is no published work known to the author that would allow to recover the reflection and absorption properties of a relatively large material sample in an impedance tube. Finally, the last section revises the existing research on the acoustics of living plants. It shows that although a considerable amount of studies focused on the sound propagation and absorption by greenery have been carried out, there has been no work which would attempt to characterise large specimens of living plants above the plane wave regime in an impedance tube.

# Chapter 3

# Sound intensity measurements

Sound intensity has been extensively used previously to describe the flow of energy in sound fields. When the acoustic velocity is in phase with pressure, it is common to take the time average of the instantaneous sound intensity and treat it as a real quantity. However, when measurements are performed in regions of sound scattering or in a vicinity of a sound source, the acoustic velocity is no longer in phase with the acoustic pressure. Treating the sound intensity as a complex value in such cases results in an additional information regarding energy transport. It is rather attractive to make use of this information, however, the quality level of such measurements remains unclear. To address this issue and quantify the degree of accuracy one may achieve while measuring the complex sound intensity under controlled laboratory conditions, a study has been performed, comparing measurement and prediction of instantaneous and non-instantaneous sound intensity in an open-ended flanged pipe. An experimental setup was adopted to perform a set of measurements, the results of which were subsequently compared to those predicted by the hybrid model, described in Section 2.4.1. The capabilities and complications of the study are discussed. Some of the results of this study

can also be found in a paper by Duan et al. (2013).

## 3.1 Experimental setup

The experimental setup used for the comparison with the complex intensity predictions is depicted in Figure 3.1. It consists of a 6 m long 150 mm diameter flanged PVC pipe with 10 mm thick walls, with a Fane compression driver (see Figure 3.2) placed at the closed end of the pipe. The driver is connected to the PVC pipe with a short tube of 15.4 mm inner diameter and 13 mm length (see Figure 3.2a). Here the use of a short tube with a relatively small diameter to connect the driver (see Figure 3.2b) to the main pipe helps to simulate an acoustically hard wall at this end of the pipe. The flange was 2 m tall and 1.3 m wide, which was sufficiently larger that an adopted wavelength, so the flange could be approximated as infinite.

A sine wave excitation was used to drive the loudspeaker, and aforementioned tri-axial Microflown (2014) USP intensity probe was used to measure the intensity field near the open end of the pipe. The Microflown "p-u" probe used in this work permits the measurement of all three velocity components simultaneously, so that the signals obtained by the pressure and velocity sensors can be Fourier transformed synchronously and used in Equations (2.2.9) and (2.2.10) to calculate the complex intensity vector components in the three orthogonal directions.

The probe was supported by a rigid plastic frame, which is shown in Figure 3.3. It allowed the position of the probe to be fixed in the axial direction. Two PVC frames were constructed, one with the probe positioned in the centre of the pipe cross section and one with the probe located 9 mm away from the wall of the pipe; this permitted measurements to be taken at different circumferential locations (at a fixed radius). The probe was oriented in such a way that the three velocity sensors were set to measure

Figure 3.1: A photograph of the open flanged pipe used for the experiments.

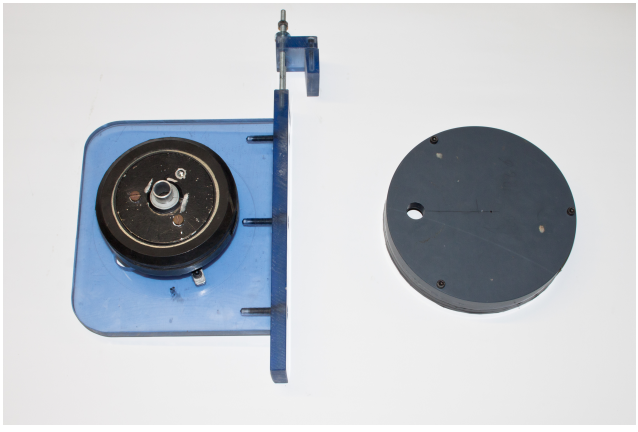

(a) Top view

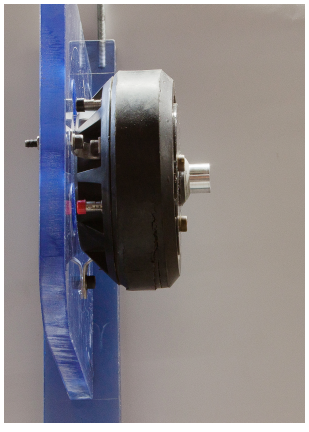

(b) Side view

Figure 3.2: Fane compression driver: top view and a lid, through which it is connected to the pipe (left); side view (right).

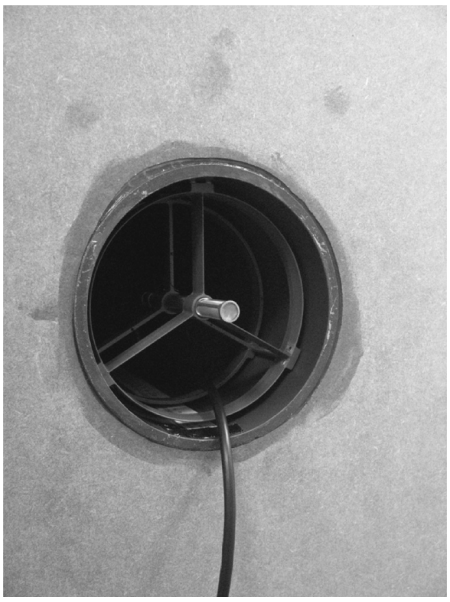

Figure 3.3: The Microflown probe and the frame supporting it in the centre of a cross-section of the pipe.

the axial, radial, and circumferential velocity components. The frame was designed to be slimline so as to minimise the disturbance to the sound intensity field, while still providing sufficient stability when supporting the probe.

A National Instruments DAQ NI PXIE-6358 system was used to acquire the signals from the USP probe. This system was controlled with LABVIEW software and it was designed to generate acoustic stimulus and synchronously record the USP probe signals at the sampling rate of 48 kHz. The Microflown USP intensity probe was chosen here because it is the smallest device available on the market for measuring the three components of the acoustic velocity vector over a broad audio frequency range. The device was calibrated using calibration formulae provided by Microflown. Generally, this calibration procedure improved the accuracy of the results. However, at very low or high frequencies when the sound field was either strongly active or reactive, the measurement accuracy strongly depended on the accuracy of the phase calibration (Stanzial et al., 2011).

### 3.1.1 Intensity measurement errors

The aim of this subsection is to assess the errors associated with the adopted experimental setup, such as influence of the supporting frame and the protective grill at the end of the probe and the probe orientation. The data are presented for different frequencies, but the focus is made on the frequency of 1800 Hz, as this is the frequency used for subsequent complex intensity measurements. This frequency was chosen due to it being situated approximately in the middle of the two cut-on frequencies of 1340 Hz and 2220 Hz. These were determined by making use of the following equation:

$$f_{mn} = \frac{\alpha_{mn}\, c_0}{2a}, \tag{3.1.1}$$

where $f_{mn}$ are the cut-off frequencies of mode $(mn)$, $\alpha_{mn}$ are the zeros of the first derivative of Bessel function of the first kind and the $m-$th order, and $a$ is the radius of a pipe. It was assumed that the sound field at this frequency is relatively unaffected by the peculiarities caused by the proximity of cut-on frequencies, making the measured results more accurate. Preliminary measurements were performed at a range of frequencies from 1500 Hz to 2000 Hz and compared to corresponding predictions, and it was observed that the match between the two weakened as the measurements frequency got closer to a cut-on frequency. The measured data are compared to the hybrid model (Duan et al., 2013), described in Section 2.4.1. The results of this model have been validated against a number of existing models and FEM predictions, and they have been found to be accurate.

At the beginning experiments were carried out to determine if the frame had any impact on the recorded signal. In order to achieve that, two sets of measurements were carried out, one with the frame present, and then the same set would be repeated, but the probe would be attached to the wall of the pipe with the help of duct tape. The results of the test are shown in Figure 3.4. It presents the axial active and reactive intensities recorded

at the frequency of 1600 Hz, 100 mm from the open pipe end. For the data obtained with no frame, only positions from 180° to 360° were tested as it was not possible to attach the probe to the upper half of the pipe without affecting the sound field, i.e. without inserting the potential scattering objects to support the probe. The frequency of 1600 Hz was chosen as it was initially assumed that this will be the frequency at which the subsequent complex intensity measurements will be performed, however, a decision was made later to use the 1800 Hz frequency due to the reasons outlined at the beginning of the section. The axial location of 100 mm from the open pipe end was chosen because the effect of evanescent waves is negligible at this depth. The measurements performed with and without the frame suggest that the results are reproducible and that agreement between the two data sets for the axial and circumferential intensities is good, with the mean error for active intensities below 10% in the case of axial and below 20% in the case of circumferential intensities. The mean error was estimated using the following procedure:

$$\epsilon_I = \frac{1}{N} \sum_{i=1}^{N} \frac{|I_i^m - I_i^{pred}|}{I_i^{pred}}, \tag{3.1.2}$$

where $I_i^m$ and $I_i^{pred}$ are the measured and predicted intensities, respectively. These values are about 5% higher for the corresponding reactive intensities. However, the match between the two data sets, with and without the frame, in the case of radial intensity is weaker, with the mean error being higher than 30%. This may be explained by the fact that the frame has the biggest influence on the radial intensity component, resulting in a higher levels of scattering. However, the errors between the sets recorded in the presence and in the absence of the frame can also be caused by the fact that the accurate positioning of the probe becomes more challenging without the frame, and the observed discrepancies may have been caused by a slight difference in location and direction of the probe. Overall, the observed error was considered acceptable, and it was further assumed that the influence of the frame was negligible.

Additionally, due to a finite size of the velocity sensors on the probe' the quality of

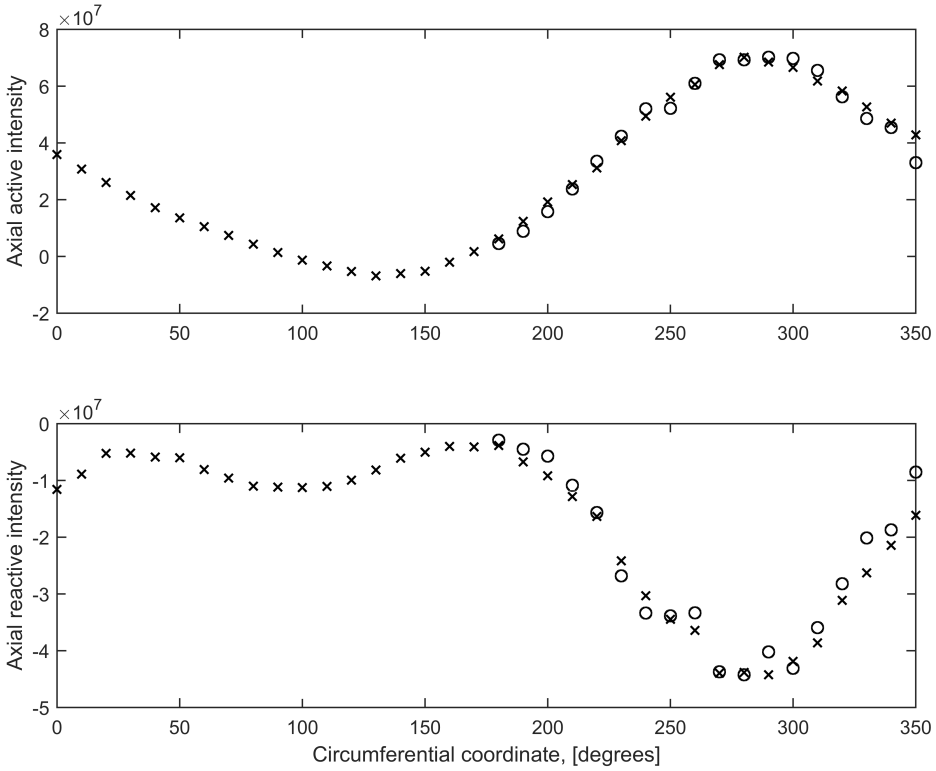


Figure 3.4: Comparison of the active and reactive intensities obtained with the supporting frame vs. obtained without the supporting frame. Black crosses: with the frame; black circles: without the frame.

the recorded data may depend on the orientation of the probe inside the frame. Two possible ways of the probe positioning are shown in Figs. 3.5a and 3.5b.

The difference between the alternative sensor orientations is that whilst the direction of the axial sensor is the same, the directions of the radial and circumferential sensors are reversed. The comparison is presented on the example of the active and reactive radial intensities in Figure 3.6. The data obtained with Orientation A are marked with black crosses, whereas the data obtained with Orientation B are denoted with black circles. The black solid line is the predicted results. It was experimentally found that Orientation B generally gives a better agreement between the experimental data and the predictions for all three intensity components. It can be attributed to the fact that with Orientation A, one of the sensors was directly facing the wall, which could affect the quality of its readings. The upper subplot of Figure 3.6 shows the active radial

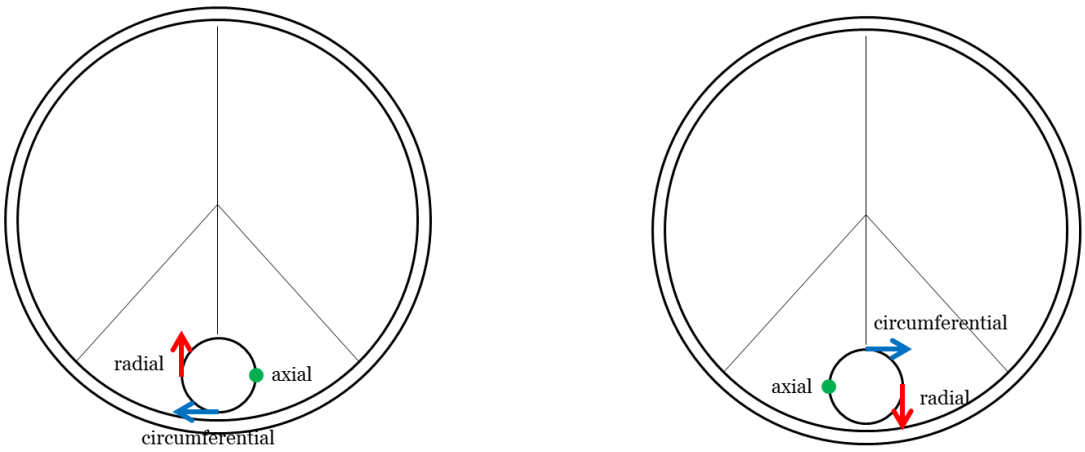


(a) Orientation A

(b) Orientation B

Figure 3.5: Two ways of probe positioning.

intensity, and it can be observed that the both experimental data sets follow the same trend as the predictions. However, from the lower subplot of Figure 3.6, presenting the reactive radial intensity, it is clear that the data measured with the Orientation B follows the predictions more closely. It is also worth mentioning that the theoretical model attempted to ideally represent the sensors' distribution on the probe, assuming that they all are not situated in one point, but assigning an individual position to each sensor. But, as a difference between the centre of the probe cross-section (where the sensors were assumed to be situated) and the sensors' actual position is rather small, approximately 3.5 mm, it did not affect the results.

The protective grill covering the tip of the probe where all the sensors are situated has also raised concerns regarding its effect on the data quality (see Figure 2.3). Therefore a set of tests was conducted, where the difference between the results obtained with and without the protective grill was quantified. The results are shown in Figure 3.7, which presents the active and reactive axial intensities. In general, the discrepancy between two sets of data is rather small, normally not exceeding 10%. In the case of active radial intensity the error between the data sets reaches the maximum of 35%. This can be attributed to the fact that the radial intensity is directed perpendicular to the walls of the protective grill, which affects its value. The similar effect was observed in

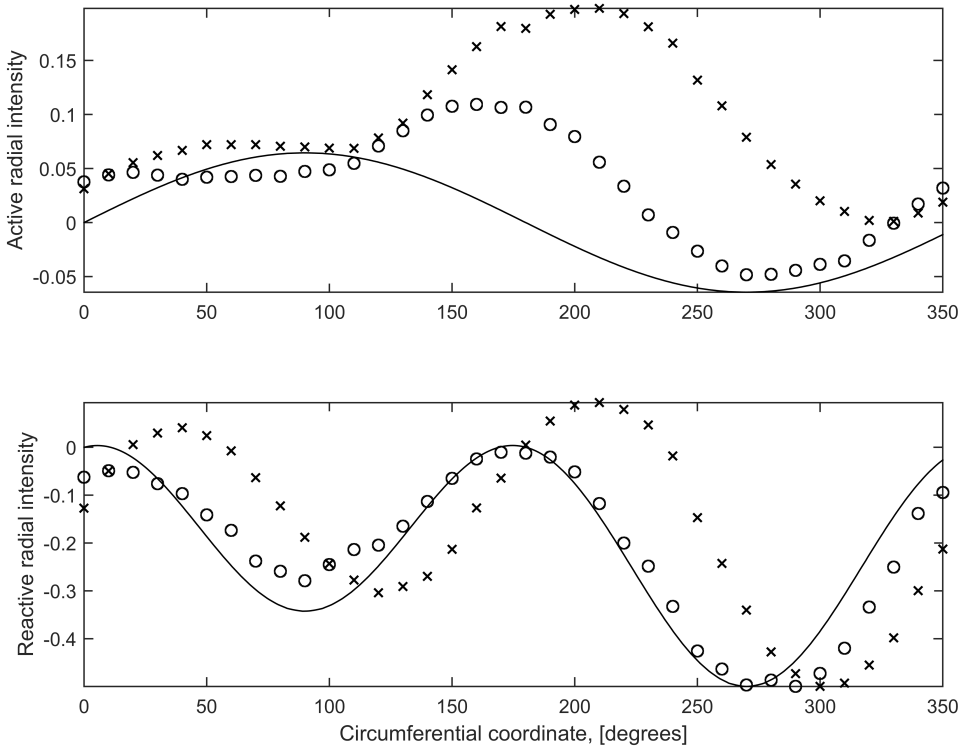


Figure 3.6: Sensor orientation comparison on an example of the complex radial intensity at 1800 Hz, 0.2 m from the open pipe end. Black crosses: Orientation A; black circles: Orientation B; solid black line: predictions.

case of active circumferential intensity, although to a lesser extent. There was a small discrepancy between active and reactive axial intensities measured with and without the protective grill. On the whole, the match between the two sets of measured intensities is reasonably good, which results in conclusion that the protective grill has no major influence on measurements.

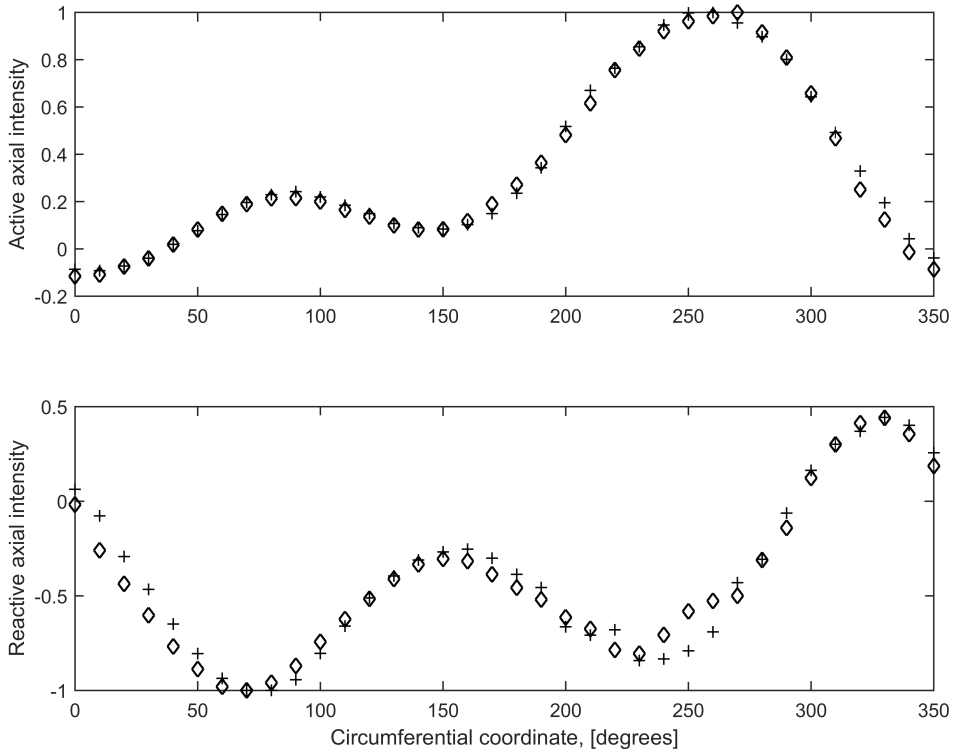


Figure 3.7: Comparison of data obtained with protective grill (diamonds) on vs. data obtained without protective grill (crosses).

## 3.2 Results and discussion

In order to examine the complexity of the complex intensity field, the theoretical predictions were studied before comparing them to the experimentally obtained data. The predictions for the complex sound intensity in the vicinity of the open pipe end were plotted as a function of position. For these predictions, the pipe facility pictured in Figure 2.6 was used, with the following dimensions: $L_1 = 75$ mm, $L_2 = 5.85$ m, and $L_3 = 75$ mm, where $L_1$ and $L_2$ denote the axial length of regions $R_1$ and $R_2$, respectively, and $L_3$ denotes the boundary between the modal representation and the finite element discretisation in the pipe. The radius of the pipe was 75 mm. The sound source was located at $r = 65$ mm, $\theta = -90°$, and $z = 6$ m.

In Figure 3.8 the active and reactive intensities are plotted for a frequency of 1000

Hz in the vicinity of the open end of the pipe. A streamline vector plot is used in which the length of the vector is proportional to the magnitude of the acoustic intensity component. At 1 kHz, only the fundamental mode propagates in the pipe, resulting in the problem being axisymmetric. It is seen in Figure 3.8 that the amplitude of the active intensity is larger than that of the reactive intensity, so the sound intensity field is mostly active. In the vicinity of the open end of the pipe a small radial component appears in the complex intensity field due to the presence of evanescent modes. This is caused by oscillatory behaviour of the sound intensity, and it is seen to be more pronounced for the reactive intensity, which illustrates why the use of complex intensity is potentially attractive.

Figure 3.9 shows the influence of a higher order mode on the non-instantaneous active and reactive intensity fields. A frequency of 1800 Hz was chosen so that the fundamental and the first circumferential modes were excited in the pipe. Figure 3.9 shows the complex intensity field for the $r-z$ plane that is coincident with the sound source (so that $\theta = -90°$). When a higher order mode was propagating in the pipe, the intensity field contained strong radial and circumferential components. Also, a circulatory pattern was observed, which repeated itself over the pipe length. This pattern surrounds the points of minimum acoustic pressure, whereas the regions of maximum acoustic pressure are indicated by regions of divergence in the reactive intensity pattern in the vicinity of the pipe wall. An important observation which can be made here is that the higher order mode has a significant influence on the reactive intensity, which becomes much more complex than the active intensity. Consequently, it is necessary to be able to capture the three-dimensional intensity field accurately in order to measure the reactive intensity. It means that the instrumentation used for these measurements has to be very precise. The theoretical predictions seen in Figures 3.8 and 3.9 confirm that the complex intensity field becomes very complicated even with just one higher mode propagating in a pipe.

After the behaviour of the complex sound intensity in the vicinity of the open end of

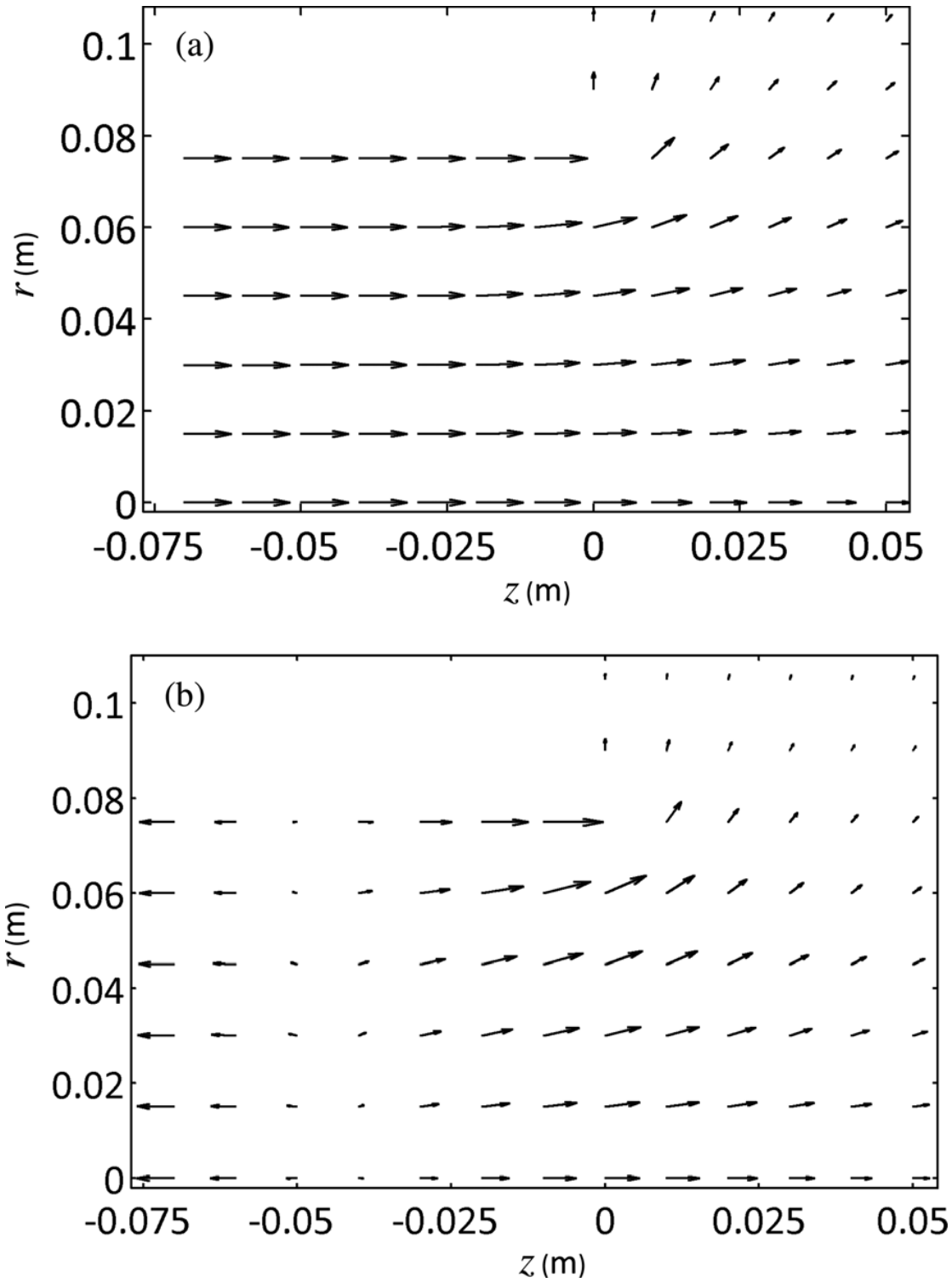


Figure 3.8: Predicted active (a) and reactive (b) intensity near the end of the pipe at 1000 Hz.

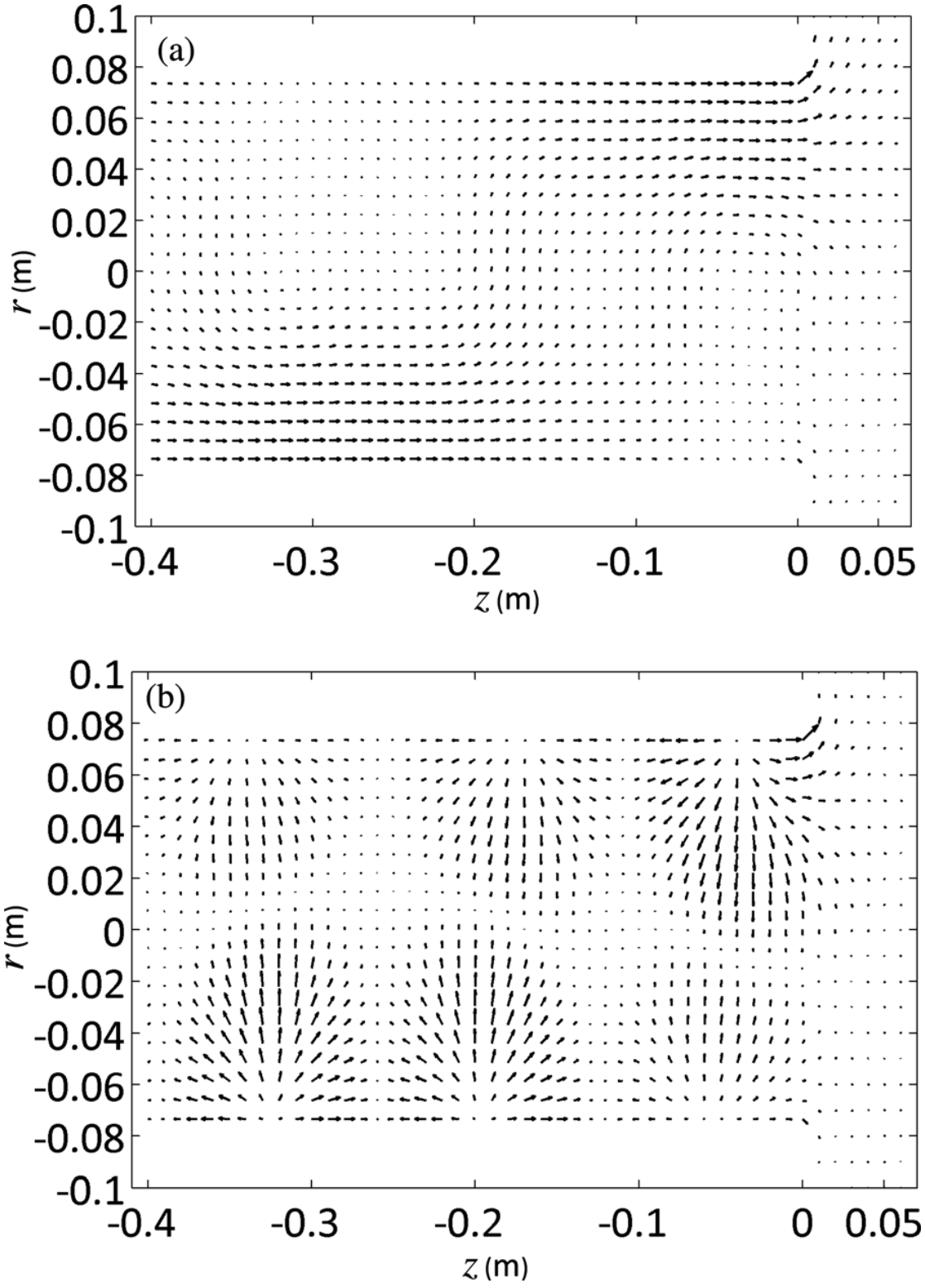


Figure 3.9: Predicted active (a) and reactive (b) intensity near the end of the pipe at 1800 Hz.

the pipe has been examined, a comparison between the predictions and measurements can be carried out. Figure 3.10 presents the instantaneous active and reactive intensities at the pipe end ($r = 0$, $z = 0$) for a sound field, excited with a sine wave signal at the frequency of 1000 Hz. This frequency was chosen to study the sound intensity field in a plane wave regime. Three sets of data are shown: predictions, denoted by the solid line, and experimental data, calculated using the methods of Heyser (1986) (short-dash line) and Stanzial and Prodi (1997) (long-dash line). Figure 3.10 shows that there is a clear difference between two sets of the experimental data. The method of Heyser shows a running average of the active intensity and an upper envelope of the reactive intensity. In contrast, the method of Stanzial and Prodi matches the oscillatory nature of the predicted active and reactive intensities. The error between the measured and predicted results for this method is about 5% for times above 2 ms. However, in the region of approximately 0-2 ms, the system response is transient, and the error is higher, being about 20% (see Figure 3.10(a)). The method of Stanzial and Prodi delivers more accurate data for the sound field excited by a sine wave below the first cut-on frequency, which supports the original findings of Schiffrer and Stanzial (1994).

Figure 3.11 shows the measured and predicted active and reactive intensities as a function of axial coordinate $z$ at the frequency of 1000 Hz. The measured data were calculated using Equations (2.2.9) and (2.2.10). There are two sets of theoretical results in the figure: the hybrid model results, which were predicted via Equations (2.2.11) and (2.2.12) (see Section 2.4.1), and the two-dimensional model results, proposed by Shenderov (1972) and briefly described in Section 2.4. A good agreement is generally observed between the experiments and predictions, with the mean difference being below 10%. There is some discrepancy between the measured and predicted active intensity data as the distance from the open pipe end increases, with the predicted active intensity becoming constant, whereas the measured active intensity exhibits the oscillatory behaviour. Nevertheless the match between the two data sets is sufficiently accurate. The two theoretical data sets generally exhibit good match, but the two-dimensional

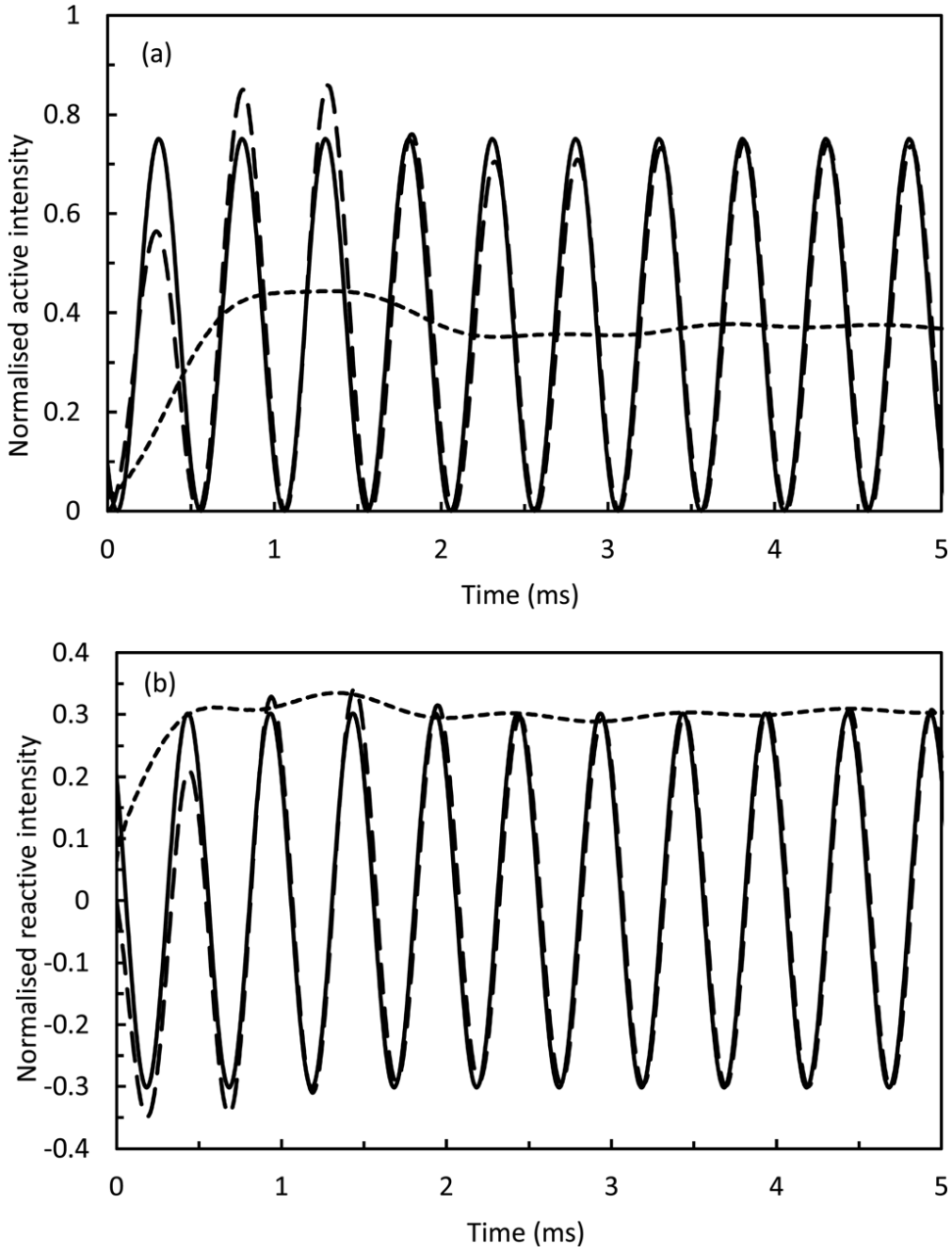


Figure 3.10: Instantaneous complex intensity at 1000 Hz: Instantaneous active (a) and instantaneous reactive (b): ———, theory; — — —, experimental data based on Stanzial and Prodi's method (Stanzial and Prodi, 1997); – – –, experimental data based on Heyser's method (Heyser, 1986).

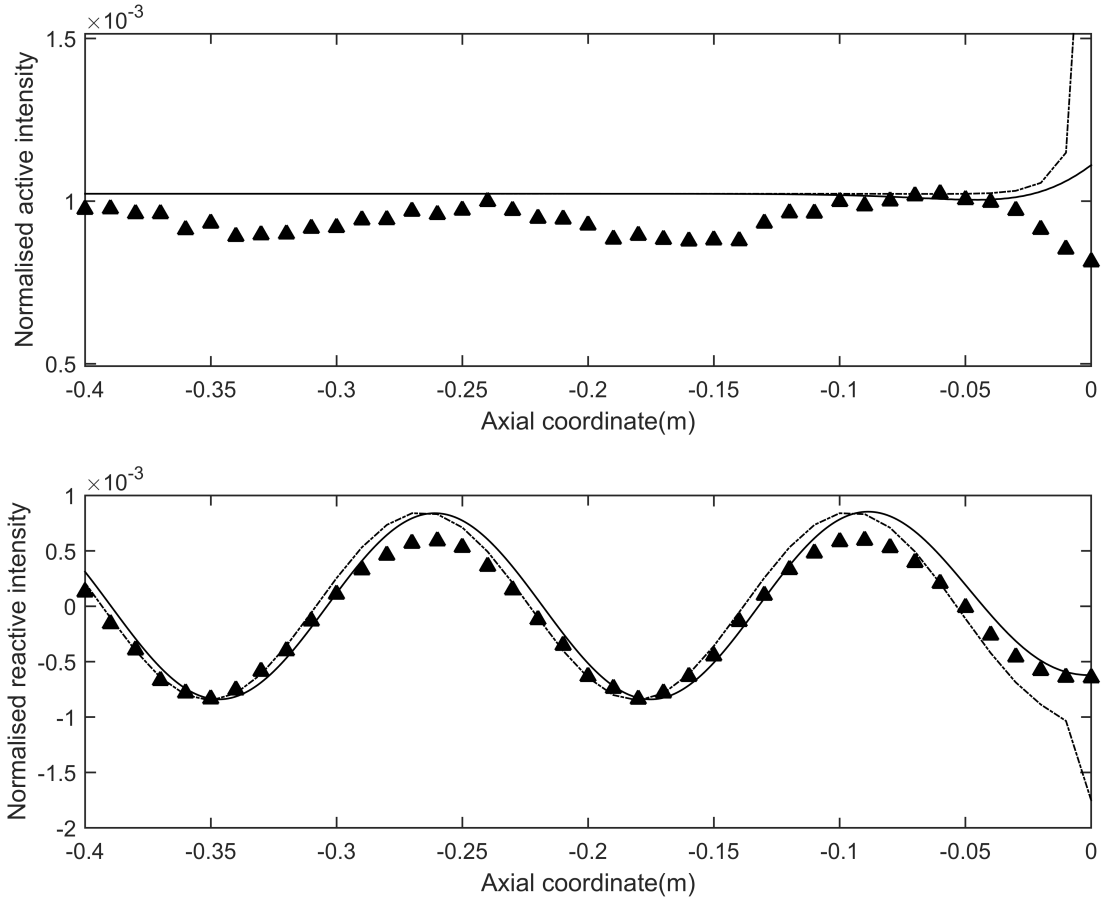


Figure 3.11: Active (a) and reactive (b) axial intensity at 1000 Hz: ———, hybrid model; −·−·−, 2D model; ▲, experiment.

model fails to represent accurately the complex sound intensity field in the vicinity of the open pipe end. With such a restriction in the plane wave regime, it is evident that the discrepancy between the two-dimensional model and experimental data will be even larger beyond the first cut-on frequency, so the hybrid model was preferred to the two-dimensional model and was used for subsequent calculations.

However, when one more mode becomes propagating in the pipe, the complex sound intensity field becomes much more complicated. Figures 3.12-3.14 show the predicted and measured data for the three components of the non-instantaneous complex intensity, excited with a sine wave at a frequency of 1800 Hz. For this experiment, the sound source was installed at a 9 mm distance from the pipe wall and at a circumferential

position of $\theta_0 = -90°$. The Microflown probe was placed inside the pipe at $z = -0.2$ m and 9 mm away from the pipe wall. Data for the axial, circumferential, and radial intensity vector components were then obtained for different circumferential locations by rotating the probe frame through a full circle and taking measurements every 10° and presented for each circumferential location.

The results presented in Figures 3.12-3.14 illustrate that when more than one mode is present in the pipe, obtaining a good agreement between the experiments and predictions becomes a challenging task. In this sound field, the dominant components of the complex sound intensity vector are axial and circumferential intensities. Figure 3.12 presents the measured and predicted active and reactive axial intensities. The agreement between the measured and predicted active intensities is generally very good, although the pattern in the measured data is shifted by approximately 20° with respect to the predicted result. The relative error between the amplitudes of the maxima in the predicted and measured active axial intensity is relatively small, being less than 1%, but this error increases significantly when the value of the circumferential coordinate $\theta$ is less than 120°, and the amplitude of the active axial intensity becomes relatively small. This suggests that the probe is able to capture well the qualitative behaviour of the sound energy radiating from the pipe, but not its exact amplitude at a given circumferential coordinate. Moreover, there is a large discrepancy between the theoretical and experimental axial reactive intensities for circumferential coordinates greater than 50°, which may be caused by the fact that most of the energy is radiated from the pipe at 1800 Hz, resulting in a reduce signal-to-noise ratio and making accurate measurements with the 'p-u' probe more challenging.

Figure 3.13 shows the measured and predicted results for the active and reactive circumferential intensities. The reactive part of the circumferential intensity component oscillates over the pipe cross section, and the agreement between the measured and predicted behaviour is good. However, a shift between the measured and predicted in-

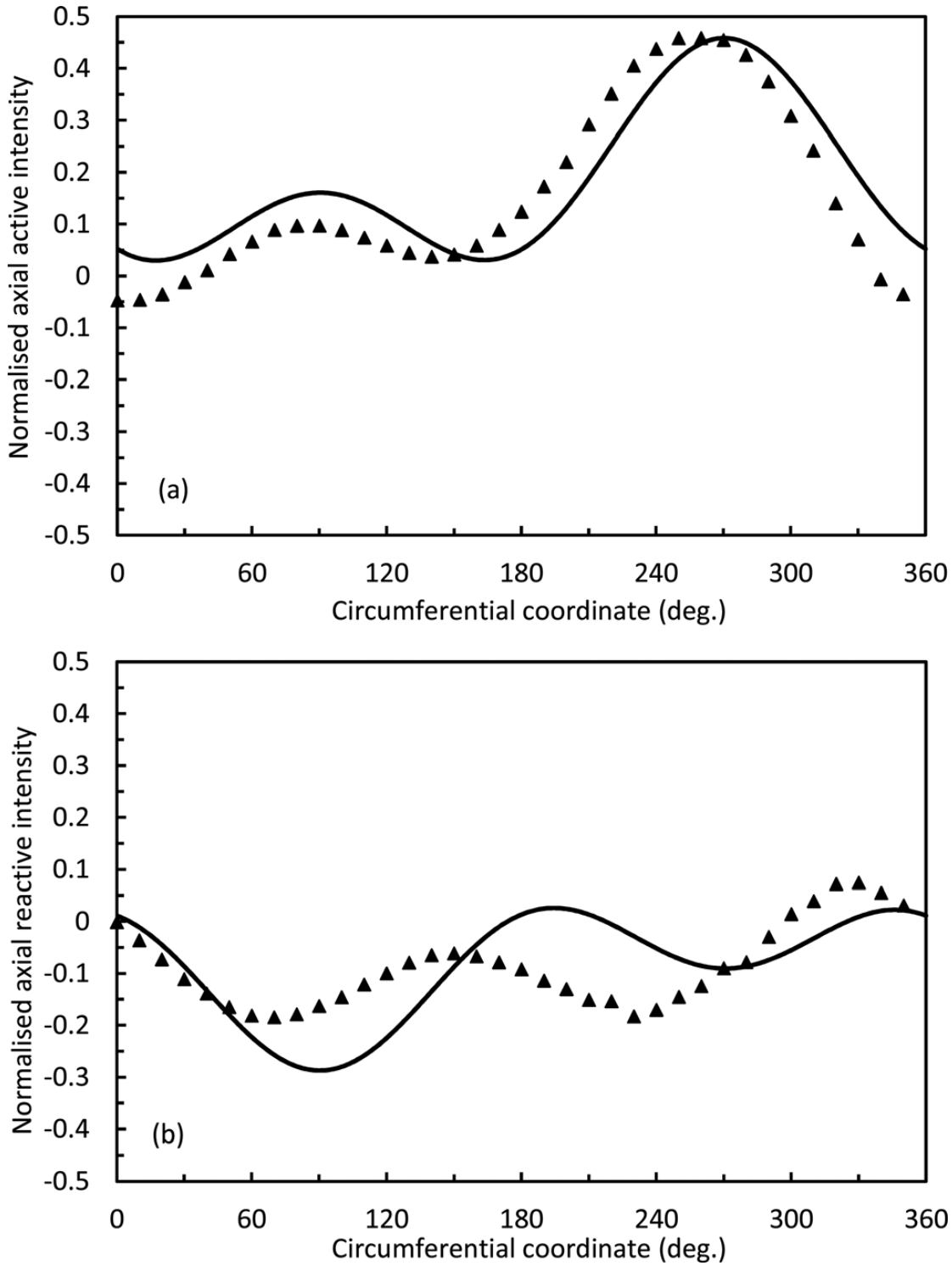


Figure 3.12: Active (a) and reactive (b) axial intensity in the pipe at 1800 Hz: ——, theory; ▲, experiment.

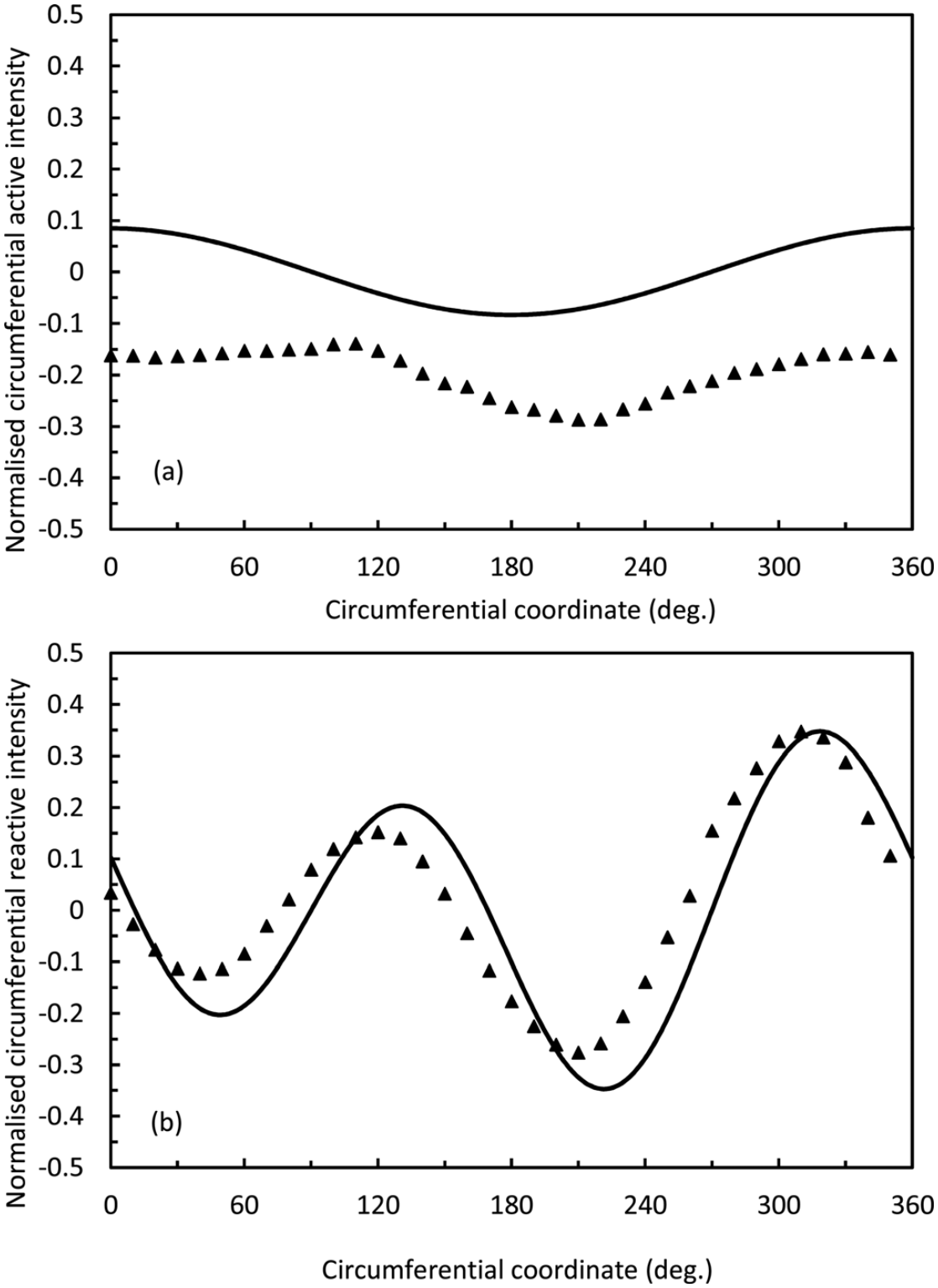


Figure 3.13: Active (a) and reactive (b) circumferential intensity in the pipe at 1800 Hz: ———, theory; ▲, experiment.

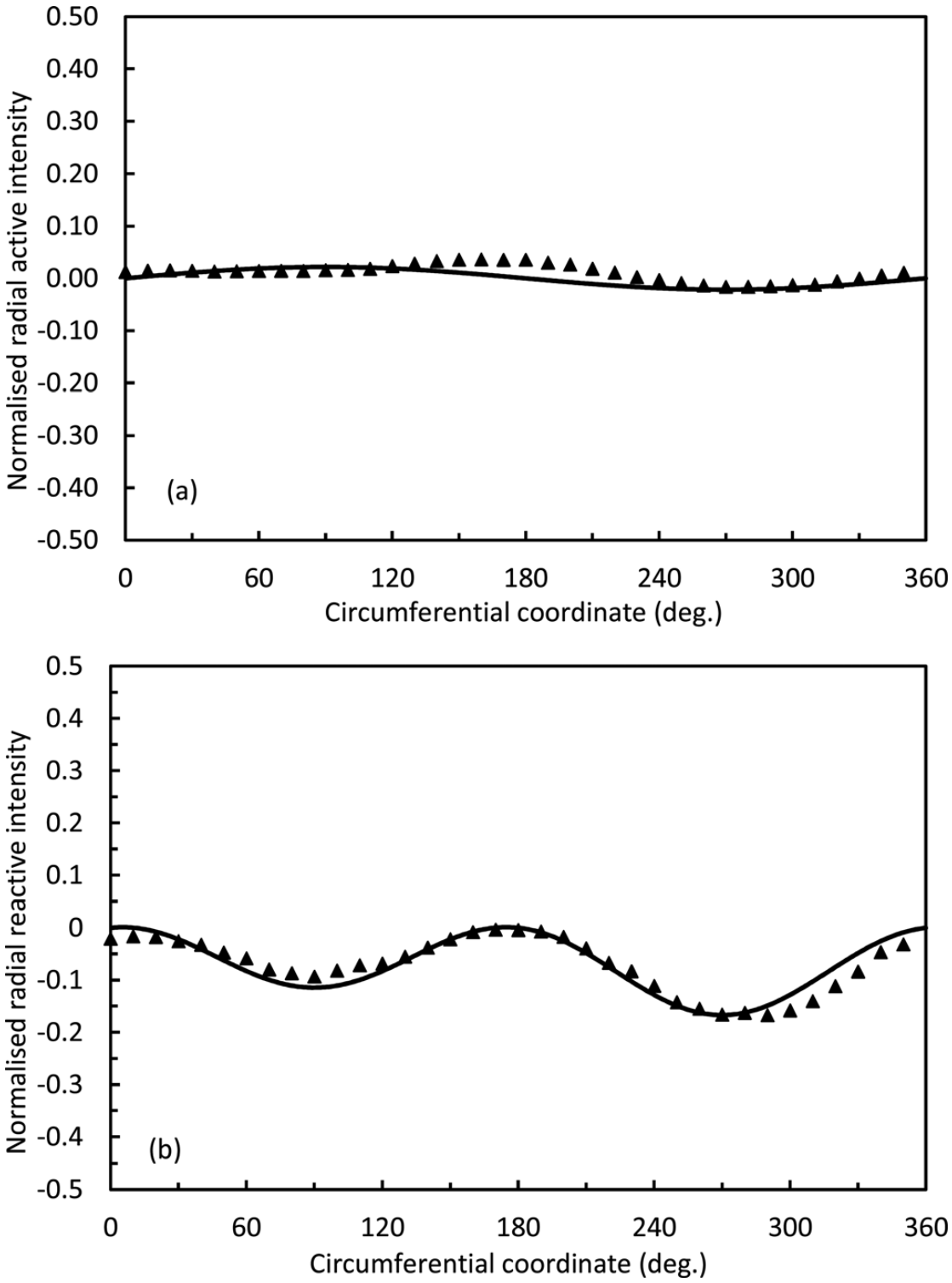


Figure 3.14: Active (a) and reactive (b) radial intensity in the pipe at 1800 Hz: ——, theory; ▲, experiment.

tensities can again be observed, this time of about 15°. The match for the active part of the circumferential intensity component is much less accurate, and the predictions and measurements do no agree even in terms of the sign. A symmetric intensity field distribution is expected, which should not be entirely negative, as it is observed in the case of the measured data. It is likely that some scattering from the frame supporting the probe has affected these measurements and that this effect is more pronounced in the case of the circumferential velocity component, especially at the higher frequencies and/or when higher-order modes are excited.

Finally, Figure 3.14 shows the radial complex intensity. This intensity vector component is smaller than the axial and circumferential components. Good agreement between the predicted and measured active and reactive intensities is observed, and the match is more accurate compared to the errors in the measured data for the axial and circumferential intensities as shown in Figures 3.12 and 3.13. This improvement may be explained by a reduced influence of the supporting frame and the probe body when taking measurements in the radial direction and more accurate response of the radially orientated velocity sensor in the USP probe.

## 3.3 Summary

The comparison between the predictions and measurements in Figures 3.12-3.14 demonstrates that obtaining a good agreement between measured and predicted complex intensity presents a significant challenge when using a tri-axial intensity probe by Microflown, even in the case of a well-defined problem such as an open ended pipe. The agreement between the measured and predicted axial reactive and circumferential active intensities is insufficiently accurate. It is possible that these problems are caused by an increase in sound scattering from the supporting frame and the body of the probe as the frequency of sound is increased. Alternatively, it is also possible that the tri-axial

probe finds it more difficult to resolve accurately all three complex intensity components at higher frequencies and/or under multimodal conditions because of errors in the acoustic velocity measurements. It can also be caused by the fact that the measured intensity can be sensitive to any imperfections in the pipe geometry which are difficult to characterise. Thus, it is clear that accurately measuring all three intensity components in a complex sound field in a pipe remains a challenge, so precautions should be taken when interpreting the complex intensity data obtained when higher order modes are propagating in a pipe.

The results presented here illustrate the difficulty of measuring the complex intensity vector accurately, even under harmonic sound field conditions. Thus the quantitative understanding of the complex intensity behaviour in a pipe remains limited even for a relatively simple and well-defined problem, such as an open end of a pipe. This is because the reactive sound intensity field is typically very complicated under those conditions, and current measurement techniques are not sufficiently accurate to enable precise assessment of the complex intensity vector. This has important consequences for the use of complex intensity in sound scattering problems, especially if one is attempting to apply inverse analysis techniques in an attempt to recover information about the sound source.

In the next chapter, the application of sound intensity measurements will be presented. Sound intensity will be used to predict the reflection and transmission coefficients of a symmetrical blockage in a cylindrical pipe.

# Chapter 4

# Application of sound intensity for blockage detection

This chapter describes some applications of complex sound intensity measurements and predictions for blockage detection and localisation in a pipe. For this purpose, controlled experiments were performed in the Hydraulics Laboratory at the University of Bradford, where blockages of different shapes were placed in the pipe and their reflection and transmission characteristics were studied. Measured data were compared to predictions, obtained using the hybrid method described in Section 2.4.1.

## 4.1 Experimental methodology

### 4.1.1 Laboratory setup

For the analysis of sound pressure, velocity and complex intensity distribution in a pipe in presence of a blockage, a set of controlled experiments was performed. For this purpose, an 18 m long 150 mm diameter air-filled PVC pipe was constructed and used to measure the effect of an obstacle on the sound pressure and particle velocity fields. Figure 4.1 shows this experimental arrangement in the Hydraulics Laboratory at the University of Bradford. It consisted of three 6 m sections in which the joints were carefully machined, connected leaving no air gaps and sealed with the duct tape. One end of this pipe was rigidly terminated and the Fane compression driver described in the previous chapter was installed. In the other end of the pipe a sound-absorbing cone was inserted to reduce the reflections from this end of the pipe.

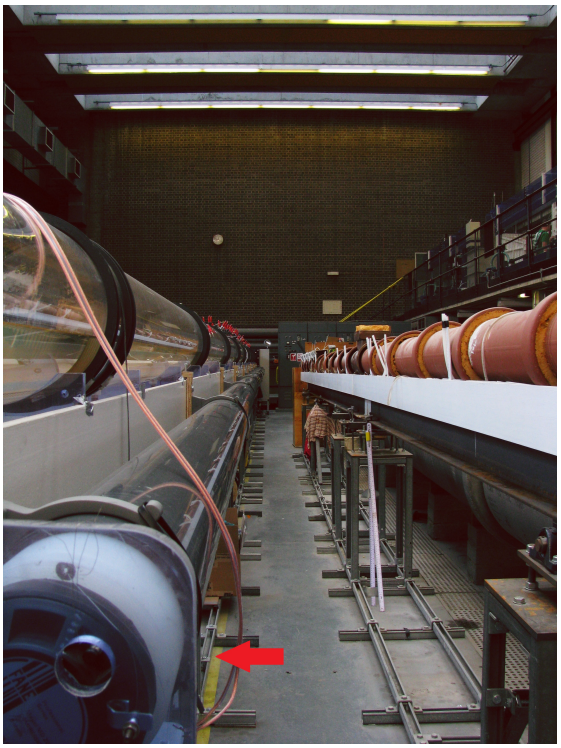

Figure 4.1: A photograph of the 18 m long, 150 mm diameter pipe. The red arrow denotes the 18 m long pipe used for the described experiments.

A coaxial cylinder was used as a blockage and is depicted in Figure 4.2. It was made of a hollow PVC tube and covered with wooden lids from both sides. The gaps between the lids and the walls of the cylinder were treated with silicon to prevent air gaps. The length of the cylinder was 305 mm and its diameter was 110 mm and it was placed at a distance of 12 m from the loudspeaker. The cylinder had 20 mm "legs" on its sides to ensure that it sits exactly in the middle of the pipe's cross-section.

Figure 4.2: A photograph of the coaxial cylinder used as a blockage.

As both transmission and reflection characteristics of the blockage were of interest, two types of experimental setup were adopted. In one, a sensor was positioned behind the blockage, in the vicinity of the absorbing end of the pipe, to record the sound transmitted through the blockage. In another, the sensor was between the blockage and the loudspeaker to record the reflected sound wave. Schematic drawings of the transmission and reflection setups are shown in Figures 4.3a and 4.3b, respectively. Furthermore, measurements were performed at the same positions in the absence of the blockage in the pipe, to determine the reference incident sound field which was needed to calculate the reflection and transmission coefficients.

For these experiments, an array of four MEMS microphones, which is shown in Figure 4.4, was used to record the signal. It allowed the measurement of the axial component of the sound velocity, from which the sound intensity along this direction was calculated in accordance with the 'p-p' method. There are six microphone pairs in total, 1-2, 1-3, 1-4, 2-3, 2-4 and 3-4. In the following experiments, microphone pair 1-2 was used

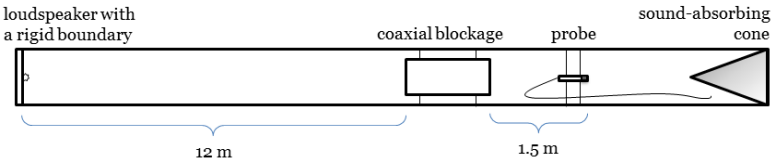


(a) Transmission mode setup

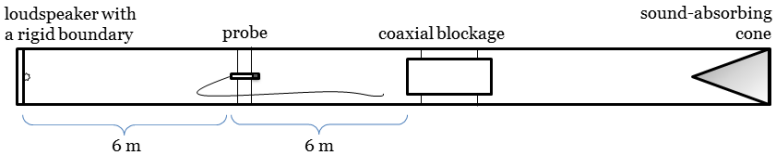


(b) Reflection mode setup

Figure 4.3: Schematic drawings of the experimental setup for transmission (a) and reflection (b) measurements.

throughout, where the separation distance was 27.5 mm.

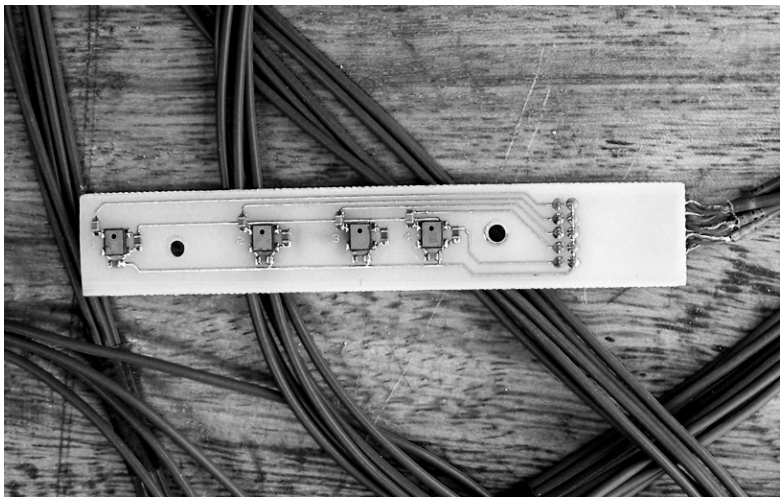

Figure 4.4: MEMS microphone array.

A separate experiment was carried out to study the performance of the MEMS microphone array and the Microflown probe in the long closed pipe and to determine if the results obtained are comparable. For these experiments, the MEMS microphone array was preferred to the Microflown probe because the intensity was measured in the axial direction only. The microphone pair was matched and did not require any compensation. In this experiment one type of sensor at the time was attached to the frame which was inserted in the empty pipe approximately 6 m away from the loudspeaker. The frame was then rotated in 10° steps to measure the angular sound field distribution. It

was discovered that the quality of data recorded by the microphone array is superior to that of the USP probe, therefore the former was preferred for all the subsequent sets of measurements. The comparison of the data recorded by both devices is shown in Figures 4.5a-4.5b. One can see that the experimental data obtained using the microphone array agree with the numerical data very well, reproducing the predicted amplitude almost spot-on. There is a mismatch between both sets of experimental data and predictions between 0 and 180 degrees in the case of the reactive intensity, but for the remaining angles, the agreement between the measurements and predictions is closer in the case of the MEMS microphone array. The mean differences between the measured and predicted data were quantified in the same manner as suggested by Equation (3.1.2). The mean differences for the MEMS microphone array were equal to 51.8% and 46.9% for active and reactive intensities, respectively. For the Microflown probe, the same mean differences were equal to 148.3% and 69.9%.

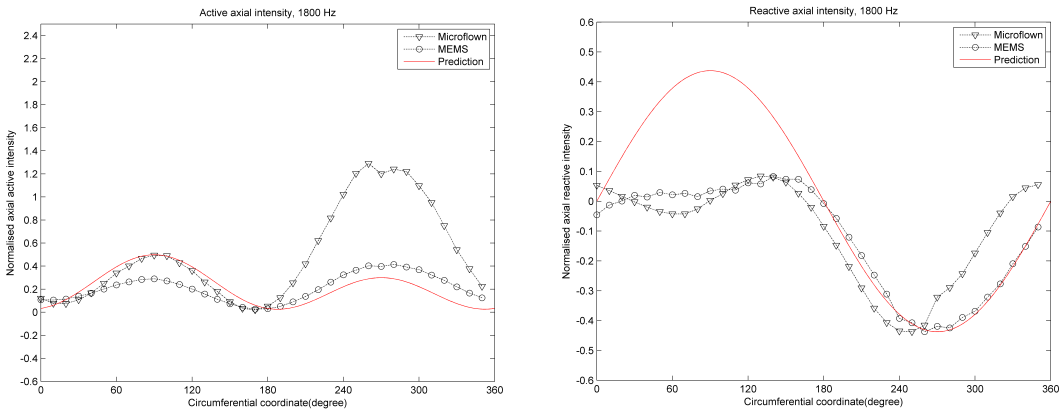


(a) Active axial intensity

(b) Reactive axial intensity

Figure 4.5: Comparison of data obtained with Microflown USP probe vs. MEMS microphone array: (a) active axial intensity; (b) reactive axial intensity. Red line: predictions; black triangles: Microflown; black circles: MEMS.

### 4.1.2 Signal

Gaussian pulse was employed for the excitation of the sound field in the pipe. The reason for its use was the possibility to window out the unnecessary reflections and

to prevent the formation of standing waves in the pipe. The form of this pulse was described with the following equation:

$$v(t) = A_0 \ \cos(\omega t) e^{-\frac{(t-t_0)^2}{\beta^2}}, \tag{4.1.1}$$

where $t$ is time, $t_0$ is delay, $\omega$ is the angular frequency and $\beta$ is a temporal variable that controls the width of the pulse. The sample Gaussian pulses at frequencies of 300 and 1800 Hz are plotted in Figure 4.6.

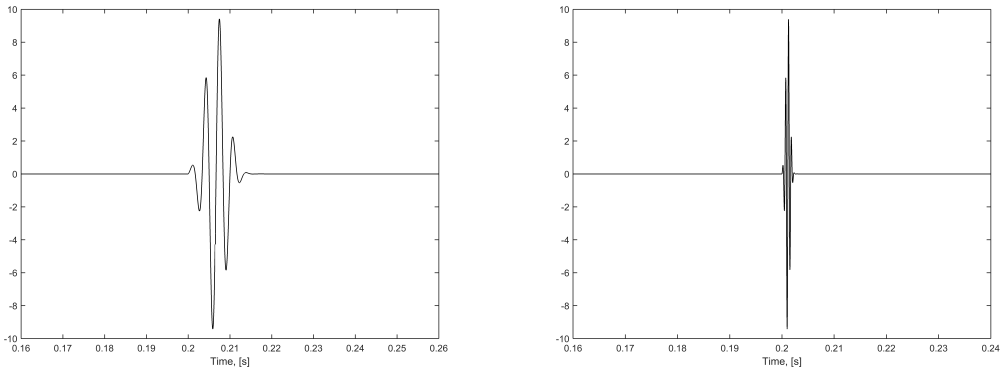


(a) 300 Hz (b) 1800 Hz

Figure 4.6: Gaussian pulse temporal data at the frequencies of (a) 300 Hz and (b) 1800 Hz.

The examples of the spectra at the frequencies of 300 and 1800 Hz are presented in Figure 4.7.

An example of the recorded time histories of the windowed signal, which was used in a later analysis, is presented in Figures 4.8-4.10. Figure 4.8 shows the time history of the sound pressure in the pipe for a 1800 Hz pulse. It can be seen that the incident pulse corresponding to the fundamental mode is followed by its higher-order mode components.

Figure 4.9 presents the time history of three components of the acoustic velocity vector, measured with Microflown at 1800 Hz frequency. These components are of the same

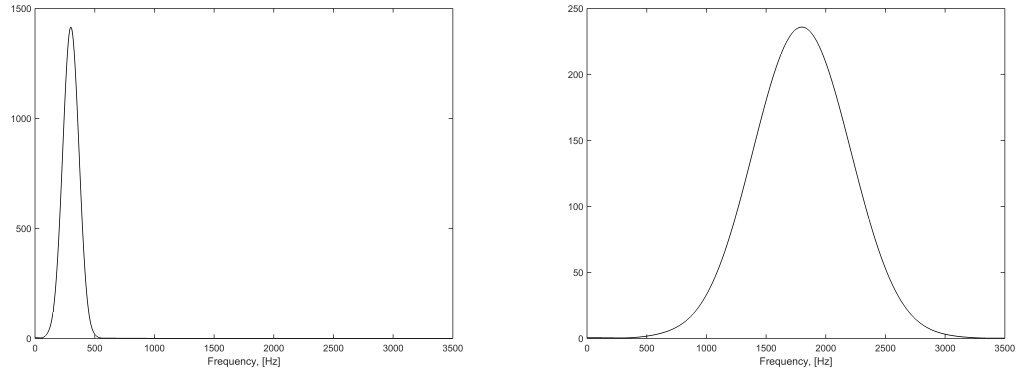


(a) 300 Hz (b) 1800 Hz

Figure 4.7: Gaussian pulse spectra at the frequencies of (a) 300 Hz and (b) 1800 Hz.

order of magnitude, which means that at frequencies higher that the first cut-on frequency, none of the components can be neglected in analysis, as opposed to plane wave regime, where the axial component alone gives a plausible picture. However, as the blockage characterisation procedure, described in what follows, focused on the plane wave regime, the use of MEMS microphones and the axial velocity component alone was sufficient.

Three components of the instantaneous acoustic intensity are shown in Figure 4.10. They were obtained by multiplying the time history of the sound pressure by the time history of the corresponding velocity component, i.e.:

$$I_j(t) = p(t)\, u_j(t), \quad j = 1, 2, 3. \tag{4.1.2}$$

The cut-on frequencies for the 150 mm diameter pipe are presented in Table 4.1. The initial goal was to recover the reflection and transmission coefficients for the plane wave (fundamental) mode and for the first few higher order modes. However, in the course of experiments it was decided to restrict this type of analysis to the plane wave mode only due to the data processing challenges. Hence, the loudspeaker and the microphone were initially placed in the middle of the tube cross-section. In this case, the first higher-order mode which can be measured with this setup cuts on at 2789 Hz, as opposed to

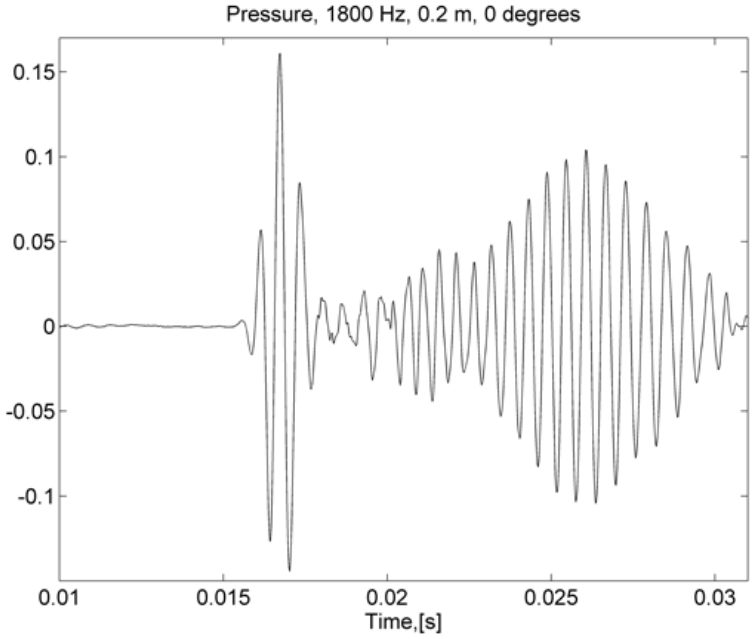


Figure 4.8: A time history of the sound pressure in the Gaussian pulse filled with the frequency of 1800 Hz, recorded at 0.2 m from the open pipe end, 0 degrees angular position.

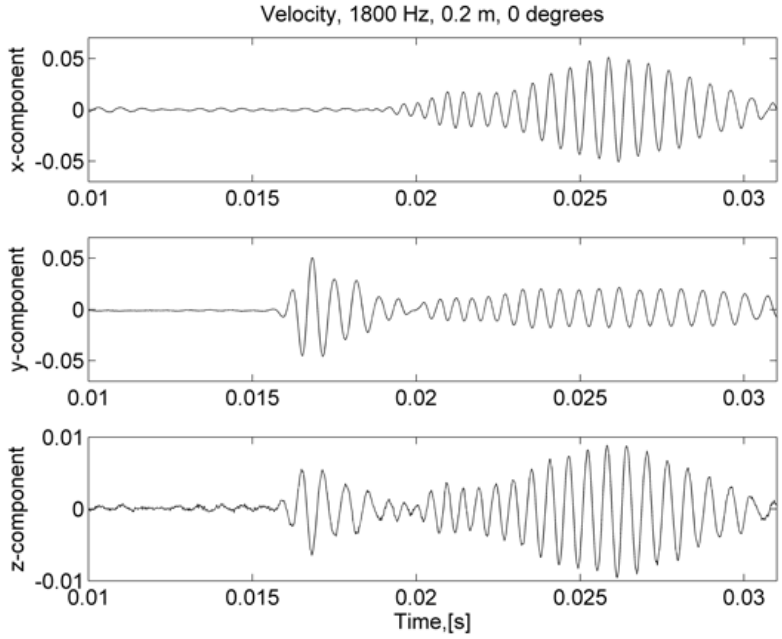


Figure 4.9: A time history of the three components of sound velocity in the Gaussian pulse filled with the frequency of 1800 Hz, recorded at 0.2 m from the open pipe end, 0 degrees angular position.

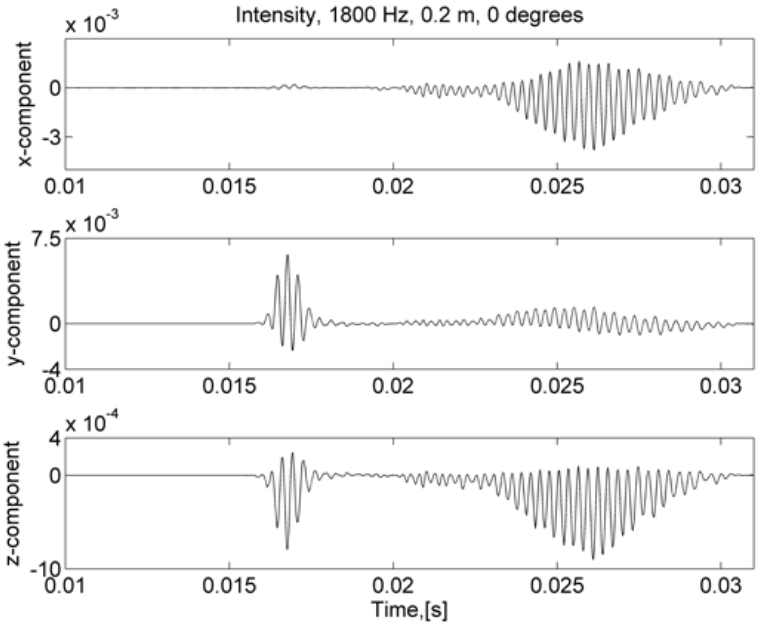


Figure 4.10: A time history of the three components of sound intensity in the Gaussian pulse filled with the frequency of 1800 Hz, recorded at 0.2 m from the open pipe end, 0 degrees angular position.

1340 Hz when the loudspeaker is placed near the edge of the tube. Gaussian pulses were emitted for a range of frequencies, starting with 300 Hz and up until 3100 Hz. The pulse central frequency step was 100 Hz until 2000 Hz and 50 Hz after, to capture the peculiar behaviour of the sound field in the vicinity of the cut-on frequency more accurately.

| n \ m | 0 | 1 | 2 | 3 |
|---|---|---|---|---|
| 0 | 0 | 2789 | 5106 | 7405 |
| 1 | 1340 | 3881 | 6213 | 8520 |
| 2 | 2223 | 4881 | 7256 | 9586 |
| 3 | 3058 | 5834 | 8258 | 10617 |

Table 4.1: The values of the cut-on frequencies in Hz for a 150 mm circular waveguide. *m* and *n* are indices of the modes propagating in the waveguide.

### 4.1.3 Data acquisition

In order to evaluate the transmission and reflection coefficients for the coaxial cylinder, two sets of experiments were conducted for each phenomenon and cross-sectional positioning of the equipment in the pipe. As a benchmark for transmission and reflection estimation, a set of measurements was first performed in the empty pipe, where the microphone array was placed at 13.5 m from the loudspeaker and then moved in the axial direction in 50 mm steps until it covered the axial distance of 1.5 m, which resulted in 31 axial positions. The described measurements were then repeated in the presence of the blockage. In order to measure the transmission coefficient, the microphone array was installed between the blockage and the sound-absorbing end of the pipe, and for reflection, it was between the loudspeaker and the blockage, starting at a 6 m distance from the loudspeaker.

A National Instruments DAQ NI PXIE-6358 was used in this experiment. A special LabVIEW based subroutine was developed to control the data acquisition process. A screen shot of the LabVIEW subroutine is shown in Figure 4.11. The features of the subroutine screen are listed in Table 4.2. The block diagram of this subroutine is presented in Figure 4.12.

The recorded data were stored automatically in text files as a six-column array, consisting of time data, pressure, three velocity vectors and reference pressure.

| No. | Field | Its function |
|---|---|---|
| 1 | Pulse file | Sets the path to a text file containing the emitted pulse data. |
| 2 | Amplitude multiplyer | Multiplies the incident signal amplitude by a specified coefficient. |
| 3 | Duration | Sets the duration of recording in seconds. |
| 4 | Sample rate | Sets the sampling frequency of the recorded data in Hz. |
| 5 | Filename | Sets the path to a text file where the recorded data are to be stored. |
| 6 | Measurement | Shows the plot presenting time histories of recorded signals. |
| 7 | Waveform graph | Shows the plot presenting the emitted signal time history. |

Table 4.2: Basic features of the LabVIEW subroutine.

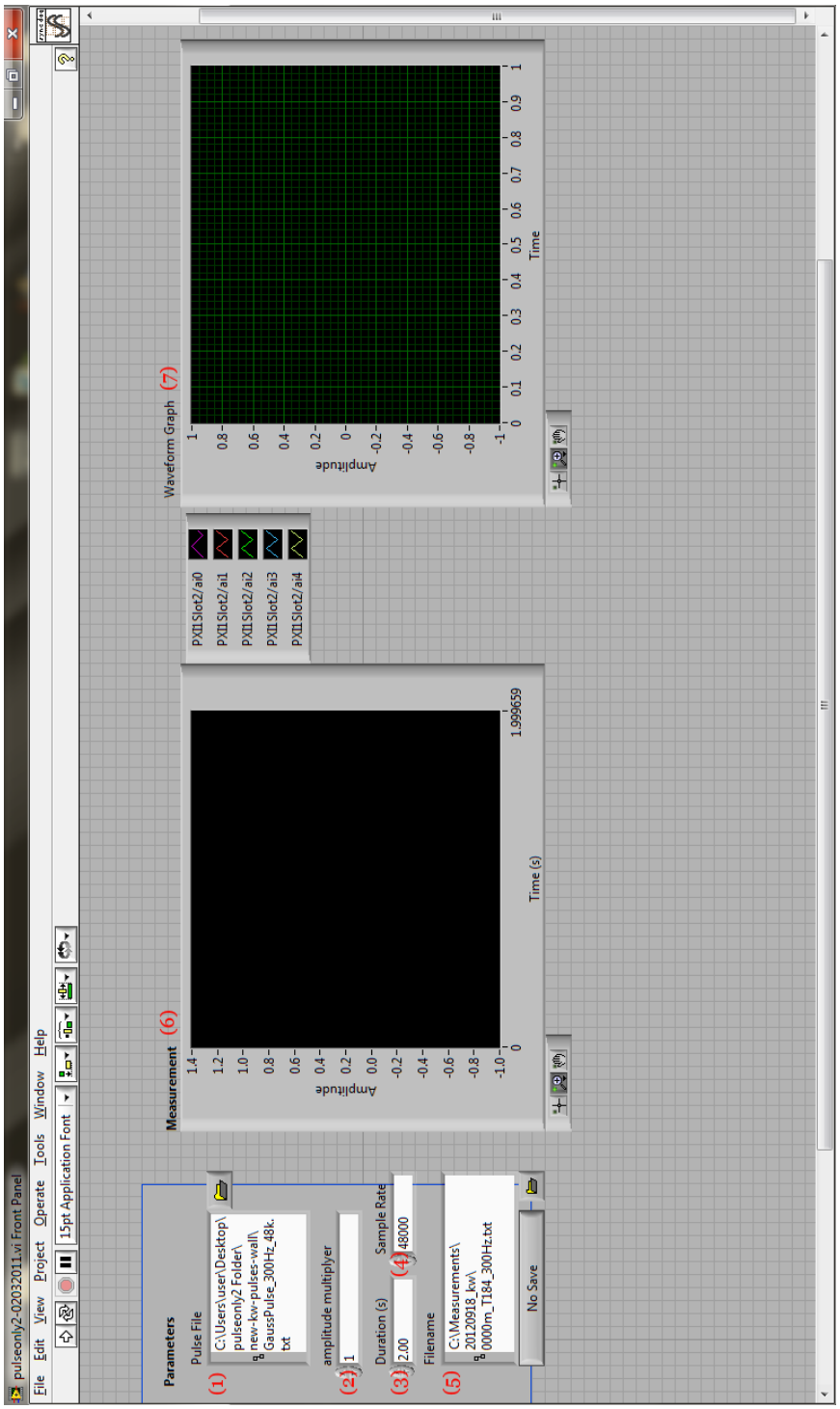


Figure 4.11: A screen shot of the GUI for the LabVIEW subroutine which was used for data acquisition.

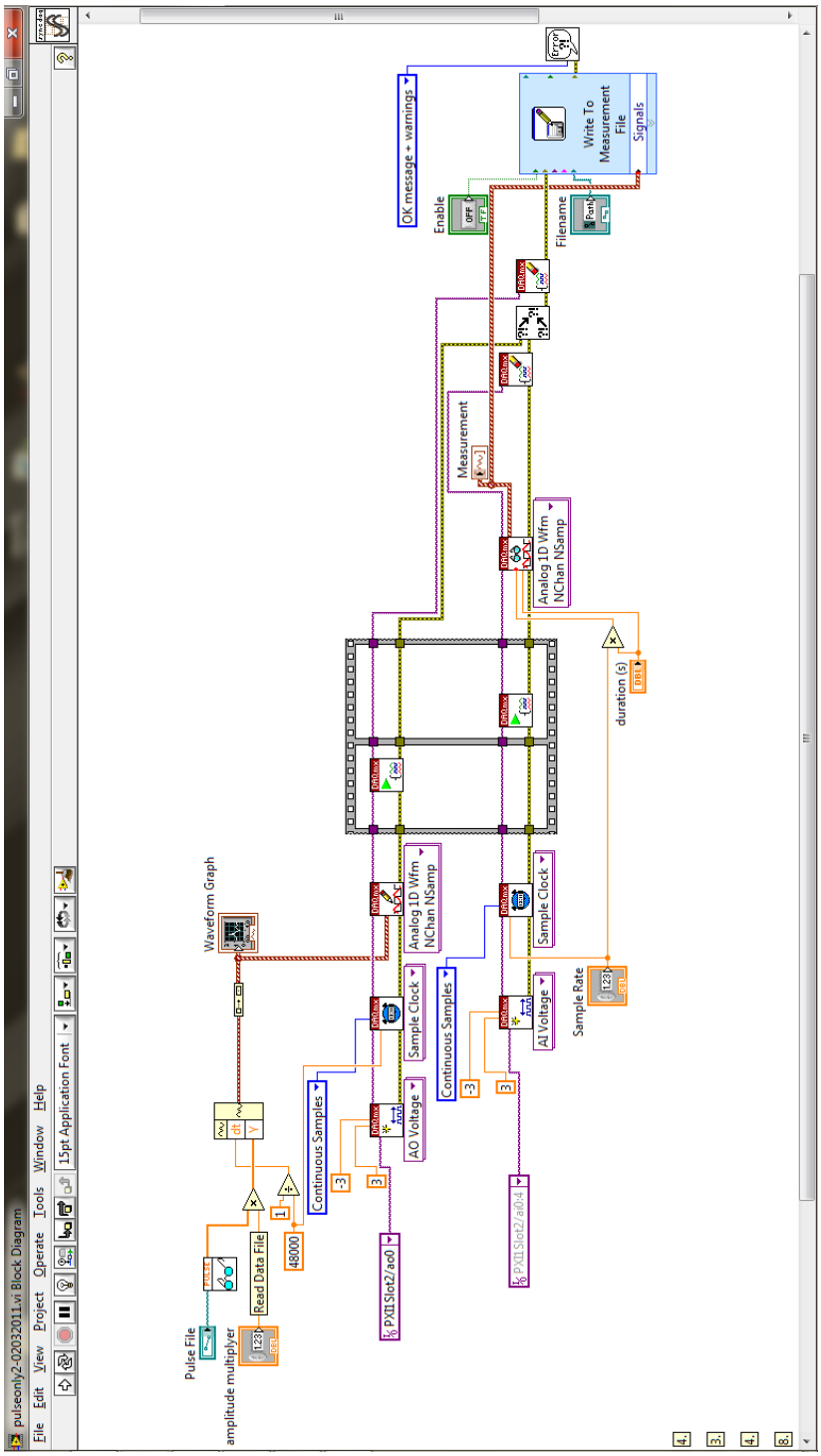


Figure 4.12: The block diagram of LabVIEW subroutine used for data acquisition.

### 4.1.4 Wavenumber-frequency analysis

After all the data were recorded, they were detrended, filtered and windowed. A time window was applied to the three sets of data (empty pipe / reflection / transmission) to control the length of the multi-modal sound pressure data recorded in the waveguide. A rectangular window with the edges rounded with Hamming window was used. Below the examples of windowed time histories at 2500 Hz frequency are presented to illustrate the part of a sound pressure signal used in the Fourier analysis. These were recorded in the centre of pipe cross-section, for both the empty pipe and the pipe with the cylinder inside in the transmission mode (see Figures 4.13 and 4.14).

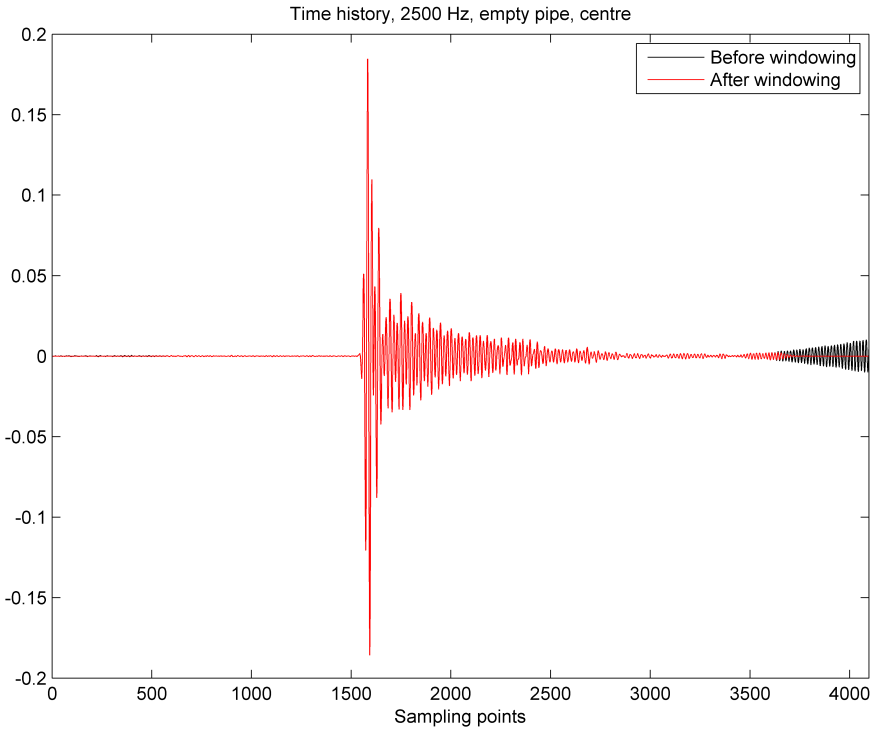


Figure 4.13: Sound pressure time history at 2500 Hz, empty pipe.

After the data were windowed and zero-padded, two-dimensional Fourier transform was applied:

$$\tilde{p}(\mathbf{k},\omega) = \int_{-\infty}^{+\infty}\int_{-\infty}^{+\infty} p(\mathbf{z},t)\exp^{-i(\omega t-\mathbf{kz})}\,d\mathbf{z}dt. \tag{4.1.3}$$

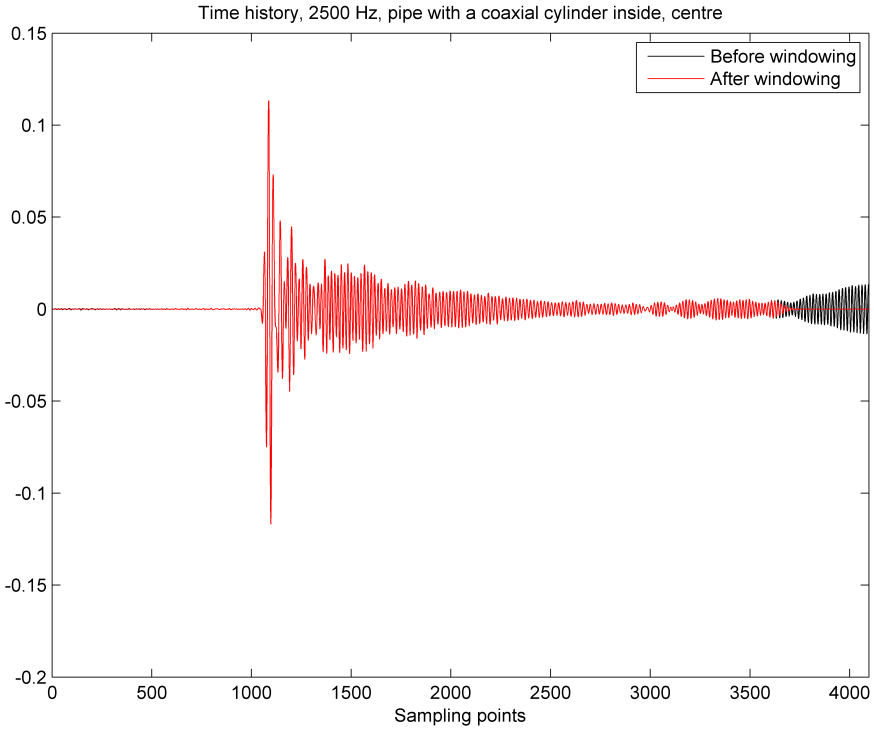


Figure 4.14: Sound pressure time history at 2500 Hz, coaxial cylinder in the pipe.

It was calculated in Matlab using the `fft()` function twice, first to perform the transform in the temporal and then in spatial domain. This procedure was repeated for the data recorded for each type of the Gaussian pulse excitation. After a series of wavenumber-frequency-dependent sound pressure spectra was obtained, it was combined into one spectrum by taking the average value of individual spectra. Three separate spectra were determined: (i) for the empty pipe; (ii) in front of the blockage; (iii) behind the blockage. The pressure transmission coefficient frequency spectra were calculated as the ratio of the integrals of the wavenumber spectra:

$$\tau_{int}(f_0) = \frac{\int_0^{k_0} p_{b,tr}(f_0,k)dk}{\int_0^{k_0} p_e(f_0,k)dk}, \tag{4.1.4}$$

$$\tau_{max}(f_0) = \frac{\max\left(p_{b,tr}(f_0,k)\right)}{\max\left(p_e(f_0,k)\right)}, \tag{4.1.5}$$

where $p_e$ is the frequency-wavenumber spectrum recorded in the empty pipe, $p_{b,tr}$ is the frequency-wavenumber spectrum measured behind the blockage, and $f_0$ is the centre frequency of the Gaussian pulse. A similar procedure was performed to calculate the pressure reflection coefficient, which was determined as:

$$R_{int}(f_0) = \frac{\int_0^{k_0} p_{b,r}(f_0, k)dk}{\int_0^{k_0} p_{e,r}(f_0, k)dk}, \tag{4.1.6}$$

$$R_{max}(f_0) = \frac{\max\left(p_{b,r}(f_0, k)\right)}{\max\left(p_e(f_0, k)\right)}, \tag{4.1.7}$$

where $p_{b,r}$ is the frequency-wavenumber spectrum measured in front of the blockage.

The intensity reflection and transmission coefficients were obtained in a likewise manner. In order to calculate them, the velocity data were retrieved from the recorded sound pressure in a following way:

$$u_z(t) \approx -\frac{1}{\rho_0 \Delta} \int_{-\infty}^{t} \left[p_{m_1}(\tau) - p_{m_2}(\tau)\right] d\tau, \tag{4.1.8}$$

Then, after these data were transformed to have frequency dependence as opposed to time dependence, the active and reactive intensity components were calculated:

$$\tilde{I}_{z,a} = 0.5\mathrm{Re}\left(p\, u_z^*\right), \tag{4.1.9}$$

$$\tilde{I}_{z,re} = 0.5\mathrm{Im}\left(p\, u_z^*\right), \tag{4.1.10}$$

where an asterisk denotes the complex conjugate.

## 4.2 Results and discussion

Figures 4.15-4.17 show the frequency-wavenumber spectra for the sound pressure recorded in the 150 mm diameter pipe in the absence and presence of a coaxial cylinder. Figure 4.15 shows the frequency-wavenumber spectrum recorded in the empty pipe, and Figures 4.16 and 4.17 shows the frequency-wavenumber spectra recorded in front of and behind the blockage, respectively. These figures present the data in a frequency range up to 3500 Hz, which includes the first axi-symmetric cut-on frequency of 2789 Hz. However, at the frequencies at which this mode is excited little energy is reflected by the cylinder. Therefore, the 3rd mode is not visible very well in Figure 4.16. On the other hand, quite a considerable amount of sound energy propagates past the cylinder, therefore the modal trace in Figure 4.17 is strong and can be used to determine the modal transmission coefficient. Nevertheless, only the plane wave (fundamental mode) was considered for the later analysis. The theoretical predictions for higher-order modes are much more challenging to compute, so by obtaining the predictions for the plane wave regime only, the time costs were significantly reduced and the method was deemed to be more attractive in terms of it practical realisation. The frequency-wavenumber spectra were subsequently used to derive the reflection and transmission coefficients as described by expressions (4.1.4)-(4.1.7). The measured and predicted absolute values of the sound pressure and active sound intensity reflection coefficients are shown in Figures 4.18 and 4.19, whereas those for the transmission coefficient are shown in Figures 4.20 and 4.21. The predictions were obtained using the hybrid model (Duan et al., 2013), described in Section 2.4.1. Three sets of data are presented in each figure: a red line denotes the theoretical predictions, black dots show the integral method results and black crosses - maximum value method results. Firstly, it is worth noticing that there is a good match between experiments and predictions. The mean error for the transmission measurements was quantified in accordance with Equation (4.2.1) and is

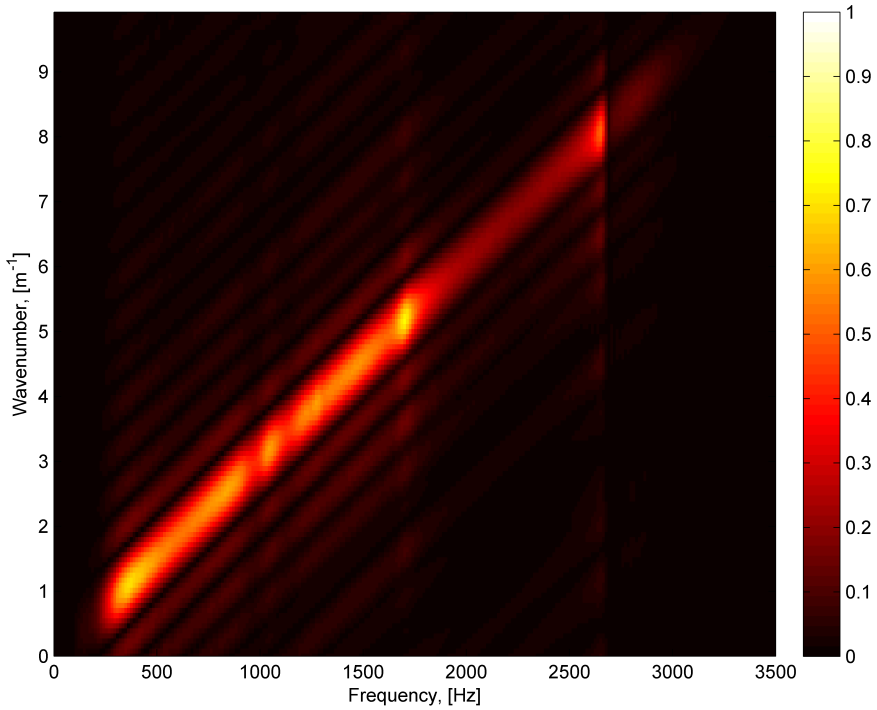


Figure 4.15: The measured k-$\omega$ spectrum for the empty 150 mm diameter pipe, with the microphone placed in the centre of the pipe cross-section.

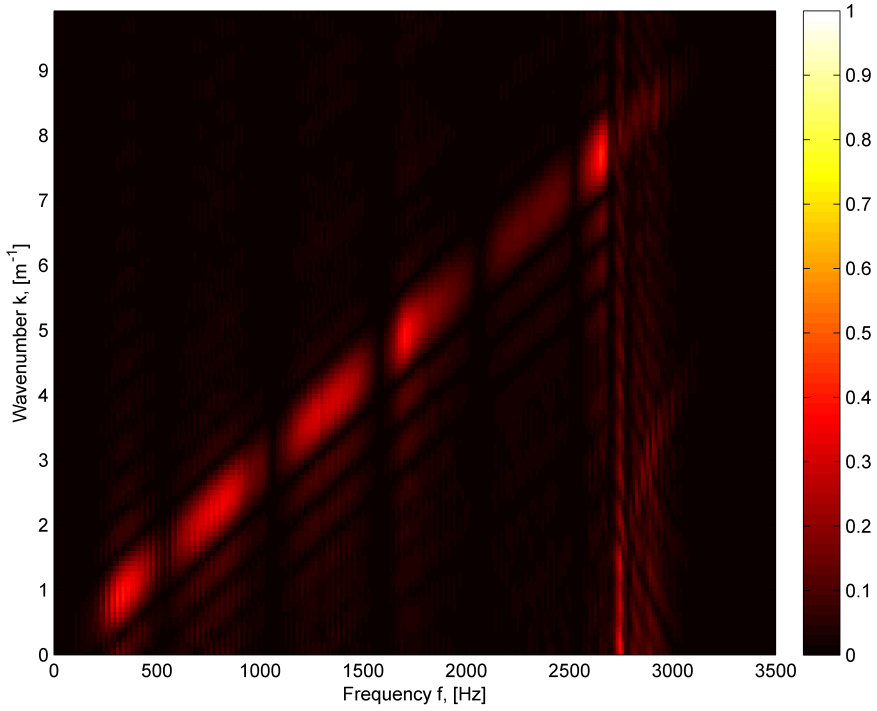


Figure 4.16: The measured pressure k-$\omega$ spectrum for the 150 mm diameter pipe in presence of a coaxial cylinder in reflection, with the microphone placed in the centre of the pipe cross-section.

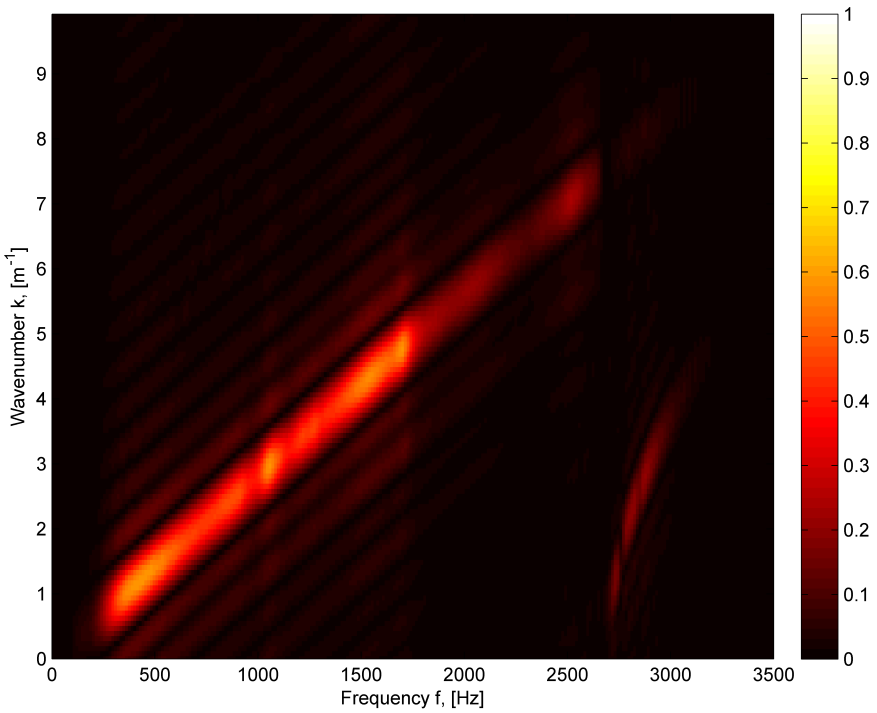


Figure 4.17: The measured k-$\omega$ spectrum for the 150 mm diameter pipe in presence of a coaxial cylinder in transmission, with the microphone placed in the centre of the pipe cross-section.

equal to 1.9%:

$$\epsilon_\tau = \frac{1}{N_i} \sum_{i=1}^{N_i} |\tau^{(\mathrm{m})}(\omega_i) - \tau(\omega_i))|, \tag{4.2.1}$$

where $\tau(\omega_i))$ and $\tau^{(\mathrm{m})}(\omega_i)$ are the measured and predicted transmission coefficients, respectively. The amplitude of the measured transmission coefficient is smaller than the one of the predicted which can be attributed to non-perfectly reflecting walls of the pipe or sound leaking through the small gaps between pipe sections. The numerical and experimental results start to diverge at a frequency of approximately 1 kHz. The discrepancy was also observed when the experiments were performed with the loudspeaker and the microphone near the wall. This leads to a conclusion that the cylinder inserted in the pipe had irregularities, such as an imperfect seal between the cylindrical shell and termination ends. As a result, the walls of the cylinder might not be perfectly reflecting as it was assumed in the model.

The reflection coefficient for this cylinder is shown in Figures 4.18 and 4.19. The error

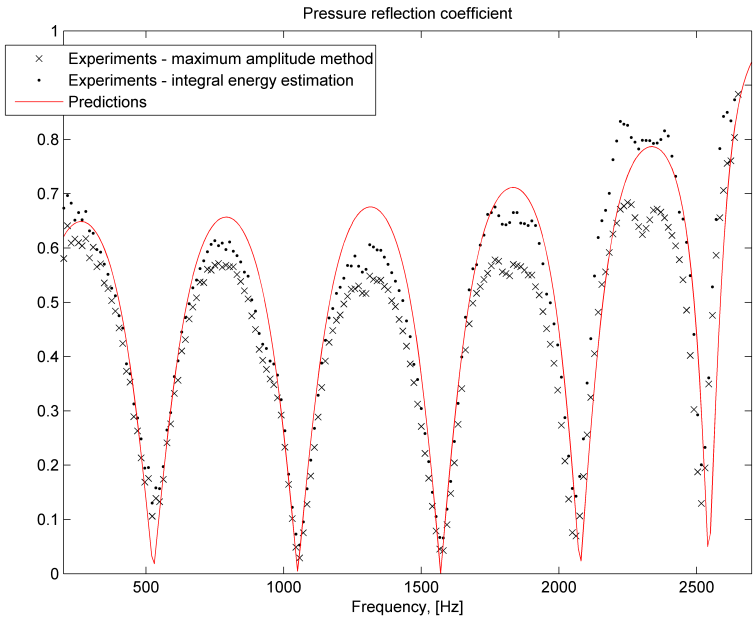


Figure 4.18: The measured and predicted values of the sound pressure reflection coefficient. Red line: predictions; black dots: integral method; black crosses: maximum value method.

between the predicted and the measured values is quantified in a similar manner as the transmission coefficient error. It is slightly higher that in the case of the transmission coefficient and is equal to 8.4%. Again, the measured reflection coefficient is lower than predicted throughout the adopted frequency range for the same reasons as described above. The measured transmission coefficient curve is not perfectly smooth which is an outcome of experimental data processing. The frequency-wavenumber spectra for sound reflection from cylinder were not as clear as for sound transmission which made the data acquisition from them challenging.

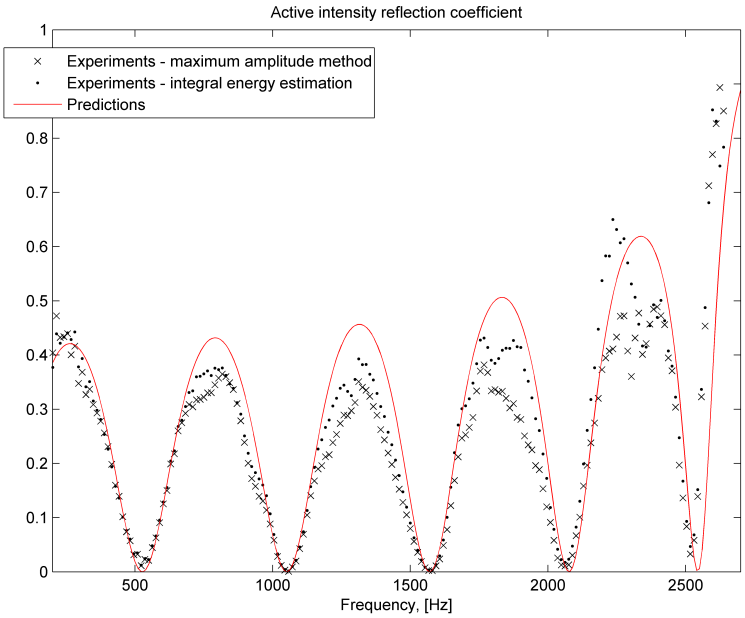


Figure 4.19: The measured and predicted values of the active sound intensity reflection coefficient. Red line: predictions; black dots: integral method; black crosses: maximum value method.

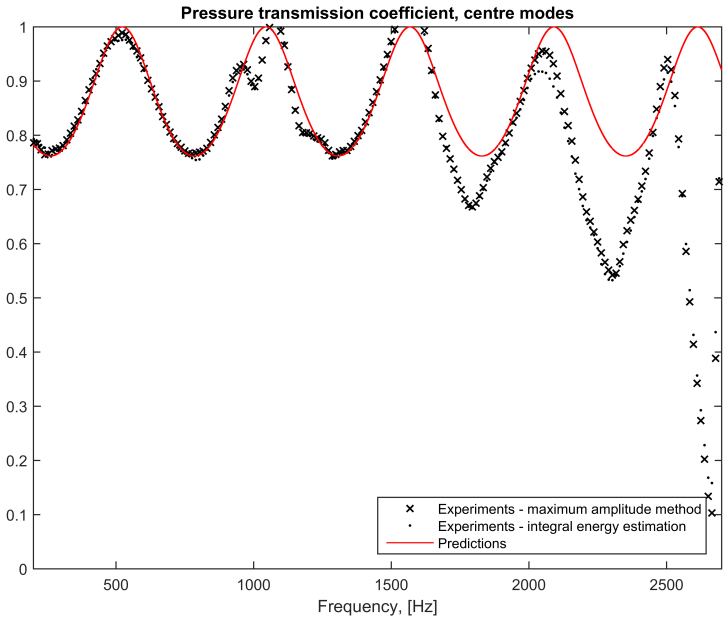


Figure 4.20: The measured and predicted values of the sound pressure transmission coefficient. Red line: predictions; black dots: integral method; black crosses: maximum value method.

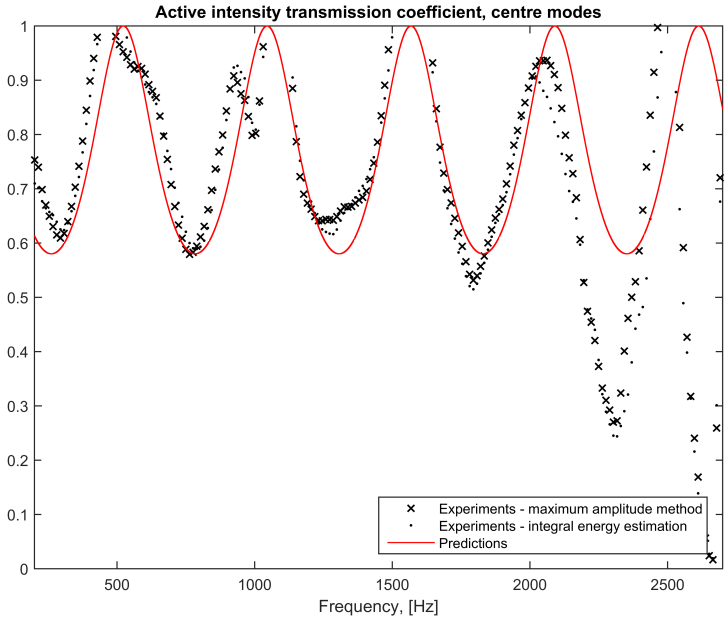


Figure 4.21: The measured and predicted values of the active sound intensity transmission coefficient. Red line: predictions; black dots: integral method; black crosses: maximum value method.

## 4.3 Summary

This chapter describes the method of characterisation of an axi-symmetrical blockage in a pipe. It is based on simulating an axial microphone array and substituting the obtained data into the two-dimensional Fourier transform. Measurements in an empty pipe have been performed in order to give a guideline to the incident signal. The obtained data have been subsequently used to estimate the blockage reflection and transmission coefficients, combined with the measurements performed in the presence of the blockage, in front of it or behind it, respectively. The results have been presented for the plane wave regime, which is up to 2789 Hz for the given pipe, with the microphone array placed in the middle of cross-section. The experimental data exhibit a good agreement with the predictions by the hybrid model. This means that the suggested method can be successfully used to locate and characterise blockages in waveguides. However, the method can be developed further to include higher modes, as well as to measure more complex blockages, which are not perfectly reflecting or misaligned with respect to the

centre of the pipe.

The next chapter will talk about another kind of inhomogeneity in a pipe, a porous termination. Sound intensity measurements will be employed to determine the total absorption coefficient of the porous termination in a wide range of frequencies.

# Chapter 5

# Material characterisation methods

This chapter focuses on sound reflection and absorption of porous materials. A new method to determine modal sound reflection coefficients at normal and oblique incidence is proposed, which allows to extend significantly the frequency range of the standard ISO 10534-2 method (1998). The method is successfully tested on a range of porous materials and its results have a good match with the predictions obtained with the Johnson-Champoux-Allard model (Champoux and Allard, 1991).

## 5.1 A new impedance tube method

The following method has been developed to overcome the restriction on the material sample size when used for sound absorption measurements in an impedance tube (Prisutova et al., 2014).

According to this new method it is proposed to measure the sound pressure spectra at a number of axial positions in an impedance tube. This provides a possibility to

obtain a set of frequency- and position-dependent sound pressure data, to which the spatial Fourier transform can then be applied to determine the relations between the wavenumber and frequency spectra (convention $e^{-i\omega t}$). Fourier integral was applied in the spatial domain and it was approximated with a sum which was taken using the trapezoidal rule. This trapezoidal rule was applied to the sound pressure data measured at the N microphone positions:

$$\tilde{p}_m(K,\omega) = \int_{-\infty}^{\infty} p_m(z,\omega)e^{iKz}dz \simeq \frac{\Delta}{2}\sum_{j=1}^{N-1}\left[p_m\left(z_{j+1},\omega\right)e^{iKz_{j+1}} + p_m\left(z_j,\omega\right)e^{iKz_j}\right], \quad (5.1.1)$$

where $\Delta$ is the separation between two subsequent microphone positions in the axial direction, $z_j$ and $z_{j+1}$ are the $j$-th and $(j+1)$-th axial positions, respectively.

For an impedance tube with the square cross-section which is terminated with an absorbing lid (e.g. a porous layer), the sound pressure can be expressed as a superposition of an infinite number of normal modes:

$$p(z,\omega) = \sum_{m=0}^{\infty}\sum_{n=0}^{\infty}\cos\frac{m\pi}{a}x\cos\frac{n\pi}{a}y\left(A_{mn}e^{-ik_{mn}z} + A_{mn}R_{mn}e^{ik_{mn}z}\right), \quad (5.1.2)$$

where $x, y$ and $z$ are the coordinates of the microphone, $m, n$ are the indices of the modes propagating in the tube, $a$ is the width of the tube cross-section, $k_{mn}$ is the modal wavenumber, $k_{mn} = \sqrt{k^2 - \left(\frac{m\pi}{a}\right)^2 - \left(\frac{n\pi}{a}\right)^2}$, with $k = 2\pi f/c_0$ , and $A_{mn}$ are the modal excitation coefficients in the incident sound wave and $R_{mn}$ are the unknown modal reflection coefficients which depend on the frequency, on the angle at which the mode is incident on the termination and on the acoustical properties of the porous material from which the specimen at this termination is constructed. The values of the cut-on frequencies for the first few normal modes for the particular impedance tubes used in this experiment are presented in Tables 5.1, 5.2 and 5.10 (at 20° C). The modal patterns for square and circular tubes are shown in Figures 5.1 and 5.2.

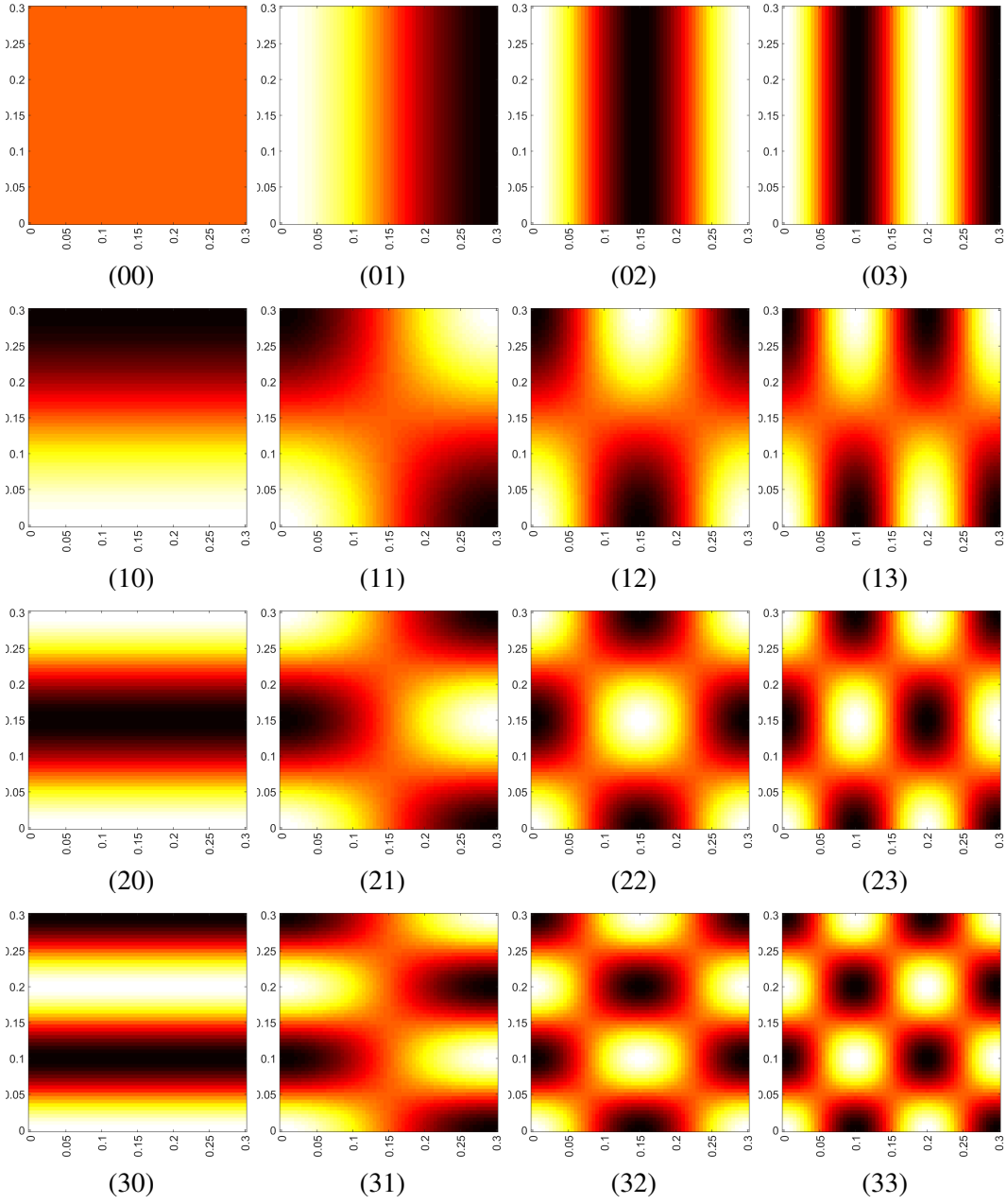


Figure 5.1: Modal patterns for the first four propagating modes in a square impedance tube. $x$-axis: $x$ coordinate, [m]; $y$-axis: $y$ coordinate, [m]. Colorbar: -1 - black, 0 - orange, 1 - white.

The Fourier transform of Equation (5.1.2) is

$$\tilde{p}(K,\omega) = \sum_{m=0}^{\infty}\sum_{n=0}^{\infty} \cos\frac{m\pi}{a}x \cos\frac{n\pi}{a}y \left( A_{mn}\int_{-\infty}^{\infty} e^{i(K-k_{mn})z}dz + A_{mn}R_{mn}\int_{-\infty}^{\infty} e^{i(K+k_{mn})z}dz \right). \tag{5.1.3}$$

Equation (5.1.3) can be analytically simplified by replacing the infinite integration lim-

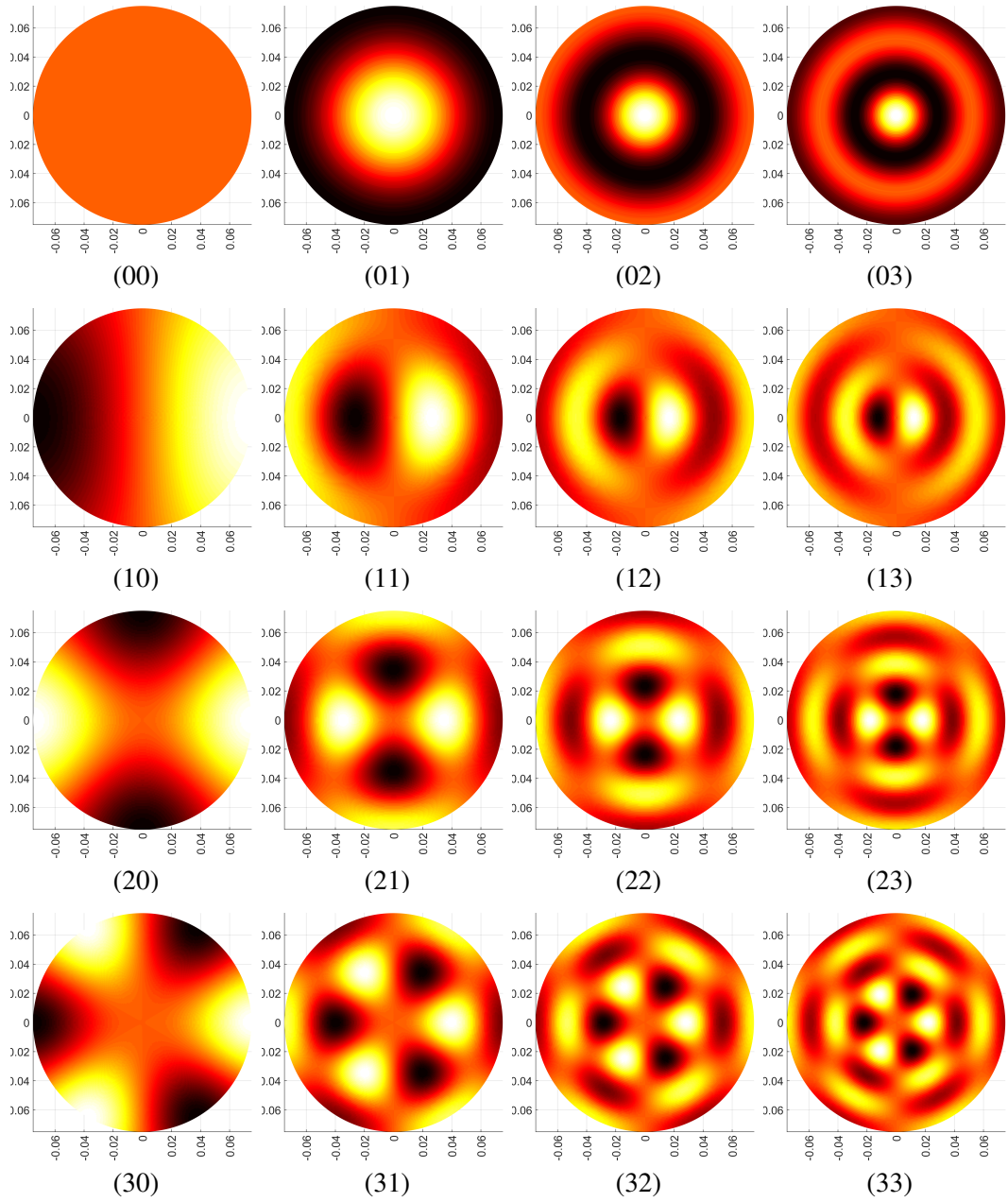


Figure 5.2: Modal patterns for the first four propagating modes in a circular impedance tube. $x$-axis: $x$ coordinate, [m]; $y$-axis: $y$ coordinate, [m]. Colorbar: -1 - black, 0 - orange, 1 - white.

its with the coordinates of the first and the last microphone measurement positions, $z_1$

and $z_2$, to take the following form:

$$\begin{aligned}\tilde{p}(K,\omega) = \sum_{m=0}^{\infty}\sum_{n=0}^{\infty} \cos\frac{m\pi}{a}x \ \cos\frac{n\pi}{a}y \ \times \cdots \\ \cdots \left[A_{mn}\ e^{i(K-k_{mn})\frac{z_2+z_1}{2}}\ (z_2-z_1)\ \mathrm{sinc}\left((K-k_{mn})\frac{z_2-z_1}{2}\right) + \cdots \right. \\ \left. \cdots \ A_{mn}\ R_{mn}\ e^{i(K+k_{mn})\frac{z_2+z_1}{2}}\ (z_2-z_1)\ \mathrm{sinc}\left((K+k_{mn})\frac{z_2-z_1}{2}\right)\right],\end{aligned} \tag{5.1.4}$$

where $\mathrm{sinc}\, z = \frac{\sin z}{z}$.

For a circular impedance tube, the sum (5.1.2) takes the following form:

$$p(z,\omega) = \sum_{m=0}^{\infty}\sum_{n=0}^{\infty} \cos(m\theta)\, J_m(\gamma_{mn}r)\left(A_{mn}e^{-ik_{mn}z} + A_{mn}R_{mn}e^{ik_{mn}z}\right), \tag{5.1.5}$$

where $\theta$, $r$ and $z$ are the cylindrical coordinates of the microphone, $J_m$ is Bessel function of the first kind and of the $m$-th order, $\gamma_{mn}$ are the wavenumbers which correspond to the zeros of the first derivative of $J_m$, and $k_{mn} = \sqrt{k^2-\gamma_{mn}^2}$. For this tube, Equations (5.1.3) and (5.1.4) become

$$\tilde{p}(K,\omega) = \sum_{m=0}^{\infty}\sum_{n=0}^{\infty} \cos(m\theta)\, J_m(\gamma_{mn}r)\left(A_{mn}\int_{-\infty}^{\infty} e^{i(K-k_{mn})z}dz + A_{mn}R_{mn}\int_{-\infty}^{\infty} e^{i(K+k_{mn})z}dz\right) \tag{5.1.6}$$

and

$$\begin{aligned}\tilde{p}(K,\omega) = \sum_{m=0}^{\infty}\sum_{n=0}^{\infty} \cos(m\theta)\, J_m(\gamma_{mn}r) \ \times \cdots \\ \cdots \left[A_{mn}\ e^{i(K-k_{mn})\frac{z_2+z_1}{2}}\ (z_2-z_1)\ \mathrm{sinc}\left((K-k_{mn})\frac{z_2-z_1}{2}\right) + \cdots \right. \\ \left. \cdots \ A_{mn}\ R_{mn}\ e^{i(K+k_{mn})\frac{z_2+z_1}{2}}\ (z_2-z_1)\ \mathrm{sinc}\left((K+k_{mn})\frac{z_2-z_1}{2}\right)\right],\end{aligned} \tag{5.1.7}$$

respectively.

In Equations (5.1.4) and (5.1.7) $A_{mn}$ and $R_{mn}$ are the unknowns which have to be determined for every mode and frequency. For this purpose, the optimisation algorithm was

applied to the cost function $F$ to minimise the difference:

$$\min_{A_{mn},R_{mn}} F(\omega) = \sum_{K_{min}}^{K_{max}} |\tilde{p}_m(K,\omega) - \tilde{p}(K,\omega)|^2, \tag{5.1.8}$$

for each of the angular frequencies $\omega$ in the measured modal pressure spectra $\tilde{p}_m(K,\omega)$. In the above expression $F$ is the cost function to be minimised, $\tilde{p}(K,\omega)$ is the predicted sound pressure expressed with Equation (5.1.4) or (5.1.7), and $K_{min}$ and $K_{max}$ are the minimum and maximum values of the wavenumber in the wavenumber spectra for which the measured data are available, respectively.

It is convenient to express the modal amplitude and the modal reflection coefficient in the following form:

$$A_{mn} = a_{mn}e^{i\phi_{mn}}, \quad A_{mn}R_{mn} = b_{mn}e^{i\psi_{mn}}, \tag{5.1.9}$$

where $a_{mn}$, $b_{mn}$ are the absolute values of the forward and backward waves, i.e. $A_{mn}$ and $A_{mn}R_{mn}$, respectively, whereas $\phi_{mn}$ and $\psi_{mn}$ are their phases. These quantities are real numbers which are convenient to use in the minimisation procedure to estimate the amplitudes and phases in the incident and reflected normal waves and which can then be combined to represent the proportion of the sound energy in the reflected sound wave and the proportion of the sound energy absorbed by the porous specimen through the decomposition of normal waves at a particular frequency.

The minimisation procedure (5.1.8) was applied to recover the absolute values of the modal amplitudes and phases in the considered range of frequencies so that the modal reflection coefficients were determined by the following expression:

$$R_{mn} = \frac{b_{mn}e^{i\psi_{mn}}}{a_{mn}e^{i\phi_{mn}}}. \tag{5.1.10}$$

The procedure was performed by making use of MATLAB in-built `fminsearch` function. It was applied to each mode separately, i.e. the adopted frequency range was

divided into several regions, limited by modal cut-on frequencies from each side (eg. 50-572 Hz, 572-808 Hz, 808-1143 Hz, 1143-1278 Hz, 1278-1617 Hz and 1617-1800 Hz for the 300 mm square tube). In each region, amplitudes and phases of incident and reflected waves were recovered for each propagating mode, frequency-by-frequency, so for the frequency band of 50-572 Hz amplitudes and phases were recovered for the fundamental mode only, for the frequency band of 572-808 Hz - for the fundamental mode and the first higher mode, etc. The recovered values were imprecise in the vicinity of cut-on frequencies, but as soon as the frequency of interest was about 40 Hz from the cut-on, the recovered values stabilised.

Four examples of the application of the minimisation procedure for the 300 mm square tube are shown in Figures 5.3-5.4, presenting the data in two different frequency regimes: plane wave (214 Hz) and fully modal (1236 Hz). These examples are for a square 82 mm hard-backed layer of melamine foam. The figures show the amplitudes and phases as functions of the wavenumber before (upper subplots) and after (lower subplots) the application of the minimisation procedure. The amplitudes $A_{mn}$ and $A_{mn}R_{mn}$ of the wavenumber in the upper subplots were assumed to be equal to 1, and the phases $\phi_{mn}$ and $\psi_{mn}$ - equal to 0. The results suggest that the minimisation procedure allows to match very closely both the amplitude and the phase of the reflection coefficient below the cut-on frequency with the mean error $\epsilon$ of 1.1% for the amplitude and 1.9% for the phase calculated using

$$\epsilon = \frac{\sum_{w=1}^{N_w} |\tilde{p}_m - \tilde{p}|}{\sum_{w=1}^{N_w} \left|\frac{\tilde{p}_m + \tilde{p}}{2}\right|}. \tag{5.1.11}$$

This error can be higher (of the mean value of 5.3% and 23.2%, respectively) when several modes have to be accounted for (see Figure 5.4).

The absorption coefficient for the plane wave regime, $\alpha_{00}$, was then calculated in the following standard manner:

$$\alpha_{00} = 1 - |R_{00}|^2. \tag{5.1.12}$$

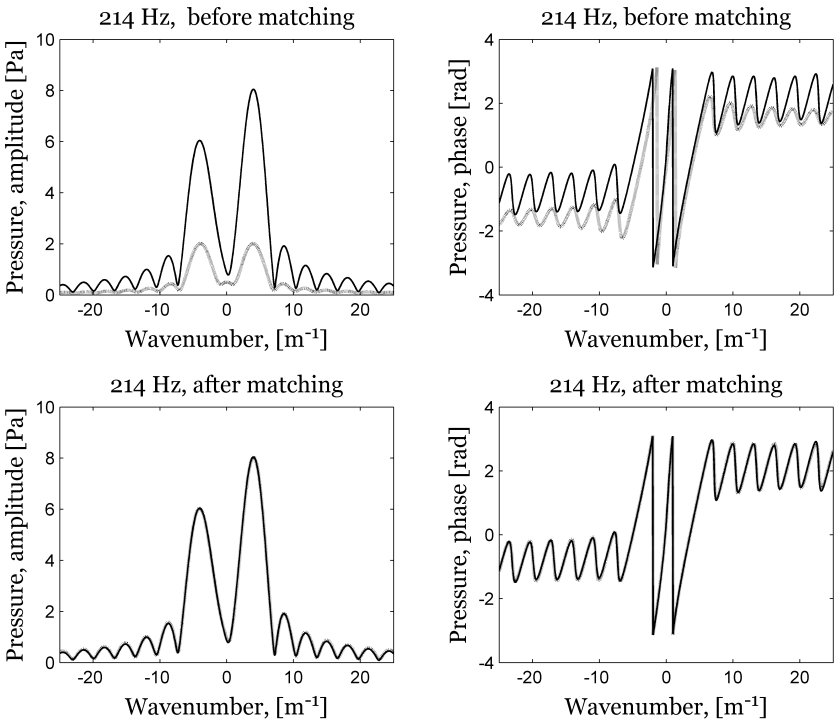


Figure 5.3: The measured and predicted sound pressure amplitude and phase for 214 Hz before and after the application of sound pressure matching procedure. Solid line: experiments; dashed line: predictions.

This acoustical quantity does not account for the energy dissipated by the higher order modes. The modal absorption coefficient defines the amount of energy which is absorbed by one particular mode only and is defined as follows:

$$\alpha_{mn} = 1 - |R_{mn}|^2, \tag{5.1.13}$$

where $R_{mn}$ is the modal reflection coefficient, given by expression (2.6.21).

The total absorption coefficient, which does include the energy transmitted by and dissipated through the high order mode absorption mechanisms can be derived from the basic knowledge of the energy relations in a waveguide. Two ways of its calculation have been used in this work. The first method makes use of the ratio of incident and reflected amplitudes in the tube. Equations (5.1.2) and (5.1.5) suggest that the modal decomposition of the sound field in the impedance tube combines two groups of waves:

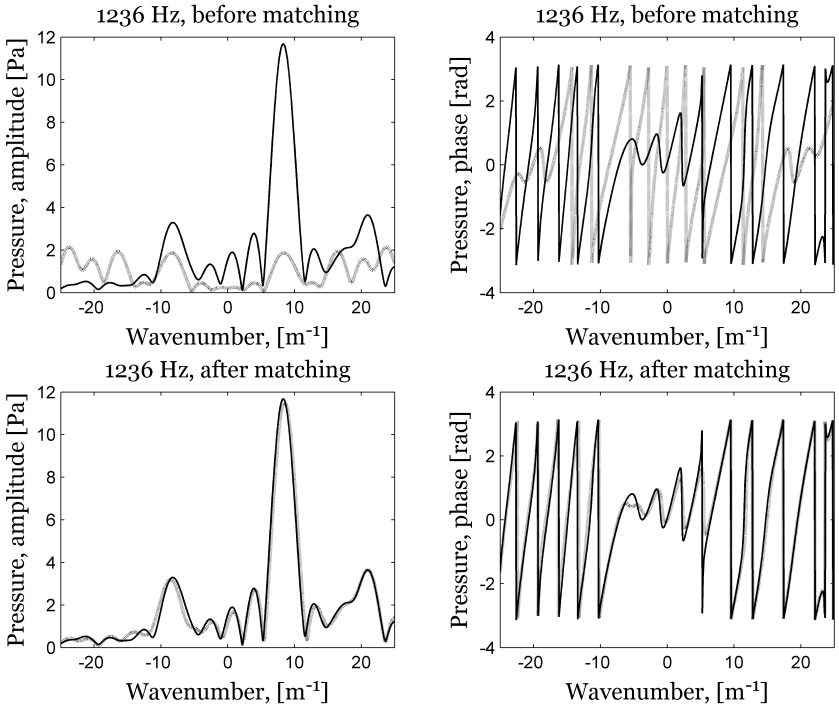


Figure 5.4: The measured and predicted sound pressure amplitude and phase for 1236 Hz before and after the application of sound pressure matching procedure. Solid line: experiments; dashed line: prediction.

those which are incident on the material specimen ($t$ being the time):

$$p_{mn}^{(i)}(x,y,z,t) = \Psi_{mn} A_{mn} e^{-ik_{mn}z + i\omega t}, \tag{5.1.14}$$

and those which are reflected from it

$$p_{mn}^{(r)}(x,y,z,t) = \Psi_{mn} A_{mn} R_{mn} e^{ik_{mn}z + i\omega t}, \tag{5.1.15}$$

where $\Psi_{mn} = \cos\frac{m\pi}{a}x \cos\frac{n\pi}{a}y$ for a square impedance tube, and $\Psi_{mn} = \cos(m\theta)J_m(\gamma_{mn}r)$ for a circular impedance tube. The difference between these two groups is in the sign in the exponential function $e^{\pm ik_{mn}z}$ and in the presence of the reflection coefficient term in (5.1.15). The $z$-component of the intensity vector in a propagating normal wave is a measure of energy which this wave carries from the source towards the material sample. This instantaneous intensity is the product of the sound pressure $I_{mn} = \mathrm{Re}\{p_{mn}^{(i)} v_{mn}\}$. The

$z$-component of the acoustic velocity vector of the mode ($mn$) is given by

$$v_{mn} = \frac{1}{i\omega\rho_0}\frac{\partial p_{mn}^{(i)}}{\partial z} = \frac{k_{mn}p_{mn}^{(i)}}{\omega\rho_0}. \tag{5.1.16}$$

This above suggests that

$$I_{mn}(x, y, x, t) = \frac{k_{mn}A_{mn}^2}{\omega\rho_0}\Psi_{mn}^2\cos^2(-k_{mn}z + \omega t), \tag{5.1.17}$$

and the time-averaged intensity is

$$\tilde{I}_{mn}(x, y) = \frac{k_{mn}A_{mn}^2}{2\omega\rho_0}\Psi_{mn}^2. \tag{5.1.18}$$

The mode ($mn$) incident on the material surface carries the energy flux through the cross-section of the impedance tube which is the integral of (5.1.18), i.e.

$$E_{mn} = \int_S \tilde{I}_{mn}dS. \tag{5.1.19}$$

It is easy to show that the integration of (5.1.19) gives the following expression for the total energy flux in the normal mode ($mn$) incident on the material specimen

$$E_{mn}^{(i)} = \frac{\mathrm{Re}(k_{mn})A_{mn}^2}{2\varepsilon_m\varepsilon_n\omega\rho_0}, \tag{5.1.20}$$

where $\varepsilon_{m\ (m=0)} = 1$ and $\varepsilon_{m\ (m>0)} = 2$ are the same as defined in Equation (5.1.28). The wavenumber $k_{mn}$ here is considered to be real because evanescent modes do not carry the energy.

The above arithmetical manipulations can be used to derive the total energy flux in the mode ($mn$) reflected from the material specimen and it is easy to show that

$$E_{mn}^{(r)} = \frac{\mathrm{Re}(k_{mn})\|A_{mn}R_{mn}\|^2}{2\varepsilon_m\varepsilon_n\omega\rho_0}, \tag{5.1.21}$$

where the norm $||A_{mn}R_{mn}||$ is applied because the quantity $A_{mn}R_{mn}$ which contains the modal reflection coefficient $R_{mn}$ is no longer real.

The total energy flux is the sum of the energies in all of the propagating modes, therefore

$$E^{(i)} = \sum_{mn} \frac{\mathrm{Re}(k_{mn})A_{mn}^2}{2\varepsilon_m\varepsilon_n\omega\rho_0}, \tag{5.1.22}$$

and

$$E^{(r)} = \sum_{m'n'} \frac{\mathrm{Re}(k_{m'n'})||A_{m'n'}R_{m'n'}||^2}{2\varepsilon_{m'}\varepsilon_{n'}\omega\rho_0}. \tag{5.1.23}$$

By its definition, the absorption coefficient is the ratio of the energy absorbed by the surface ($E^{(i)} - E^{(r)}$) to the incident sound energy ($E^{(i)}$), i.e. $\alpha = (E^{(i)} - E^{(r)})/E^{(i)}$. Making use of this definition and Equations (5.1.22) and (5.1.23) yields

$$\alpha_{amp}(\omega) = 1 - \frac{\sum\limits_{m'n'} \dfrac{\mathrm{Re}(k_{m'n'})||A_{m'n'}R_{m'n'}||^2}{\varepsilon_{m'}\varepsilon_{n'}}}{\sum\limits_{mn} \dfrac{\mathrm{Re}(k_{mn})A_{mn}^2}{\varepsilon_m\varepsilon_n}}, \tag{5.1.24}$$

For the second method, the total absorption coefficient was calculated using the sound intensity data. The sound intensity was calculated by making use of the mean sound pressure between two closely spaced microphone positions and sound velocity measured as the integral of the pressure difference, i.e.:

$$p(z_j, \omega) = \frac{1}{2}\Big(p(z_j, \omega) + p(z_{j-1}, \omega)\Big), \tag{5.1.25}$$

$$u(z_j, \omega) = -\frac{1}{i\omega\rho_0\Delta}\Big(p(z_j, \omega) - p(z_{j-1}, \omega)\Big), \tag{5.1.26}$$

where $z_j$ denotes the $j$-th position of the microphone and $\Delta$ is the separation between these two positions. Such an expression for sound velocity was chosen for its simplicity

and to avoid the need to deal with separate modes during the calculations. The spatial Fourier transform was applied subsequently to determine the wavenumber spectra of the quantities in Equations (5.1.25) and (5.1.26). However, in the case of the 150 mm circular tube, the measurements were performed with the Microflown probe, which records both sound pressure and velocity. Hence, the recorded pressure and velocity readings were used at each position for the substitution in the Fourier transform, so Equations (5.1.25) and (5.1.26) were not used for the 150 mm circular tube. The total absorption coefficient was then calculated from the knowledge of the measured intensities in the incident and the reflected sound waves from:

$$I_i(K,\omega) = \frac{1}{2}\mathrm{Re}\Big(p_i(K,\omega)\,u_i^*(K,\omega)\Big),\ I_r(K,\omega) = \frac{1}{2}\mathrm{Re}\Big(p_r(K,\omega)\,u_r^*(K,\omega)\Big). \tag{5.1.27}$$

$$\alpha_{int}(\omega) = 1 - \left|\frac{\int\limits_K I_r(K,\omega)\,dK}{\int\limits_K I_i(K,\omega)\,dK}\right|, \tag{5.1.28}$$

where $K$ is the wavenumber and the asterisk symbol denotes the complex conjugation. Equation (5.1.28) can also be used to predict the total absorption coefficient in the case when the sound pressures are calculated using Equation (5.1.4).

The angles at which the higher modes impinged on the porous material surface were calculated separately for each mode by making use of the following formula:

$$\theta_{mn}(\omega) = \arccos\left(\frac{\sqrt{\left(\frac{\omega}{c_0}\right)^2 - \left(\frac{m\pi}{a}\right)^2 - \left(\frac{n\pi}{a}\right)^2}}{\omega/c_0}\right), \tag{5.1.29}$$

where $m, n$ are the indices of the modes propagating in the tube.

## 5.2 Measurements in square cross-section tube

### 5.2.1 Acoustic setup

The reported experiments were carried out using the impedance tube facilities available at the Laboratoire d'Acoustique de l'Université du Maine (LAUM) in France. Two impedance tubes were used and both had square cross-sections, which makes subsequent data processing easier than that in a rectangular cross-section tube. One of them was a square waveguide, a sketch of which is presented in Figure 5.5. It was constructed from 38 mm thick panels of medium density fibreboard which were varnished to ensure that the walls are sufficiently reflective so that they do not contribute noticeably to the level of air attenuation expected for this tube. The tube was 4.15 m long and the dimensions of the square cross-section were 300 mm x 300 mm. According to the standard method the high frequency limit for the plane wave regime in this tube was 572 Hz assuming that the sound speed was $c_0 = 343$ m/s at 20° C (ISO 10534-2, 1998) (see Table 5.1). One end of this tube was terminated with a 30 mm thick metal lid, and at the opposite end there were three loudspeakers (S1-S3) which were connected in parallel as shown in Figure 5.5. The coordinates of the centres of these three speakers were (50 mm, 50 mm), (50 mm, 150 mm), (150 mm, 150 mm), for speakers S1, S2 and S3, respectively. Such distribution was necessary to increase the number of propagating modes which can be excited in the adopted frequency range of 50 to 1800 Hz. A porous material sample was accurately cut to fit the cross-section of the tube and attached to the metal lid end without an air gap. The signal used for the sound field excitation was a step-by-step sine sweep, ranging from 50 to 1800 Hz, with a step of 12 Hz.

The second impedance tube is a square 3 m long waveguide with a 150 x 150 mm cross-section. Its walls are constructed of 30 mm thick PVC panels. Its both ends are terminated with transparent PVC, one of them having two openings for the microphone insertion. The loudspeaker was installed at the side of the tube in the vicinity of one

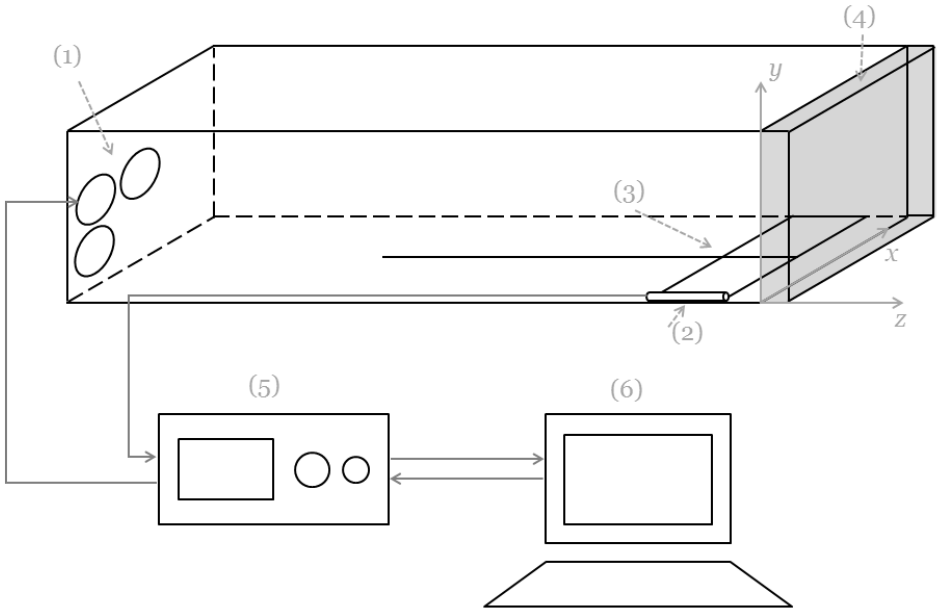


Figure 5.5: A schematic illustration of the 300 mm wide tube setup: (1) loudspeakers; (2) microphone; (3) microphone frame designed to maintain the microphone's position in a corner of tube; (4) porous material sample; (5) signal analyser; (6) PC.

end, as shown in Figure 5.6. At the opposite end, a porous material sample of the same cross-sectional size as the tube was installed, both with and without an air gap. The higher modes cut-on frequencies for this tube are presented in Table 5.2 at 20° C, and the high frequency limit of this tube was 1143 Hz. The adopted frequency range for this setup was from 50 to 3500 Hz. It was implemented using the step-by-step sine sweep of the same frequency range.

For both impedance tubes, a single 1/4" B&K microphone was used to avoid problems with phase and amplitude mismatch. Two cross-sectional positions were used, one in the corner of the pipe's cross-section, at $x_m$ = 5 mm, $y_m$ = 5 mm, where the amplitude of all the modes was maximum. Another position was at the middle of the cross-section, at $x_m$ = 150 mm, $y_m$ = 150 mm for the wooden tube, and at $x_m$ = 75 mm, $y_m$ = 75 mm for the PVC tube. In this way, the amplitude of the plane wave was maximum. The pressure readings were taken at 52 axial positions and the movement of the mi-

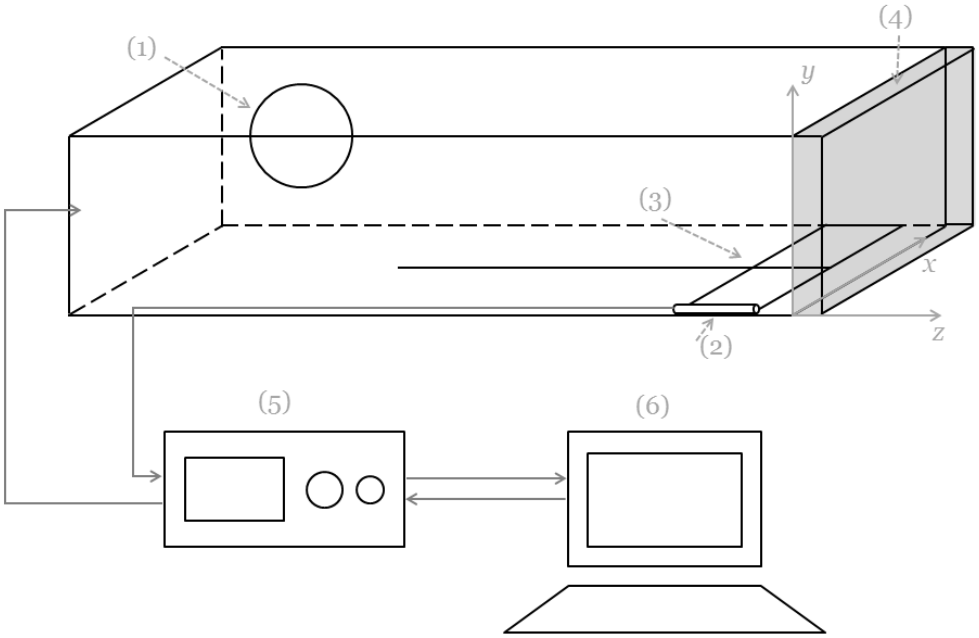


Figure 5.6: A schematic illustration of the 150 mm tube setup: (1) loudspeaker; (2) microphone; (3) microphone frame designed to maintain the microphone's position in a corner of tube; (4) porous material sample; (5) signal analyser; (6) PC.

| m / n | 0 | 1 | 2 | 3 |
|---|---|---|---|---|
| 0 | 0 | 572 | 1143 | 1715 |
| 1 | 572 | 808 | 1278 | 1807 |
| 2 | 1143 | 1278 | 1617 | 2061 |
| 3 | 1715 | 1807 | 2061 | 2425 |

Table 5.1: The values of the cut-on frequencies in Hz for a 300 mm square waveguide.

crophone was controlled by a robotic arm. The first position of the microphone was at the 5 mm distance from the porous material sample, and then the microphone was moved at a 40 mm step, which is consistent with the minimum spacing interval permitted by the Nyquist sampling theorem. This spacing allows to measure the spatial spectrum with the minimum wavelength of 80 mm. Also, this combination of spacing and maximum adopted frequency allows to avoid the spatial aliasing problem in frequency-wavenumber space. The data were acquired using a Stanford Research Systems SR785 signal analyser which allowed to measure and store the sound pressure spectra in the text file format. The frequency resolution of this system was 12 Hz.

| m / n | 0 | 1 | 2 | 3 |
|---|---|---|---|---|
| 0 | 0 | 1143 | 2287 | 3430 |
| 1 | 1143 | 1617 | 2557 | 3616 |
| 2 | 2287 | 2557 | 3234 | 4122 |
| 3 | 3430 | 3616 | 4122 | 4851 |

Table 5.2: The values of the cut-on frequencies in Hz for a 150 mm square waveguide.

### 5.2.2 Materials

Several materials were used for the experiments described above, such as (a) melamine foam, (b) wood fibre, (c) Armasound foam (Armacell, 2014), and (d) porous foam. These materials were characterised in the Centre of Technology Transfer of Le Mans (CTTM) and their non-acoustical properties are provided in Table 5.3.

| Parameter | Melamine foam | Wood fibre | Armasound | Porous foam | Units |
|---|---|---|---|---|---|
| $\phi$ | 0.99 | 0.98 | 0.79 | 0.95 | - |
| $\alpha_\infty$ | 1.01 | 1.07 | 2.06 | 1.42 | - |
| $\sigma$ | $1.1 \cdot 10^4$ | $5.0 \cdot 10^3$ | $8.3 \cdot 10^4$ | $8.9 \cdot 10^3$ | N s/m$^4$ |
| $\Lambda$ | $1.2 \cdot 10^{-4}$ | $1.0 \cdot 10^{-4}$ | $1.7 \cdot 10^{-5}$ | $1.8 \cdot 10^{-4}$ | m |
| $\Lambda'$ | $2.4 \cdot 10^{-4}$ | $2.0 \cdot 10^{-4}$ | $5.3 \cdot 10^{-5}$ | $3.6 \cdot 10^{-4}$ | m |
| $d_s$ | 0.082 | 0.095 | 0.026 | 0.01 | m |

Table 5.3: Characteristics of porous materials: porosity ($\phi$), tortuosity ($\alpha_\infty$), flow resistivity ($\sigma$), viscous characteristic length ($\Lambda$), thermal characteristic length ($\Lambda'$), layer thickness ($d_s$).

### 5.2.3 Results and discussion

#### Results from the 300 mm impedance tube

Figure 5.7 presents the frequency-wavenumber spectrum for the empty 300 mm square tube, measured at the corner of the tube cross-section. It shows a clear separation between the first six cross-sectional modes (including the fundamental mode) which are excited in the impedance tube in the frequency range of 50 - 1800 Hz and at a range of angles of incidence $-\pi/2 < \theta_{mn}(\omega) < +\pi/2$. The waves with positive wavenumbers

in Figure 5.7 correspond to those modes which propagate towards the end of the tube, terminated with a rigid lid, whereas the waves with the negative wavenumbers are the modes reflected by the lid. Figure 5.8 presents the modal absorption coefficients measured in the corner of the same tube for modes (00), (01), (11) and (02). These were calculated in the following way:

$$\alpha_{mn} = 1 - |R_{mn}|^2, \tag{5.2.1}$$

where $R_{mn}$ are the modal reflection coefficients. It is clear from the graph that the absorption of the fundamental mode does not exceed 15% and thus can be neglected in the analysis of the porous materials fundamental mode reflection coefficients. However, for higher modes the modal absorption coefficients take larger values and are more scattered, which can affect the accuracy of the measured reflection absorption coefficients of porous materials. All possible precautions were made to minimise the residual absorption by the tube, such as varnishing its inner walls and sealing the gaps between the tube and its terminations. One might also argue that higher levels of residual absorption may be caused by vibrating walls of the tube.

Figures 5.9 and 5.10 show the frequency-wavenumber spectra for a layer of Armasound foam, measured in the corner and in the middle of the tube, respectively. There is a clear separation between the dispersion curves of the first six propagating modes. This provides a possibility to determine the acoustic reflection coefficient of the porous layer in the frequency range that is much broader than that suggested in the ISO 10534 document ISO 10534-2 (1998) and for a range of the angles of incidence. This can be achieved using the modal decomposition method and optimisation technique detailed in Section 5.1. The relationship between the value of the angles $\theta_{mn}(\omega)$, $\theta_t(\omega)$, the frequency $f = \omega/2\pi$ and the modal number is illustrated graphically in Figure 5.11 for the case of melamine foam (see Equation (2.6.22)). The frequency-wavenumber plots for the remaining materials, measured in the 300 mm square tube, are presented in Ap-

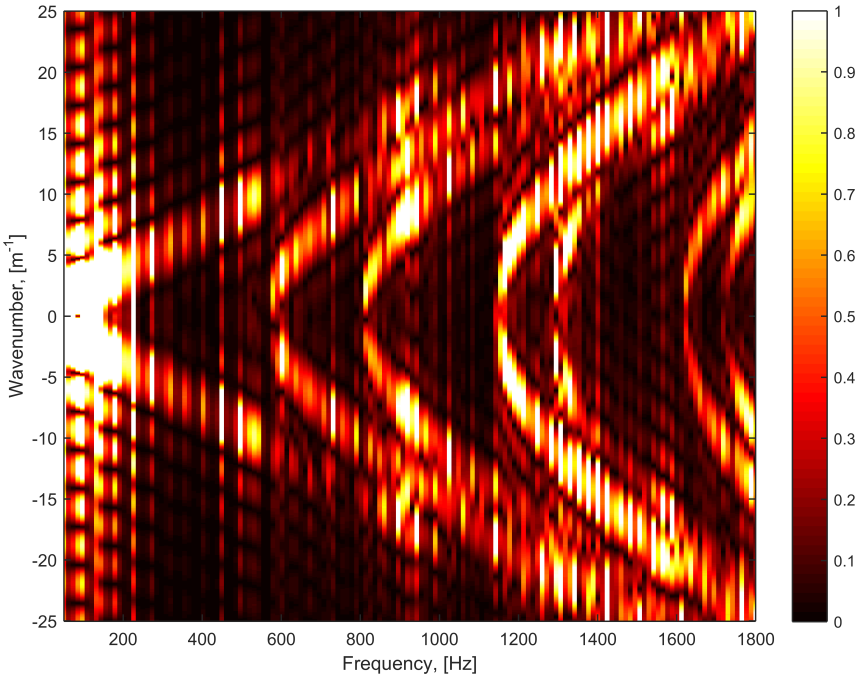


Figure 5.7: The frequency-wavenumber spectrum measured in the empty 300 mm wide square tube, with the microphone placed in the corner of the tube cross-section.

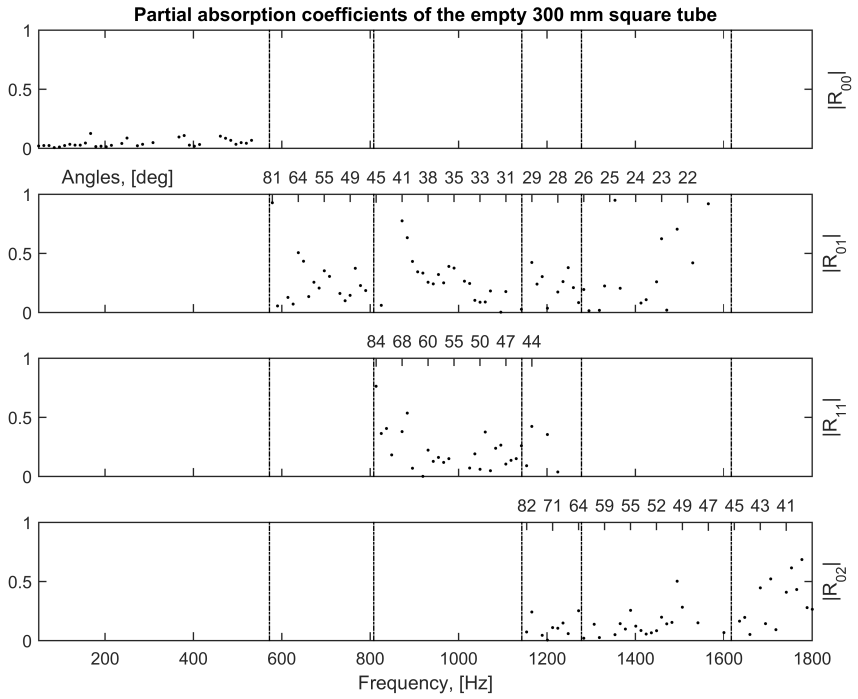


Figure 5.8: The first four modal absorption coefficients measured in the empty 300 mm square tube, with the microphone placed in the corner of the tube cross-section.

pendix A. However, for the melamine foam and wood fibre samples only measurements in the corner are available.

Figures 5.12 and 5.13 show the measured and predicted real and imaginary parts of the modal reflection coefficients, measured in the corner and in the middle of the tube cross-section, respectively. These were obtained as a function of the frequency and the incidence angle which were obtained from the analysis of the wavenumber-frequency spectra for the layer of Armasound foam. The reason for measuring at two cross-sectional locations was the ability to recover the reflection coefficient for mode (00) beyond the first higher-order mode cut-on frequency, as opposed to the method specified in ISO 10534-2 standard (1998). With the middle cross-sectional microphone positioning, it was not possible to measure the reflection coefficients for modes (01) and (11), however, the mode (22) became sufficiently pronounced to measure its reflection coefficient. The discrepancies between the measurements and predictions have been quantified in terms of the mean difference given by

$$\epsilon_{\mathrm{Re}} = \frac{1}{N_q}\sum_{q=1}^{N_q} |\mathrm{Re}(R_{mn}^{(\mathrm{m})}(\omega_q) - R_{mn}(\omega_q))|, \;\; \epsilon_{\mathrm{Im}} = \frac{1}{N_q}\sum_{q=1}^{N_q} |\mathrm{Im}(R_{mn}^{(\mathrm{m})}(\omega_q) - R_{mn}(\omega_q))|, \quad (5.2.2)$$

where $R_{mn}^{(\mathrm{m})}(\omega_q)$ is the experimentally determined modal reflection coefficient, $R_{mn}(\omega_q)$ is the predicted reflection coefficient and $N_q$ is the number of frequency points in the reflection coefficient spectrum. This difference for the fundamental mode reflection coefficient does not change significantly from the corner to the middle of the tube measurements (5.07% error in the real part of the reflection coefficient measured in the corner as opposed to 7.52% error in the middle of the tube, and 7.76% and 5.67% errors for the imaginary part, measured in the corner and in the middle, respectively). However, the ability to recover the fundamental mode reflection coefficient in a much broader frequency range makes the measurements in the middle rather useful. After the mode (02) cuts on at 1278 Hz, the amplitude of the fundamental mode drastically decreases, which makes the measurement of the reflection coefficient of the fundamental

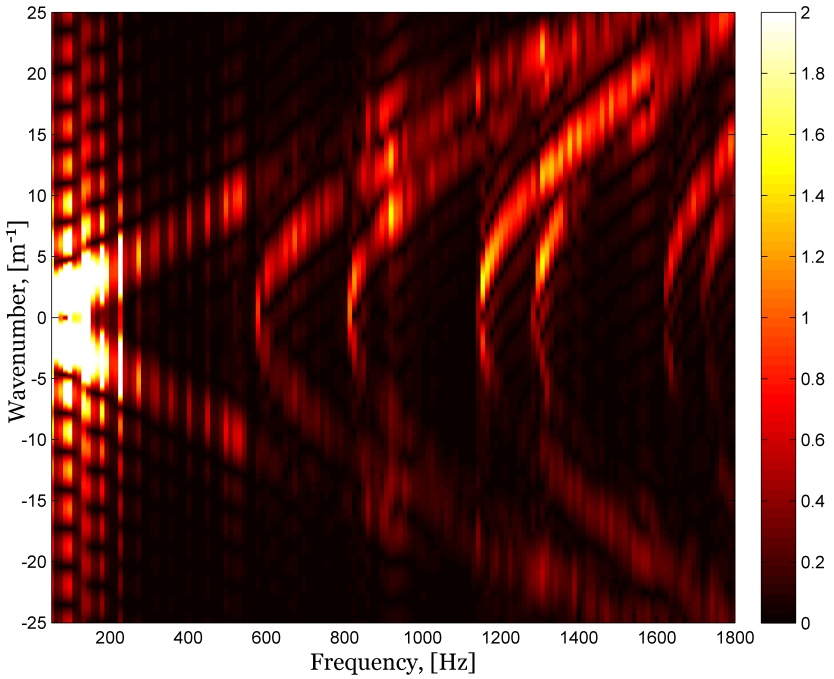


Figure 5.9: The frequency-wavenumber spectrum for the layer of Armasound foam measured in 300 mm wide square tube, with the microphone placed in the corner of the tube cross-section.

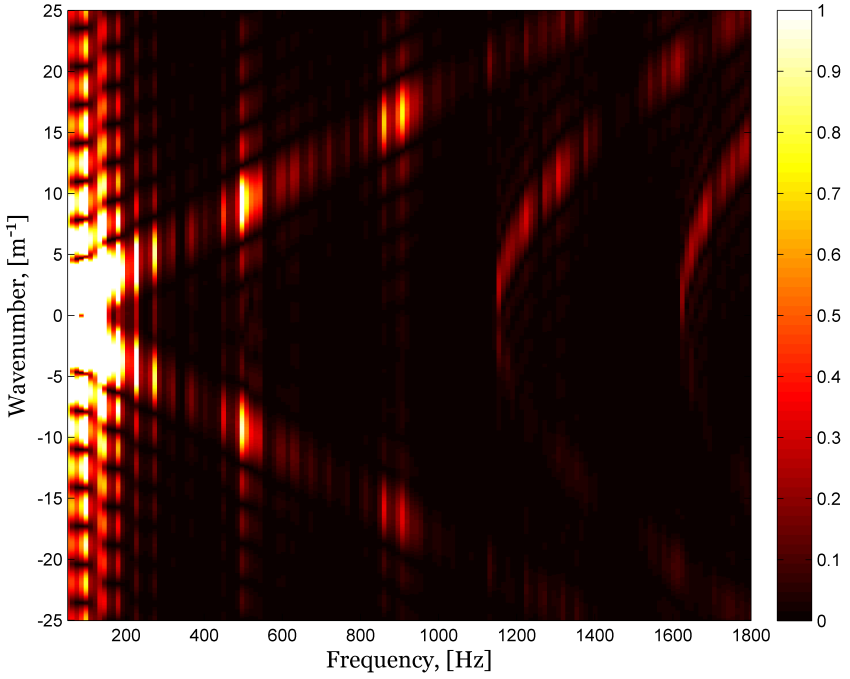


Figure 5.10: The frequency-wavenumber spectrum for the layer of Armasound foam measured in 300 mm wide square tube, with the microphone placed in the middle of the tube cross-section.

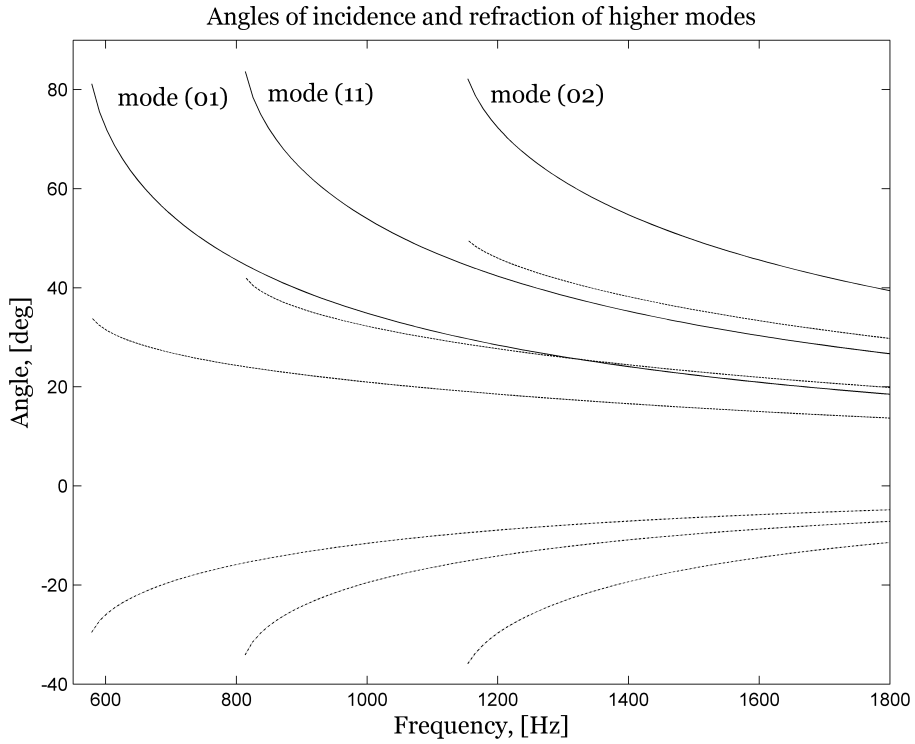


Figure 5.11: The mode angle of incidence and real and imaginary parts of the corresponding refraction angle as a function of a frequency for melamine foam in the 300 mm wide square tube. Solid line: angle of incidence; dashed line: real part of the refracted angle; dotted line: imaginary part of the refracted angle.

mode problematic. For the thin foam sample, the data measured in the middle and in the corner will be combined in one graph, mode (00) being recovered in the middle and the remaining modes - in the corner. For the melamine and wood fibre samples only the data measured in the corner of the tube are available. This resulted in the reflection coefficient for mode (00) being recovered only up to the first cut-on frequency of 572 Hz.

Figures 5.14 - 5.16 show the real and imaginary parts of the modal reflection coefficients as a function of the frequency and the incidence angle for the layer of melamine, wood fibre and porous foam, respectively. Black dots denote the experimental data obtained through the application of the optimisation algorithm (5.1.8), whereas the solid line is the numerical simulation results obtained using the Johnson-Champoux-Allard equivalent fluid model via expression (2.6.21). The experimental data are only provided

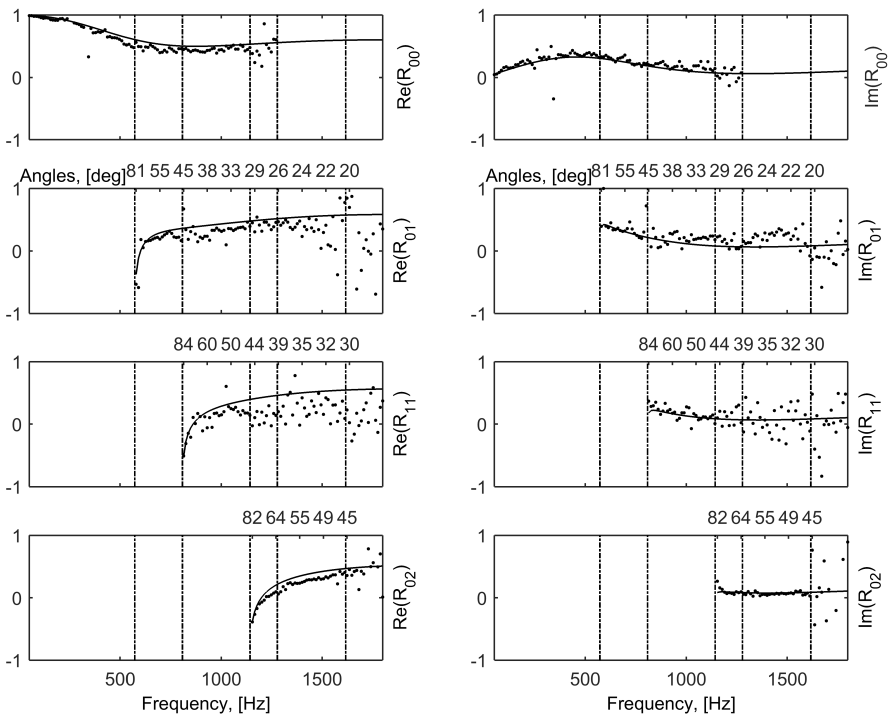


Figure 5.12: The modal reflection coefficients for the layer of Armasound foam, when the microphone was placed in the corner of the 300 mm tube cross-section. Solid line: predictions; dots: experiments.

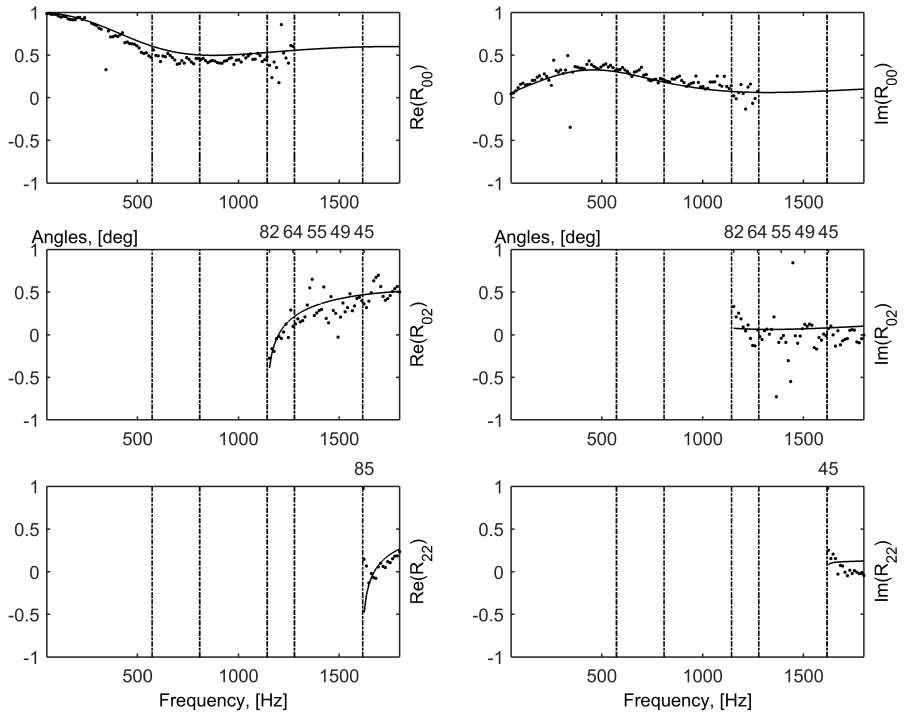


Figure 5.13: The modal reflection coefficients for the layer of Armasound foam, when the microphone was placed in the middle of the 300 mm tube cross-section. Solid line: predictions; dots: experiments.

for those frequencies at which the signal to noise ratio was better than 20 dB. The differences between the measured and predicted plane wave reflection coefficient do not exceed 7.5% for all the materials except the thin foam, for which the difference between the prediction and measurements is below 15%. The maximum difference is observed between the real parts for mode (01) for the case of the thin foam sample. The most probable cause for that is the fact that the thin foam sample was the least absorbing of all. It exhibits higher mean differences between the predicted and measured data for all modal reflection coefficients, which may signify that the optimisation algorithm is more susceptible to errors when the absorbing abilities of the sample present in the tube are weak. It can also be observed that the mean difference between real parts of the predicted and measured reflected coefficient for mode (01) is one of the highest for three out of four material samples. This may attributed to the close proximity of the dispersion curves for modes (01) and (11) beyond the cut-on frequency of the latter (808 Hz). Furthermore, the dispersion curves for modes (01) and (11) are difficult to separate beyond the cut-on frequency of mode (02) at 1143 Hz, making the modal reflection coefficient recovery even more challenging. This also may explain a relatively high mean difference between the real parts of the predicted and measured reflection coefficients for mode (11), observed for all four material samples.

The excitation of some modes can be favoured compared to that for the other modes because of the adopted speaker arrangement (see Figure 5.5) and cross-sectional position of the microphone array in the corner of the tube. As a result, the signal to noise ratio for some modes at some frequencies and angles was limited so that the recovered reflection coefficient data for those modes were less accurate. It is also likely that a better speaker arrangement is required to make use of the orthogonality of the mode shapes in the tube so that the mode filtering which is currently attained with Equation (5.1.3) can be enhanced as suggested by Vinogradov and Gavrilov (1987). Another solution is to make use of the orthogonality of normal modes to maximise the excitation coefficients by adopting speakers connected in the form of a phased array.

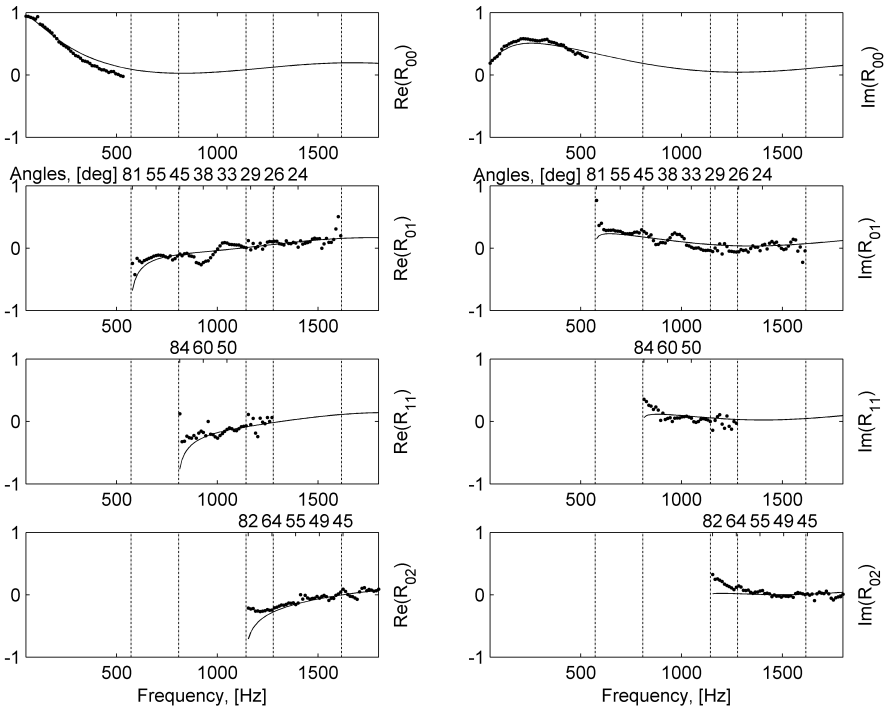


Figure 5.14: The modal reflection coefficients for the layer of melamine foam, recovered in the 300 mm square tube cross-section. Solid line: predictions; dots: experiments.

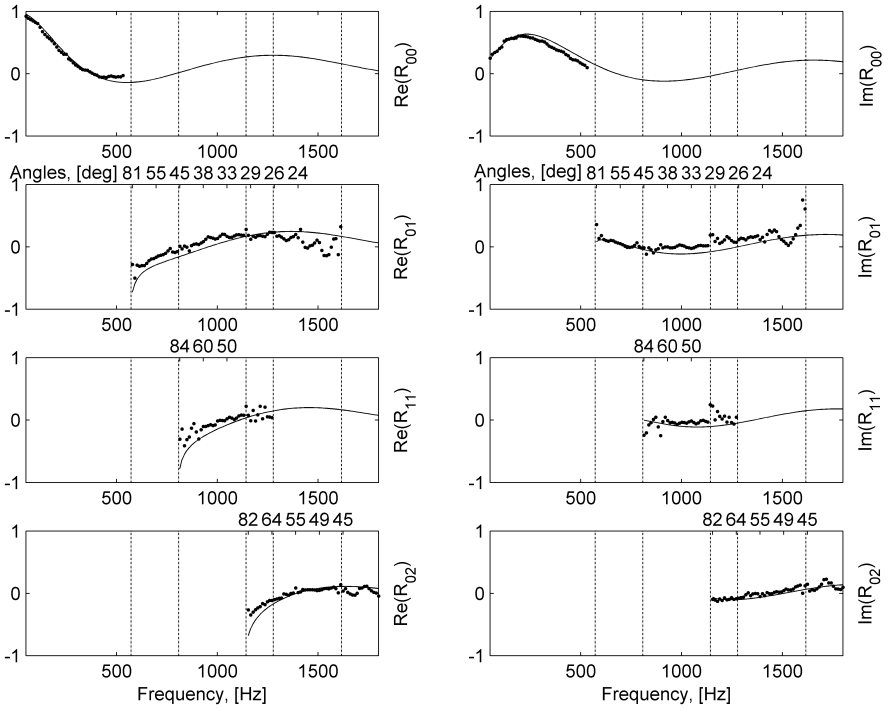


Figure 5.15: The modal reflection coefficients for the layer of wood fibre, recovered in the 300 mm square tube cross-section. Solid line: predictions; dots: experiments.

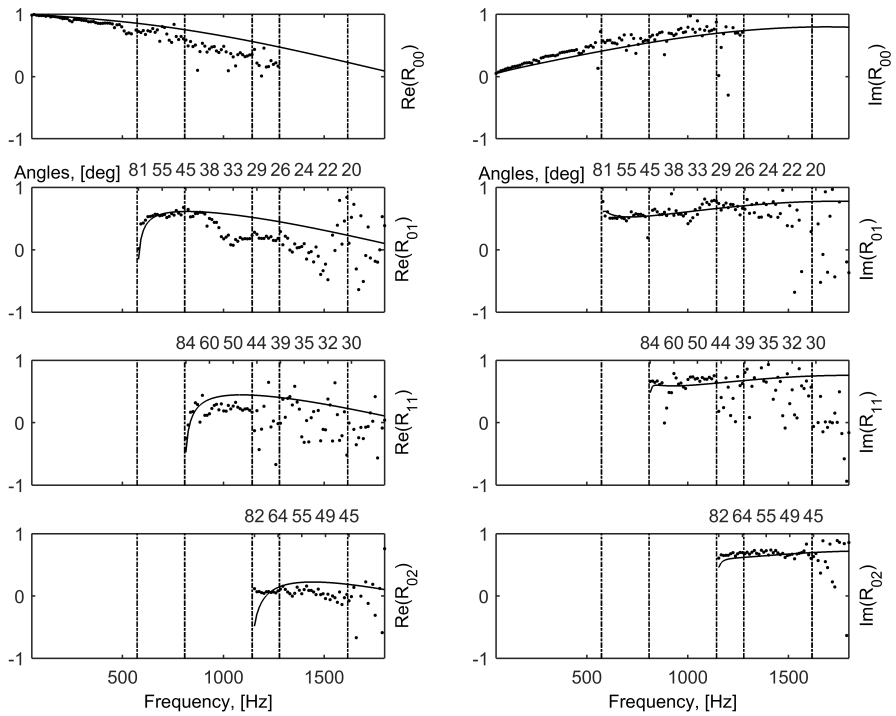


Figure 5.16: The modal reflection coefficients for the layer of thin foam, recovered in the 300 mm square tube cross-section. Solid line: predictions; dots: experiments.

A common feature between Figures 5.12,5.13 and 5.14-5.16 is that the largest discrepancies between the measured and predicted values of the modal reflection coefficients are in the vicinity of the modal cut-on frequencies. Otherwise, the model and measurement agree and the errors are small. The possible explanation of this is that the integration limits in the Fourier transform analysis were not sufficiently large to capture the modal pressures at or near a cross-sectional resonance. At a cut-on frequency or near it the modal attenuation is relatively low whereas the modal phase velocity is relatively high so that the adopted spatial length of the FFT window in Equation (5.1.1) may not be sufficiently long to capture a representative lengths of the modal wavefront. The other issue is cross-sectional modes were not properly excited above the frequency of the next cross-sectional resonance.

Figures 5.17-5.20 show the measured and predicted values of the total absorption coefficient for the layer of Armasound foam, measured in the 300 mm square tube. Figures 5.17 and 5.18 present the data measured in the corner and in the middle of the 300 mm

| Mode | Melamine foam | Wood fibre | Armasound foam | Porous foam |
|---|---|---|---|---|
| $\epsilon_{\mathrm{Re}(R_{00})}$ | 0.0696 | 0.0406 | 0.0752 | 0.1499 |
| $\epsilon_{\mathrm{Im}(R_{00})}$ | 0.0486 | 0.0599 | 0.0567 | 0.1074 |
| $\epsilon_{\mathrm{Re}(R_{01})}$ | 0.0661 | 0.1189 | 0.1943 | 0.3353 |
| $\epsilon_{\mathrm{Im}(R_{01})}$ | 0.0736 | 0.0979 | 0.1355 | 0.1917 |
| $\epsilon_{\mathrm{Re}(R_{11})}$ | 0.0998 | 0.1273 | 0.1818 | 0.2808 |
| $\epsilon_{\mathrm{Im}(R_{11})}$ | 0.0770 | 0.0980 | 0.0766 | 0.1538 |
| $\epsilon_{\mathrm{Re}(R_{02})}$ | 0.0711 | 0.0664 | 0.1597 | 0.1961 |
| $\epsilon_{\mathrm{Im}(R_{02})}$ | 0.0630 | 0.0437 | 0.2014 | 0.0833 |

Table 5.4: A summary of the mean differences between the real and imaginary parts of the measured and predicted modal reflection coefficients for the four material samples, when the microphone was placed in the corner of the 300 mm tube cross-section.

square tube, respectively. These were calculated according to the incident and reflected amplitudes ratio method, given by Equation (5.1.24). Figures 5.19 and 5.20 also present the total absorption coefficient measured in the corner (Figure 5.19) and in the middle (Figure 5.20) of the 300 mm square tube, but calculated using the intensity method given by Equation (5.1.28). The mean differences between the measurements and predictions are summarised in Table 5.5. It is worth noting, that for the incident and reflected amplitude ratio method, the data for each mode were not available throughout the whole frequency range. For example, as it can be seen on the frequency-wavenumber plot for the Armasound foam, obtained in the corner of the tube (Figure 5.9), the dispersion curve for mode (00) disappears after the first cut-on frequency of 572 Hz. This means that the information on the fundamental mode incident and reflected amplitudes was available only in the frequency range between 50 and 572 Hz, instead of 50 to 1800 Hz. Similarly, other modes were also considered in the frequency ranges, where they had a sufficient signal-to-noise ratio. Due to this limitation, two ways of calculating the total absorption coefficient predictions were employed: full theoretical reflection coefficient (full $R_{theo}$), where each mode exists starting from its cut-on frequency and until the maximum adopted frequency of 1800 Hz, and partial theoretical reflection coefficient (partial $R_{theo}$), where a frequency range for each mode was matched to that of the measured data. These two different ways of the total theoretical absorption coefficient

calculation are reflected in Table 5.5, which presents the mean differences between the measured and predicted data. However, the partial theoretical reflection coefficient does not reflect the real picture of the sound field in the tube, whereas the full theoretical reflection coefficient cannot be directly compared to the measured data as the latter does not have all the information contained in the theoretical predictions. Due to this issue, it was chosen to use the intensity ratio method for the remaining plants. In addition, Figures 5.17-5.20 show the data obtained both in the corner and in the middle of the tube. As the difference between the two is small, for the remaining materials the average total absorption coefficient will be presented.

| | $\epsilon_{\alpha_{total}}$ |
|---|---|
| Amp method, corner (full $R_{theo}$) | 0.082 |
| Amp method, corner (partial $R_{theo}$) | 0.039 |
| Amp method, middle (full $R_{theo}$) | 0.084 |
| Amp method, middle (partial $R_{theo}$) | 0.022 |
| Int method, corner | 0.100 |
| Int method, middle | 0.178 |

Table 5.5: A summary of the mean differences between the measured and predicted total absorption coefficient for the layer of Armasound foam in the 300 mm square tube. Amp method: incident and reflected amplitudes ratio method; Int method: intensity ratio method.

Figures 5.21, 5.22 and 5.23 present the total absorption coefficients for the layer of melamine foam, wood fibre and thin porous foam, respectively. These data were calculated using the intensity method (Equation (5.1.28)). The presented total absorption coefficient for the thin foam layer is the averaged value of the total absorption coefficients obtained in the corner and in the middle of the tube. As for the layers of melamine foam and wood fibre, the experimental data were available only for the corner of the tube. The match between the measurements and predictions for the melamine foam and wood fibre is remarkably close, with the mean difference being equal to 1.5% in the case of melamine foam and 2.2% in the case of wood fibre. However, the observed agreement is worse for the thin foam layer, with the mean difference equal to 18.5%. This may be caused by the same reason as the mismatch in the measured and predicted

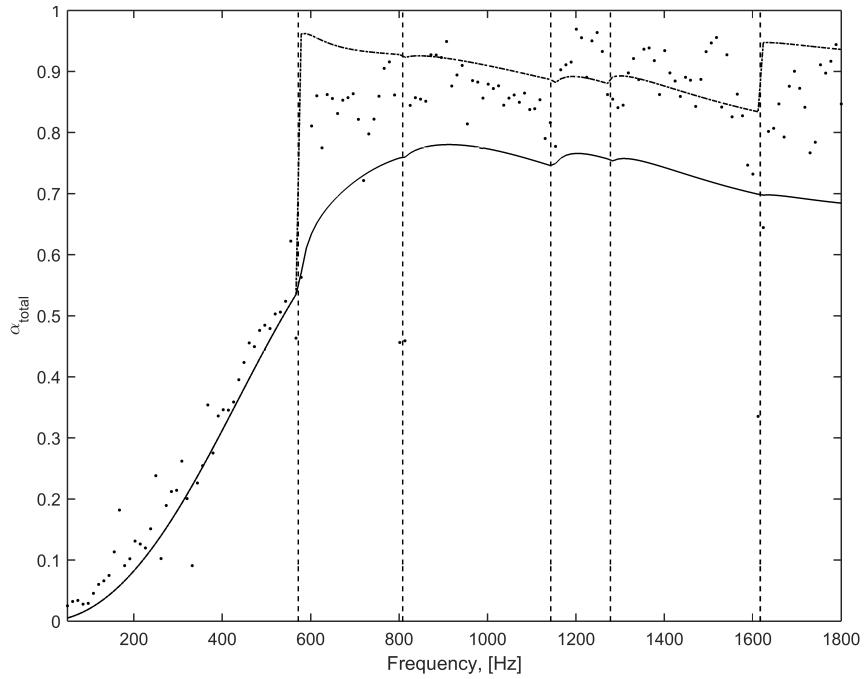


Figure 5.17: The measured and predicted total absorption coefficients for the layer of Armasound foam calculated using the amplitude method, measured in 300 mm wide square tube, with the microphone placed in the corner of the tube cross-section. Solid line: full absorption coefficient predictions; dashed line: partial absorption coefficient predictions; dots: experiments.

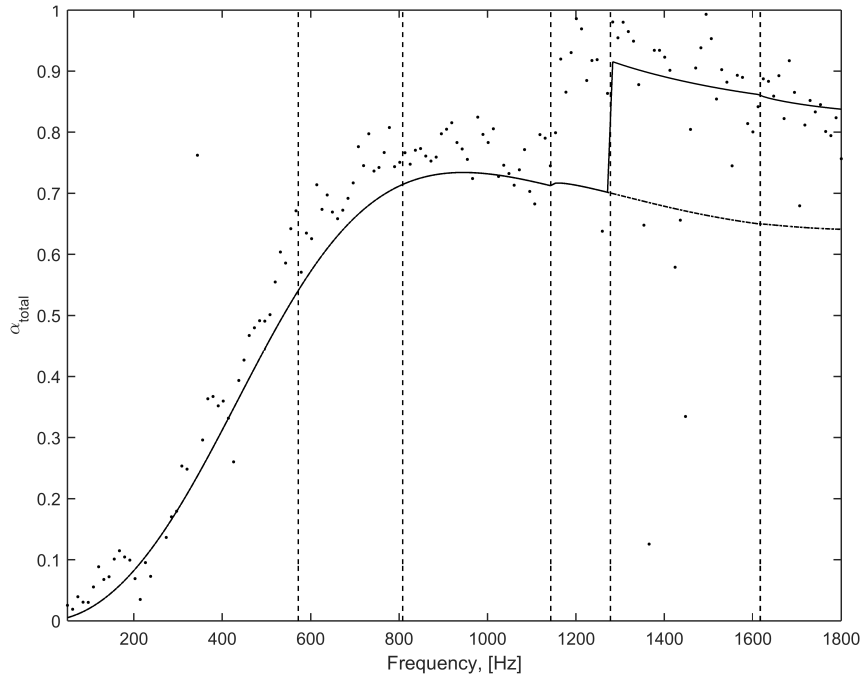


Figure 5.18: The measured and predicted total absorption coefficients for the layer of Armasound foam calculated using the amplitude method, measured in 300 mm wide square tube, with the microphone placed in the middle of the tube cross-section. Solid line: full absorption coefficient predictions; dashed line: partial absorption coefficient predictions; dots: experiments.

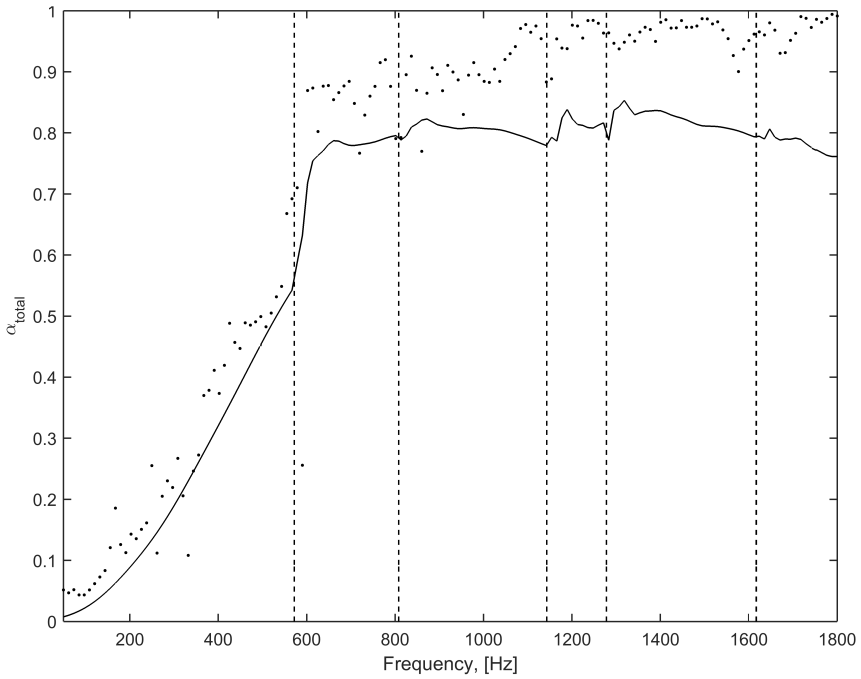


Figure 5.19: The measured and predicted total absorption coefficients for the layer of Armasound foam calculated using the intensity method, measured in 300 mm wide square tube, with the microphone placed in the corner of the tube cross-section. Solid line: predictions; dots: experiments.

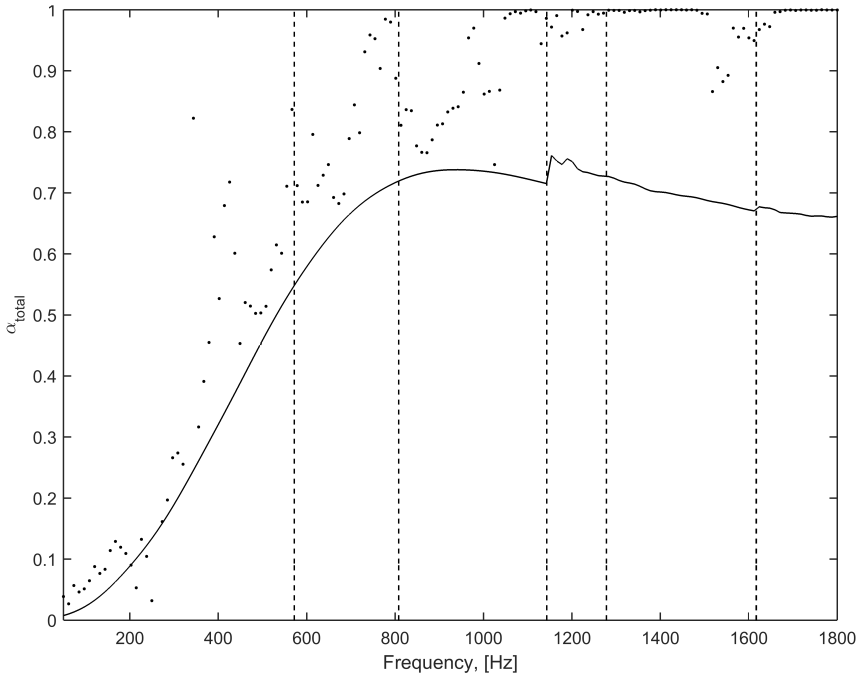


Figure 5.20: The measured and predicted total absorption coefficients for the layer of Armasound foam calculated using the intensity method, measured in 300 mm wide square tube, with the microphone placed in the middle of the tube cross-section. Solid line: predictions; dots: experiments.

reflection coefficients for the thin foam. This porous foam sample was the thinnest of all tested samples and thus exhibited inferior absorbing properties, which prevented the optimisation algorithm to predict the measured absorption with high accuracy.

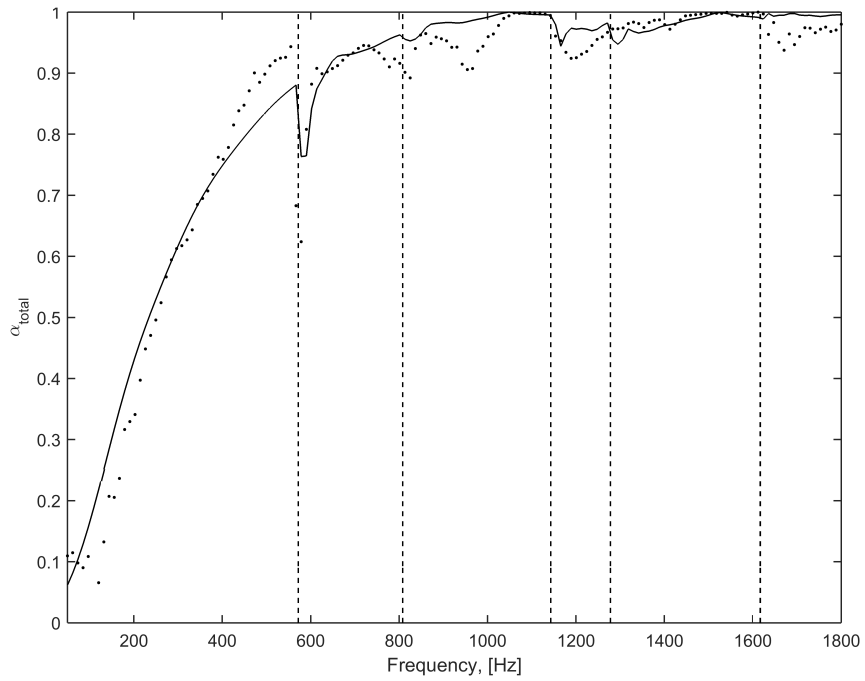


Figure 5.21: The measured and predicted total absorption coefficients for the layer of melamine foam measured in 300 mm wide square tube. Solid line: predictions; dots: experiments.

| Material | $\epsilon_{\alpha_{total}}$ |
|---|---|
| Melamine foam | 0.015 |
| Wood fibre | 0.022 |
| Thin foam | 0.185 |

Table 5.6: A summary of the mean differences between the measured and predicted total absorption coefficient for the three material specimens in the 300 mm square tube.

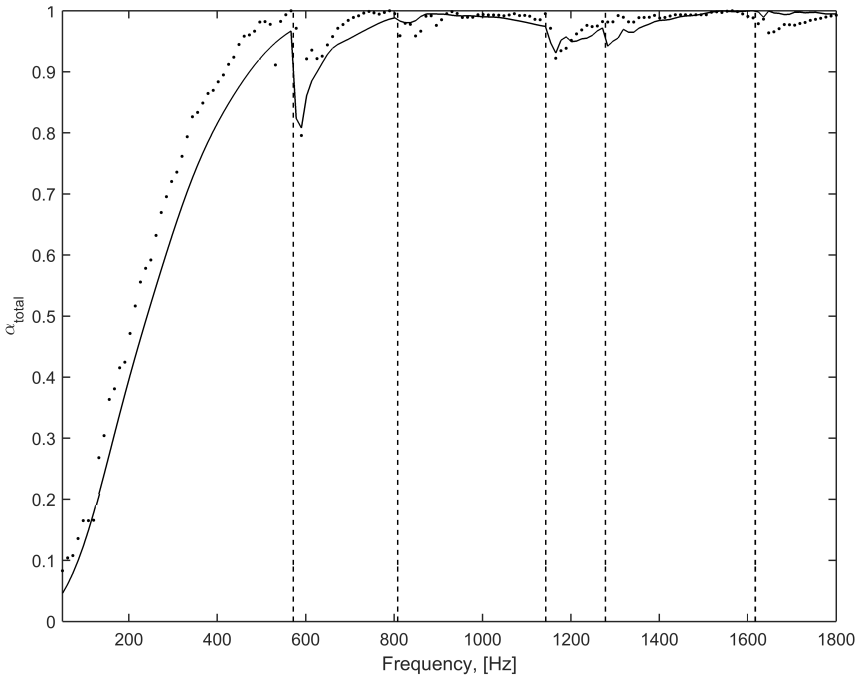


Figure 5.22: The measured and predicted total absorption coefficients for the layer of wood fibre measured in 300 mm wide square tube. Solid line: predictions; dots: experiments.

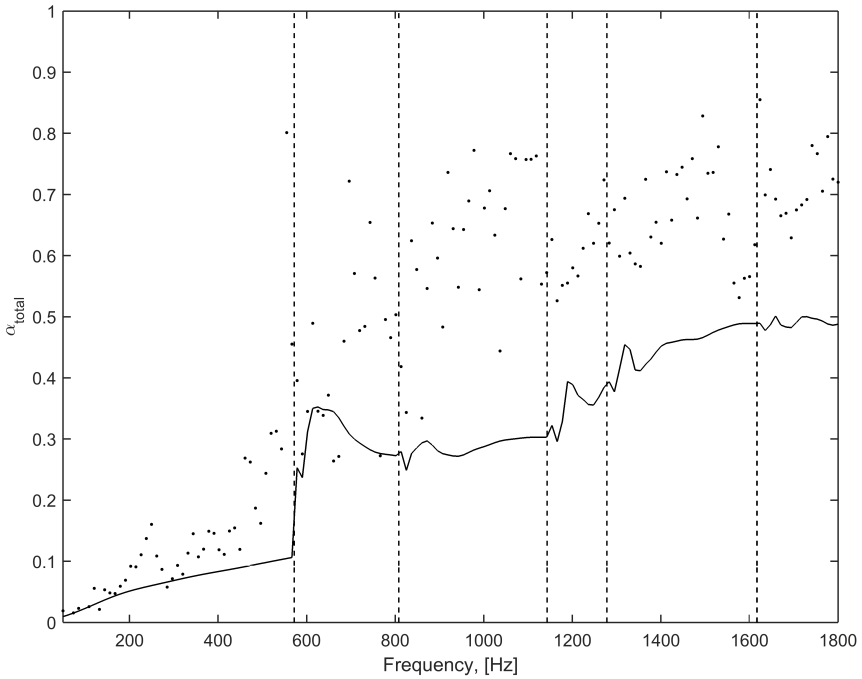


Figure 5.23: The measured and predicted total absorption coefficients for the layer of thin foam measured in 300 mm wide square tube. Solid line: predictions; dots: experiments.

**Results for the 150 mm impedance tube**

Figures 5.24 and 5.25 show the frequency-wavenumber spectrum and the partial modal absorption coefficients measured in the 150 mm square tube, respectively. The frequency-wavenumber plot shows a clear separation between the dispersion curves for propagating modes, which allows to use these data to recover the modal reflection and total absorption coefficients of tested materials. However, mode (11) with the cut-on frequency of 1617 Hz is excited much less than other propagating modes (see Figure 5.24). This may be caused by the loudspeaker positioning, which does not favour the excitation of this particular mode. This peculiarity explains the partial absorption coefficient of this mode being very scattered (Figure 5.25). Furthermore, this can affect the recovery of the reflection coefficient for mode (11) for the tested porous materials.

Figures 5.26 and A.8 present the frequency-wavenumber sound pressure spectra obtained in the 150 mm square tube for the Armasound foam sample and two microphone positions. As previously, positive wavenumbers carry information about the incident sound field, and negative wavenumbers correspond to the reflected sound field. The data depicted in Figures 5.26 and 5.27 were subsequently used for the modal reflection coefficient recovery. The frequency-wavenumber plots for other two porous material setups, which are Armasound foam with 100 mm air gap and Armasound foam with 200 mm air gap can be found in Appendix A1.

Figures 5.28 and 5.29 show the first four modal reflection coefficients for the Armasound foam layer with no air gap, measured in the corner and in the middle of the tube cross-section, respectively. The mean differences between the measured and the predicted results are shown in Table 5.7. These differences were estimated using expression (5.2.2). The theoretical predictions for the no air gap case were calculated using the Johnson-Champoux-Allard model (1991). It is clear from the plots that the quality of the recovered fundamental mode reflection coefficient is much higher when

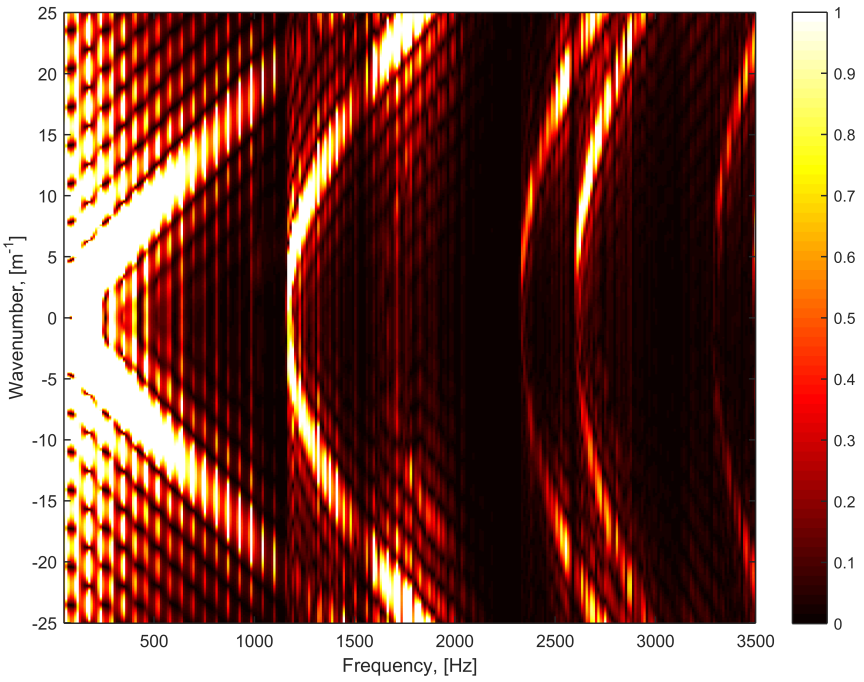


Figure 5.24: The frequency-wavenumber spectrum measured in the empty 150 mm wide square tube, with the microphone placed in the corner of the tube cross-section.

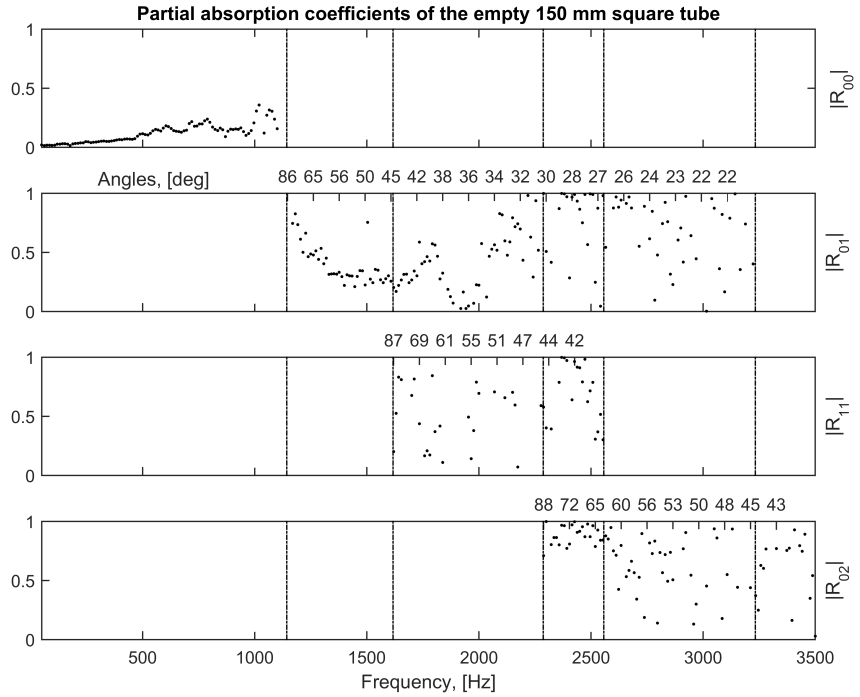


Figure 5.25: The first four modal absorption coefficients measured in the empty 150 mm square tube, with the microphone placed in the corner of the tube cross-section.

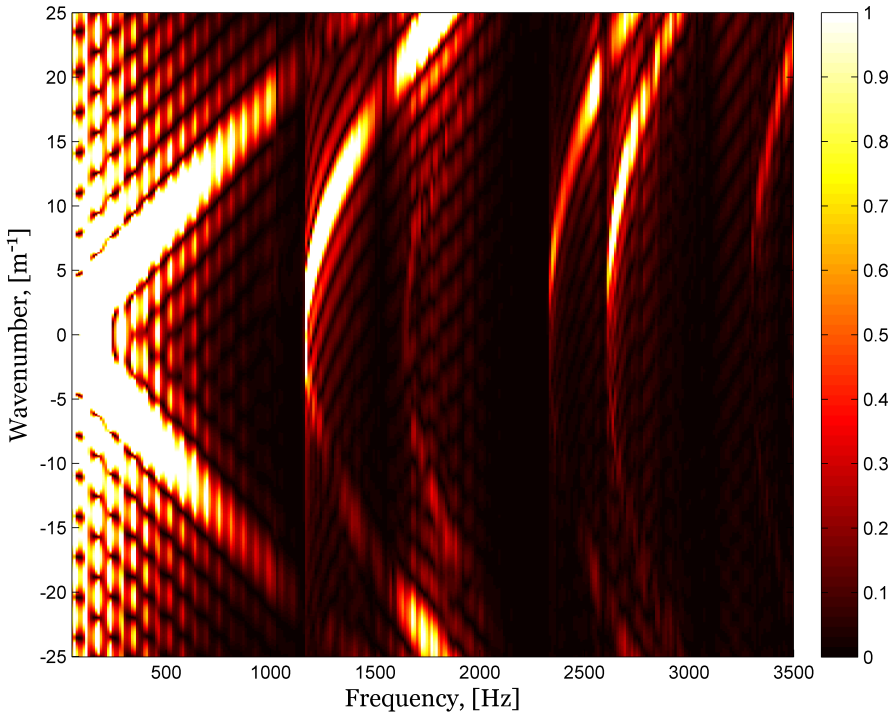


Figure 5.26: The frequency-wavenumber spectrum for the layer of Armasound foam, measured in the empty 150 mm wide square tube, with the microphone placed in the corner of the tube cross-section.

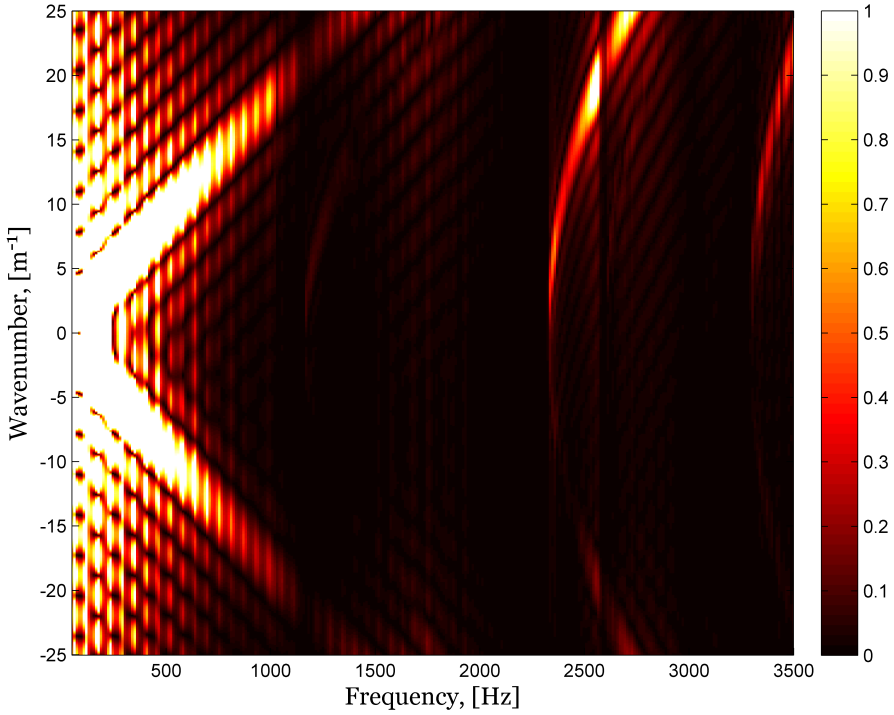


Figure 5.27: The frequency-wavenumber spectrum for the layer of Armasound foam, measured in the empty 150 mm wide square tube, with the microphone placed in the middle of the tube cross-section.

measured in the middle of the tube (24.3% error for the real part and 19.4% for the imaginary part in the corner as opposed to 9.3% error for the real part and 9.0% for the imaginary part in the middle). Moreover, the measurements in the middle enable the recovery of the fundamental mode reflection coefficient up to 2557 Hz. This extends the plane wave regime limit more than by a factor of two, which the first higher mode cut-on frequency being 1143 Hz (see Table 5.2). Due to this fact, the reflection coefficient plots for the other two materials will present the plane wave reflection coefficient data recovered in the middle, whereas the remaining three modes reflection coefficients have been recovered in the corner of the tube.

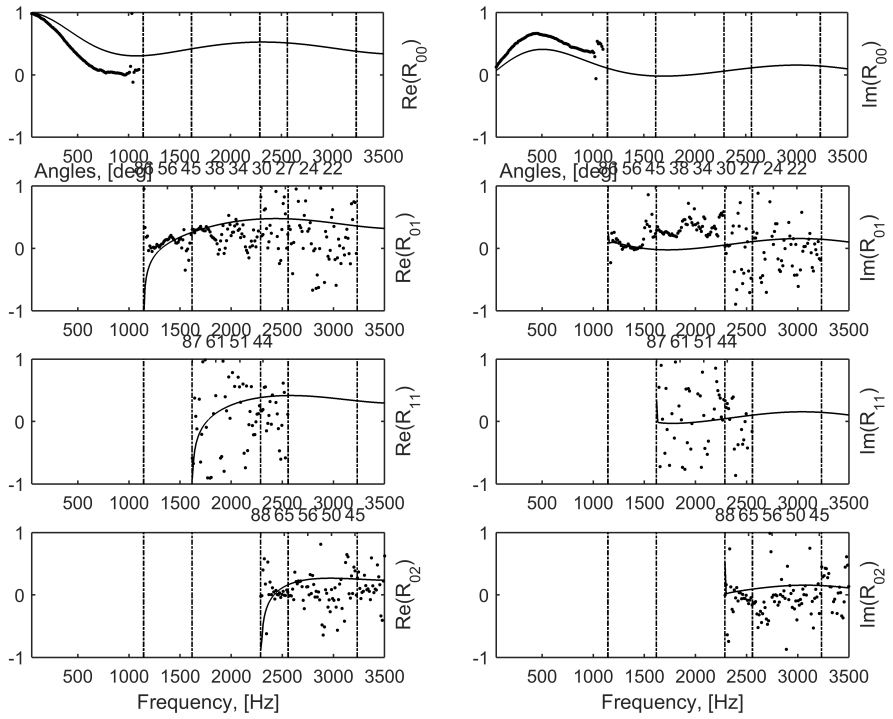


Figure 5.28: The modal reflection coefficients for the layer of Armasound foam, when the microphone was placed in the corner of the 150 mm tube cross-section. Solid line: predictions; dots: experiments.

Figures 5.30 and 5.31 show the predicted and measured modal reflection coefficients for the Armasound foam layer with 100 mm and 200 mm air gap, respectively, measured in the 150 mm square tube. The predictions for the case of the presence of air gap were calculated using the Pade approximants model (Horoshenkov et al., 1998), which proved to be the most suitable to characterise the behaviour of such complex porous

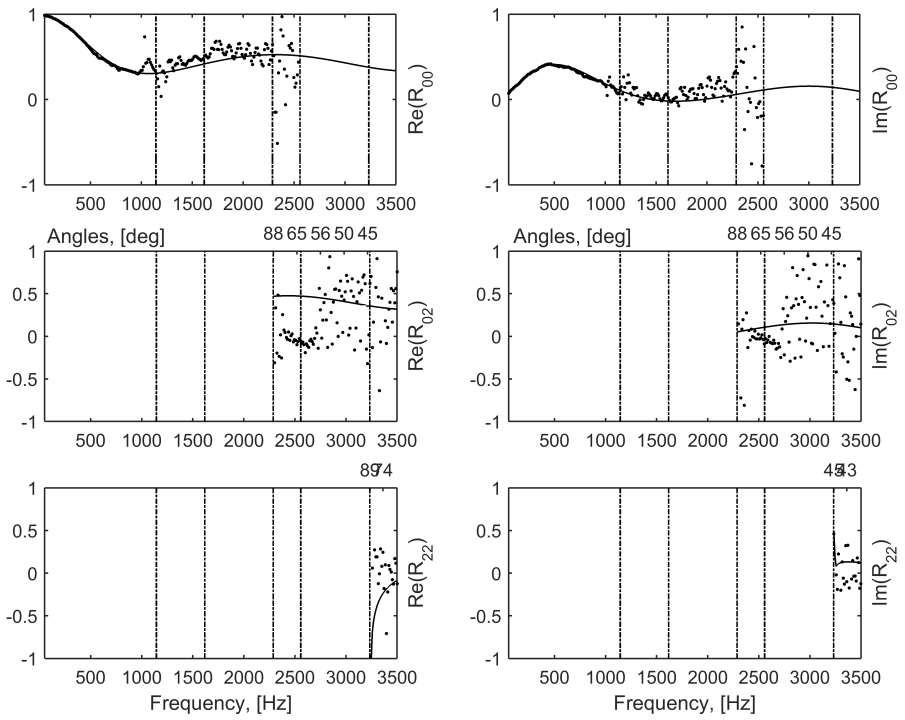


Figure 5.29: The modal reflection coefficients for the layer of Armasound foam, when the microphone was placed in the middle of the 150 mm square tube cross-section. Solid line: predictions; dots: experiments.

materials as the Armasound foam. The agreement between the measured and predicted modal reflection coefficients for the 150 mm tube is not as close as it is for 300 mm tube. This can be attributed to several reasons. Firstly, the Armasound material is manufactured from recycled materials, which makes it rather heterogeneous. This makes the prediction of its acoustical behaviour challenging, as the non-acoustical parameters depend on the position in the sample and can differ significantly from one sample to another (Horoshenkov et al., 2007). Ideally, each material sample has to be characterised separately to estimate its non-acoustical parameters for the accurate prediction of its acoustical behaviour, which is not always feasible. Secondly, it was discovered that the residual absorption of the tube may have some influence on the measured reflection and absorption coefficients. This issue will be discussed in more detail in Chapter 7. The residual absorption may contribute to the mismatch between the predictions and the experiment. Finally, the reflection coefficients for the higher-order modes are more challenging to predict, as they decrease significantly with the increased mode order.

This may make their amplitude comparable to that of background noise or processing artefacts, which appear after applying the finite Fourier transform (Equation (5.1.1)), which influences the quality of the recovered data.

| Mode | Armasound foam, no gap | Armasound foam, 100 mm gap | Armasound foam, 200 mm gap |
|---|---|---|---|
| $\epsilon_{\mathrm{Re}(R_{00})}$ | 0.0932 | 0.0308 | 0.0318 |
| $\epsilon_{\mathrm{Im}(R_{00})}$ | 0.0905 | 0.0954 | 0.0416 |
| $\epsilon_{\mathrm{Re}(R_{01})}$ | 0.3275 | 0.3069 | 0.3206 |
| $\epsilon_{\mathrm{Im}(R_{01})}$ | 0.3969 | 0.3370 | 0.3653 |
| $\epsilon_{\mathrm{Re}(R_{11})}$ | 0.8748 | 0.6698 | 0.6130 |
| $\epsilon_{\mathrm{Im}(R_{11})}$ | 0.8018 | 0.6076 | 0.6389 |
| $\epsilon_{\mathrm{Re}(R_{02})}$ | 0.2896 | 0.7748 | 0.5578 |
| $\epsilon_{\mathrm{Im}(R_{02})}$ | 0.2908 | 0.9432 | 0.3720 |

Table 5.7: A summary of the mean differences between the real and imaginary parts of the measured and predicted modal reflection coefficients for the three material setups, when the microphone was placed in the corner of the 150 mm tube cross-section.

Figures 5.32-5.35 show the measured and predicted total absorption coefficients measured in the 150 mm square tube. Figures 5.32 and 5.33 present the data obtained using the incident and reflected amplitude ratio, and measured in the corner and in the middle of the tube, respectively. Figures 5.34 and 5.35 present the similar data, but obtained using the intensity method. As in the case of the 300 mm square tube, two ways of calculating the total absorption coefficient predictions were employed: full theoretical reflection coefficient (full $R_{theo}$) and partial theoretical reflection coefficient (partial $R_{theo}$). Table 5.8 presents the mean differences between the measured and predicted data, where for the data, obtained with the amplitude method, two sets of theoretical predictions are given. However, the partial theoretical reflection coefficient does not reflect the real picture of the sound field in the tube, whereas the full theoretical reflection coefficient cannot be directly compared to the measured data as the latter does not have all the information contained in the theoretical predictions. For the remaining materials, tested in the 150 mm square tube, the intensity method will be preferred, and the data measured in the corner and in the middle of the tube will be averaged.

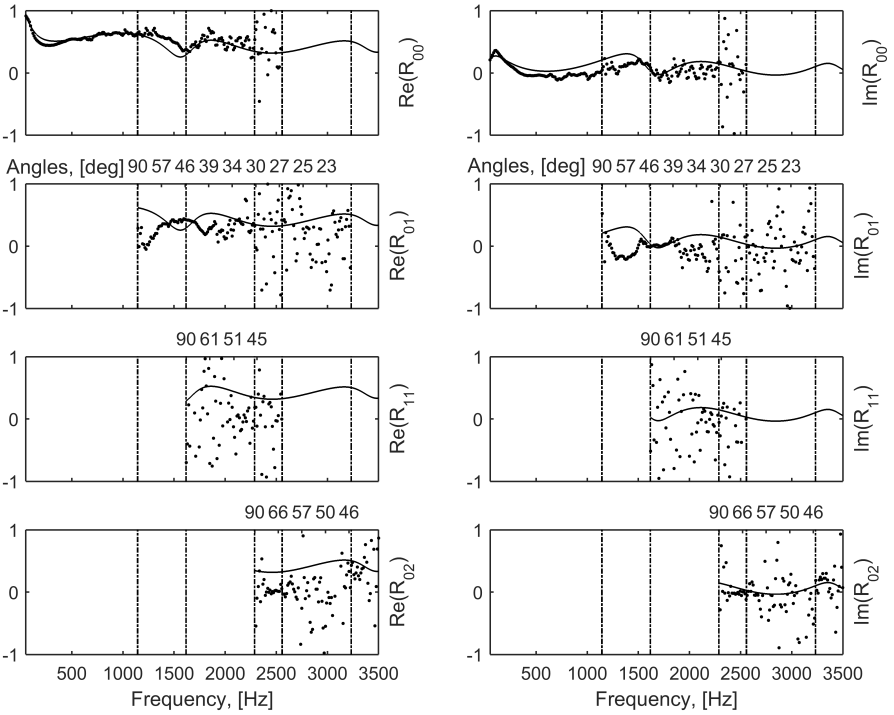


Figure 5.30: The modal reflection coefficients for the layer of Armasound foam with 100 mm air gap, recovered in the 150 mm square tube cross-section. Solid line: predictions; dots: experiments.

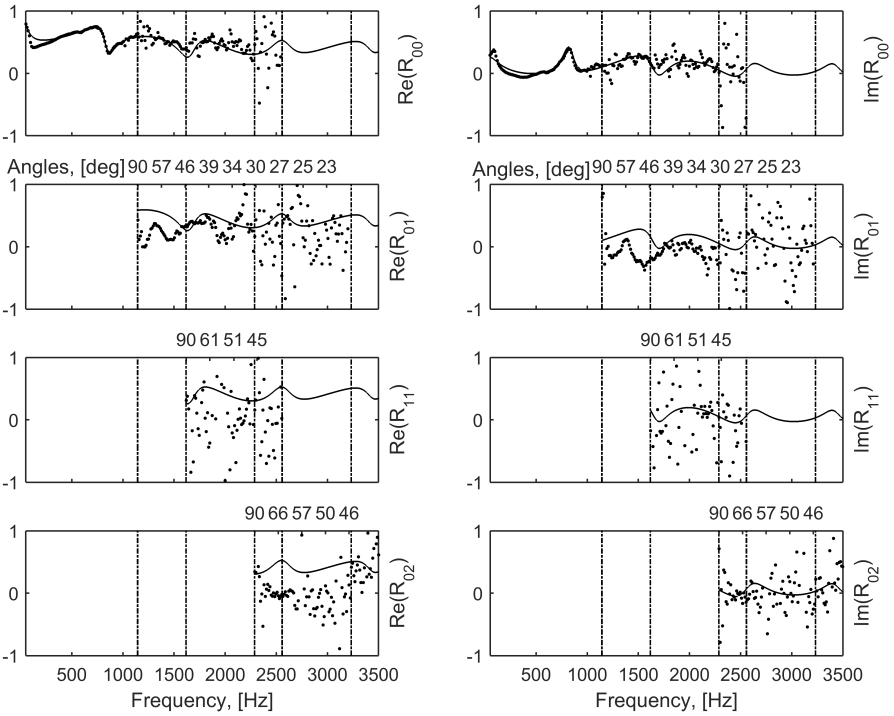


Figure 5.31: The modal reflection coefficients for the layer of Armasound foam with 200 mm air gap, recovered in the 150 mm square tube cross-section. Solid line: predictions; dots: experiments.

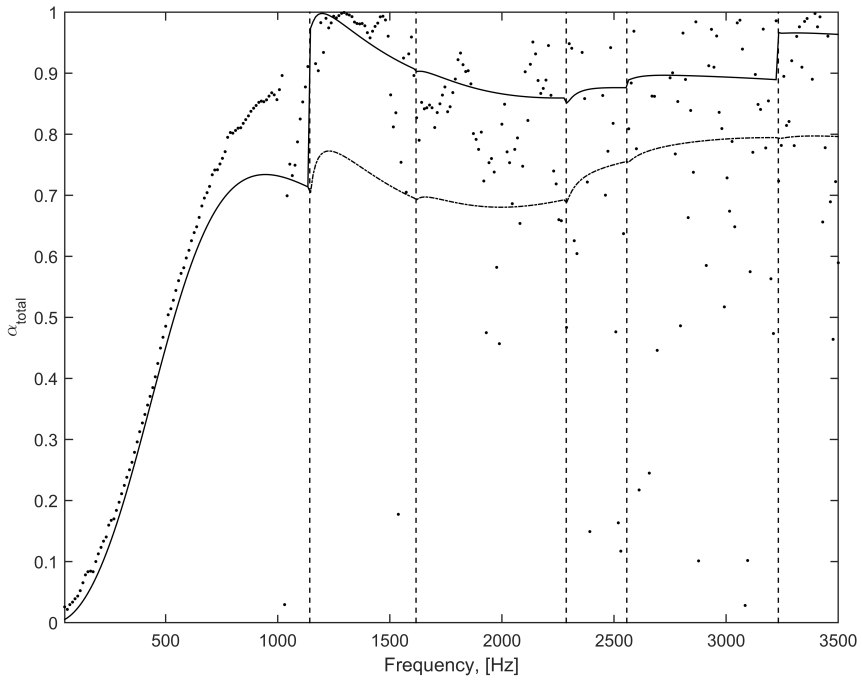


Figure 5.32: The measured and predicted total absorption coefficients for the layer of Armasound foam calculated using the amplitude method, measured in 150 mm wide square tube, with the microphone placed in the corner of the tube cross-section. Solid line: predictions (full); dashed line: predictions (partial); dots: experiments.

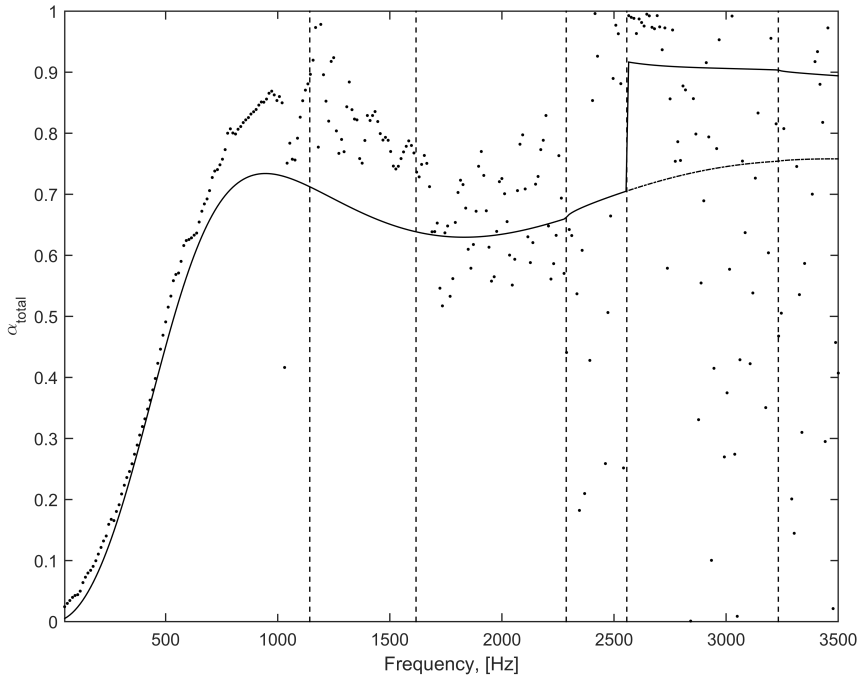


Figure 5.33: The measured and predicted total absorption coefficients for the layer of Armasound foam calculated using the amplitude method, measured in 150 mm wide square tube, with the microphone placed in the middle of the tube cross-section. Solid line: predictions (full); dashed line: predictions (partial); dots: experiments.

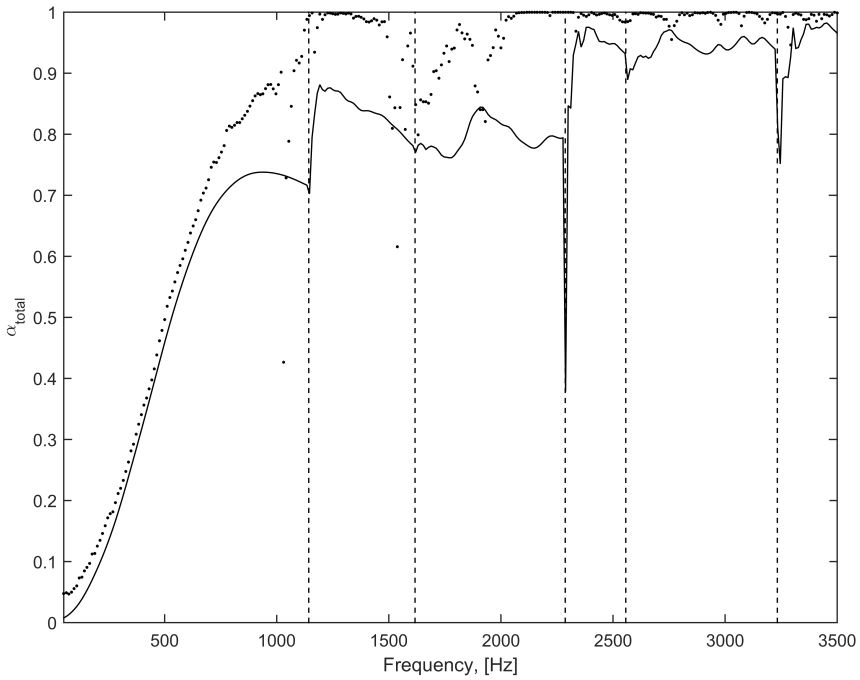


Figure 5.34: The measured and predicted total absorption coefficients for the layer of Armasound foam calculated using the intensity method, measured in 150 mm wide square tube, with the microphone placed in the corner of the tube cross-section. Solid line: predictions; dots: experiments.

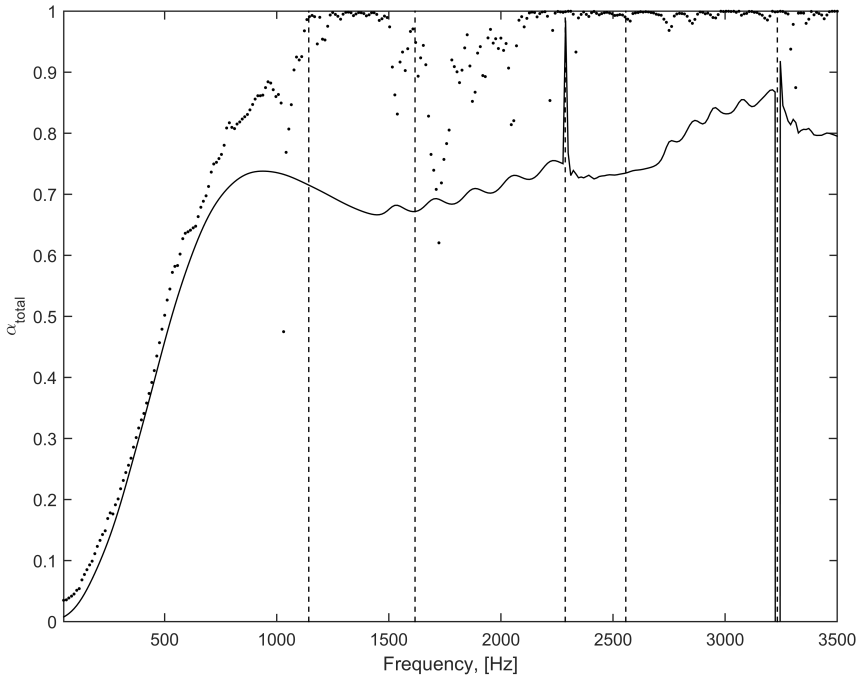


Figure 5.35: The measured and predicted total absorption coefficients for the layer of Armasound foam calculated using the intensity method, measured in 150 mm wide square tube, with the microphone placed in the middle of the tube cross-section. Solid line: predictions; dots: experiments.

| | $\epsilon_{\alpha_{total}}$ |
|---|---|
| Amp method, corner (full $R_{theo}$) | 0.092 |
| Amp method, corner (partial $R_{theo}$) | 0.204 |
| Amp method, middle (full $R_{theo}$) | 0.154 |
| Amp method, middle (partial $R_{theo}$) | 0.198 |
| Int method, corner | 0.086 |
| Int method, middle | 0.218 |

Table 5.8: A summary of the mean differences between the measured and predicted total absorption coefficient for the layer of Armasound foam in the 150 mm square tube. Amp method: incident and reflected amplitudes ratio method; Int method: intensity ratio method.

Figures 5.36 and 5.37 show the measured and predicted total absorption coefficients for the 26 mm wide layer of Armasound foam, backed with 100 mm and 200 mm air gap, respectively, measured in the 150 mm square tube. The mean differences between the predictions and experiments are presented in Table 5.9. Both figures show that the match between the predicted and measured total absorption coefficients in very close until the first cut-on frequency of 1143 Hz. However, beyond this frequency there is a high scatter in the measured data, and the agreement is weaker. This may be due to the low signal-to-noise ratio observed in the case of higher order modes.

| Material | $\epsilon_{\alpha_{total}}$ |
|---|---|
| Armasound with 100 mm air gar | 0.123 |
| Armasound with 200 mm air gar | 0.122 |

Table 5.9: A summary of the mean differences between the measured and predicted total absorption coefficient for the two material specimens in the 150 mm square tube.

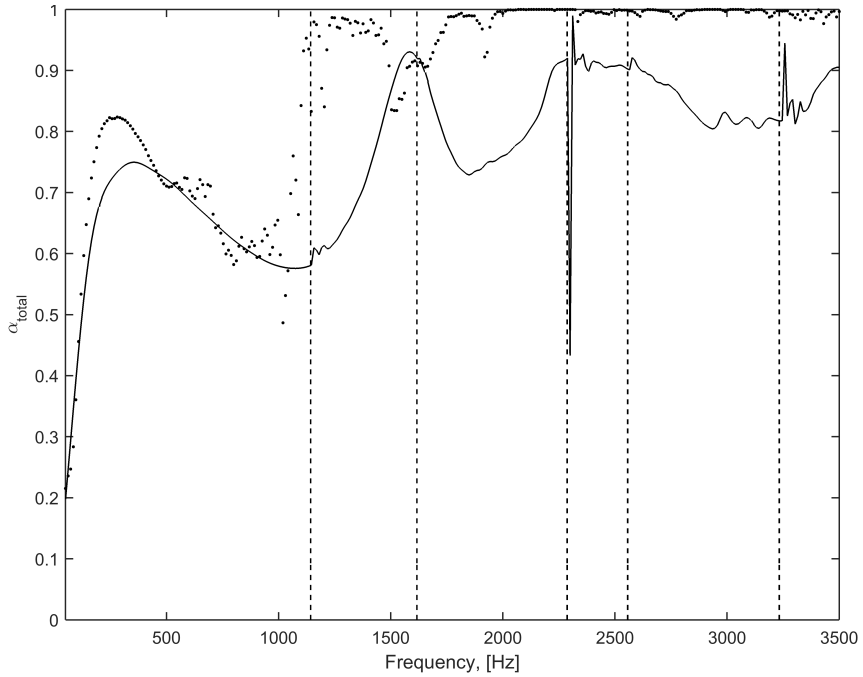


Figure 5.36: The measured and predicted total absorption coefficients for the layer of Armasound foam with 100 mm air gap measured in 150 mm wide square tube. Solid line: predictions; dots: experiments.

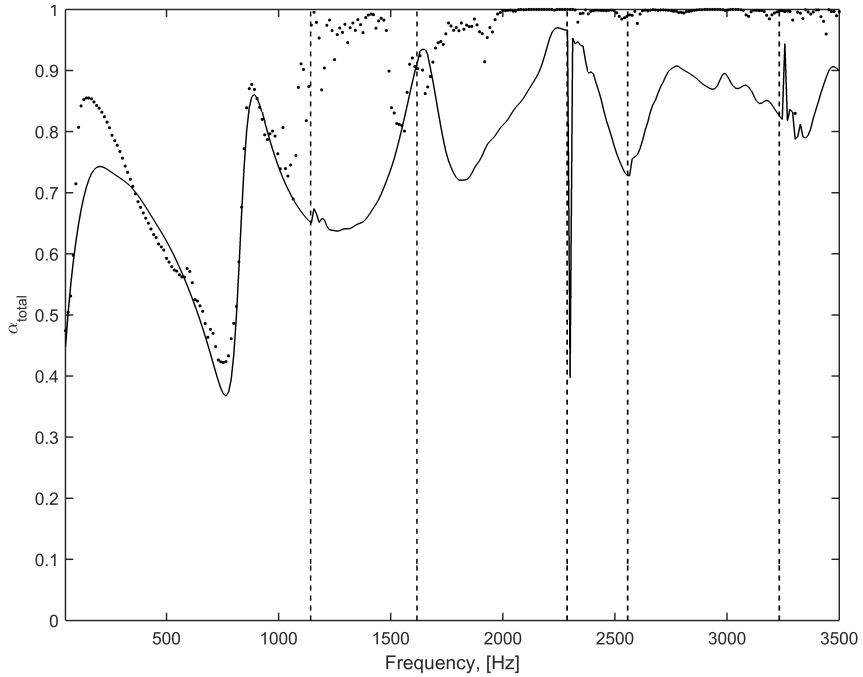


Figure 5.37: The measured and predicted total absorption coefficients for the layer of Armasound foam with 200 mm air gap measured in 150 mm wide square tube. Solid line: predictions; dots: experiments.

## 5.3 Measurements in round cross-section tube

### 5.3.1 Acoustic setup

A schematic drawing of an experimental setup at the University of Sheffield is shown in Figure 5.38. The setup consisted of a 6 m long 150 mm diameter pipe, which was made of 10 mm thick PVC. Assuming the sound speed of $c_0 = 343$ m/s at 20° C, the first cut-on frequency for this tube was 1340 Hz (see Table 5.10). One end of the pipe was terminated with a Fane compression driver, which was attached to the pipe via a PVC lid (see Section 3.1). The opposite end of the pipe was covered with a thick metal lid, which ensured the boundary conditions close to rigid. A porous material sample was fitted at this end inside the pipe without an air gap between the sample and the lid. The signal used to excite the sound field was a sine chirp, which is described in a following way:

$$s(t) = \sin\left(\omega_0 t + \frac{\Delta\Omega}{2T}t^2\right), \tag{5.3.1}$$

where $s(t)$ is the sine chirp signal, $\omega_0 = 2\pi f_0$ is the initial frequency, with $f_0 = 100$ Hz, $\Delta\Omega = 2\pi\Delta F$ is the swept frequency range, with $\Delta F = 4900$ Hz, and $T = 10$ s is the total duration of the signal. The signal was generated using a Matlab subroutine, saved in a text file and used for subsequent measurements through LabVIEW subroutine and National Instruments NI PXie-6538 DAQ system, which were also responsible for recording the signal. The sampling frequency of the system was 12 kHz. The factors which determined its choice were the compatibility with the Nyquist criterion and the quality of the sound pressure spectra which were subsequently used to obtain the impulse response.

The sound signal was recorded using the Microflown intensity probe, described in Chapter 3. As seen in Figure 5.38, two loudspeaker and two microphone cross-sectional configurations were used. In order to capture both the axisymmetric and non-axisymmetric

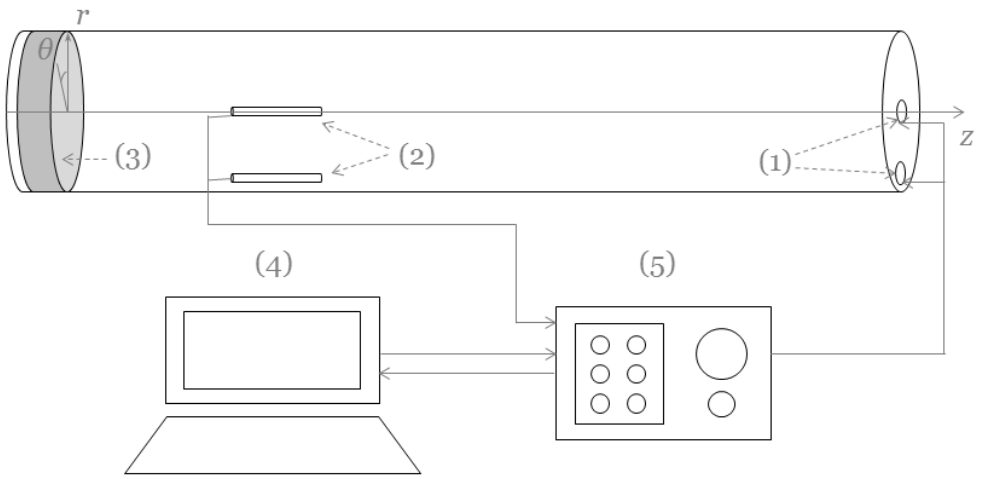


Figure 5.38: A schematic illustration of the 150 mm diameter tube setup: (1) two loudspeaker configurations (centre and wall); (2) two microphone configurations (centre and wall); (3) porous material sample; (4) PC; (5) data acquisition system.

| m / n | 0 | 1 | 2 | 3 |
|---|---|---|---|---|
| 0 | 0 | 2789 | 5106 | 7405 |
| 1 | 1340 | 3881 | 6213 | 8520 |
| 2 | 2223 | 4881 | 7256 | 9586 |
| 3 | 3058 | 5834 | 8258 | 10617 |

Table 5.10: The values of the cut-on frequencies in Hz for a 150 mm circular waveguide.

modes, two sets of measurements were conducted for each material sample: with the loudspeaker and microphone in the middle of tube cross-section and with the loudspeaker and microphone near the wall. The $(r, \theta, z)$ coordinates of the loudspeaker centre were (0, 0, 6) and (0.065, $-\pi/2$, 6) for the middle and the edge of the cross-section, respectively. The $(r, \theta)$ coordinates of the probe cross-section centre when placed in the middle and near the wall were (0, 0) and (0.07, $-\pi/2$), respectively. The data from both sets were subsequently combined to obtain a full summary of a sound field in the pipe.

For each set of data, measurements were taken at $N = 301$ axial positions in the pipe. The probe was moved manually at a step of approximately 10 mm, simulating the axial microphone array. The recorded sound pressure $p(z, t)$ was transformed into an impulse response using the deconvolution procedure and synchronised. MATLAB built-in `fft` function was subsequently used in order to obtain sound pressure spectra $\tilde{p}(z, \omega)$. Com-

bined with the temperature readings to obtain the exact speed of sound, these data were used to estimate the exact axial locations of the probe using the following expression:

$$z_i = \frac{n_i - n_0}{f_s \, c_{0,i}}, \tag{5.3.2}$$

where $z_i$ is the $i-$th axial location of the probe, $n_i$ and $n_0$ are the $i-$th and the initial sampling position of the impulse response maximum (dimensionless), respectively, $f_s$ is the sampling frequency and $c_{0,i}$ is the speed of sound at the $i-$th location, provided the temperature readings were taken at each measurement position. Also, the Hamming window was applied to the pressure data along the spatial dimension of the array, to smooth them out at the initial and the final spatial positions and weaken the effect of the Gibb's phenomenon (expression (5.1.1)) on the quality of the estimated spectral data with finite spatial limits. After the frequency and wavenumber sound pressure spectra $p(K, \omega)$ were obtained, the expression (5.1.8) was used to recover the modal reflection coefficients.

### 5.3.2 Materials

For the measurements in a circular waveguide, one material sample was used. It was made of 106 mm thick melamine foam. The foam was characterised using a one-parameter model. A 20 mm thick material sample was cut out of the large melamine foam block and its sound absorption was determined in a 100 mm impedance tube. The thickness of the sample was known and the porosity and tortuosity were assumed to be equal to 1, as these values are typical for melamine foam. The flow resistivity was recovered via a fitting procedure, based on the Miki model (1990) described in Section 2.6, and was equal to 9000 $\mathrm{N\,s/m^4}$. The fitting procedure was based on the minimisation of the difference between the measured and the fitted absorption coefficients, and searching for the flow resistivity value which gives the smallest difference. Then

the three non-acoustical parameters were substituted in the Miki model to obtain the theoretical predictions for reflection and absorption coefficients.

### 5.3.3 Results and discussion

Figures 5.39 and 5.40 depict the wavenumber spectra of the sound pressure measured in the empty 150 mm circular tube with the microphone being near the wall and in the centre. In these plots, the negative wavenumbers correspond to the incident sound field, and the positive wavenumbers - to the reflected sound field. These figures prove that there is a separation between different modes propagating in the waveguide in the adopted frequency regime. Figure 5.39 shows the fundamental mode and the first axisymmetric mode, (01), and Figure 5.40 - the first several non-axisymmetric modes, namely (10), (20) and (30). Figure 5.41 presents the absolute values of the partial absorption coefficients measured in the empty 150 mm circular tube and recovered from the frequency-wavenumber plots, described above. These were calculated in accordance with Equation 5.2.1. Although it appears from the figure, that the absorption values in the empty tube are high, it is highly likely that a range of reasons contributed to that. Firstly, the multiple reflections in the empty tube complicated the data analysis procedure. Secondly, the vibration of pipe walls might have influenced the measured data, which compromised the accuracy of the obtained results.

Figure 5.43 presents the frequency-wavenumber spectrum for the layer of melamine foam placed in the 150 mm circular tube and measured near the wall of the tube. These data, together with the frequency-wavenumber spectrum measured in the middle of the tube and presented in the Appendix A, were used for the subsequent recovery of the modal reflection coefficients. Figure 5.44 presents real and imaginary parts of the predicted and measured modal reflection coefficients for a layer of melamine foam in the circular tube. It combines the data from two sets of measurements, when the loud-

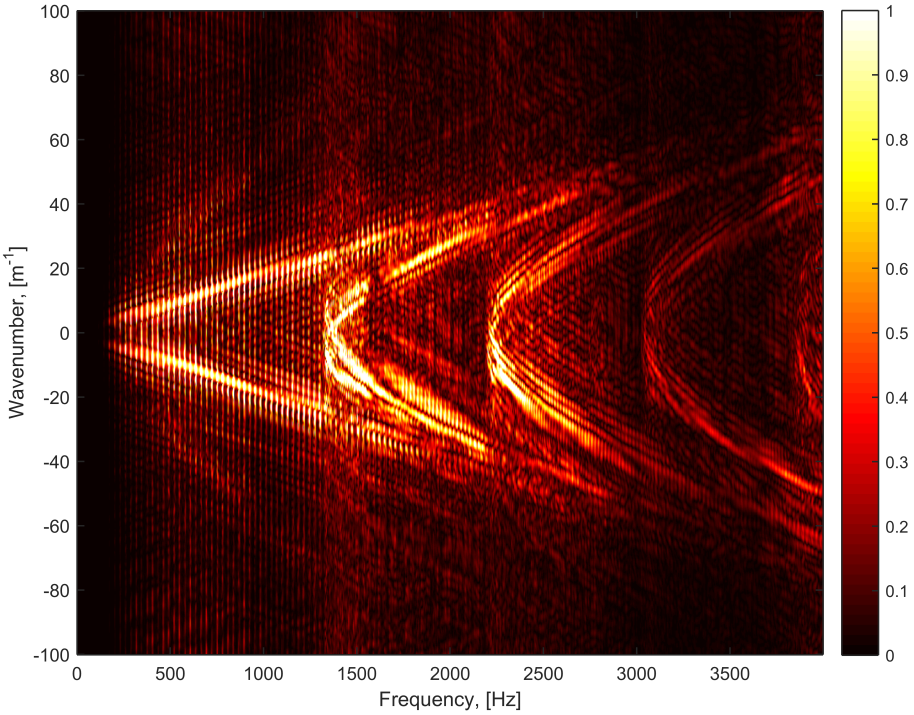


Figure 5.39: The frequency-wavenumber spectrum measured in the empty 150 mm circular tube, with the microphone placed near the wall of the tube cross-section.

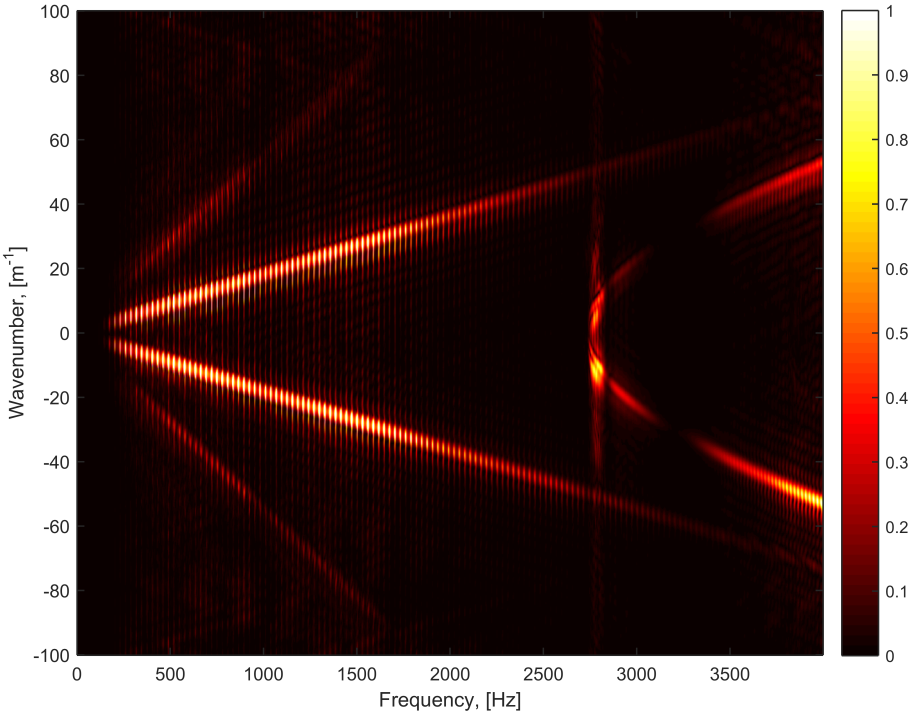


Figure 5.40: The frequency-wavenumber spectrum measured in the empty 150 mm circular tube, with the microphone placed in the middle of the tube cross-section.

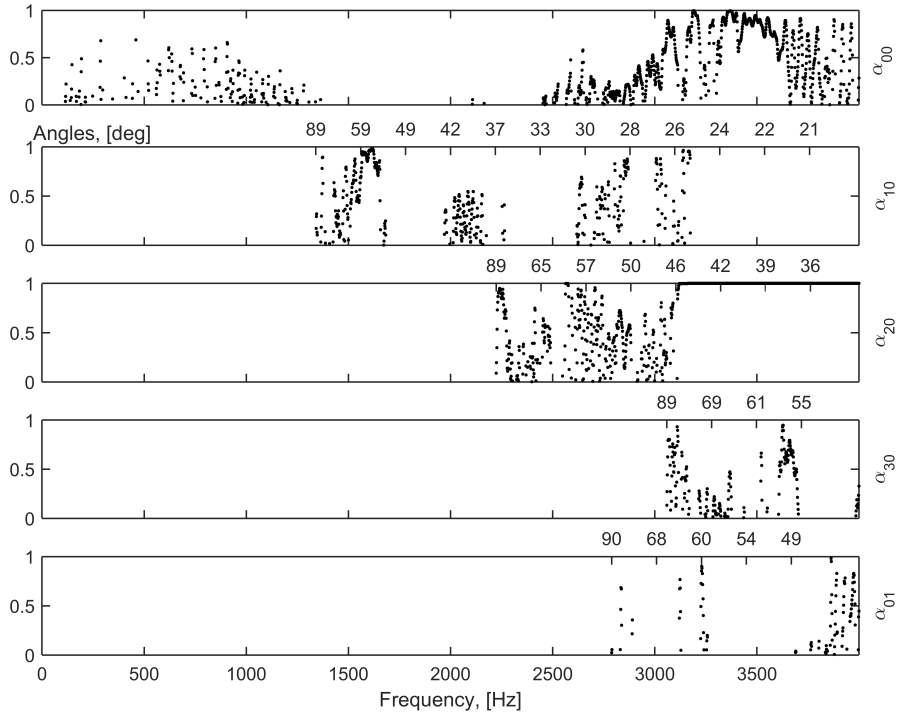


Figure 5.41: The first five modal absorption coefficients for the empty 150 mm circular tube.

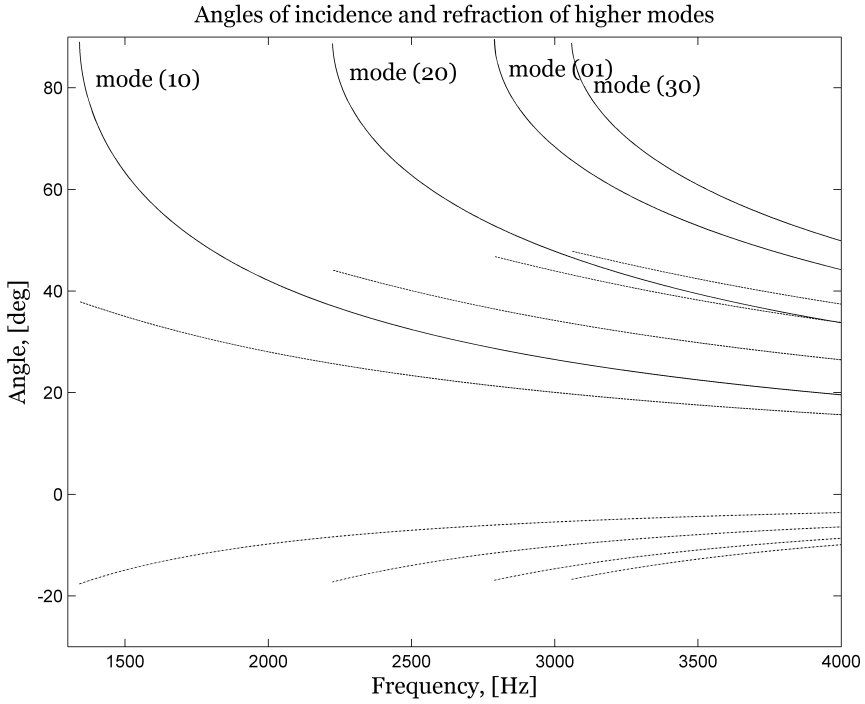


Figure 5.42: The modal angle of incidence and real and imaginary parts of the corresponding refraction angle as a function of a frequency for melamine foam in the 150 mm diameter circular tube. Solid line: angle of incidence; dashed line: real part of the refracted angle; dotted line: imaginary part of the refracted angle.

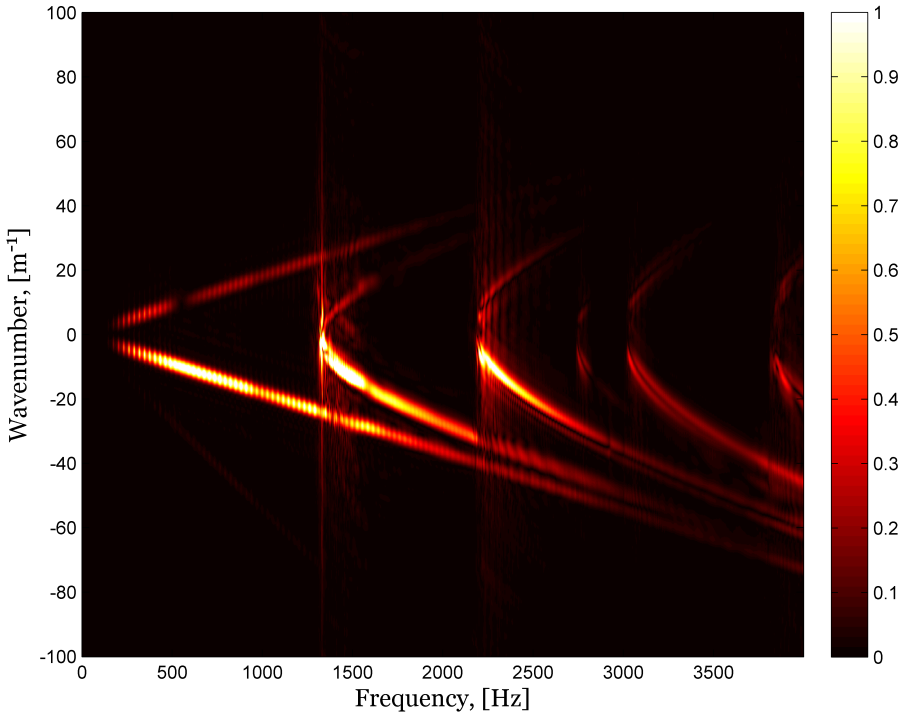


Figure 5.43: The wavenumber-frequency spectra (k-$\omega$ plot) for the layer of melamine foam in the 150 mm circular tube, when the microphone was placed near the wall of the tube cross-section.

speaker and the microphone were placed in the middle (modes (00) and (01)) and when they were near the wall (modes (10), (20) and (30)). The solid lines denote the predictions, calculated using the Miki equivalent fluid model (1990), and the dots denote the experimental data obtained through the application of the algorithm (5.1.8). It is worth noting here that the fundamental mode reflection coefficient could have been recovered from the measurements near the edge of the tube cross-section, but the measurements in the middle of the cross-section were favoured for its recovery as it allowed measurement over the wider frequency range. The differences between the theory and the measurements were quantified in accordance with Equation (5.2.2) and are summarised in Table 5.11. The largest difference of 17% is observed in case of the imaginary part of the fundamental mode. Here, after about 500 Hz, the match between the predicted and the measured reflection coefficient values becomes worse, although they follow the similar trend. After the first axisymmetric cut-on frequency of 2789 Hz, the behaviour of the measured reflection coefficient becomes rather oscillatory. This may be

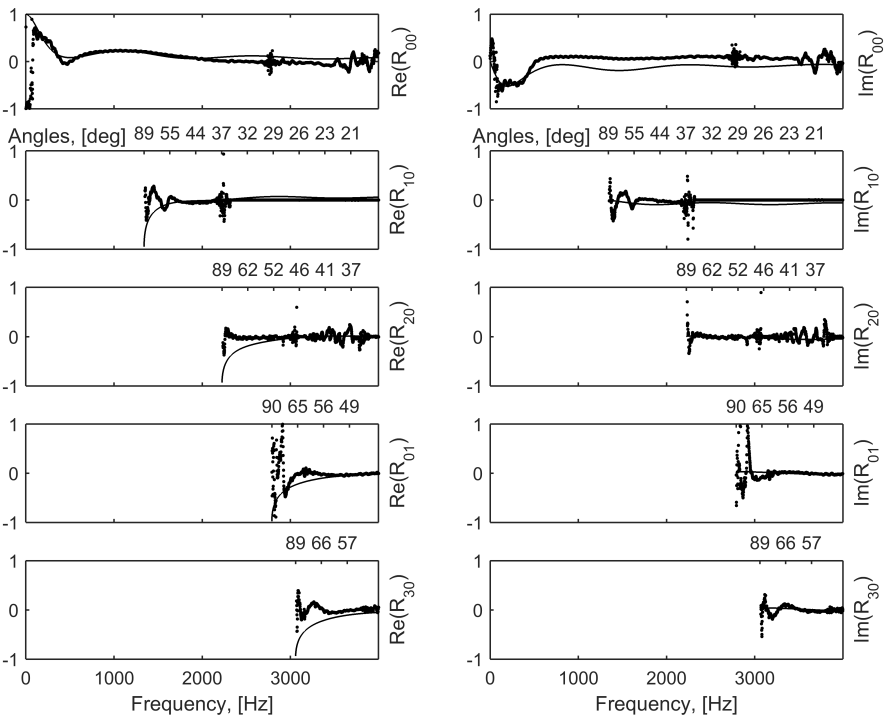


Figure 5.44: The modal reflection coefficients for the layer of melamine foam, recovered in the 150 mm circular tube cross-section. Solid line: predictions; dots: experiments.

explained by the fact that the fundamental mode lacks energy once the sound field in the tube becomes modal, which compromises the accuracy of the recovered higher modes reflection coefficients.

Figures 5.45, 5.46 and 5.47 present the measured and predicted absolute values of the total absorption coefficient, measured in the 150 mm circular tube. The mean differences between the experiments and predictions are summarised in Table 5.12. Figure 5.45 shows the absorption coefficients, calculated using the incident and reflected amplitude method, given by Equation (5.1.24). It can be noted here that the data recorded in the middle and near the wall of the tube were combined for the calculations, which resulted in one graph. Figures 5.46 and 5.47 present the results calculated using the intensity method (Equation (5.1.28)), obtained near the wall and in the middle of the tube, respectively. It is clear from these figures that although all three figures exhibit a very good match between the predictions and measurements, the intensity method is more

| Mode | $\epsilon_{\mathrm{Re}}$ | $\epsilon_{\mathrm{Im}}$ |
|---|---|---|
| $R_{00}$ | 0.1054 | 0.1764 |
| $R_{01}$ | 0.1497 | 0.0838 |
| $R_{10}$ | 0.0729 | 0.0740 |
| $R_{20}$ | 0.1114 | 0.0569 |
| $R_{30}$ | 0.2080 | 0.0542 |

Table 5.11: A summary of the mean differences between the real and imaginary parts of the measured and predicted modal reflection coefficients for the melamine foam material sample, when the microphone was placed in the centre of the 150 mm circular tube cross-section (modes (00) and (01)) and near the edge of the cross-section (modes (10), (20) and (30)).

susceptible to an error in the vicinity of the cut-on frequencies (1300 Hz, 2200 Hz and 3000 Hz in Figure 5.46 and 2800 Hz in Figure 5.47). The respective mean differences between the measured and predicted data for these figures are 5.76% and 0.83%. This may be caused by the fact that the spacing between the microphone positions (approximately 10 mm) is too small for a given wavelength at the cut-on frequencies, which results in big phase errors in intensity. The mean difference between the predictions and experiments, calculated using the amplitude method, is 0.46%, which means that the amplitude method seems to work best for the 150 mm circular tube experimental setup, as opposed to the square tube setups. The most probable reason for this is the fact that for the 150 mm circular tube experimental data analysis, the modal amplitudes recorded both in the middle and near the wall were combined. This eliminated the need to calculate the full and partial total absorption coefficients (as in Figures 5.17-5.18 and 5.32-5.33), and resulted in a higher accuracy results.

| | $\epsilon_{\alpha_{total}}$ |
|---|---|
| Amp method, combined | 0.005 |
| Int method, corner | 0.057 |
| Int method, middle | 0.008 |

Table 5.12: A summary of the mean differences between the measured and predicted total absorption coefficient for the layer of melamine foam in the 150 mm circular tube. Amp method: incident and reflected amplitudes ratio method; Int method: intensity ratio method.

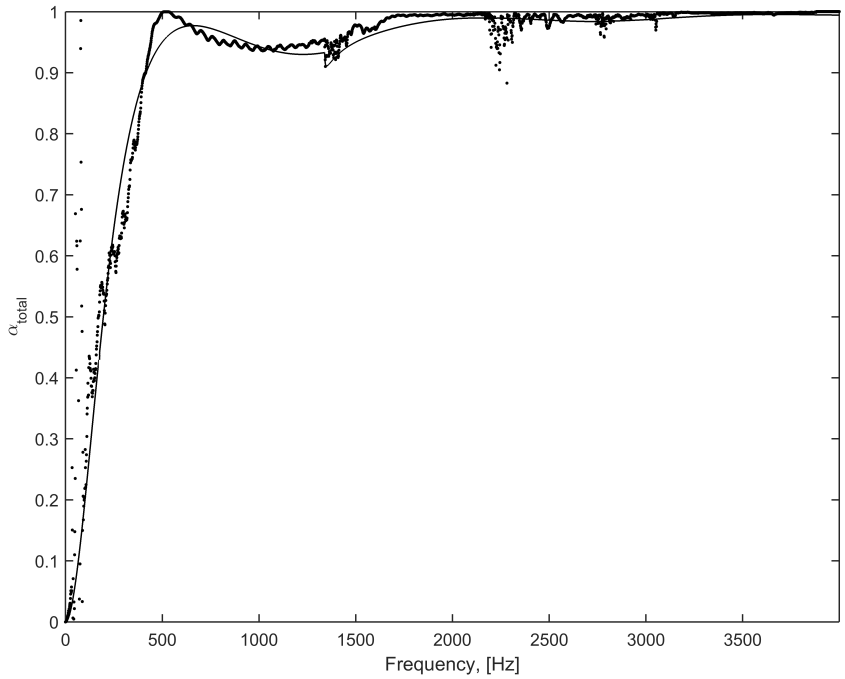


Figure 5.45: The measured and predicted total absorption coefficients for the layer of melamine foam calculated using the amplitude method, measured in 150 mm circular tube, with the microphone placed near the wall of the tube cross-section. Solid line: predictions; dots: experiments.

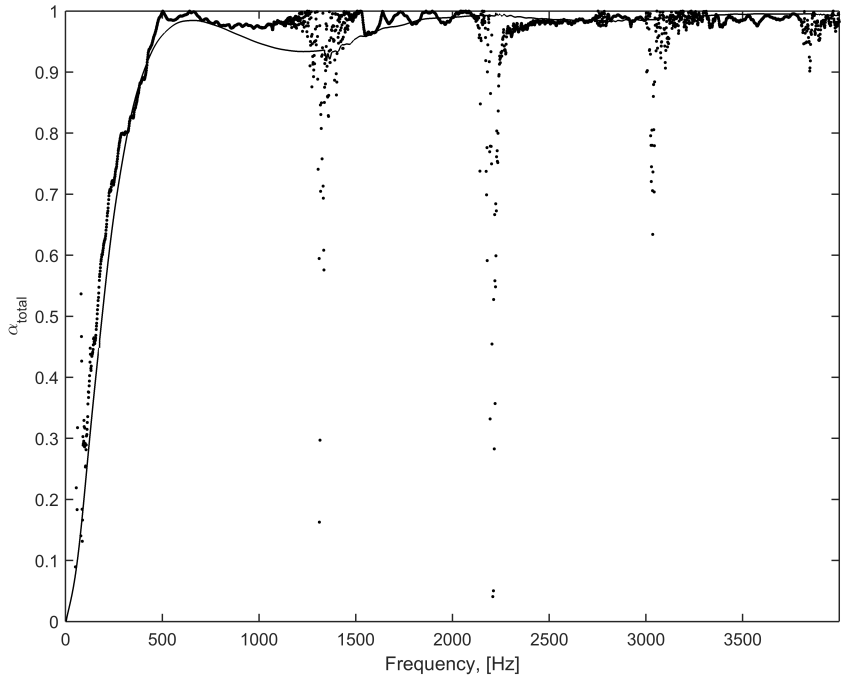


Figure 5.46: The measured and predicted total absorption coefficients for the layer of melamine foam calculated using the intensity method, measured in 150 mm circular tube, with the microphone placed near the wall of the tube cross-section. Solid line: predictions; dots: experiments.

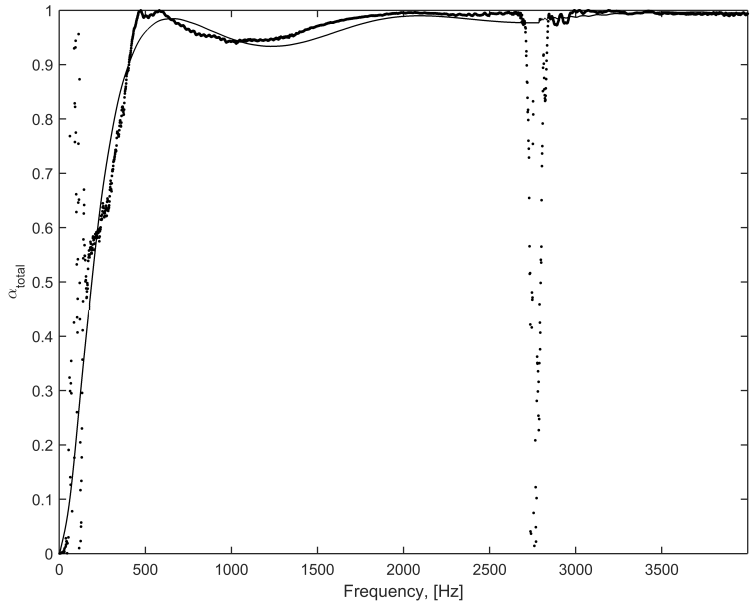


Figure 5.47: The measured and predicted total absorption coefficients for the layer of melamine foam calculated using the intensity method, measured in 150 mm circular tube, with the microphone placed in the middle of the tube cross-section. Solid line: predictions; dots: experiments.

## 5.4 Summary

This chapter presents a novel method to measure the sound absorption by porous materials in an impedance tube. The proposed method is based on measuring the sound pressure spectra with a horizontal microphone array and then applying the spatial Fourier transform to these data to separate the incident modal field from the modal field reflected from the porous layer. It has been shown that in this way the high frequency limit of a rectangular impedance tube can be extended at least by a factor of three. An attractive feature of this method is that it yields both frequency and angular dependent complex reflection coefficient data for a porous layer. This allows the laboratory measurements of the acoustical properties of a large porous specimen at a range of the angles of incidence and in a relatively wide frequency band. Furthermore, the proposed experimental setup is time-efficient and easy to run and it does not require a very large material specimen, as suggested in the standard ISO 354 (2003) reverberation chamber method.

This method has been validated with the controlled laboratory experiments, performed in three tubes: 300 mm and 150 mm wide square tubes and 150 mm diameter circular tube, and such materials as melamine, Armasound and a thin porous foams, as well as wood fibre have been tested. The experimental results have been compared to the predictions of the existing equivalent fluid models, such as Johnson-Champoux-Allard model (1991) and Pade approximants model (1998). The measured modal reflection coefficients agree with the predictions well, with the mean difference being around 15% and less for the plane wave, and normally not exceeding 30% in the case of higher modes. These values are higher for the 150 mm square tube, which may be caused by the residual absorption of the tube affecting the accuracy of the measured data. In the case of the total absorption coefficient, the mean differences between the measurements and predictions do not exceed 22%, but are generally lower. In general, the method has been successfully tested and can be employed to characterise large porous material samples in an impedance tube.

The sound reflection and absorption coefficient determination method, presented in this chapter, will be applied to living plants in the next. Several plants species will be tested in an impedance tube and be treated as porous media for the prediction calculation.

# Chapter 6

# Application of material characterisation methods to living plants

In the recent years, novel sustainable means to reduce the noise pollution in urban and rural areas have been used together with traditional, man-made sound absorbing materials. One of such means is the use of living plants, which are planted on green walls and barriers to provide the noise insulation. However, the process of plant selection for this purpose remains unclear, as there are no studies, directly linking plants' geometry with their sound absorbing abilities. To address this issue, a study was performed, in which several plants of different size and shape were chosen, characterised and tested in an impedance tube to estimate their sound absorption coefficient. It has been shown that living plants can be regarded as porous media (Horoshenkov, 2013), so that their acoustical behaviour can be predicted using equivalent fluid models. The non-acoustical parameters of in these models can be linked to the plant morphology. In

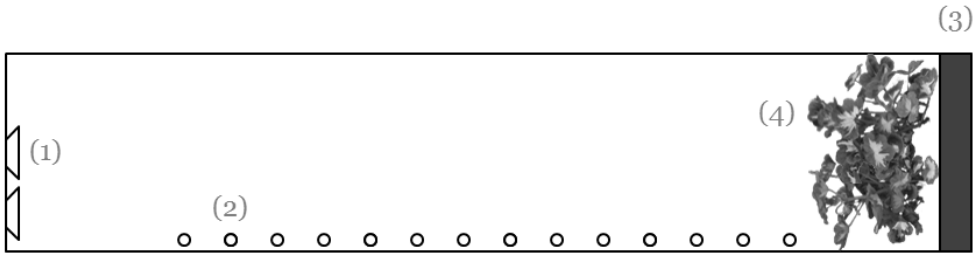


Figure 6.1: A schematic illustration of the experimental setup: (1) loudspeakers, (2) simulated horizontal microphone array, (3) metal lid, (4) plant specimen.

this way, plants can be selected to control noise with particular spectral characteristics. This chapter shows how the intensity-based methods can be used to measure the acoustical properties of relatively large plant specimens. The predicted and measured results are compared and the capabilities and limitations of the study are discussed.

## 6.1 Experimental methodology

For measurements of sound absorption by living plants, the same experimental facilities were employed as those described in Section 5.2.1. Two square cross-section tubes, 300 mm wide and 150 mm wide, were used to accommodate plant specimen of a reasonable size. Instead of a porous material specimen, a layer of living plants foliage was inserted in the tube, as shown in Figure 6.1. Stems with leaves were cut from their pots and arranged at the end of the tube in a way which provides the best coverage of the cross-section with greenery. A square wooden frame of the same width as the tube and with a wire mesh across its cross-section was used to hold the plants parallel to the bottom of the tube, with additional help of thin wires which supported the plants in horizontal position (see Figure 6.2. The frame with the plants was inserted at the end of the tube which was subsequently terminated with the metal lid.

side view back view

Figure 6.2: The wooden frame used for holding the living plants parallel to the bottom of the tube. On the left: side view; on the right: back view.

## 6.2 Plant analysis

To study sound characteristics by living plants, six plant species were chosen: (1) garden geranium (*Pelargonium hortorum*); (2) ficus (*Ficus benjamina*); (3) ivy (*Hedera helix*); (4) begonia (*Begonia benariensis*); (5) rudbeckia (*Rudbeckia hirta*); (6) kalanchoe (*Kalanchoe blossfeldiana*). These plants were purchased from a local garden center. Figure 6.4 shows the photographs of these plants, and Figure 6.5 illustrates the shape and dimensions of their leaves. For the reported experiments plant stems with the foliage were cut off from their roots and placed in the impedance tube with the stems parallel to the direction of sound propagation. The amount of water in the plants was not measured, but all dry and faded leaves were removed, so that only fresh greenery remained. The following morphological characteristics of these plants were measured: mean weight of a single leaf $w_f$, mean thickness of a single leaf $h_f$, mean area of a single leaf $s_f$, number of leaves on a plant $n_f$, estimated thickness of a plant layer $h_p$ (which coincides with the estimated height of the plant), and dominant angle of leaf orientation $\theta_f$. The latter parameter defines an angle between a leaf and the direction

of sound wave propagation, and is shown in Figure 6.3. These values are presented in

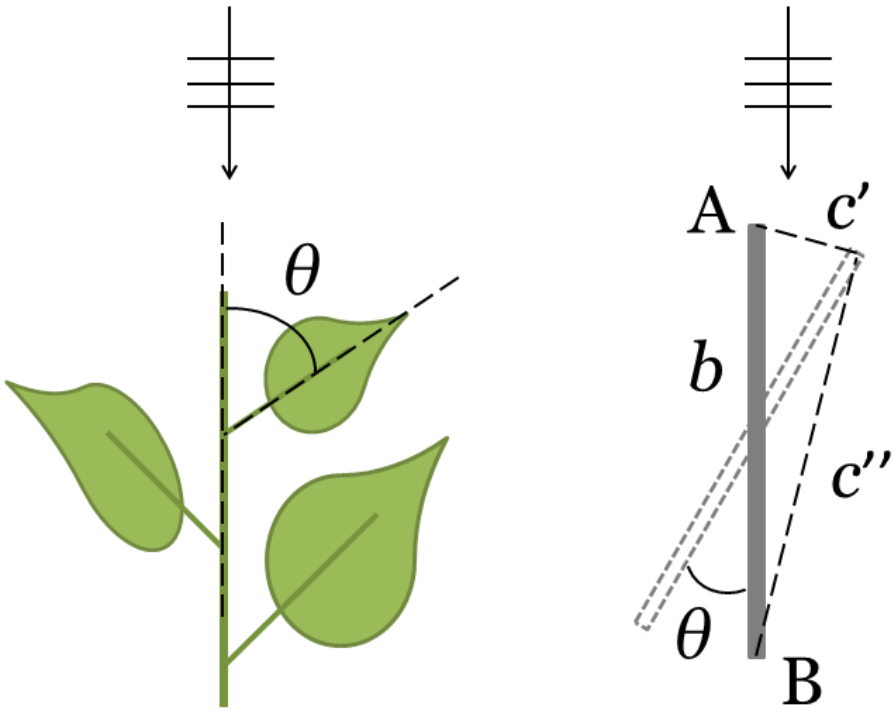


Figure 6.3: A schematic illustration of a dominant angle of leaf orientation.

Table 6.1, except the thickness of the plant layer. This parameter is presented together with derived characteristics of plants in Tables 6.2 and 6.3, as it differed for the two tubes used for the experiments. Twenty-five leaves from the tested plants were randomly chosen for the determination of plant characteristics. The weight of leaves was measured using electronic scales the precision of which was ±0.005 g. The thickness was estimated with the electronic caliper which is capable of measuring distance to ±0.01 mm. For the leaf area estimation, a picture of a leaf framed by rulers was taken as shown in Figure 6.5a. Then the picture was imported to Adobe Photoshop software and the amount of pixels in the leaf was determined. Subsequently the leaf area was calculated using the following formula:

$$s_f = p_f \, p_s^{-1} \, s_s \tag{6.2.1}$$

where $p_f$ is the number of pixels in a single leaf, $p_s$ is the number of pixels in a reference square and $s_s$ is the area of a reference square. The leaf orientation angles were also estimated using digital images of plants and the screen protractor tool, as shown in Figure 6.3. The above characteristics were used to derive the following quantities: equivalent volume occupied by the plant $V_p$, leaf area per unit volume $A_v$, total area of leaves on a plant $s_p$, total weight of leaves/stems $w_p$, and volume of plant foliage $V_f$. These values were derived separately for two tubes used for experiments and are presented in Tables 6.2 and 6.3.

| Plant | $w_f$ (g) | $h_f$ (mm) | $s_f$ ($m^2$) | $n_f$ (-) | $\theta_f$ (degrees) |
|---|---|---|---|---|---|
| Geranium | 0.794 | 0.383 | 0.0020 | 41 | 42.6 |
| Ficus | 0.091 | 0.160 | 0.0005 | 700 | 35.7 |
| Ivy | 0.124 | 0.308 | 0.0006 | 228 | 60.9 |
| Begonia | 1.010 | 0.461 | 0.0032 | 37 | 35.9 |
| Rudbeckia | 0.982 | 0.636 | 0.0025 | 16 | 13.1 |
| Kalanchoe | 6.227 | 1.974 | 0.0037 | 53 | 36.9 |

Table 6.1: Measured characteristics of plant specimen: average weight of single leaf $w_f$; average thickness of single leaf $h_f$; average area of single leaf $s_f$; number of leaves on plant $n_f$; dominant angle of leaf orientation $\theta_f$.

| Plant | $h_p$ | $V_p$ ($m^3$) | $A_v$ ($m^{-1}$) | $s_p$ ($m^2$) | $w_p$ (kg) | $V_f$ ($m^3$) |
|---|---|---|---|---|---|---|
| Geranium | 0.35 | 0.0079 | 12.31 | 0.097 | 0.0319 | 0.000055 |
| Ficus | 0.15 | 0.0034 | 107.58 | 0.363 | 0.0633 | 0.000058 |
| Ivy | 0.09 | 0.0027 | 51.01 | 0.138 | 0.0282 | 0.000042 |
| Begonia | 0.18 | 0.0032 | 37.76 | 0.122 | 0.0390 | 0.000056 |
| Rudbeckia | 0.23 | 0.0021 | 19.98 | 0.041 | 0.0161 | 0.000026 |
| Kalanchoe | 0.20 | 0.0045 | 43.45 | 0.196 | 0.3269 | 0.000386 |

Table 6.2: Calculated characteristics for the 6 plant specimens in the 300 mm wide square tube: estimated plant layer thickness $h_p$; equivalent volume occupied by plant $V_p$; leaf area per unit volume $A_v$; total area of leaves on plant $s_p$; total weight of leaves/stems $w_p$; total volume of plant foliage $V_f$.

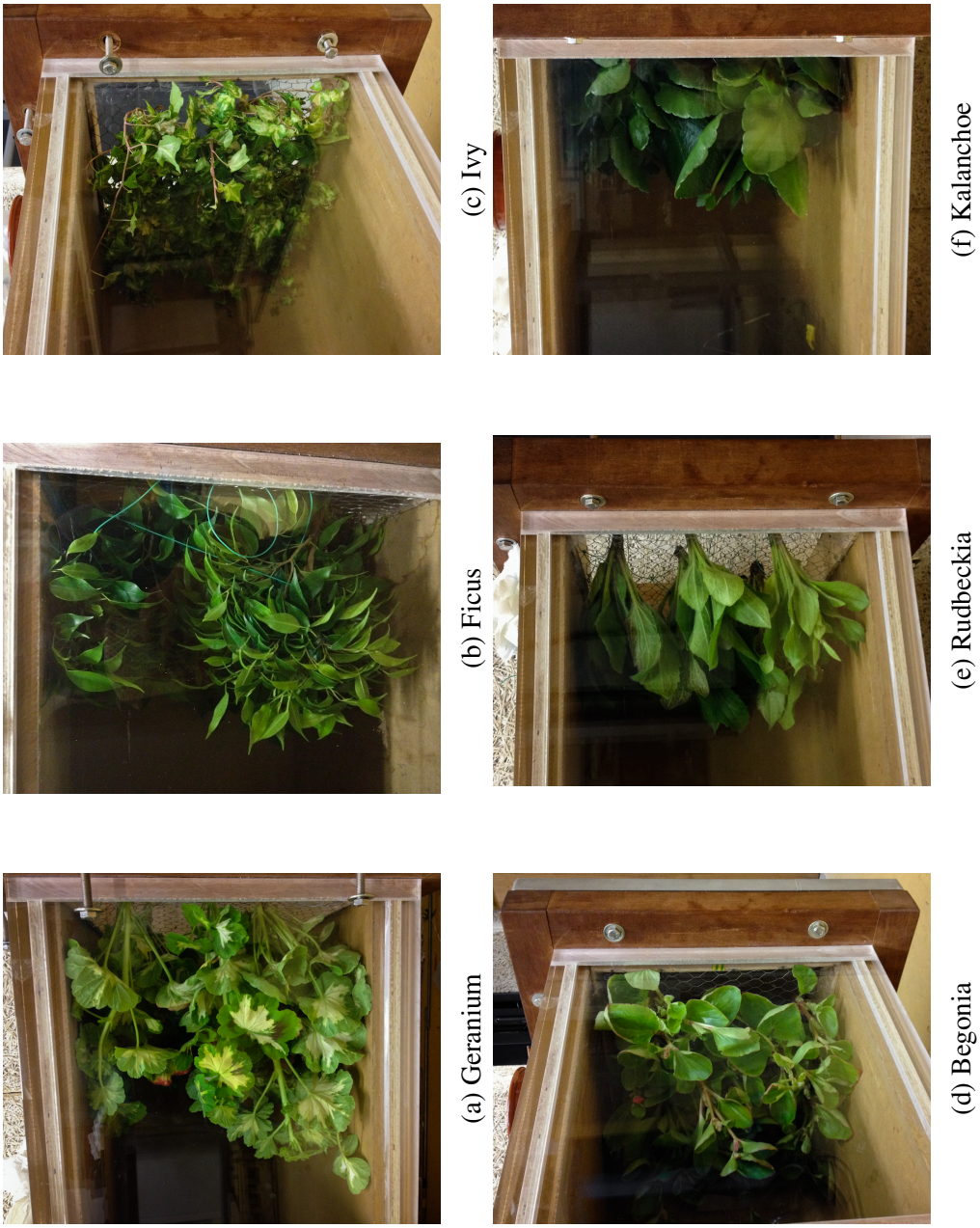


Figure 6.4: Photographs of the six plant species used in the experiments inserted at the end of the 300 mm tube in horizontal orientation.

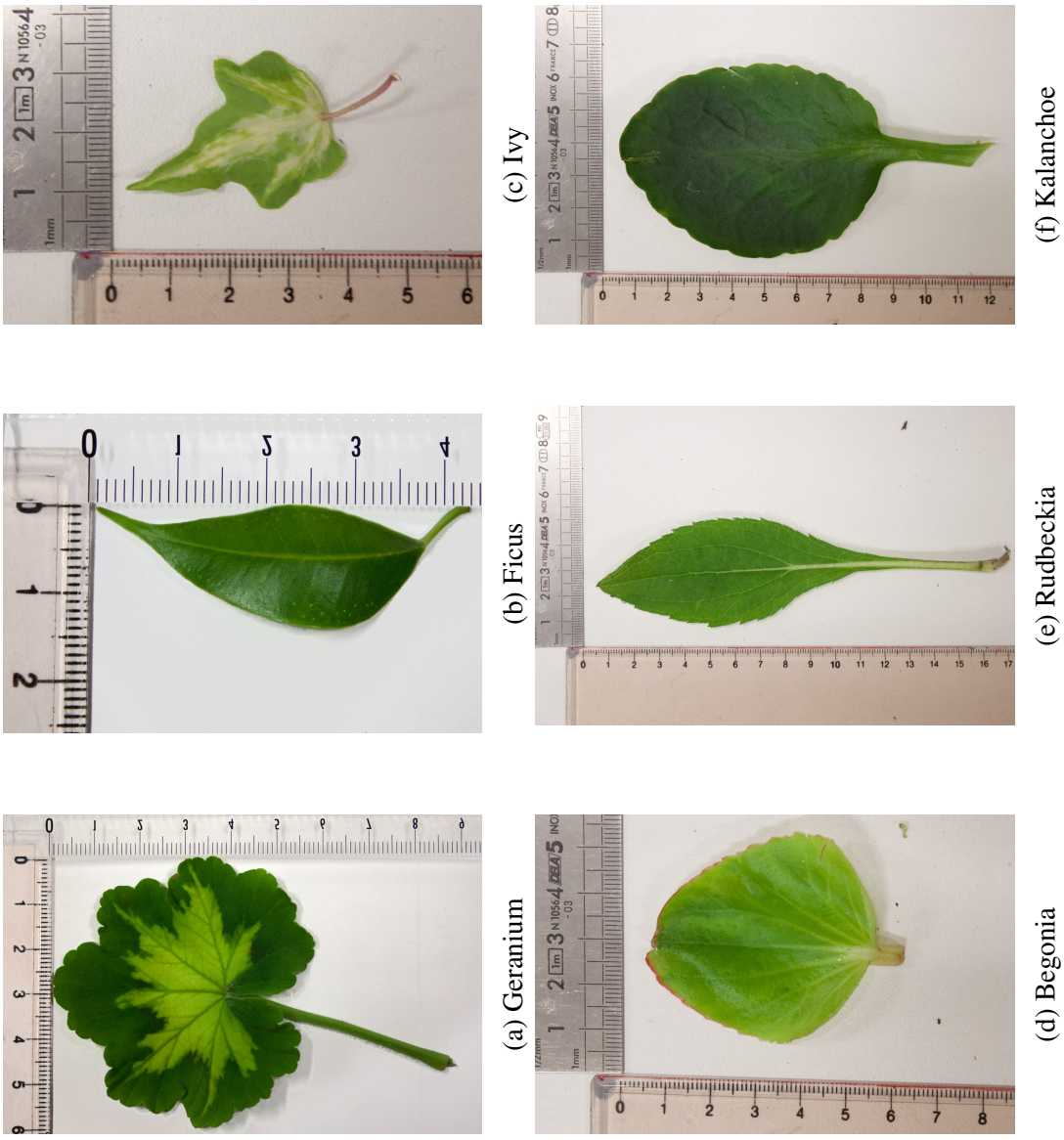


Figure 6.5: Photographs of leaves of the six plant species used in the experiments.

| Plant | $h_p$ | $V_p$ (m$^3$) | $A_v$ (m$^{-1}$) | $s_p$ (m$^2$) | $w_p$ (kg) | $V_f$ (m$^3$) |
|---|---|---|---|---|---|---|
| Geranium | 0.36 | 0.0081 | 11.96 | 0.097 | 0.0319 | 0.000055 |
| Ivy | 0.16 | 0.0018 | 76.52 | 0.138 | 0.0282 | 0.000042 |
| Begonia | 0.21 | 0.0024 | 51.78 | 0.122 | 0.0390 | 0.000056 |
| Rudbeckia | 0.25 | 0.0014 | 29.41 | 0.041 | 0.0161 | 0.000026 |
| Kalanchoe | 0.20 | 0.0022 | 86.91 | 0.196 | 0.3269 | 0.000386 |

Table 6.3: Calculated characteristics for the 5 plant specimens in the 150 mm wide square tube: estimated plant layer thickness $h_p$; equivalent volume occupied by plant $V_p$; leaf area per unit volume $A_v$; total area of leaves on plant $s_p$; total weight of leaves/stems $w_p$; total volume of plant foliage $V_f$.

## 6.3 Theoretical predictions for plants acoustical behaviour

Recently, it was proposed by Horoshenkov (2013) to use an equivalent fluid model to estimate the sound absorption by living plants (see Section 2.6). The authors suggested to link the key morphological parameters of plants, described in the previous section, to the non-acoustical characteristics used in the model: porosity, flow resistivity and tortuosity. These characteristics were estimated in the following manner. The porosity was deduced from the total volume of the plant foliage, $V_f$, and volume occupied by the plant, $V_p$, i.e.:

$$\phi = 1 - \frac{V_f}{V_p}, \tag{6.3.1}$$

The flow resistivity of the equivalent fluid occupied by the plant was estimated using the empirical relations suggested in the aforementioned reference (Horoshenkov, 2013):

$$\log_{10} \sigma = 0.0083\, A_v + 1.413, \quad \text{for } \theta > 70^\circ, \tag{6.3.2}$$

$$\log_{10} \sigma = 0.0067\, A_v + 0.746, \quad \text{for } \theta < 40^\circ. \tag{6.3.3}$$

where $A_v$ is the leaf area density of the plant and $\theta$ is the difference between the dominant angle of leaf orientation and the angle of incidence of sound. Finally, the tortuosity was estimated from the knowledge of the dominant angle of leaf orientation and the angle of incidence of sound (Horoshenkov, 2013). It is shown in Figure 6.3 how the value

of tortuosity depends on the effective path between points A and B. The schematic representation of the problem, shown on the right in Figure 6.3 corresponds to the leaf staying in the middle of the path of the wave propagation between points A and B, which is a valid assumption. Then the obstruction created by this leaf is symmetrical, so that the effective path length $c = c' + c''$, which the sound wave travels along on the either side of the leaf is identical. It is assumed here that the leaf area density in the plants under consideration is rather high. In this case, the height of the plant or the length of leave stems have no impact on the maximum value of tortuosity. Hence, it is easy to show that the effective path length for the sound wave travelling through the plant is controlled solely by the leaf orientation angle and is given by

$$c = b\left(\cos\frac{\theta}{2} + 2\sin\frac{\theta}{2}\right). \tag{6.3.4}$$

Then, the tortuosity can be expressed as follows (Zwikker and Kosten, 1949):

$$\alpha_\infty = \cos\frac{\theta}{2} + 2\sin\frac{\theta}{2}. \tag{6.3.5}$$

The estimated values of these parameters for the plants adopted for this work are listed in Tables 6.4 and 6.5. Table 6.4 lists the characteristics of the plants tested in the 300 mm wide tube, and Table 6.5- in the 150 mm wide square tube. As porosity and flow resistivity depend on the volume occupied by a plant and its height, and these parameters were different for two tubes, the estimated values are presented in separate tables for each tube.

After these parameters were measured, they were substituted into Equations (2.6.17) and (2.6.18). These two parameters enabled the calculation of the surface impedance and the modal reflection coefficients in accordance with Equation (2.6.21).

| Plant | $\phi$ [-] | $\alpha_\infty$ [-] | $\sigma$ [ N s/m$^4$] |
|---|---|---|---|
| Geranium | 0.99 | 1.51 | 6.74 |
| Ficus | 0.98 | 1.56 | 29.29 |
| Ivy | 0.98 | 1.57 | 68.61 |
| Begonia | 0.98 | 1.57 | 9.98 |
| Rudbeckia | 0.99 | 1.22 | 7.58 |
| Kalanchoe | 0.91 | 1.58 | 10.89 |

Table 6.4: Estimated non-acoustical parameters for the 6 plant specimen in the 300 mm tube: porosity, $\phi$; tortuosity, $\alpha_\infty$; flow resistivity, $\sigma$.

| Plant | $\phi$ [-] | $\alpha_\infty$ [-] | $\sigma$ [ N s/m$^4$] |
|---|---|---|---|
| Geranium | 0.99 | 1.41 | 6.70 |
| Ivy | 0.98 | 1.57 | 18.14 |
| Begonia | 0.98 | 1.57 | 12.39 |
| Rudbeckia | 0.98 | 1.22 | 8.77 |
| Kalanchoe | 0.83 | 1.58 | 21.29 |

Table 6.5: Estimated non-acoustical parameters for the 5 plant specimen in the 150 mm tube: porosity, $\phi$; tortuosity, $\alpha_\infty$; flow resistivity, $\sigma$.

## 6.4 Results and discussion

This section presents the modal reflection and total absorption coefficients measured with the proposed method. Figures 6.6 and 6.7 show the frequency-wavenumber plots for the geranium plant, measured in the 300 mm tube, with the microphone placed in the corner and in the middle of the tube cross-section, respectively. The separation of the first few higher order modes is evident from these plots, which makes them suitable for the subsequent recovery of reflection and absorption information. The frequency-wavenumber plots for the remaining plant specimens are provided in Appendix B.

Figures 6.8-6.9 present the predicted (solid line) and measured (black dots) absolute values of the modal reflection coefficients for the geranium specimen, obtained in the corner and in the middle of the cross-section, respectively. The measured data were recovered from the frequency-wavenumber data using the optimisation technique described in Section 5.1. The predictions for the modal reflection coefficient were calcu-

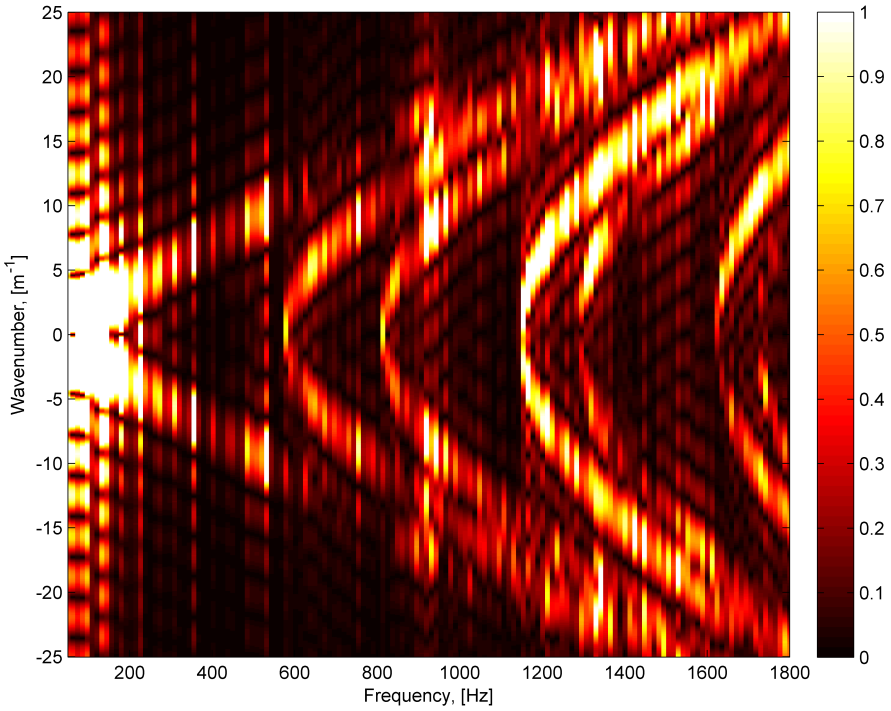


Figure 6.6: The frequency-wavenumber spectrum for geranium plants measured in 300 mm wide square tube, with the microphone placed in the corner of the tube cross-section.

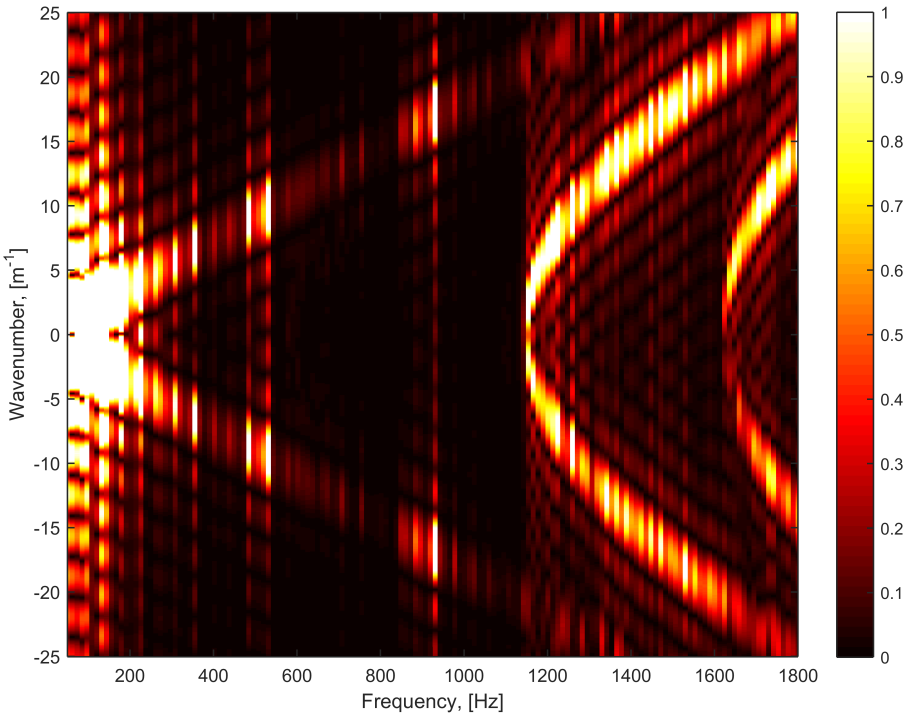


Figure 6.7: The frequency-wavenumber spectrum for geranium plants measured in 300 mm wide square tube, with the microphone placed in the middle of the tube cross-section.

lated according to the method explained in Section 6.2. The reflection coefficients are plotted as a function of frequency (bottom axis) and incidence angle (top axis for higher order modes). Figure 6.8 presents the reflection coefficients for the first four modes, (00),(01), (11) and (02), whereas Figure 6.9 shows the reflection coefficients of the axisymmetric modes, (00), (02) and (22). One of the reasons to perform the measurements at two cross-sectional locations was to extend the frequency range where the fundamental mode reflection coefficient can be recovered. Fewer modes can be recorded in the middle of the cross-section, and the cut-on frequency of the first axisymmetric mode, (02), is 1143 Hz. This provides a possibility to increase the frequency range by a factor of two, compared to the cut-on frequency of 572 Hz for mode (01). Although the scattering is still rather strong beyond 572 Hz, the quality of the recovered fundamental mode reflection coefficient in the higher frequency range is better than that recovered with the microphone in the corner of the cross-section. Another important observation is the fact that the model overpredicts the reflection coefficient of mode (00) above the first cross-sectional resonance. This may be due to the scattering processes in the greenery, which the model does not account for. For the remaining plants, the reflection coefficient for mode (00) measured in the middle of the tube will be combined with reflection coefficients for modes (01), (11) and (02) measured in the corner of the tube and presented in one figure for each plant. The exception is ficus, as for this plant specimen only the data measured in the corner of the tube are available.

The mean differences between the measurements and predictions were quantified in accordance with Equation (5.2.2) and presented on the plots, as well as in Table 6.6. Generally, the differences are low and they do not exceed the maximum of 10%. This allows for an important conclusion that the proposed plant characterisation method generally works well and it is possible to use it to measure the acoustic behaviour of plants. However, the match for higher modes is worse than that for the fundamental mode, and the model mainly overpredicts the absolute reflection coefficient of the plant above the first cross-sectional resonance frequency (572 Hz). This may signify that the acoustical

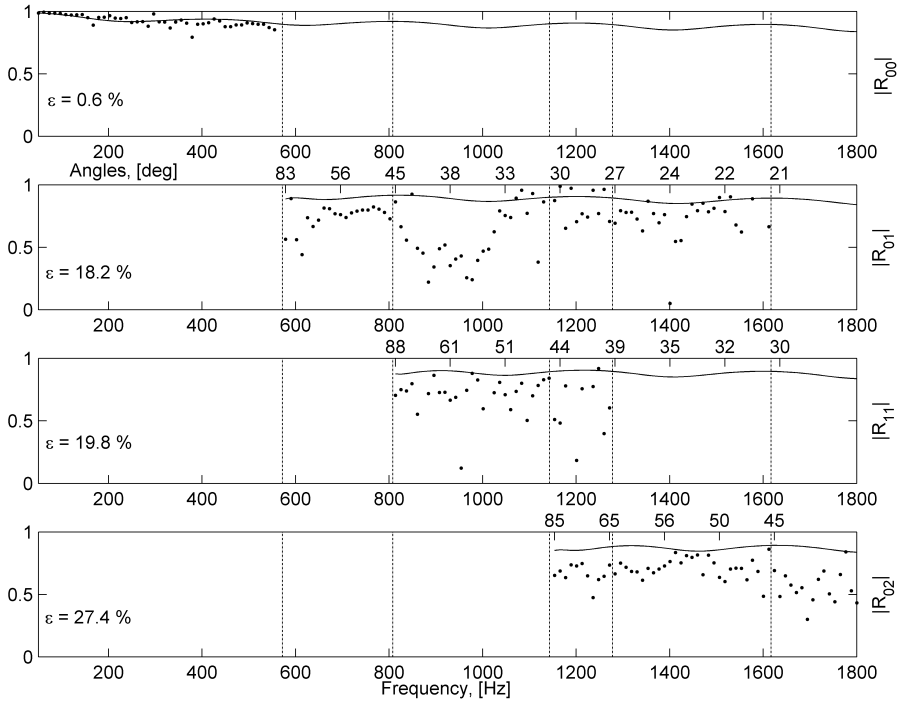


Figure 6.8: The measured and predicted modal reflection coefficients for geranium plants measured in 300 mm wide square tube, with the microphone placed in the corner of the tube cross-section. Solid line: predictions; dots: experiments.

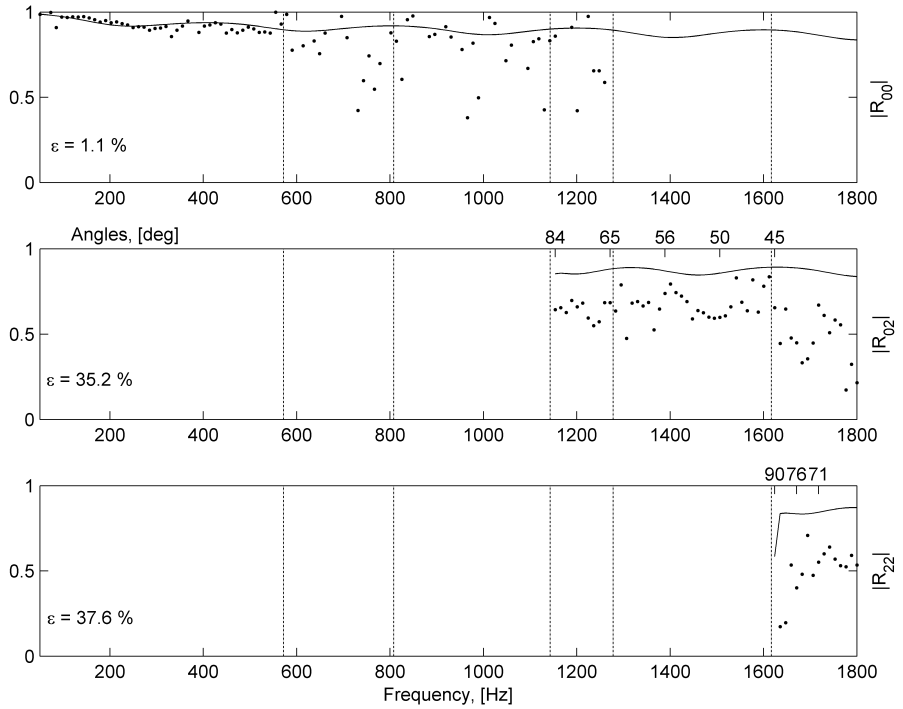


Figure 6.9: The measured and predicted modal reflection coefficients for geranium plants measured in 300 mm wide square tube, with the microphone placed in the middle of the tube cross-section. Solid line: predictions; dots: experiments.

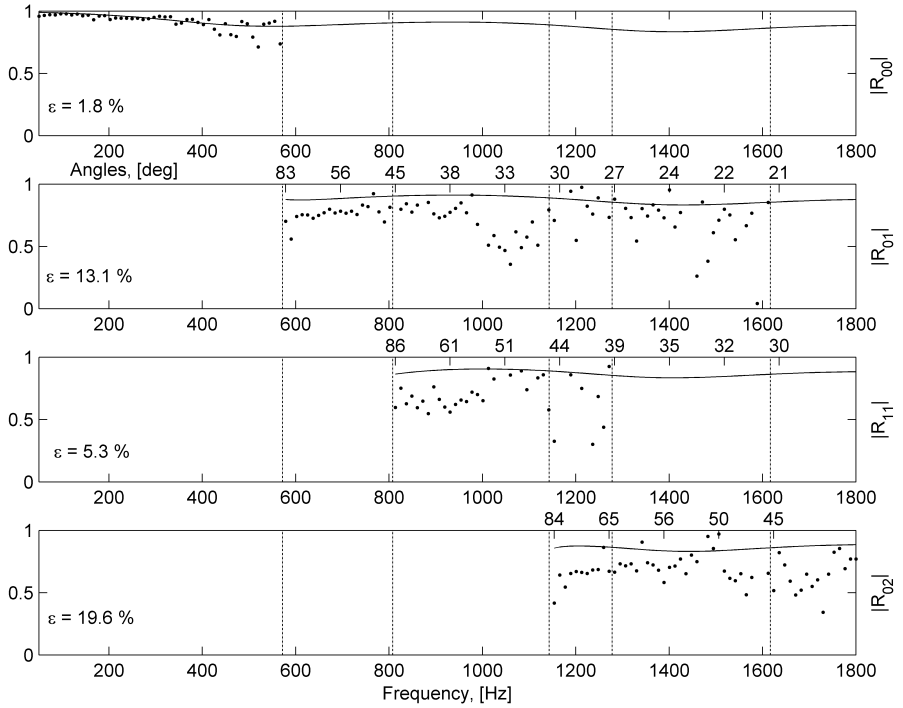


Figure 6.10: The measured and predicted modal reflection coefficients for ficus plants measured in 300 mm wide square tube, with the microphone placed in the corner of the tube cross-section. Solid line: predictions; dots: experiments.

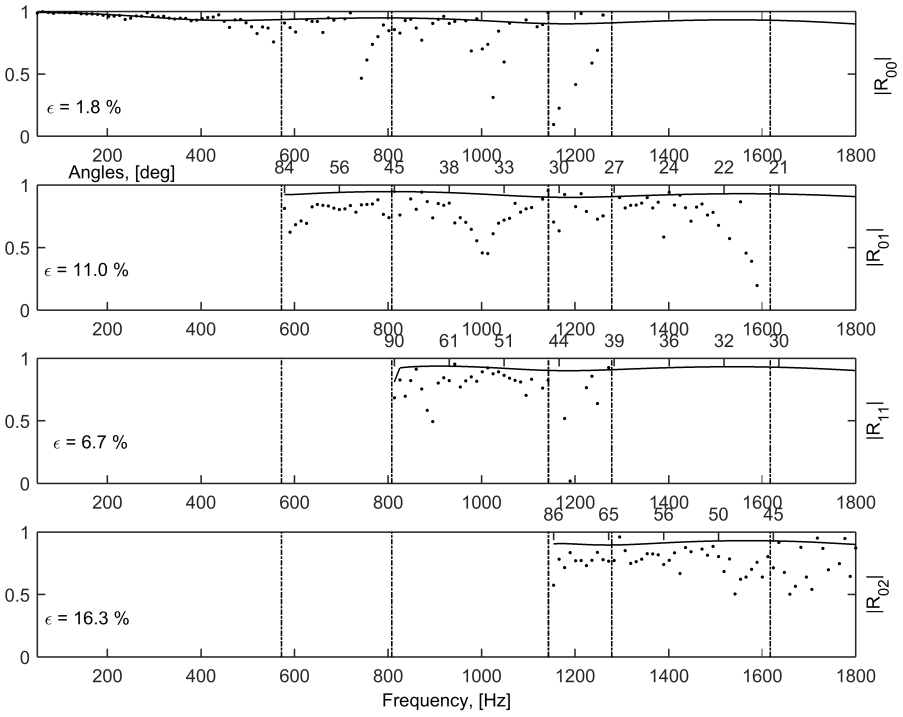


Figure 6.11: The measured and predicted modal reflection coefficients for begonia plants measured in 300 mm wide square tube, with the microphone placed in the corner of the tube cross-section. Solid line: predictions; dots: experiments.

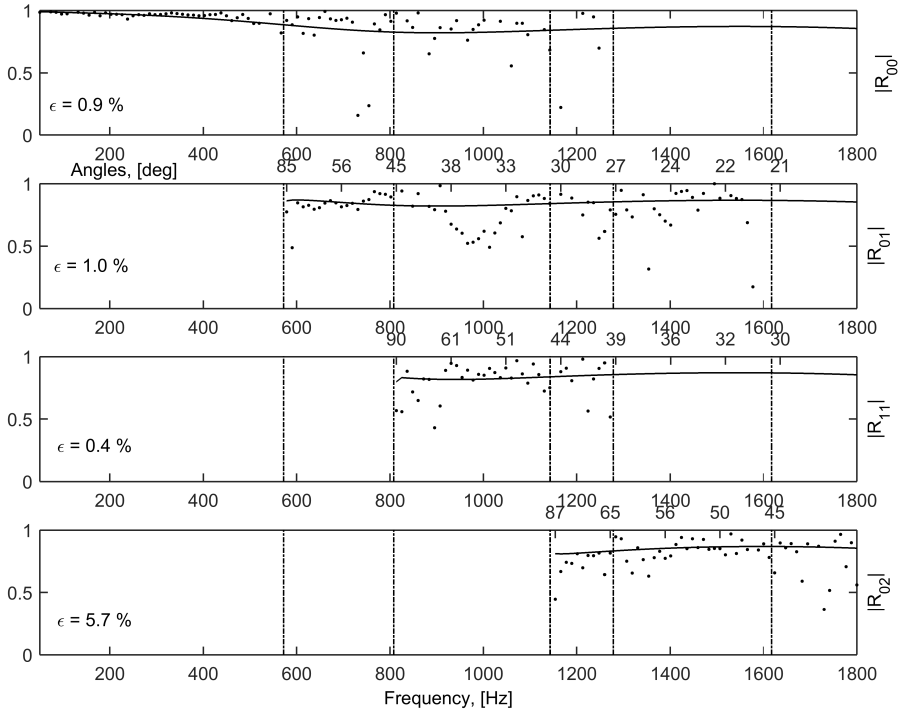


Figure 6.12: The measured and predicted modal reflection coefficients for ivy plants measured in 300 mm wide square tube, with the microphone placed in the corner of the tube cross-section. Solid line: predictions; dots: experiments.

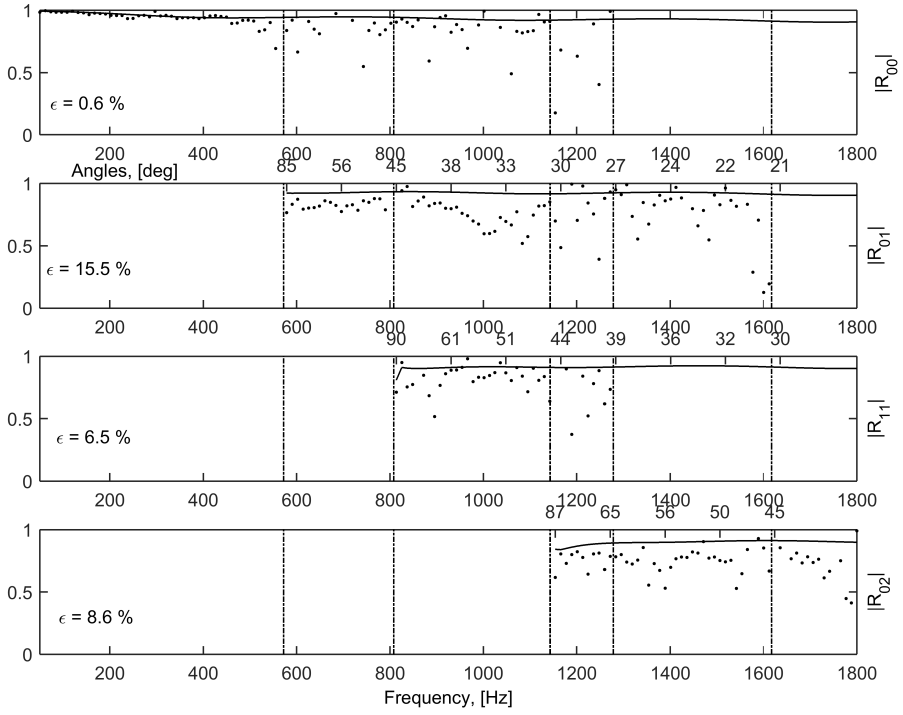


Figure 6.13: The measured and predicted modal reflection coefficients for rudbeckia plants measured in 300 mm wide square tube, with the microphone placed in the corner of the tube cross-section. Solid line: predictions; dots: experiments.

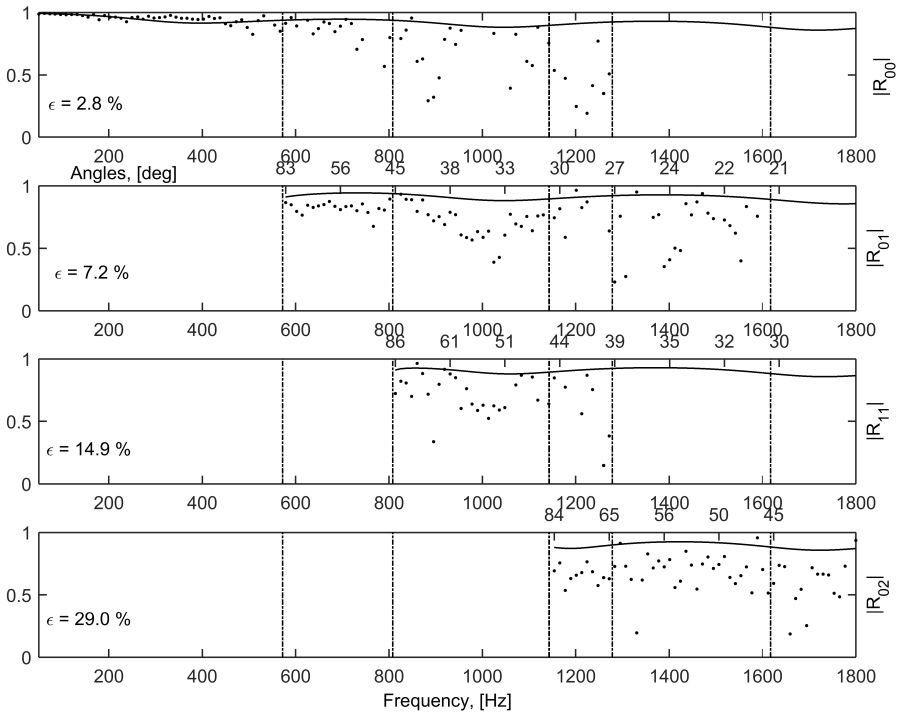


Figure 6.14: The measured and predicted modal reflection coefficients for kalanchoe plants measured in 300 mm wide square tube, with the microphone placed in the corner of the tube cross-section. Solid line: predictions; dots: experiments.

behaviour of plants above the first cut-on frequency is more complex than that predicted by the model. There is a decrease in the measured reflection coefficient for the angles of incidence in the range of $30^\circ < \theta_{01} < 45^\circ$ for mode (01), which is observed for the six plants. This may happen due to the increase in the effective value of plant tortuosity, calculated via expression (6.3.5).

| Plant | $\epsilon_{\lvert R_{00}\rvert}$ | $\epsilon_{\lvert R_{01}\rvert}$ | $\epsilon_{\lvert R_{11}\rvert}$ | $\epsilon_{\lvert R_{02}\rvert}$ |
|---|---|---|---|---|
| Geranium | 0.009 | 0.088 | 0.043 | 0.078 |
| Ficus | 0.005 | 0.073 | 0.013 | 0.057 |
| Begonia | 0.003 | 0.057 | 0.016 | 0.051 |
| Ivy | 0.050 | 0.005 | 0.001 | 0.018 |
| Rudbeckia | 0.003 | 0.079 | 0.015 | 0.028 |
| Kalanchoe | 0.029 | 0.038 | 0.039 | 0.085 |

Table 6.6: The mean difference between the absolute values of the measured and predicted modal reflection coefficients for the first four modes for the 300 mm tube.

Figures 6.15-6.18 show the measured and predicted values of the total absorption coefficient for the geranium plant in the 300 mm square tube, calculated using Equations

5.1.24 and 5.1.28. Figures 6.15 and 6.16 present the total absorption coefficients measured in the corner and in the middle of the tube, respectively, and calculated using the incident and reflected amplitudes ratio method, as specified by Equation (5.1.24). Figures 6.17 and 6.18 present the same type of data, but obtained using the intensity method, given by Equation (5.1.28). The mean differences between the measurements and predictions for these four data sets are shown in Table 6.7. It is worth noting, that for the incident and reflected amplitude ratio method, the data for each mode were not available throughout the whole frequency range. For example, as it can be seen on the frequency-wavenumber plot for geranium, obtained in the corner of the tube (Figure 6.6), the dispersion curve for mode (00) disappears after the first cut-on frequency of 572 Hz. This means that the information on the fundamental mode incident and reflected amplitudes was available only in the frequency range between 50 and 572 Hz, instead of 50 to 1800 Hz. Similarly, other modes were also considered in the frequency ranges, where they had a sufficient signal-to-noise ratio. Due to this limitation, two ways of calculating the total absorption coefficient predictions were employed: full theoretical reflection coefficient (full $R_{theo}$), where each mode exists starting from its cut-on frequency and until the maximum adopted frequency of 1800 Hz, and partial theoretical reflection coefficient (partial $R_{theo}$), where a frequency range for each mode was matched to that of the measured data. Both of these sets of the theoretical predictions are given in Table 6.7. However, the partial theoretical reflection coefficient does not reflect the real picture of the sound field in the tube, whereas the full theoretical reflection coefficient cannot be directly compared to the measured data as the latter does not have all the information contained in the theoretical predictions. Due to this issue, it was chosen to use the intensity ratio method for the remaining plants. In addition, Figures 6.15-6.18 show the data obtained both in the corner and in the middle of the tube. As the difference between the two is small, for the remaining plants the average total absorption coefficient will be presented.

Figures 6.19-6.23 show the measured and predicted total absorption coefficients for the

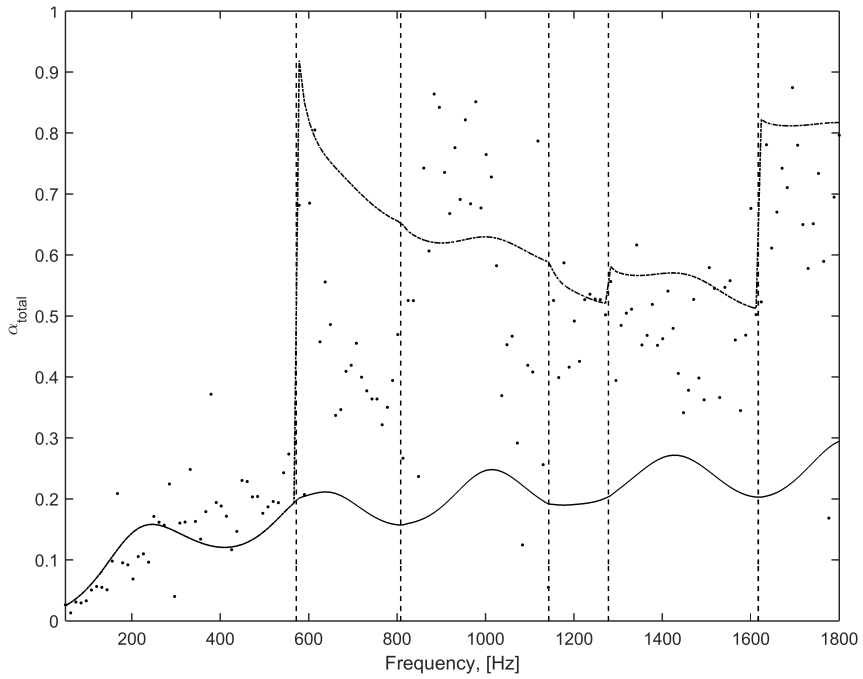


Figure 6.15: The measured and predicted total absorption coefficients for geranium plants calculated using the amplitude method, measured in 300 mm wide square tube, with the microphone placed in the corner of the tube cross-section. Solid line: full absorption coefficient predictions; dashed line: partial absorption coefficient predictions; dots: experiments.

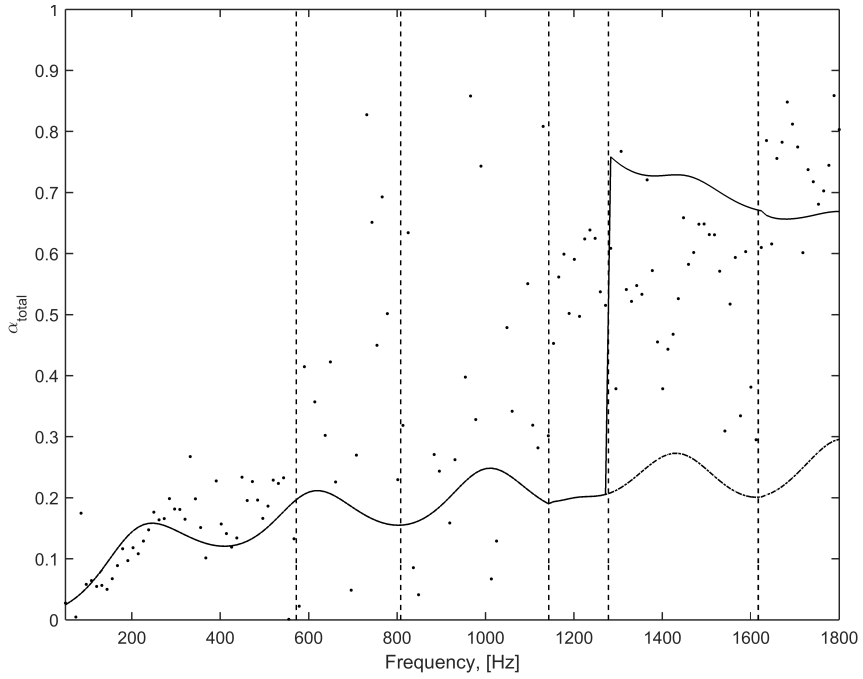


Figure 6.16: The measured and predicted total absorption coefficients for geranium plants calculated using the amplitude method, measured in 300 mm wide square tube, with the microphone placed in the middle of the tube cross-section. Solid line: full absorption coefficient predictions; dashed line: partial absorption coefficient predictions; dots: experiments.

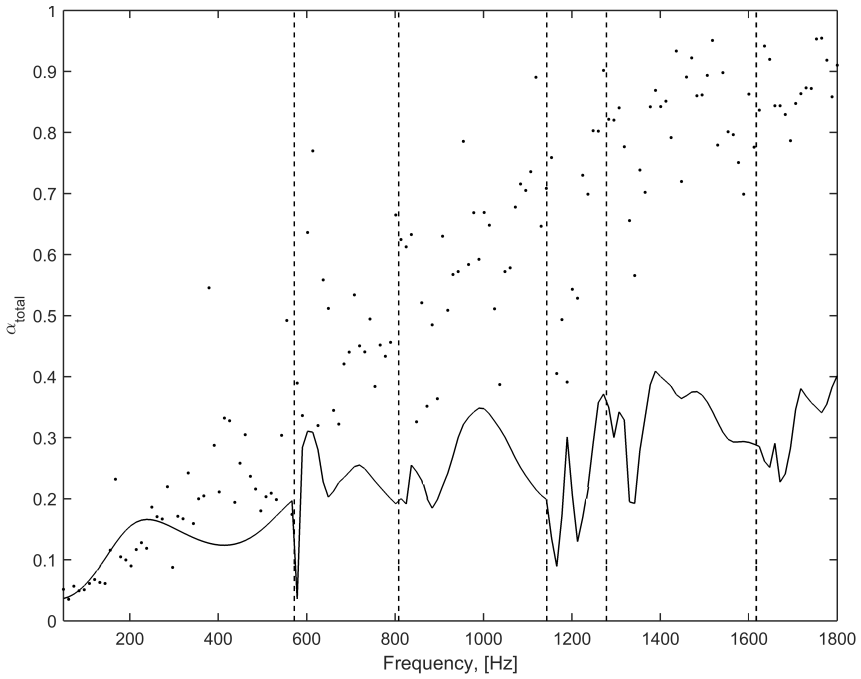


Figure 6.17: The measured and predicted total absorption coefficients for geranium plants calculated using the intensity method, measured in 300 mm wide square tube, with the microphone placed in the corner of the tube cross-section. Solid line: predictions; dots: experiments.

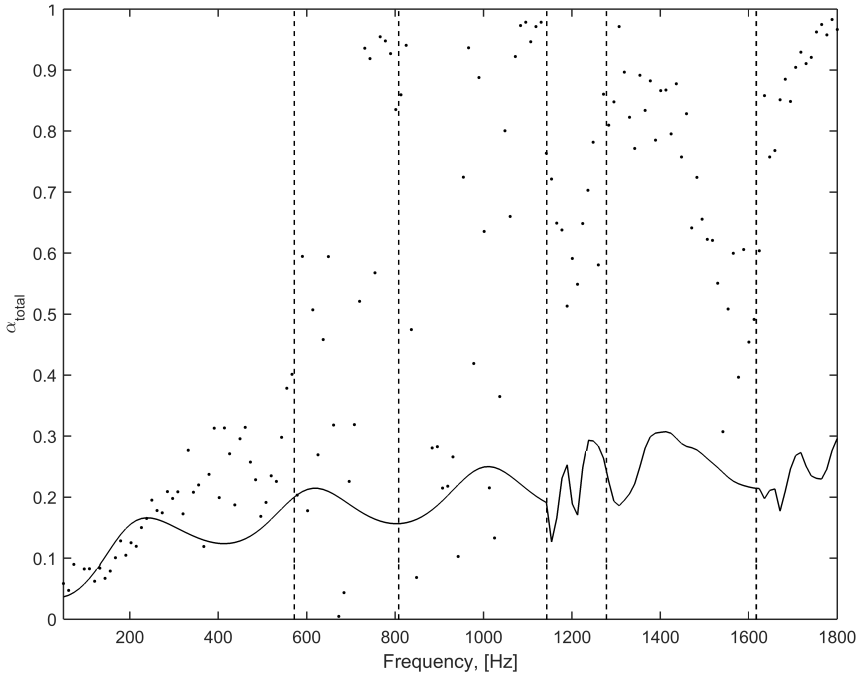


Figure 6.18: The measured and predicted total absorption coefficients for geranium plants calculated using the intensity method, measured in 300 mm wide square tube, with the microphone placed in the middle of the tube cross-section. Solid line: predictions; dots: experiments.

| | $\epsilon_{\alpha_{total}}$ |
|---|---|
| Amp method, corner (full $R_{theo}$) | 0.217 |
| Amp method, corner (partial $R_{theo}$) | 0.082 |
| Amp method, middle (full $R_{theo}$) | 0.144 |
| Amp method, middle (partial $R_{theo}$) | 0.007 |
| Int method, corner | 0.294 |
| Int method, middle | 0.314 |

Table 6.7: A summary of the mean differences between the measured and predicted total absorption coefficient for the geranium plant in the 300 mm square tube. Amp method: incident and reflected amplitudes ratio method; Int method: intensity ratio method.

remaining five plant specimens. It can be seen that for all tested plants the match between the measurements and predictions is close up to the first cut-on frequency. However, the graphs suggest that the model generally underpredicts the absorption by plants beyond this frequency and indicate a presence of a strong scattering in the tube. As in the case of the reflection coefficients, this discrepancy is caused by the fact that the theoretical model does not take into account the scattering and leaf vibration phenomena, which become stronger as the frequency increases. Also, it can be due to the method - the plants may cause too much scattering which results in the evanescent modes and energy exchange between modes, introducing an error to the phase. This affects the quality of the dispersion curves which are subsequently used in the optimisation analysis.

| Plant | $\epsilon_{\alpha_{total}}$ |
|---|---|
| Begonia | 0.240 |
| Ivy | 0.081 |
| Ficus | 0.157 |
| Rudbeckia | 0.223 |
| Kalanchoe | 0.244 |

Table 6.8: A summary of the mean differences between the measured and predicted total absorption coefficient for the five plant specimens in the 300 mm square tube.

For the experiments in the 150 mm wide square tube, the geranium, begonia, ivy, rudbeckia and kalanchoe plants were used. The ficus plants were not available at the moment of performng the experiments in the 150 mm square tube. The frequency-

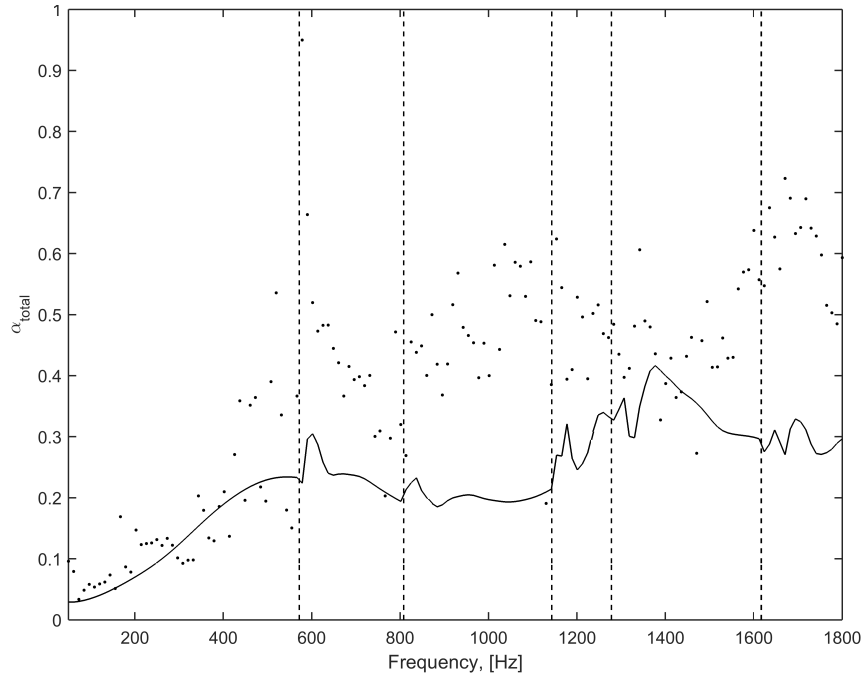


Figure 6.19: The measured and predicted total absorption coefficients for ficus plants measured in 300 mm wide square tube. Solid line: predictions; dots: experiments.

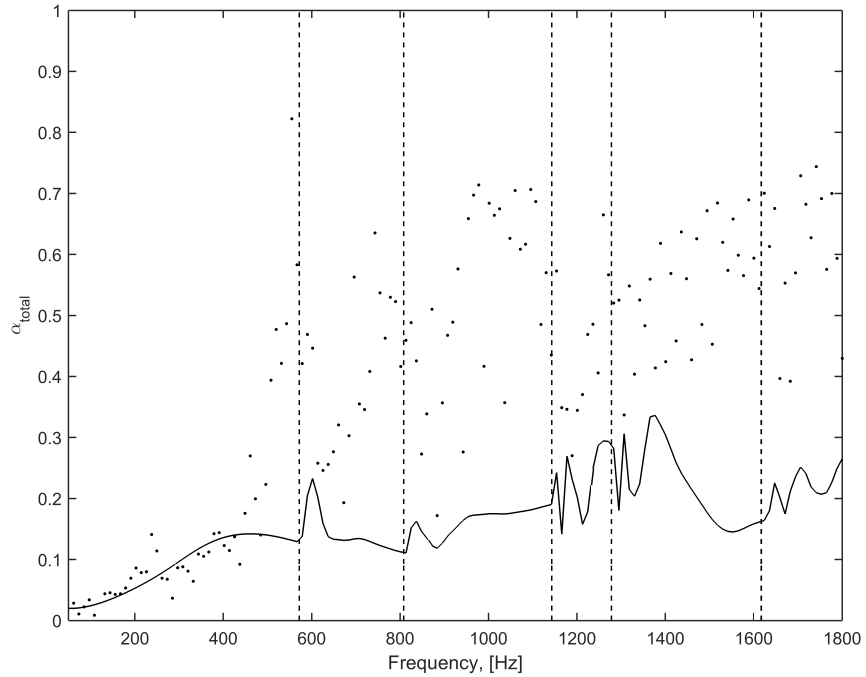


Figure 6.20: The measured and predicted total absorption coefficients for begonia plants measured in 300 mm wide square tube. Solid line: predictions; dots: experiments.

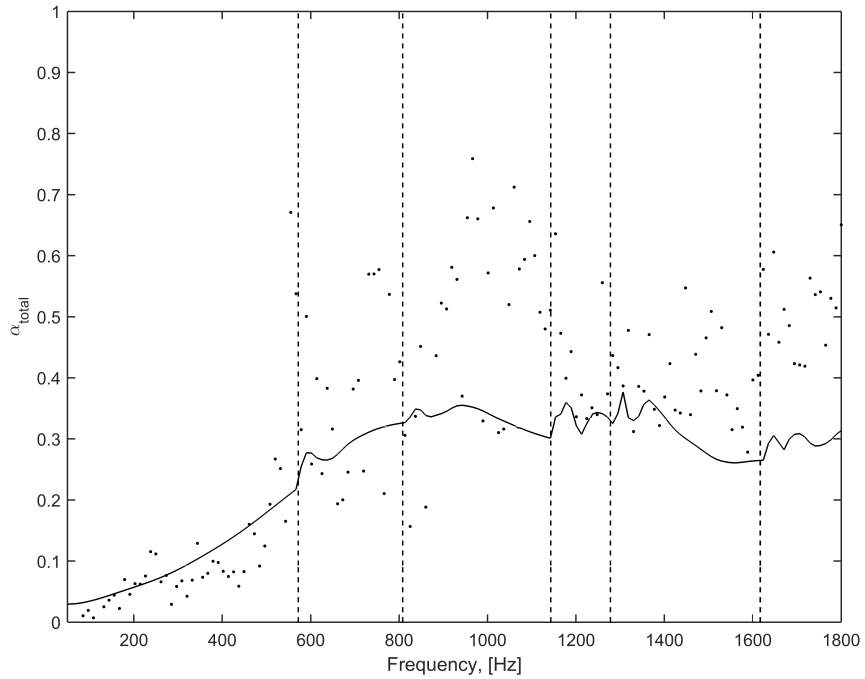


Figure 6.21: The measured and predicted total absorption coefficients for ivy plants measured in 300 mm wide square tube. Solid line: predictions; dots: experiments.

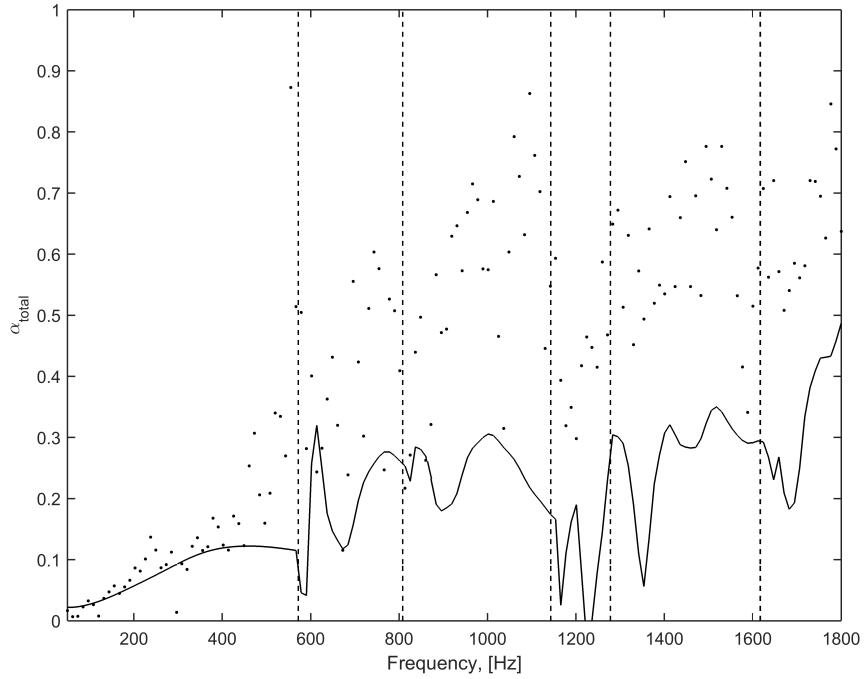


Figure 6.22: The measured and predicted total absorption coefficients for rudbeckia plants measured in 300 mm wide square tube. Solid line: predictions; dots: experiments.

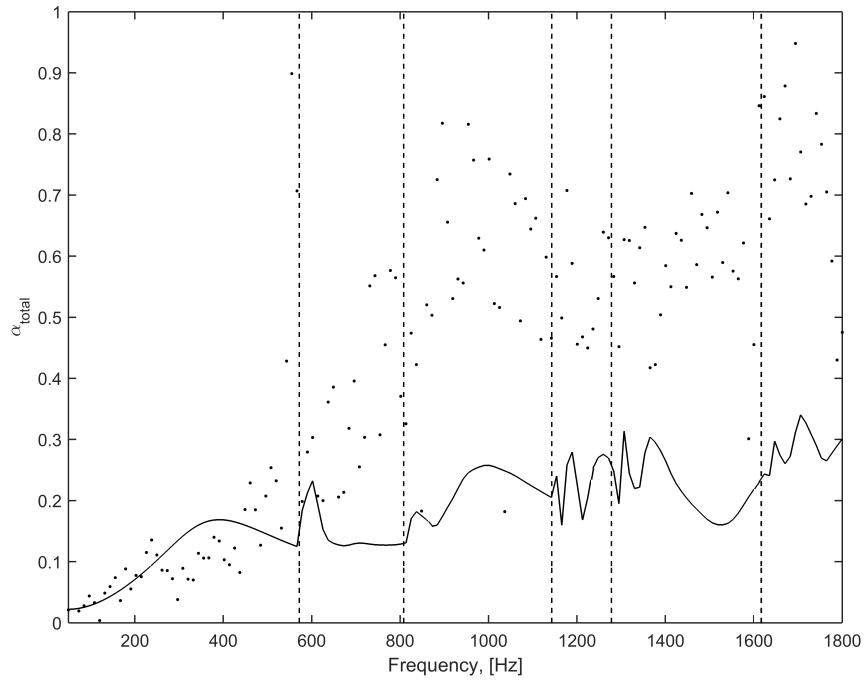


Figure 6.23: The measured and predicted total absorption coefficients for kalanchoe plants measured in 300 mm wide square tube. Solid line: predictions; dots: experiments.

wavenumber spectra for the geranium plants measured in the corner and in the middle of the tube cross-section are presented in Figures 6.24-6.25, respectively. The frequency range was extended up to 3500 Hz and the number of frequencies at which measurements were performed was doubled, but the spatial step was the same as in case of the 300 mm tube experiments, 40 mm. This resulted in dispersion curves covering relatively narrow frequency ranges compared to the whole adopted frequency range. In order to recover the modal reflection coefficients from the frequency-wavenumber plots for wider frequency ranges, the spatial step should be decreased. However, for the present work it was chosen to leave it equal to 40 mm as otherwise the measurements would be rather time consuming. Nevertheless, Figures 6.24-6.25 show a clear separation between the first several higher modes and can be used for the recovery of modal reflection coefficients.

Figures 6.26 and 6.27 show the predicted and measured absolute values of modal reflection coefficients for the geranium plant measured in 150 mm wide square tube in the

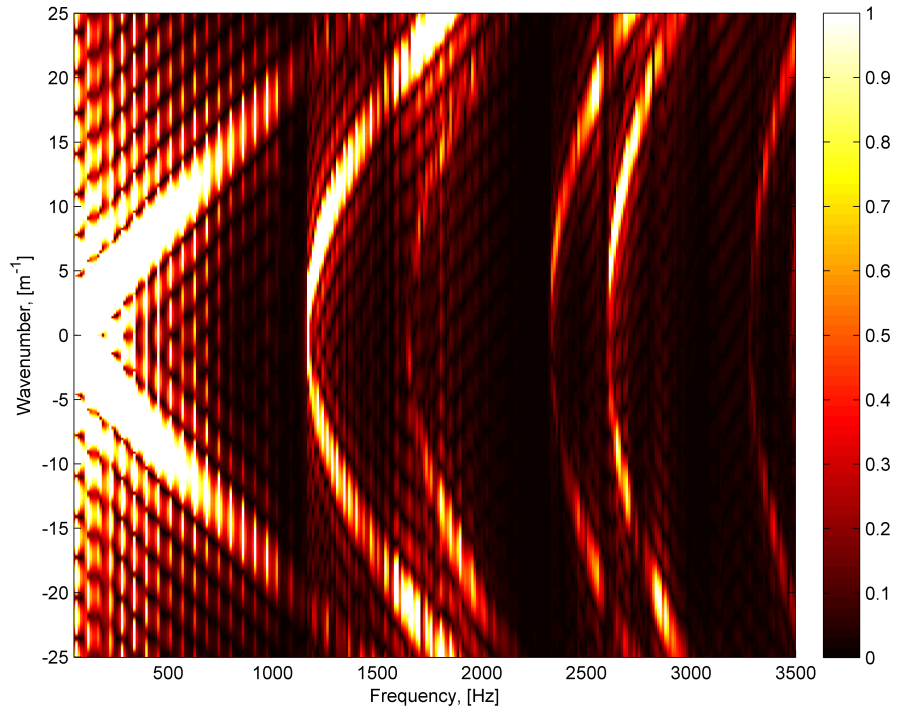


Figure 6.24: The frequency-wavenumber spectrum for geranium plants measured in 150 mm wide square tube, with the microphone placed in the corner of the tube cross-section.

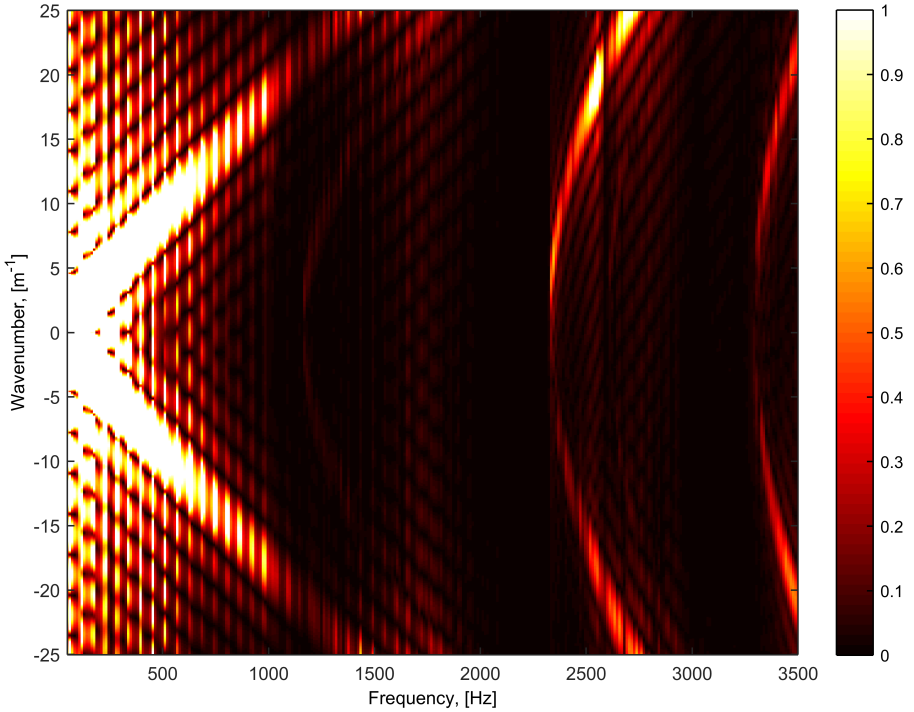


Figure 6.25: The frequency-wavenumber spectrum for geranium plants measured in 150 mm wide square tube, with the microphone placed in the middle of the tube cross-section.

corner and in the middle of the tube, respectively. As in the case of the 300 mm square tube, placing the microphone in the middle of the cross-section allowed to recover the plane wave reflection coefficient in a frequency range, the upper limit of which is twice the first cut-on frequency. The central cross-sectional positioning of the microphone also resulted in a better match between the predicted and experimental values for mode (00) (see Figure 6.26). For a majority of tested plants, the mean difference between the predictions and measurements is smaller in the case of the central microphone position. However, there is no improvement in the quality of the measured reflection coefficient data for mode (02), compared to the data collected in the corner of the cross-section. This may suggest that its quality does not depend on the microphone positioning and signal-to-noise ratio, nor it is caused by the optimisation procedure, but rather is beyond the scope of the method. A living plant is a complex material, with no exact data on its thickness and lacking a flat surface. Furthermore, scattering is present, and it is more pronounced at higher frequencies, when sound waves impinge at angles different from a straight angle. This complicates analysis in three ways. Firstly, the collection of stable and consistent data is compromised, as each frequency may be scattered at a different angle, because the sound energy in a given mode can be scattered in a plurality of directions, affecting the amount of energy which gets reflected back. Secondly, it influences the optimisation procedure, which is based on the modal decomposition that assumes that the normal modes are orthogonal and that there is no modal cross-talk, as assumed in Equations (5.1.2) and (5.1.5).

Figures 6.28-6.31 show the predicted and measured absolute values of modal reflection coefficients for the four plants measured in 150 mm wide square tube, recovered from the frequency-wavenumber spectra. The reflection coefficient for mode (00) was measured in the middle of the tube, whereas the reflection coefficients for modes (01), (11) and (02) were measured in the corner. It is clear from the graphs that the predicted and measured fundamental mode reflection coefficients exhibit a good match. This means that the proposed reflection and absorption coefficient recovery method works well for

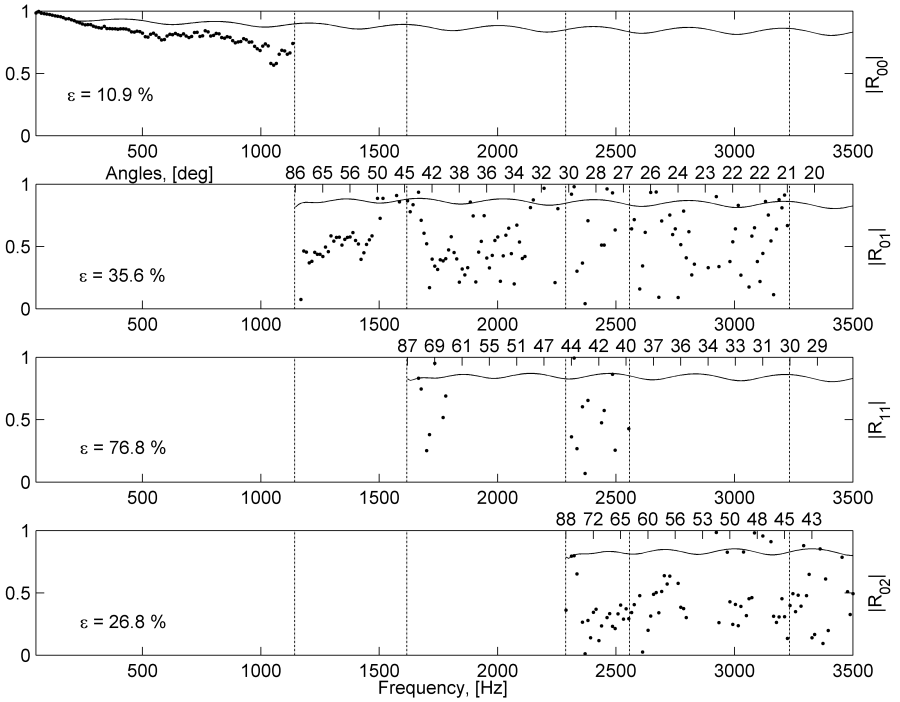


Figure 6.26: The measured and predicted modal reflection coefficients for geranium plants measured in 150 mm wide square tube, with the microphone placed in the corner of the tube cross-section. Solid line: predictions; dots: experiments.

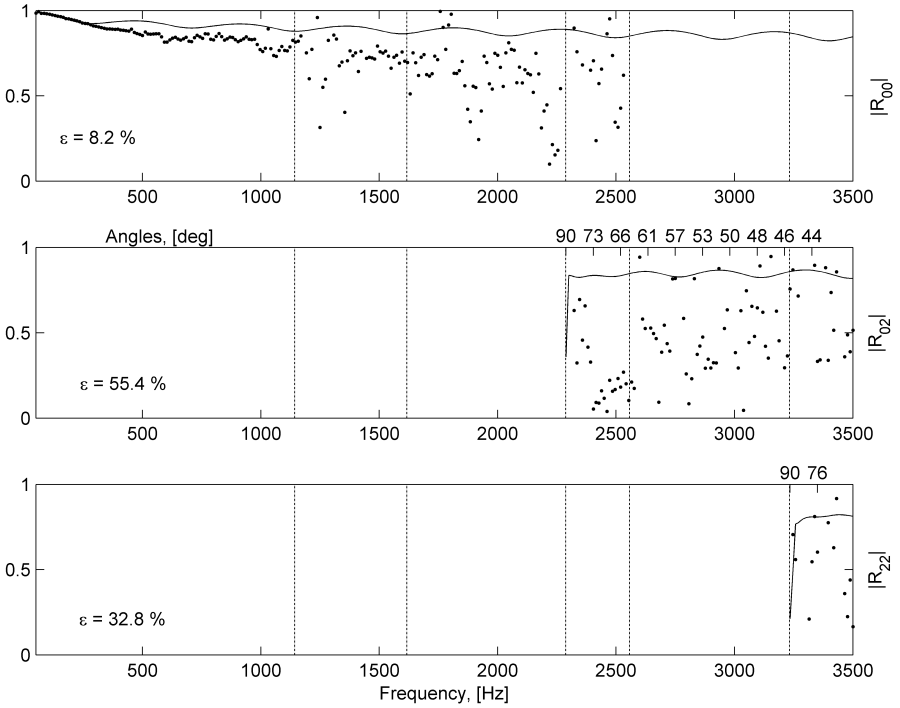


Figure 6.27: The measured and predicted modal reflection coefficients for geranium plants measured in 150 mm wide square tube, with the microphone placed in the middle of the tube cross-section. Solid line: predictions; dots: experiments.

tubes of different size. However, it is evident that for some modal reflection coefficients the match between the predictions and measurements is better than for others. There are a few possible causes to that. Firstly, the adopted loudspeaker positioning may have favoured the excitation of some modes compared to others. It can be observed in frequency-wavenumber plots shown in Figures 6.24-6.25, that some dispersion curves have much lower amplitude in comparison to others, e.g. mode (11). This leads to the amplitude of the mode being comparable to the level of background noise, which results in large errors. This phenomenon is clearly shown in Figures 6.26 and 6.28-6.31, where for every plant the reflection coefficient for mode (11) is highly scattered. Secondly, the residual absorption of the tube can influence the quality of the recorded data. It has been quantified and the first six partial absorption coefficients of the empty 150 mm tube are shown in Figure 5.25 in Section 5.2.3. The fundamental mode absorption coefficient stays rather low throughout the frequency range, slightly increasing in the vicinity of the first cut-on frequency, which results in a good quality of the recovered reflection coefficient for this mode for tested material and plants specimen. The partial absorption coefficient for mode (01) is generally low as well, with higher values at its cut-on frequency and beyond 2000 Hz. The partial absorption coefficients for the remaining four modes are relatively large and scattered, which places limitations on the quality of the recovered modal reflection coefficients for these modes. The other possible origin of the discrepancy between the predictions and measurements which is caused by the experimental setup may be the vibration of pipe walls. Finally, the theoretical model has previously only been used for predicting the behaviour of the fundamental mode and may not capture the complex behaviour of higher modes. Moreover, it may be challenging to estimate some morphological parameters of plants precisely, such as a plant layer thickness, as it is not clear which point should be regarded as the end of the layer. Also, although every precaution was taken to ensure that the measured plant parameters (leaf size, thickness, angle of orientation, etc) are representative for the whole tested group of plant specimens, it is possible that there are some discrepancies, which may

influence the recovered results.

| Plant | $\epsilon_{\|R_{00}\|}$ | $\epsilon_{\|R_{01}\|}$ | $\epsilon_{\|R_{11}\|}$ | $\epsilon_{\|R_{02}\|}$ |
|---|---|---|---|---|
| Geranium | 0.051 | 0.223 | 0.289 | 0.091 |
| Begonia | 0.014 | 0.092 | 0.563 | 0.071 |
| Ivy | 0.008 | 0.115 | 0.203 | 0.158 |
| Rudbeckia | 0.013 | 0.090 | 0.292 | 0.018 |
| Kalanchoe | 0.062 | 0.185 | 0.233 | 0.138 |

Table 6.9: The mean difference between the absolute values of the measured and predicted modal reflection coefficients for the first four modes for the 150 mm tube.

Figures 6.32-6.35 show the measured and predicted total absorption coefficients for the geranium plant specimen for the 150 mm square tube. Figures 6.32 and 6.33 present the data obtained using the incident and reflected amplitude ratio method for the corner and middle cross-sectional positions, respectively. Figures 6.34 and 6.35 show the corner and middle data obtained using the intensity ratio method. As it was discussed in the case of the 300 mm square tube, the intensity ratio method is preferred to the incident and reflected amplitude ratio method and will be used to estimate the acoustical properties of the remaining plants. Also, the average value of the total absorption coefficients measured in the corner and in the middle will be presented for the four remaining plant specimens.

| | $\epsilon_{\alpha_{total}}$ |
|---|---|
| Amp method, corner (full $R_{theo}$) | 0.854 |
| Amp method, corner (partial $R_{theo}$) | 1.123 |
| Amp method, middle (full $R_{theo}$) | 16.743 |
| Amp method, middle (partial $R_{theo}$) | 16.280 |
| Int method, corner | 0.269 |
| Int method, middle | 0.360 |

Table 6.10: A summary of the mean differences between the measured and predicted total absorption coefficient for the geranium plant in the 150 mm square tube. Amp method: incident and reflected amplitudes ratio method; Int method: intensity ratio method.

In the case of the total plant absorption coefficient, the agreement between the theory and experiments for the 1500 mm square tube is not as good as that for the 300 mm

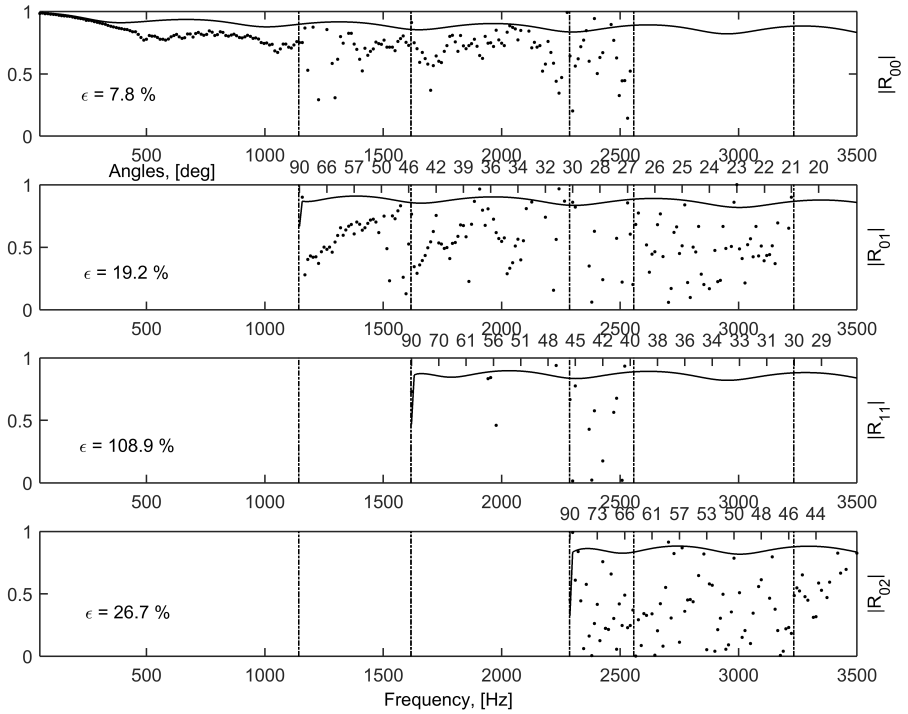


Figure 6.28: The measured and predicted modal reflection coefficients for begonia plants measured in 150 mm wide square tube. Solid line: predictions; dots: experiments.

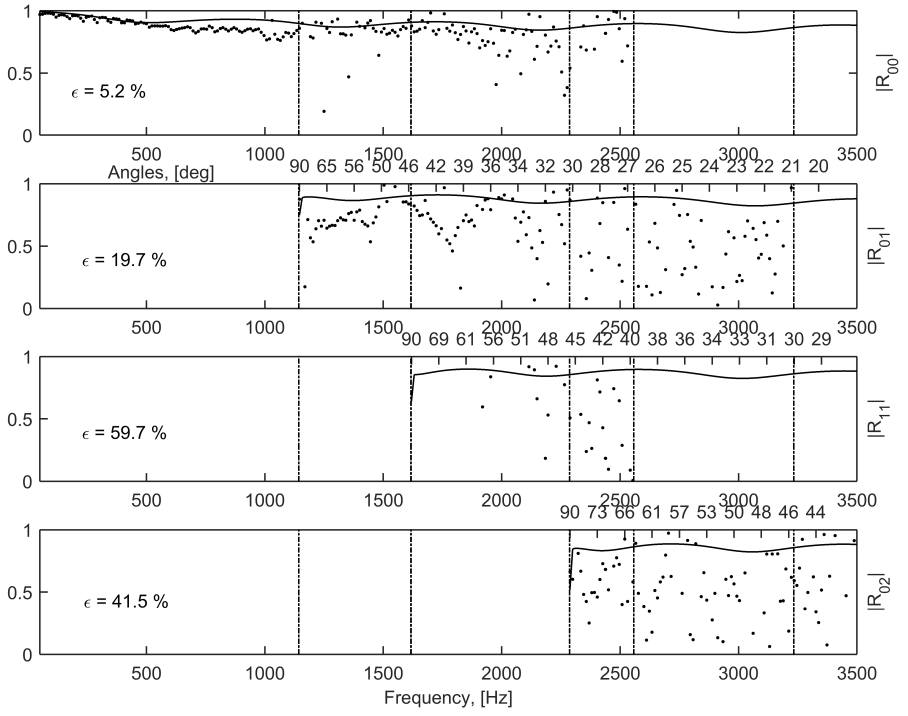


Figure 6.29: The measured and predicted modal reflection coefficients for ivy plant measured in 150 mm wide square tube. Solid line: predictions; dots: experiments.

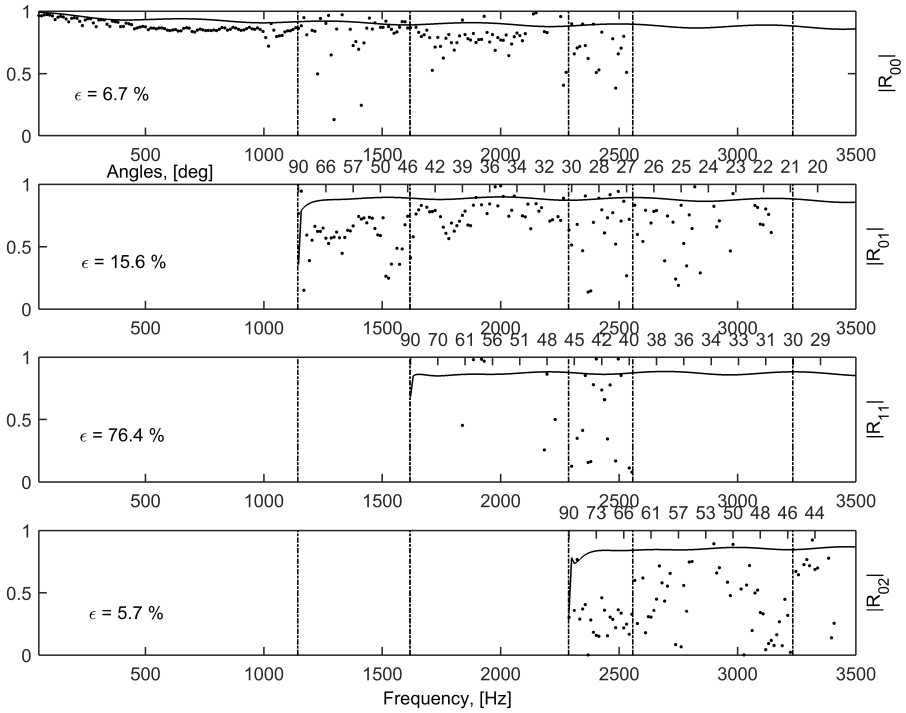


Figure 6.30: The measured and predicted modal reflection coefficients for rudbeckia plants measured in 150 mm wide square tube. Solid line: predictions; dots: experiments.

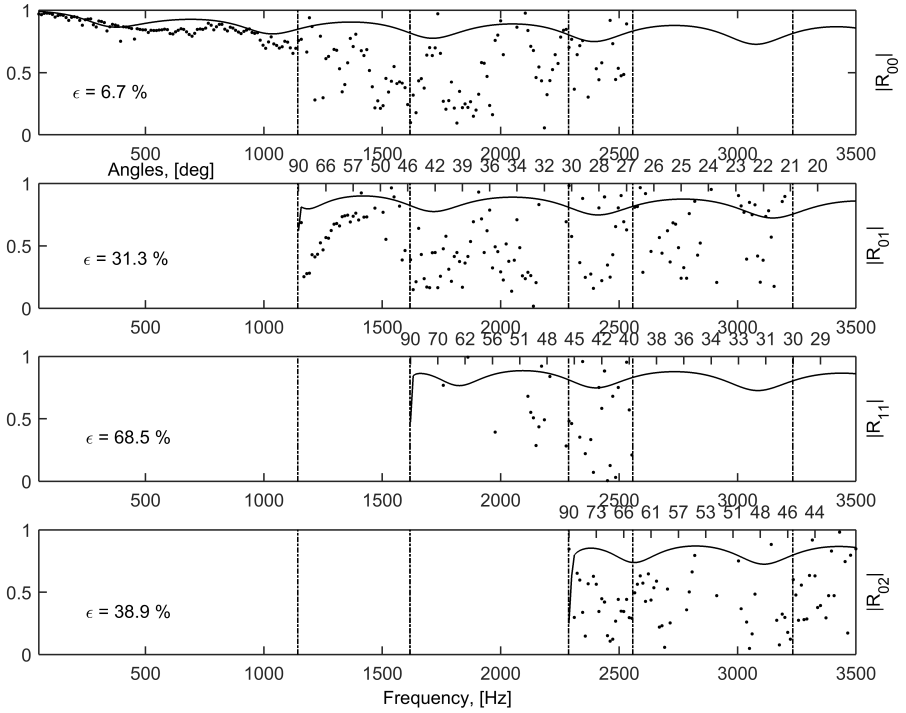


Figure 6.31: The measured and predicted modal reflection coefficients for kalanchoe plant measured in 150 mm wide square tube. Solid line: predictions; dots: experiments.

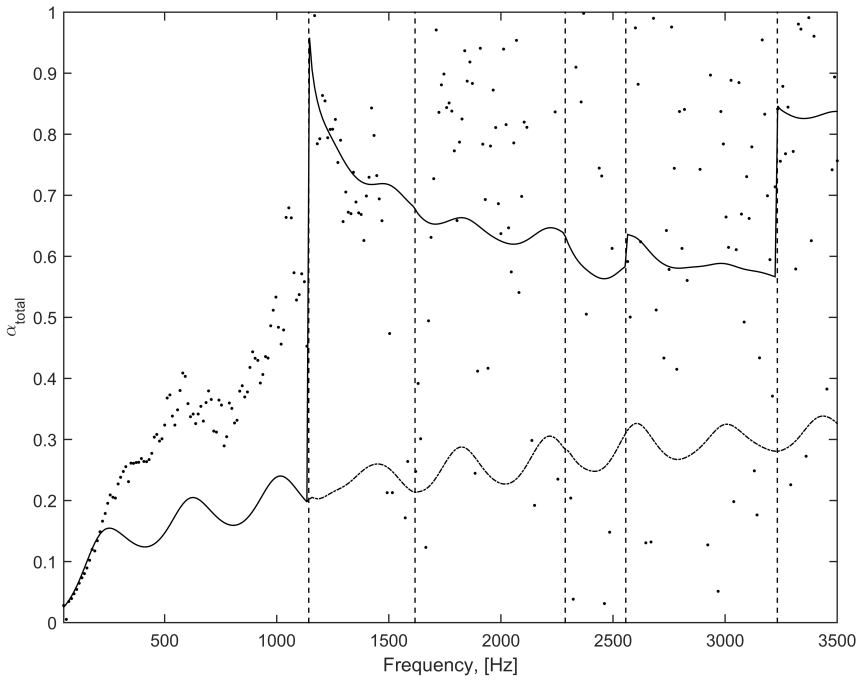


Figure 6.32: The measured and predicted total absorption coefficients for geranium plants calculated using the amplitude method, measured in 150 mm wide square tube, with the microphone placed in the corner of the tube cross-section. Solid line: predictions; dots: experiments.

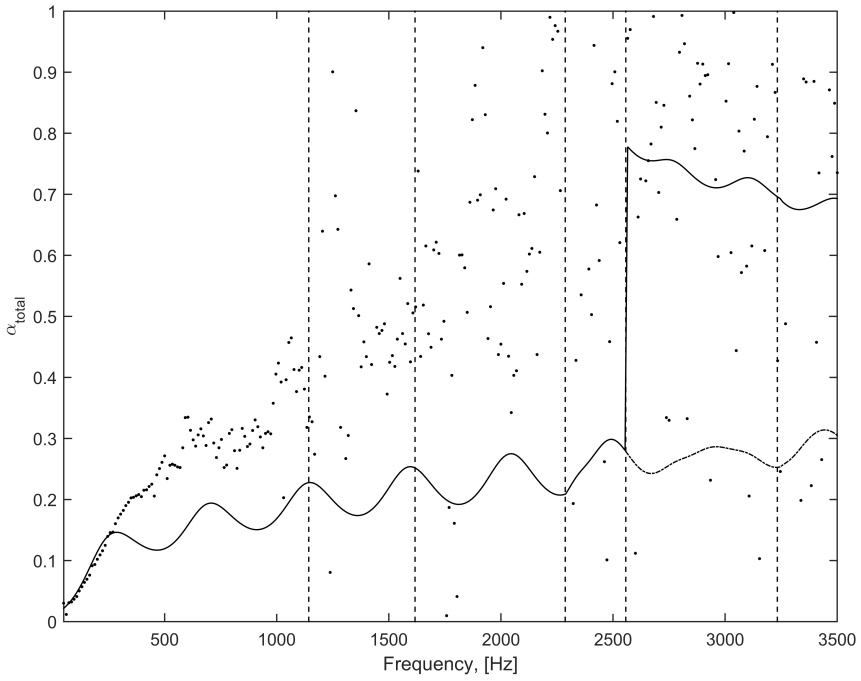


Figure 6.33: The measured and predicted total absorption coefficients for geranium plants calculated using the amplitude method, measured in 150 mm wide square tube, with the microphone placed in the middle of the tube cross-section. Solid line: predictions; dots: experiments.

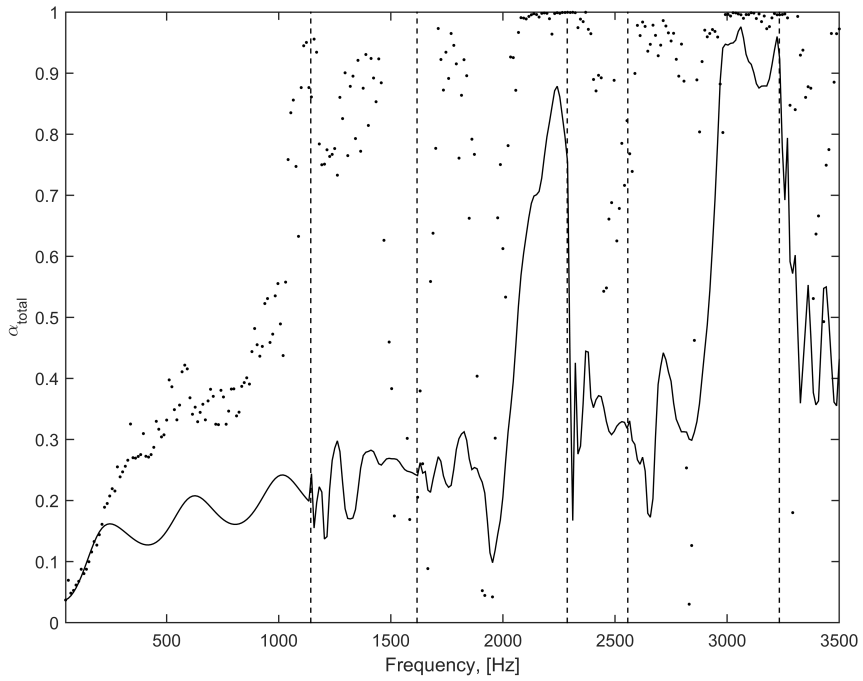


Figure 6.34: The measured and predicted total absorption coefficients for geranium plants calculated using the intensity method, measured in 150 mm wide square tube, with the microphone placed in the corner of the tube cross-section. Solid line: predictions; dots: experiments.

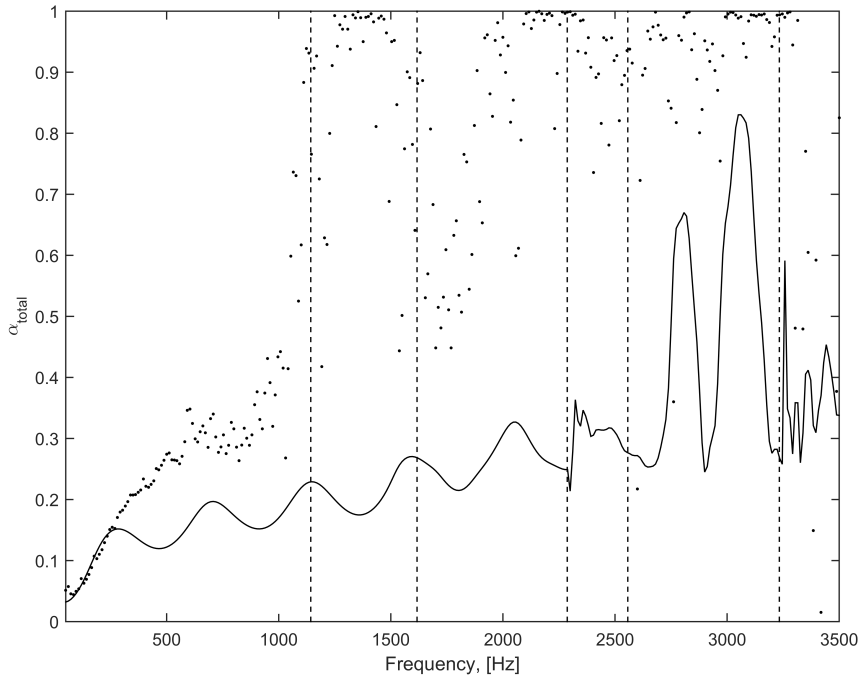


Figure 6.35: The measured and predicted total absorption coefficients for geranium plants calculated using the intensity method, measured in 150 mm wide square tube, with the microphone placed in the middle of the tube cross-section. Solid line: predictions; dots: experiments.

square tube. The predictions match the experimental data in the plane wave frequency range. However, the model constantly underpredicts the absorption beyond the first cut-on frequency. In addition, the measured values are highly scattered, which may be caused by the same factors as the lack of the agreement for the modal reflection coefficients. As the total absorption coefficient for all the tested plants exhibited a very similar behaviour, it was decided to present the plots only for the geranium plant and not to include the plots for the remaining tested plants. The mean difference values between the measured and predicted total absorption coefficients for the remaining plants are shown in Table 6.11.

| Plant | $\epsilon_{\alpha_{total}}$ |
|---|---|
| Begonia | 0.420 |
| Ivy | 0.377 |
| Rudbeckia | 0.268 |
| Kalanchoe | 0.322 |

Table 6.11: A summary of the mean differences between the measured and predicted total absorption coefficient for the five plant specimens in the 150 mm square tube.

## 6.5 Summary

This chapter describes the measurements of the reflection and absorption coefficients of living plants in an impedance tube, using the method outlined in Chapter 5. The particularities of the plant selection process are explained in the light of their sound-absorbing properties, and the link between these properties and the key morphological parameters of plants is established (Horoshenkov, 2013). Six plant species have been chosen for the subsequent experiments: *Pelargonium hortorum*, *Ficus benjamina*, *Hedera helix*, *Begonia benariensis*, *Rudbeckia hirta* and *Kalanchoe blossfeldiana*, and these have been tested in two square impedance tubes, 300 mm and 150 mm wide.

The observed agreement between the measurements and predictions in the plane wave

regime is relatively good for the 300 mm square tube, but is weaker for 150 mm square tube. In the case of the 300 mm square tube, the mean differences between the measured and predicted modal reflection coefficients are less than 10%, and for the total absorption coefficients - less than 25%. The agreement is weaker for the 150 mm square tube - the mean differences between the predicted and measured modal reflection coefficients are generally below 30%, and these for the total absorption coefficient are below 42%. This can be attributed to the higher residual absorption of the latter tube. The agreement between the measurements and predictions becomes worse beyond the fist cut-on frequency. Hence it is clear that the success of the proposed method is limited. The method can be useful provided some important improvements are applied to it, but in its current state it is relatively raw. It can benefit from better tube facilities with harder walls, where their residual absorption and vibration are lower. Alternatively, the wall vibration may be accounted for in the model, but this will significantly complicate it. Also, the experimental procedure may be improved by taking measurements over a longer distance in the tube and in smaller steps. Furthermore, the theoretical model may be improved to accommodate for all peculiarities of behaviour of living plants at higher frequencies. Currently, the model does not take into account the scattering processes which become more pronounced in living plants as the frequency increases. However, it is clear from the obtained results that these processed cannot be neglected in order to achieve a better match between the measured and predicted data. Nevertheless, the performed study, outlined in this chapter, confirms that plants do contribute to the sound absorption and thus can be successfully used as a means of noise reduction. In addition, it has been shown that plants can be characterised as porous media in a plane wave regime. With several modifications to the method, this can be extended into higher frequency regime as well.

The next chapter will focus on the errors, which could have been induced by any imperfections in the experimental setups, such as imprecise microphone positioning, influence of windowing and effect of a loudspeaker location.

# Chapter 7

# Sensitivity analysis

In order to estimate what influence the measurement errors may have on the measured modal reflection coefficients, a sensitivity analysis was carried out. Firstly, several types of error were artificially introduced to examine to which extent they influence the recovered modal reflection coefficients. Three materials with different sound-absorbing abilities were examined: (1) melamine foam, (2) Armasound foam, (3) geranium plants. The analysis was performed for three different impedance tubes, to determine whether any of them was more susceptible to measurement errors. Furthermore, for the 150 mm circular tube the experimental data were available to determine sensitivity to such factors as the microphone step length, the length of the spatial window and the spatial window shape. Finally, for the 300 mm square tube experiments were performed engaging only one of the three loudspeakers at a time, to study how it affects the excitation of different modes in the tube.

## 7.1 Sensitivity to simulated error

The Johnson-Champoux-Allard equivalent fluid model (Champoux and Allard, 1991) was used to predict the modal reflection coefficients for melamine and Armasound foam samples, whereas the Miki model (Miki, 1990) was used for a geranium plant layer. The characteristics of the samples, such as thickness, porosity, flow resistivity and tortuosity, were assumed to be equal to those of the actual samples used for the predictions described in the previous chapters. The predicted reflection coefficients were then substituted in the equation for the frequency spectrum of the sound pressure (see Equation (5.1.2)) in which measurement errors, $e(\omega)$ were artificially added, i.e. $p_e(z,\omega) = p(z,\omega) + e(\omega)$. The simulated sound pressure with errors, $p_e(z,\omega)$, was then used to calculate the spatial Fourier transform $\tilde{p}_e(K,\omega)$ in accordance with Equation (5.1.1). The simulated spatial spectra, $\tilde{p}_e(K,\omega)$, were used in the optimization analysis (see Equation (5.1.8)) instead of the measured sound pressure, $\tilde{p}_m(K,\omega)$, to study how the artificially added errors affect the ability of the proposed measurement affect the values of the modal reflection coefficients, $R_{mn}$.

Three types of error were considered in this analysis: (i) a random error to the sound pressure phase spectrum within 20%; (ii) a random ±10 mm positioning error applied separately to the sound pressure at each of the microphone positions; and (iii) a constant 10 mm bias in positioning applied to the whole microphone array. These errors were chosen as rough estimates of measured errors. A microphone phase mismatch error can reach ±5%, which results in a total error of 10%. A factor of 2 was applied to this number to study the worst-case scenario. For the random positioning error, it was noticed that the final microphone axial position can be as far as 0.5 m off the expected position (measurements in the 150 mm circular tube), i.e. 3.5 m instead of 3 m. These discrepancies were accounted for in the data analysis by using a variable step Fourier transform, however, it showed that each axial microphone position can be off by at least 1 mm. This error was also multiplied by 10 to account for a possible human error

while moving the microphone manually. This was also the reason for choosing the constant bias equal to 10 mm. The thickness of the cable, which was pulled to move the microphone in the pipe was of the same order of magnitude, so it is possible for it to cause errors in microphone positioning as large as 10 mm.

The mean difference between the modal reflection coefficient computed exactly for the 52 microphone positions as assumed in Section 5.2.1 and the simulated one containing the added error was then determined. This difference was quantified for the real and imaginary parts of the reflection coefficient according to the following expressions:

$$\epsilon_{Re} = \frac{1}{N}\sum_{i=1}^{N} |\mathrm{Re}(R_{mn}^{pred}(\omega_i)) - \mathrm{Re}(R_{mn}^{sim}(\omega_i))|, \quad \epsilon_{Im} = \frac{1}{N}\sum_{i=1}^{N} |\mathrm{Im}(R_{mn}^{pred}(\omega_i)) - \mathrm{Im}(R_{mn}^{sim}(\omega_i))|, \tag{7.1.1}$$

where $R_{mn}^{pred}$ is the frequency-dependent reflection coefficient calculated exactly, and $R_{mn}^{sim}$ is the frequency-dependent reflection coefficient with simulated error.

### 7.1.1 300 mm square tube

The results suggest that the ±20 % uncertainty in the measured phase results in the 0.0280 maximum difference between the exact value of the modal reflection coefficient and its simulated counterpart for melamine foam, which is approximately 2.5 times less than the measured error value. For the same type of uncertainty for Armasound foam, the maximum mean difference is 0.1695, being 1.1 times larger than its measured counterpart, and 0.1084 for geranium plants, which is also 2.5 times less than the measured value. A 10 mm misalignment in any of the 52 the microphone positions results in the maximum difference of 0.0268 for melamine foam, being approximately 5 times less that the measured mean difference, 0.1716 for Armasound foam and 0.1073 for geranium plants, resulting in 1.1 times more and 2.5 times less than their measured counterparts, respectively. The constant axial bias introduced to the microphone array as a whole results in the maximum difference of 0.0382 for melamine foam, which is

half as much as the measured result, 0.1615 for Armasound foam, again 1.1 times larger than the measured value, and 0.1087 for geranium plants, 3 times less than its measured counterpart. The complete summary of the mean differences is presented in Tables 7.1 - 7.3.

After comparing the mean difference between the predictions and the simulated data and between the predictions and the measured data, it becomes evident that the simulated mean difference is consistently smaller than the measured for melamine and geranium specimen, but is of comparable magnitude for Armasound foam. This may be explained by the fact that Armasound foam is manufactured from recycled materials, which causes variability in the foam structure. The heterogeneous structure of the foam leads to a higher level of unpredictability of material behaviour (Horoshenkov et al., 2007). Moreover, Armasound is a medium-absorbing material, as opposed to highly absorbing melamine foam and low absorbing geranium plants. The reflection coefficients for materials with either high or low absorbing properties (as two latter examples) tend to converge better than those for materials with medium absorbing properties, like Armasound, which is more sensitive to errors either in the experimental procedure or data processing, and hence exhibit weaker convergence.

However, these differences are not enough to explain the observed mismatch between the predicted modal reflection coefficients and the measured data. The measured reflection coefficient seems to exhibit a greater sensitivity to other factors which may influence the accuracy of the collected data. One of such factors may be the residual absorption of the impedance tube (see Figure 5.8). Although the empty tube absorption is relatively small in comparison to melamine foam and on average does not exceed 15%, there are certain frequencies at which the residual absorption is relatively high and can be of the same magnitude as the material's absorption. This places a restriction on the accuracy of the absorption coefficient data which can be measured with the proposed method in this particular impedance tube.

| | | Exp. data MD | Sim. data MD | | $R_{mn}$, predicted | $R_{mn}$, measured |
|---|---|---|---|---|---|---|
| | | | *Phase error 5%* | *Phase error 20%* | | |
| Melamine | Re ($R_{00}$) | 0.0696 | 0.0007 | 0.0013 | 0.4329 | 0.3805 |
| | Im ($R_{00}$) | 0.0486 | 0.0007 | 0.0012 | 0.4307 | 0.4408 |
| | Re ($R_{01}$) | 0.0661 | 0.0264 | 0.0261 | -0.0289 | -0.0428 |
| | Im ($R_{01}$) | 0.0736 | 0.0273 | 0.0280 | 0.1038 | 0.0751 |
| | Re ($R_{11}$) | 0.0998 | 0.0259 | 0.0260 | -0.1981 | -0.0287 |
| | Im ($R_{11}$) | 0.0770 | 0.0251 | 0.0253 | 0.0781 | 0.0305 |
| | Re ($R_{02}$) | 0.0711 | 0.0218 | 0.0221 | -0.1350 | -0.0879 |
| | Im ($R_{02}$) | 0.0630 | 0.0182 | 0.0178 | 0.0137 | 0.0396 |
| Armasound | Re ($R_{00}$) | 0.0752 | 0.0914 | 0.0914 | 0.8338 | 0.7832 |
| | Im ($R_{00}$) | 0.0567 | 0.0661 | 0.0662 | 0.2455 | 0.3239 |
| | Re ($R_{01}$) | 0.1943 | 0.1084 | 0.1086 | 0.4252 | 0.3154 |
| | Im ($R_{01}$) | 0.1355 | 0.1705 | 0.1695 | 0.1448 | 0.2448 |
| | Re ($R_{11}$) | 0.1818 | 0.1539 | 0.1535 | 0.2554 | 0.0991 |
| | Im ($R_{11}$) | 0.0766 | 0.0919 | 0.0911 | 0.1277 | 0.1605 |
| | Re ($R_{02}$) | 0.1597 | 0.0822 | 0.0823 | 0.3361 | 0.1868 |
| | Im ($R_{02}$) | 0.2014 | 0.1467 | 0.1452 | 0.0874 | 0.2413 |
| Geranium | Abs ($R_{00}$) | 0.0090 | 0.0005 | 0.0010 | 0.9354 | 0.9298 |
| | Abs ($R_{01}$) | 0.0881 | 0.0651 | 0.0647 | 0.8871 | 0.7389 |
| | Abs ($R_{11}$) | 0.0427 | 0.0956 | 0.0961 | 0.8875 | 0.7274 |
| | Abs ($R_{02}$) | 0.0779 | 0.1084 | 0.1089 | 0.8693 | 0.6599 |

Table 7.1: A summary of the mean differences (MD) between the predictions and measurement (second column) and simulations (third and fourth column) for the 300 mm square tube, where a random phase error was introduced.

| | | Exp. data | Sim. data | | | $R_{mn}$, pred. | $R_{mn}$, meas. |
|---|---|---|---|---|---|---|---|
| | | | *XY, 5 mm tol.* | *Z, 1 mm tol.* | *Z, 10 mm tol.* | | |
| Melamine | Re ($R_{00}$) | 0.0696 | 0.0006 | 0.0005 | 0.0011 | 0.4329 | 0.3805 |
| | Im ($R_{00}$) | 0.0486 | 0.0006 | 0.0006 | 0.0009 | 0.4307 | 0.4408 |
| | Re ($R_{01}$) | 0.0661 | 0.0264 | 0.0263 | 0.0268 | -0.0289 | -0.0428 |
| | Im ($R_{01}$) | 0.0736 | 0.0273 | 0.0276 | 0.0251 | 0.1038 | 0.0751 |
| | Re ($R_{11}$) | 0.0998 | 0.0259 | 0.0257 | 0.0245 | -0.1981 | -0.0287 |
| | Im ($R_{11}$) | 0.0770 | 0.0251 | 0.0251 | 0.0225 | 0.0781 | 0.0305 |
| | Re ($R_{02}$) | 0.0711 | 0.0219 | 0.0218 | 0.0219 | -0.1350 | -0.0879 |
| | Im ($R_{02}$) | 0.0630 | 0.0184 | 0.0184 | 0.0179 | 0.0137 | 0.0396 |
| Armasound | Re ($R_{00}$) | 0.0752 | 0.0915 | 0.0915 | 0.0917 | 0.8338 | 0.7832 |
| | Im ($R_{00}$) | 0.0567 | 0.0662 | 0.0662 | 0.0662 | 0.2455 | 0.3239 |
| | Re ($R_{01}$) | 0.1943 | 0.1083 | 0.1079 | 0.1075 | 0.4252 | 0.3154 |
| | Im ($R_{01}$) | 0.1355 | 0.1711 | 0.1704 | 0.1716 | 0.1448 | 0.2448 |
| | Re ($R_{11}$) | 0.1818 | 0.1533 | 0.1543 | 0.1527 | 0.2554 | 0.0991 |
| | Im ($R_{11}$) | 0.0766 | 0.0912 | 0.0915 | 0.0926 | 0.1277 | 0.1605 |
| | Re ($R_{02}$) | 0.1597 | 0.0824 | 0.0826 | 0.0828 | 0.3361 | 0.1868 |
| | Im ($R_{02}$) | 0.2014 | 0.1463 | 0.1457 | 0.1491 | 0.0874 | 0.2413 |
| Geranium | Abs ($R_{00}$) | 0.0090 | 0.0004 | 0.0004 | 0.0004 | 0.9354 | 0.9298 |
| | Abs ($R_{01}$) | 0.0881 | 0.0651 | 0.0652 | 0.0666 | 0.8871 | 0.7389 |
| | Abs ($R_{11}$) | 0.0427 | 0.0960 | 0.0958 | 0.0932 | 0.8875 | 0.7274 |
| | Abs ($R_{02}$) | 0.0779 | 0.1085 | 0.1084 | 0.1073 | 0.8693 | 0.6599 |

Table 7.2: A summary of the mean differences between the predictions and measurement (second column) and simulations (third, fourth and fifth column) for the 300 mm square tube, where a random positioning error was introduced. *XY* denotes the error introduced to the cross-sectional coordinates, and *Z* denotes the error in the axial coordinate.

| | | Exp. data | Sim. data | | | $R_{mn}$, pred. | $R_{mn}$, meas. |
|---|---|---|---|---|---|---|---|
| | | | *XY* *5 mm bias + 5 mm tol.* | *Z* *10 mm bias + 0 mm tol.* | *Z* *10 mm bias + 10 mm tol.* | | |
| Melamine | Re ($R_{00}$) | 0.0696 | 0.0006 | 0.0035 | 0.0043 | 0.4329 | 0.3805 |
| | Im ($R_{00}$) | 0.0486 | 0.0006 | 0.0022 | 0.0026 | 0.4307 | 0.4408 |
| | Re ($R_{01}$) | 0.0661 | 0.0266 | 0.0289 | 0.0309 | -0.0289 | -0.0428 |
| | Im ($R_{01}$) | 0.0736 | 0.0274 | 0.0196 | 0.0201 | 0.1038 | 0.0751 |
| | Re ($R_{11}$) | 0.0998 | 0.0261 | 0.0365 | 0.0383 | -0.1981 | -0.0287 |
| | Im ($R_{11}$) | 0.0770 | 0.0252 | 0.0226 | 0.0224 | 0.0781 | 0.0305 |
| | Re ($R_{02}$) | 0.0711 | 0.0221 | 0.0299 | 0.0322 | -0.1350 | -0.0879 |
| | Im ($R_{02}$) | 0.0630 | 0.0185 | 0.0186 | 0.0195 | 0.0137 | 0.0396 |
| Armasound | Re ($R_{00}$) | 0.0752 | 0.0915 | 0.0932 | 0.0931 | 0.8338 | 0.7832 |
| | Im ($R_{00}$) | 0.0567 | 0.0662 | 0.0661 | 0.0662 | 0.2455 | 0.3239 |
| | Re ($R_{01}$) | 0.1943 | 0.1078 | 0.0971 | 0.0983 | 0.4252 | 0.3154 |
| | Im ($R_{01}$) | 0.1355 | 0.1711 | 0.1606 | 0.1615 | 0.1448 | 0.2448 |
| | Re ($R_{11}$) | 0.1818 | 0.1540 | 0.1439 | 0.1421 | 0.2554 | 0.0991 |
| | Im ($R_{11}$) | 0.0766 | 0.0919 | 0.0978 | 0.0985 | 0.1277 | 0.1605 |
| | Re ($R_{02}$) | 0.1597 | 0.0812 | 0.0747 | 0.0752 | 0.3361 | 0.1868 |
| | Im ($R_{02}$) | 0.2014 | 0.1454 | 0.1469 | 0.1472 | 0.0874 | 0.2413 |
| Geranium | Abs ($R_{00}$) | 0.0090 | 0.0004 | 0.0003 | 0.0004 | 0.9354 | 0.9298 |
| | Abs ($R_{01}$) | 0.0881 | 0.0651 | 0.0686 | 0.0676 | 0.8871 | 0.7389 |
| | Abs ($R_{11}$) | 0.0427 | 0.0969 | 0.1082 | 0.1087 | 0.8875 | 0.7274 |
| | Abs ($R_{02}$) | 0.0779 | 0.1088 | 0.1052 | 0.1035 | 0.8693 | 0.6599 |

Table 7.3: A summary of the mean differences between the predictions and measurement (second column) and simulations (third, fourth and fifth column) for the 300 mm square tube, where a constant positioning bias and random positioning error was introduced. *XY* denotes the error introduced to the cross-sectional coordinates, and *Z* denotes the error in the axial coordinate.

### 7.1.2 150 mm square tube

For the 150 mm square tube, the experimental data were available for Armasound foam and geranium, but measurements of a melamine foam layer were not performed, hence they are omitted from the sensitivity analysis. Furthermore, as the absolute values of the measured modal reflection coefficients were presented for geranium rather than the real and imaginary values, the sensitivity analysis for this specimen has been consistent with that and offers also the absolute values only.

When the ±20 % uncertainty in the measured phase results was introduced, the mean difference between the simulated results with the uncertainty and the predicted results did not exceed 28% (see Table 7.4). However, the maximum mean difference between the experimentally obtained and measured results was 87 % for mode (11), which is about 3.5 times than that observed in the simulated data. For geranium specimen, the simulated and experimentally observed mean difference differ by about a factor of 2. When a random uncertainty was introduced in the cross-sectional or axial position of the microphone, the simulated and measured mean differences were similar except for mode (11), for which the mean difference was 70-80 % for the both materials (Table 7.5). The same situation was observed in the case of the constant microphone positioning error (Table 7.6). This suggests that the experimental setup was particularly unfavourable for mode (11) excitation and recording. The discrepancies between the measured and predicted results in the case of other modes can be explained by errors in microphone positioning. The residual absorption of the tube (see Figure 5.25) may also contribute to the lack of match between the experiments and predictions.

| | | Exp. data MD | Sim. data MD | | $R_{mn}$, pred. | $R_{mn}$, meas. |
|---|---|---|---|---|---|---|
| | | | *Phase error 5%* | *Phase error 20%* | | |
| Armasound | Re ($R_{00}$) | 0.0932 | 0.0990 | 0.0991 | 0.6719 | 0.3525 |
| | Im ($R_{00}$) | 0.0905 | 0.0956 | 0.0957 | 0.2071 | 0.4742 |
| | Re ($R_{01}$) | 0.3275 | 0.2518 | 0.2294 | 0.4416 | 0.2322 |
| | Im ($R_{01}$) | 0.3969 | 0.2702 | 0.2574 | 0.1214 | 0.1482 |
| | Re ($R_{11}$) | 0.8748 | 0.1782 | 0.1470 | 0.3311 | 0.3538 |
| | Im ($R_{11}$) | 0.8018 | 0.1600 | 0.1385 | 0.1423 | 0.1448 |
| | Re ($R_{02}$) | 0.2896 | 0.1608 | 0.1812 | 0.2438 | 0.0443 |
| | Im ($R_{02}$) | 0.2908 | 0.1624 | 0.1748 | 0.1497 | -0.0141 |
| Geranium | Abs ($R_{00}$) | 0.0514 | 0.0023 | 0.0023 | 0.9151 | 0.8205 |
| | Abs ($R_{01}$) | 0.2228 | 0.3088 | 0.4153 | 0.8552 | 0.7869 |
| | Abs ($R_{11}$) | 0.2893 | 0.1363 | 0.1410 | 0.8481 | 1.0000 |
| | Abs ($R_{02}$) | 0.0909 | 0.1841 | 0.1908 | 0.8268 | 0.9827 |

Table 7.4: A summary of the mean differences (MD) between the predictions and measurement (second column) and simulations (third and fourth column) for the 150 mm square tube, where a random phase error was introduced.

| | | Exp. data | Sim. data | | | $R_{mn}$, pred. | $R_{mn}$, meas. |
|---|---|---|---|---|---|---|---|
| | | | *XY, 5 mm tol.* | *Z, 1 mm tol.* | *Z, 10 mm tol.* | | |
| Armasound | Re ($R_{00}$) | 0.0932 | 0.0991 | 0.0991 | 0.0992 | 0.6719 | 0.3525 |
| | Im ($R_{00}$) | 0.0905 | 0.0956 | 0.0956 | 0.0954 | 0.2071 | 0.4742 |
| | Re ($R_{01}$) | 0.3275 | 0.4372 | 0.2171 | 0.5639 | 0.4416 | 0.2322 |
| | Im ($R_{01}$) | 0.3969 | 0.4878 | 0.2785 | 0.4768 | 0.1214 | 0.1482 |
| | Re ($R_{11}$) | 0.8748 | 0.1418 | 0.1706 | 0.2875 | 0.3311 | 0.3538 |
| | Im ($R_{11}$) | 0.8018 | 0.1518 | 0.1678 | 0.3181 | 0.1423 | 0.1448 |
| | Re ($R_{02}$) | 0.2896 | 0.1622 | 0.1604 | 0.2536 | 0.2438 | 0.0443 |
| | Im ($R_{02}$) | 0.2908 | 0.1520 | 0.1656 | 0.2738 | 0.1497 | -0.0141 |
| Geranium | Abs ($R_{00}$) | 0.0514 | 0.0023 | 0.0023 | 0.0023 | 0.9151 | 0.8205 |
| | Abs ($R_{01}$) | 0.2228 | 0.3168 | 0.3467 | 0.6294 | 0.8552 | 0.7869 |
| | Abs ($R_{11}$) | 0.2893 | 0.1388 | 0.1300 | 1.5380 | 0.8481 | 1.0000 |
| | Abs ($R_{02}$) | 0.0909 | 0.1911 | 0.1794 | 1.3344 | 0.8268 | 0.9827 |

Table 7.5: A summary of the mean differences between the predictions and measurement (second column) and simulations (third, fourth and fifth column) for the 150 mm square tube, where a random positioning error was introduced. *XY* denotes the error introduced to the cross-sectional coordinates, and *Z* denotes the error in the axial coordinate.

| | | Exp. data | Sim. data | | | $R_{mn}$, pred. | $R_{mn}$, meas. |
|---|---|---|---|---|---|---|---|
| | | | *XY* *5 mm bias + 5 mm tol.* | *Z* *10 mm bias + 0 mm tol.* | *Z* *10 mm bias + 10 mm tol.* | | |
| Armasound | Re ($R_{00}$) | 0.0932 | 0.0991 | 0.0994 | 0.0993 | 0.6719 | 0.3525 |
| | Im ($R_{00}$) | 0.0905 | 0.0956 | 0.0931 | 0.0933 | 0.2071 | 0.4742 |
| | Re ($R_{01}$) | 0.3275 | 0.3872 | 0.2801 | 0.2928 | 0.4416 | 0.2322 |
| | Im ($R_{01}$) | 0.3969 | 0.3581 | 0.2994 | 0.3194 | 0.1214 | 0.1482 |
| | Re ($R_{11}$) | 0.8748 | 0.1574 | 0.2058 | 0.1674 | 0.3311 | 0.3538 |
| | Im ($R_{11}$) | 0.8018 | 0.2001 | 0.1989 | 0.2080 | 0.1423 | 0.1448 |
| | Re ($R_{02}$) | 0.2896 | 0.1533 | 0.1706 | 0.2758 | 0.2438 | 0.0443 |
| | Im ($R_{02}$) | 0.2908 | 0.1594 | 0.2078 | 0.2592 | 0.1497 | -0.0141 |
| Geranium | Abs ($R_{00}$) | 0.0514 | 0.0023 | 0.0020 | 0.0021 | 0.9151 | 0.8205 |
| | Abs ($R_{01}$) | 0.2228 | 0.4466 | 2.4375 | 1.9148 | 0.8552 | 0.7869 |
| | Abs ($R_{11}$) | 0.2893 | 0.1337 | 0.3146 | 0.2684 | 0.8481 | 1.0000 |
| | Abs ($R_{02}$) | 0.0909 | 0.1909 | 0.1950 | 0.5345 | 0.8268 | 0.9827 |

Table 7.6: A summary of the mean differences between the predictions and measurement (second column) and simulations (third, fourth and fifth column) for the 150 mm square tube, where a constant positioning bias and random positioning error was introduced. *XY* denotes the error introduced to the cross-sectional coordinates, and *Z* denotes the error in the axial coordinate.

### 7.1.3 150 mm circular tube

The sensitivity analysis for the simulated data for the 150 mm circular tube was performed on melamine foam only as that was the only material the laboratory measurements were performed with. The mean differences between the simulated and predicted data for a phase uncertainty and random and constant microphone positioning uncertainties are summarised in Tables 7.7, 7.8 and 7.9, respectively. It is evident from the tables that the differences between simulated and predicted data for all three uncertainty scenarios barely exceed 2 %, whereas the differences between the measured and the simulated data reach about 20 %. Again, it is likely that it may be due to the residual tube absorption, as well as background noise or tube wall vibration.

| | | Exp. data MD | Sim. data MD | | $R_{mn}$, pred. | $R_{mn}$, meas. |
|---|---|---|---|---|---|---|
| | | | *Phase error 5%* | *Phase error 20%* | | |
| Melamine | Re ($R_{00}$) | 0.1054 | 0.0004 | 0.0005 | 0.1457 | 0.3617 |
| | Im ($R_{00}$) | 0.1764 | 0.0006 | 0.0007 | 0.1413 | 0.1549 |
| | Re ($R_{10}$) | 0.0729 | 0.0010 | 0.0012 | 0.0021 | -0.0009 |
| | Im ($R_{10}$) | 0.0740 | 0.0014 | 0.0015 | 0.0701 | 0.0282 |
| | Re ($R_{20}$) | 0.1114 | 0.0022 | 0.0024 | -0.0825 | -0.0099 |
| | Im ($R_{20}$) | 0.0569 | 0.0025 | 0.0026 | 0.0306 | 0.0012 |
| | Re ($R_{30}$) | 0.2080 | 0.0046 | 0.0045 | -0.2069 | 0.0020 |
| | Im ($R_{30}$) | 0.0542 | 0.0138 | 0.0138 | -0.0121 | 0.0053 |

Table 7.7: A summary of the mean differences (MD) between the predictions and measurement (second column) and simulations (third and fourth column) for the 150 mm circular tube, where a random phase error was introduced.

| | | Exp. data | Sim. data | | | $R_{mn}$, pred. | $R_{mn}$, meas. |
|---|---|---|---|---|---|---|---|
| | | | *XY, 5 mm tol.* | *Z, 1 mm tol.* | *Z, 10 mm tol.* | | |
| Melamine | Re ($R_{00}$) | 0.1054 | 0.0004 | 0.0004 | 0.0025 | 0.1457 | 0.3617 |
| | Im ($R_{00}$) | 0.1764 | 0.0005 | 0.0005 | 0.0024 | 0.1413 | 0.1549 |
| | Re ($R_{10}$) | 0.0729 | 0.0010 | 0.0010 | 0.0059 | 0.0021 | -0.0009 |
| | Im ($R_{10}$) | 0.0740 | 0.0013 | 0.0014 | 0.0056 | 0.0701 | 0.0282 |
| | Re ($R_{20}$) | 0.1114 | 0.0022 | 0.0022 | 0.0071 | -0.0825 | -0.0099 |
| | Im ($R_{20}$) | 0.0569 | 0.0025 | 0.0025 | 0.0072 | 0.0306 | 0.0012 |
| | Re ($R_{30}$) | 0.2080 | 0.0048 | 0.0045 | 0.0087 | -0.2069 | 0.0020 |
| | Im ($R_{30}$) | 0.0542 | 0.0144 | 0.0137 | 0.0150 | -0.0121 | 0.0053 |

Table 7.8: A summary of the mean differences between the predictions and measurement (second column) and simulations (third, fourth and fifth column) for the 150 mm circular tube, where a random positioning error was introduced. *XY* denotes the error introduced to the cross-sectional coordinates, and *Z* denotes the error in the axial coordinate.

| | | Exp. data | Sim. data | | | $R_{mn}$, pred. | $R_{mn}$, meas. |
|---|---|---|---|---|---|---|---|
| | | | *XY* *5 mm bias + 5 mm tol.* | *Z* *10 mm bias + 0 mm tol.* | *Z* *10 mm bias + 10 mm tol.* | | |
| Melamine | Re ($R_{00}$) | 0.1054 | 0.0004 | 0.0027 | 0.0031 | 0.1457 | 0.3617 |
| | Im ($R_{00}$) | 0.1764 | 0.0006 | 0.0028 | 0.0034 | 0.1413 | 0.1549 |
| | Re ($R_{10}$) | 0.0729 | 0.0010 | 0.0055 | 0.0067 | 0.0021 | -0.0009 |
| | Im ($R_{10}$) | 0.0740 | 0.0014 | 0.0054 | 0.0072 | 0.0701 | 0.0282 |
| | Re ($R_{20}$) | 0.1114 | 0.0023 | 0.0081 | 0.0085 | -0.0825 | -0.0099 |
| | Im ($R_{20}$) | 0.0569 | 0.0026 | 0.0066 | 0.0085 | 0.0306 | 0.0012 |
| | Re ($R_{30}$) | 0.2080 | 0.0048 | 0.0083 | 0.0090 | -0.2069 | 0.0020 |
| | Im ($R_{30}$) | 0.0542 | 0.0143 | 0.0193 | 0.0204 | -0.0121 | 0.0053 |

Table 7.9: A summary of the mean differences between the predictions and measurement (second column) and simulations (third, fourth and fifth column) for the 150 mm circular tube, where a constant positioning bias and random positioning error was introduced. *XY* denotes the error introduced to the cross-sectional coordinates, and *Z* denotes the error in the axial coordinate.

## 7.2 Sensitivity to array dimensions

For the 150 mm circular pipe, measured data with a small step (10 mm) and over a large spatial window (3 m) were available. This provided a possibility to conduct an analysis which would estimate how the length of a spatial step, the length of a spatial window and the shape of the spatial window influence the recovered modal reflection coefficients. The analysis was performed for the wall loudspeaker and microphone position, resulting in the recovery of the reflection coefficients for modes (00), (10), (20) and (30).

Figure 7.1 shows the measured and predicted real and imaginary values of the non-axisymmetric modal reflection coefficients for a layer of melamine foam measured in 150 mm circular tube. There are five sets of data in the figure, the solid black line being the predictions, and the green, blue, magenta and red dots denote 10 mm, 20 mm, 40 mm and 80 mm step, respectively. The mean differences between the predictions and the four measured data sets are summarised in Table 7.10. It is evident from the collected data that an increase of the measurement step from 10 to 20 mm does not significantly affect the final result. There is a scatter in both data sets beyond 3000 Hz in the reflection coefficient for mode (20), but it is likely to happen due to the lack of energy for this mode in the higher frequency range, which results in the inferior quality of the recovered data. The 40 mm step is marked with magenta dots, and the reflection coefficient recovered with this step is notably more oscillatory. However, for modes (00) and (10) it is stable until the cut-on of the next mode. The 80 mm step provides with the most inaccurate result. For mode (00) the reflection coefficient starts to oscillate at about 600 Hz, and almost immediately after the cut-on for mode (10).

Figure 7.2 shows the influence of the window length on the quality of the real and imaginary parts of the measured modal reflection coefficients. The green dots denote the 3 m long spatial window, blue dots - 1 m long window, magenta dots - 2 m long window,

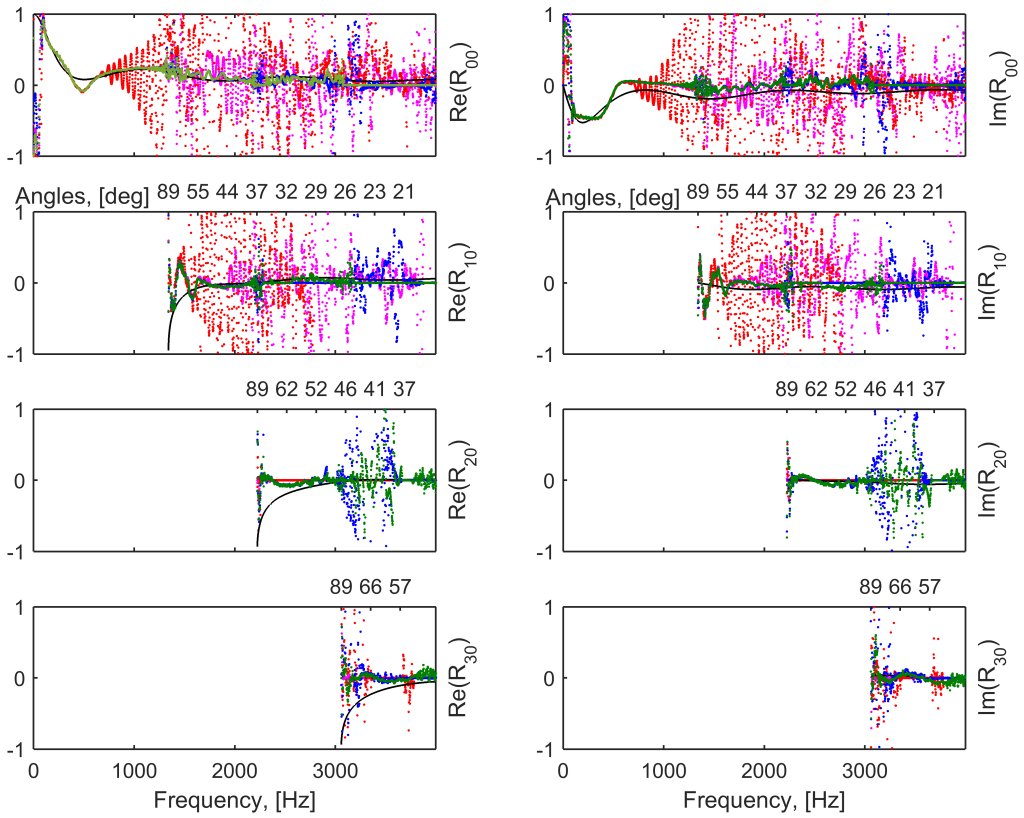


Figure 7.1: The measured and predicted real and imaginary values of the modal reflection coefficients in the 150 mm circular tube for a layer of melamine foam. Solid black line: predictions; green dots: 10 mm step; blue dots: 20 mm step; magenta dots: 40 mm step; red dots: 80 mm step.

all starting at the first measurement position (approximately 10 mm from the material sample), red dots - 2 m long window, starting at the 100th measurements position (approximately 1 m from the material sample). The predictions are plotted with a solid black line. The figure suggests that the 1 m long window results are more oscillatory than the other results, which is expected, as this window provides less data for the reflection coefficient recovery, affecting its accuracy. The 2 m long window also gives a rather scattered result, although to a lesser extent than the 1 m long window. An interesting result is obtained with the 2 m long window, starting at the 100th microphone position. The quality of this result is superior to that of the 2 m long window starting at the 1st position. This may lead to a conclusion that the spatial locations of the microphone are more precise further from the material sample, which results in more accurate recovered reflection coefficients. Also, the effect of evanescent modes may be

| | 10 mm | 20 mm | 40 mm | 80 mm |
|---|---|---|---|---|
| Re ($R_{00}$) | 0.0830 | 0.1134 | 0.2710 | 0.5977 |
| Im ($R_{00}$) | 0.1259 | 0.1636 | 0.2888 | 0.5818 |
| Re ($R_{10}$) | 0.0682 | 0.1121 | 13.2139 | 0.5031 |
| Im ($R_{10}$) | 0.0745 | 0.1032 | 14.0054 | 0.5287 |
| Re ($R_{20}$) | 0.1459 | 0.6141 | 0.0912 | 0.0894 |
| Im ($R_{20}$) | 0.0901 | 0.5622 | 0.0332 | 0.0355 |
| Re ($R_{30}$) | 0.2104 | 0.4470 | 0.2073 | 6.7666 |
| Im ($R_{30}$) | 0.0579 | 0.3177 | 0.0322 | 20.5068 |

Table 7.10: A summary of the mean differences between the real and imaginary parts of the measured and predicted modal reflection coefficients for the four step lengths, 10 mm, 20 mm, 40 mm and 80 mm.

smaller when the microphone array is far away from the sample.

| | 0 - 3 m | 0 - 1 m | 0 - 2 m | 1 - 3 m |
|---|---|---|---|---|
| Re ($R_{00}$) | 0.0830 | 0.0869 | 0.0724 | 0.0894 |
| Im ($R_{00}$) | 0.1259 | 0.1005 | 0.1061 | 0.1413 |
| Re ($R_{10}$) | 0.0682 | 0.0695 | 0.1477 | 0.0672 |
| Im ($R_{10}$) | 0.0745 | 0.0886 | 0.1304 | 0.0705 |
| Re ($R_{20}$) | 0.1459 | 0.0757 | 0.0916 | 0.1238 |
| Im ($R_{20}$) | 0.0901 | 0.0539 | 0.0429 | 0.0589 |
| Re ($R_{30}$) | 0.2104 | 0.2029 | 0.2365 | 0.2327 |
| Im ($R_{30}$) | 0.0579 | 0.0439 | 0.0765 | 0.0795 |

Table 7.11: A summary of the mean differences between the real and imaginary parts of the measured and predicted modal reflection coefficients for the four window lengths, 3 m from the initial position, 1 m from the initial position, 2 m from the initial position and 2 m from the 1 m position.

Figure 7.3 presents the analysis of the influence of different window shapes on the recovered reflection coefficient accuracy. Four windows are considered: plain rectangular window (green dots), rectangular window with first and last 10 points rounded with the Hamming window (blue dots), Blackman window (magenta dots) and Hamming window (red dots). The solid black line denotes the predicted reflection coefficients. As the figure suggests, there is no big difference between different window results for the plane wave mode. However, there is a visible scatter in the data windowed with the Blackman and Hamming windows in higher modes reflection coefficients, even where there is no scatter in the rectangular window data (eg. 3500 Hz and higher for modes (10)

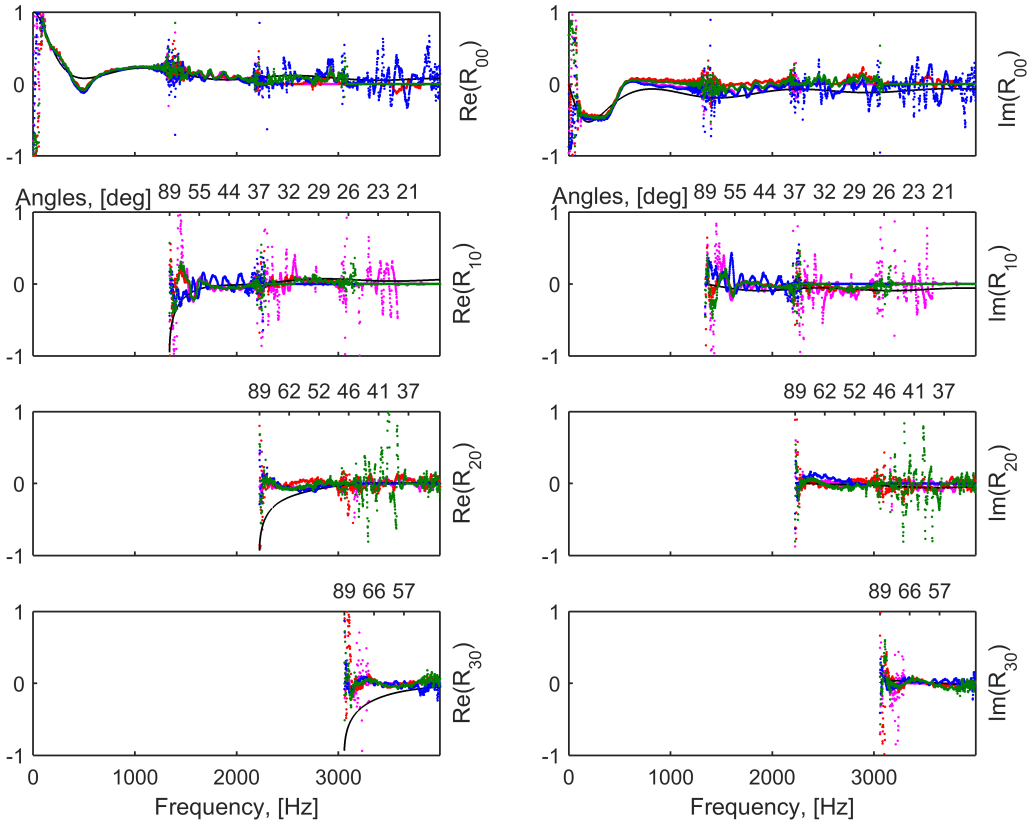


Figure 7.2: The measured and predicted real and imaginary values of the modal reflection coefficients in the 150 mm circular tube for a layer of melamine foam. Solid black line: predictions; green dots: 3 m long window (0 - 3 m); blue dots: 1 m long window (0 - 1 m); magenta dots: 2 m long window (0 - 2 m); red dots: 2 m long window (1 - 3 m).

and (20)). This may suggest that although data windowing results in cleaner frequency-wavenumber plots, without the artefact lines caused by non-infinite bounds of Fourier transform, it also contributes to the loss of data to some extent, which decreases the quality of the recovered reflection coefficients. This leads to the conclusion that the balance between the extent of data windowing and the quality of a final result is crucial.

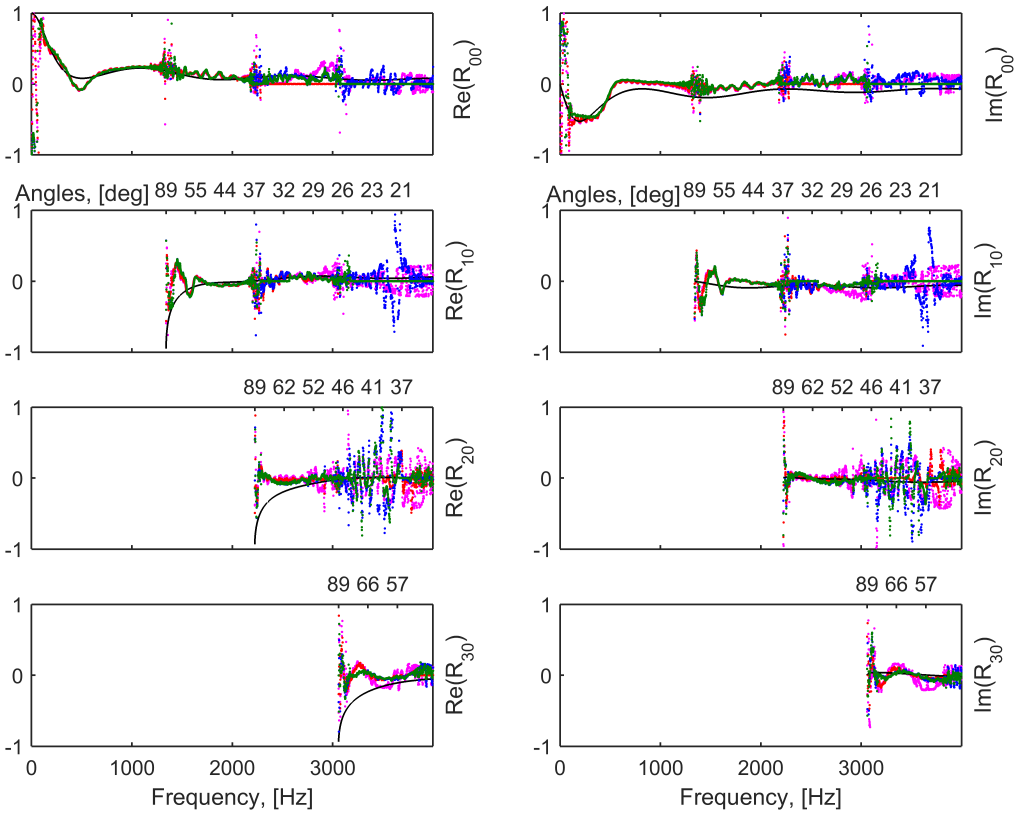


Figure 7.3: The measured and predicted real and imaginary values of the modal reflection coefficients in the 150 mm circular tube for a layer of melamine foam. Solid black line: predictions; green dots: rectangular window; blue dots: rectangular window with rounded edges; magenta dots: Blackman window; red dots: Hamming window.

| | Rectangular | Rectangular with round edges | Blackman | Hamming |
|---|---|---|---|---|
| Re ($R_{00}$) | 0.0830 | 0.0854 | 0.1081 | 0.0829 |
| Im ($R_{00}$) | 0.1259 | 0.1412 | 0.1584 | 0.1185 |
| Re ($R_{10}$) | 0.0682 | 0.1018 | 0.0932 | 0.0728 |
| Im ($R_{10}$) | 0.0745 | 0.0989 | 0.0942 | 0.0739 |
| Re ($R_{20}$) | 0.1459 | 0.1721 | 0.2016 | 0.1114 |
| Im ($R_{20}$) | 0.0901 | 0.1138 | 0.1428 | 0.0569 |
| Re ($R_{30}$) | 0.2104 | 0.2740 | 0.2144 | 0.2080 |
| Im ($R_{30}$) | 0.0579 | 0.1776 | 0.1253 | 0.0542 |

Table 7.12: A summary of the mean differences between the real and imaginary parts of the measured and predicted modal reflection coefficients for the four window shapes, rectangular, rectangular with rounded edges, Blackman and Hamming.

## 7.3 Source positioning influence

For measurements in the 300 mm square tube, three loudspeakers were employed to excite the sound field inside the tube (see Figure 5.5). It seems of interest to conduct a study, which would determine how the cross-sectional position of each loudspeaker influences the modal field excitation in the tube. For this purpose, the loudspeakers were activated one after another, and for each loudspeaker a set of measurements, described in Chapter 5, was performed, resulting in a total of three sets. A sketch of the loudspeaker positioning is presented in Figure 7.4. The cross-sectional coordinates of loudspeaker centres are as follows: (50 mm, 50 mm) for the corner loudspeaker, (50 mm, 150 mm) for the wall loudspeaker and (150 mm, 150 mm) for the middle loudspeaker. Other than the loudspeaker setup, the experimental apparatus was consistent with that described in subsection 5.2.1 of Chapter 5. The end, opposite to the loudspeakers was terminated with a layer of Armasound foam, the characteristics of which are provided in Table 5.3.

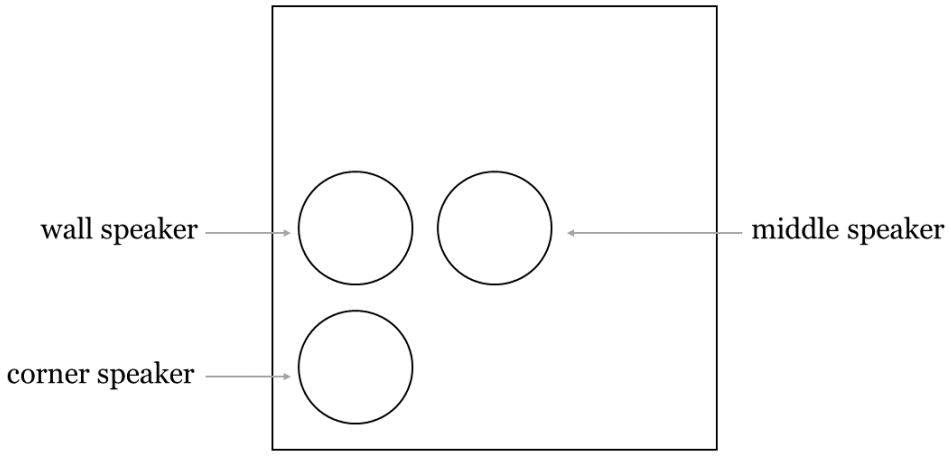


Figure 7.4: A sketch of the cross-sectional positioning of loudspeakers. The x- and y-coordinates of the speakers are: (50 mm, 50 mm) for the corner speaker; (50 mm, 150 mm) for the wall speaker; (150 mm, 150 mm) for the middle speaker.

Figures 7.5-7.7 present the frequency-wavenumber sound pressure plots for the corner, wall and middle loudspeaker positions, respectively. It is evident from the graphs

that the cross-sectional location of a loudspeaker had an influence on a modal field pattern in the tube. The highest number of modes was excited with the corner loudspeaker activated. All propagating modes in the adopted frequency range are visible in the frequency-wavenumber plot. Modes (12) and (22) have a lower amplitude than the other modes, but still within the reasonable signal-to-noise ratio of 20dB. The wall loudspeaker also excited almost all the modes, with the exception of mode (11), the amplitude of which was significantly lower than that of the other modes. This is to be expected, as the amplitude of this mode is zero at this cross-sectional position (see Figure 5.1). The middle loudspeaker excited modes (00), (02) and (22), but the remaining modes either did not have enough energy to propagate or their amplitudes were relatively low. In general, all three loudspeakers excited all the modes which are capable of propagating in the tube in the adopted frequency range.

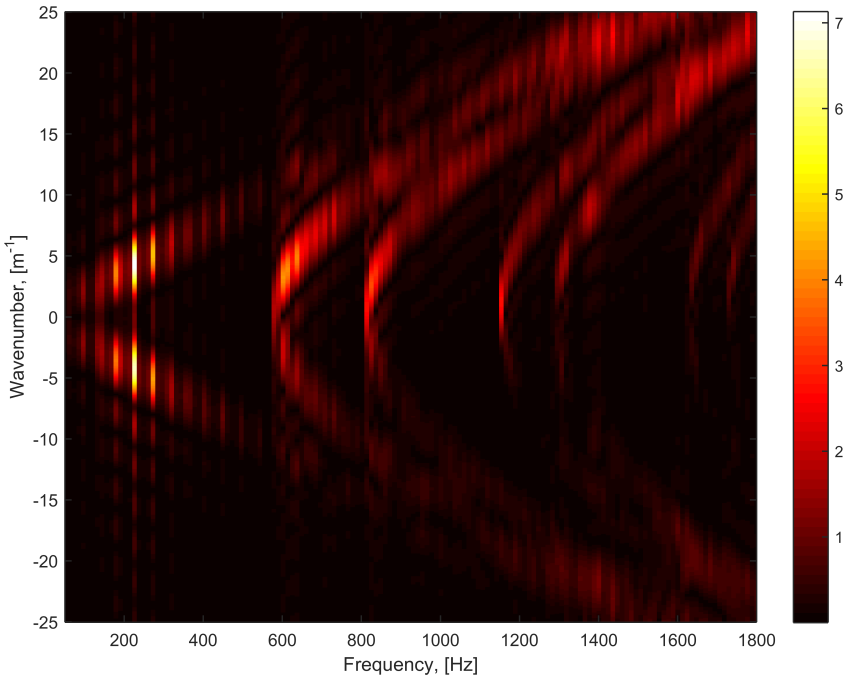


Figure 7.5: A frequency-wavenumber spectrum of an Armasound foam layer, excited with a loudspeaker in a corner of the 300 mm square tube cross-section.

Figure 7.8 provides the comparison of the measured and predicted real and imaginary parts of the first four modal reflection coefficients for the Armasound foam layer. It presents three measured reflection coefficients recovered separately from the mea-

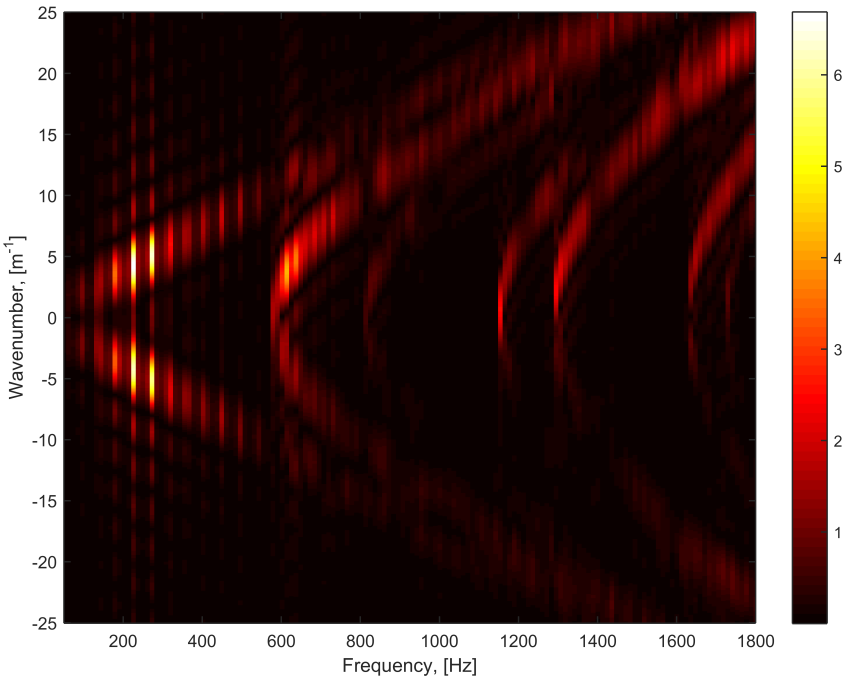


Figure 7.6: A frequency-wavenumber spectrum of an Armasound foam layer, excited with a loudspeaker near the wall of the 300 mm square tube cross-section.

surements with only one loudspeaker active. The predictions were calculated using the Johnson-Champoux-Allard model (see Equation (2.6.21)). The measured results marked with black dots correspond to the corner loudspeaker, blue dots - to the wall loudspeaker, and red dots - to the middle loudspeaker. The mean differences between these three sets of measured data and the predictions were quantified and are summarised in Table 7.13. Generally, the smallest mean difference is found in the case of the corner loudspeaker being active. This outcome is anticipated as the loudspeaker placed in the corner of the tube cross-section is capable of exciting all the modes which can propagate in the adopted frequency range. The largest mean difference is observed when the loudspeaker is in the middle of the tube cross-section. Again, this is expected as this source positioning excites only even modes. However, even for modes (01) and (11) the reflection coefficient measured with the middle loudspeaker provides a reasonable match with the predictions, despite the higher level of scattering in the data. Moreover, it provides more accurate data for mode (22), which is not sufficiently excited with the corner loudspeaker. The mean differences between the predicted modal

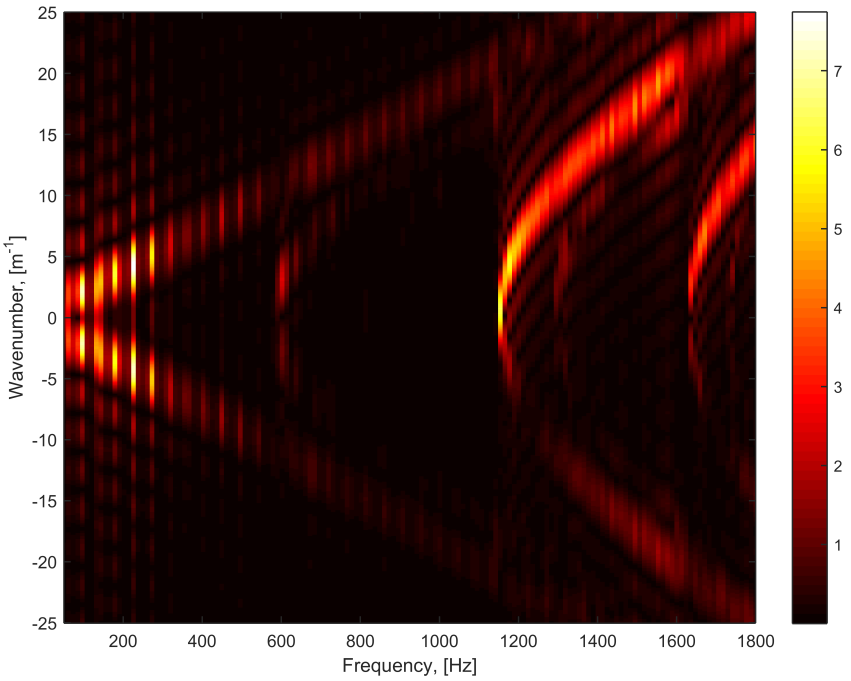


Figure 7.7: A frequency-wavenumber spectrum of an Armasound foam layer, excited with a loudspeaker in the middle of the 300 mm square tube cross-section.

reflection coefficients and those measured near the wall are comparable to the ones estimated for the corner loudspeaker data. Hence, it can be concluded that in order to have a complete and sufficiently accurate picture of the sound field distribution in the pipe, two loudspeaker positions should be used, in the corner and in the middle. This will ensure a relatively high signal-to-noise ratio for all the modes which can propagate in the adopted frequency range.

| | Corner | Wall | Middle |
|---|---|---|---|
| Re ($R_{00}$) | 0.0133 | 0.0239 | 0.0231 |
| Im ($R_{00}$) | 0.0448 | 0.0222 | 0.0211 |
| Re ($R_{01}$) | 0.1675 | 0.1451 | 0.4149 |
| Im ($R_{01}$) | 0.1564 | 0.1173 | 0.3301 |
| Re ($R_{11}$) | 0.2053 | 0.2409 | 0.3028 |
| Im ($R_{11}$) | 0.1055 | 0.1734 | 0.2966 |
| Re ($R_{02}$) | 0.1491 | 0.1911 | 0.1816 |
| Im ($R_{02}$) | 0.0933 | 0.1278 | 0.0620 |

Table 7.13: A summary of the mean differences between the real and imaginary parts of the measured and predicted modal reflection coefficients for the three loudspeaker cross-sectional locations.

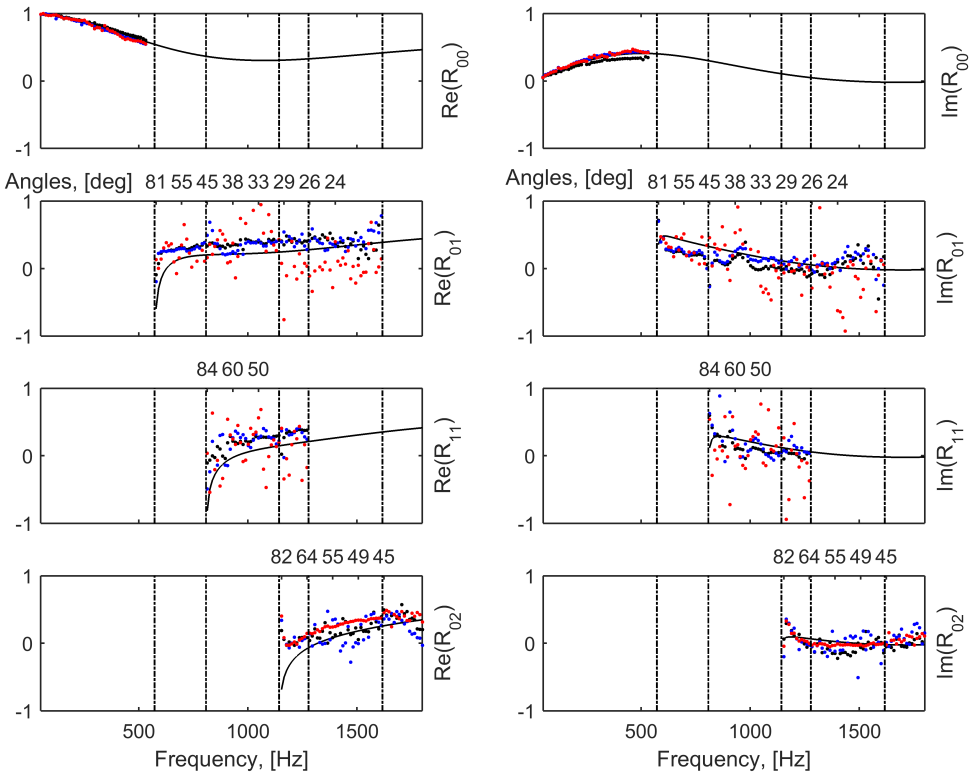


Figure 7.8: The measured and predicted real and imaginary values of the modal reflection coefficients in the 300 mm square tube for a layer of Armasound foam. Solid black line: predictions; black dots: corner loudspeaker; blue dots: wall loudspeaker; red dots: middle loudspeaker.

## 7.4 Summary

A sensitivity analysis has been performed and its results have been described in this chapter. Artificial errors were introduced to the pressure spectra phase and axial and cross-sectional positions of the microphone array. This has been done in order to estimate which factors may have influenced the accuracy of the data measured in the laboratory. However, none of the mean differences in the simulated data have been sufficiently large to explain discrepancies between the predictions and experimentally obtained data. This means that the errors in the laboratory measurements were most likely caused by such factors as residual wall absorption, wall vibration or background noise.

The experimental data collected in the 150 mm circular tube allowed to study the sen-

sitivity of the measured acoustical properties to the step, window length and shape. It has been found that the steps of 10 and 20 mm have a similar effect on the accuracy of obtained data, and then the quality of data deteriorated with the increase of the step. An interesting result has been observed when the influence of the window length was examined, showing that the starting position of the window can strongly influence the quality of the experimental data. The shape of the window also has been noted to affect the data, which suggests that the balance between the cleaner frequency-wavenumber spectra and the accurate reflection coefficients is important.

Finally, the influence of the loudspeaker positioning has been analysed, where three loudspeaker cross-sectional positions have been tested. It was concluded that, although the corner loudspeaker position excites all the modes capable of propagating in the adopted frequency range and their amplitude is sufficiently high to recover the corresponding reflection coefficients, it is preferable to employ both corner and middle loudspeaker positions, as such setup will result in the most accurate experimental results due to the high signal-to-noise ratio for all the modes.

# Chapter 8

# Conclusions

This chapter summarises the results of the research described in this thesis. An overview of achievements and limitations of the conducted study are presented and discussed. In addition, recommendations for the future work are listed.

## 8.1 Achievements

This project was aimed at studying and understanding the complex sound intensity in pipes, with application to inhomogeneity analysis, such as an open pipe end and blockages, and porous media characterisation, which included regular porous materials and living plants. To fulfil the aim of this work, the objectives, listed in Chapter 1 were met. Several experimental facilities have been employed to study the sound field distribution in a pipe, of different length and cross-sectional size and shape. This variability was necessary to suit the needs of each set of experiments, and to validate the methods using various experimental setups.

For the study on the complex intensity vector in an open-ended pipe and a pipe with an obstacle, a suitable numerical model was found and validated through sets of experiments. The hybrid model by Duan et al. (2013) was chosen due to its robustness, accuracy and time efficiency. This model combined modal decomposition in the regions where the calculations were relatively straightforward (straight section of a pipe, open space, etc), with finite element modelling for the regions which required more complex computations, such as a monopole sound source or an open end of a pipe. The hybrid model was used for subsequent comparison with measured data to gain understanding of the complex sound intensity field in the vicinity of an open end of a pipe at a frequency beyond the first cut-on frequency of the pipe and to recognise the capabilities and limitations of its measurements. The measurements were performed with the tri-axial Microflown probe, which was capable of simultaneously measuring the sound pressure and three components of the sound velocity. The probe was rotated in a supporting frame with a 10° step to cover a full circumference of the pipe, and the active and reactive axial, radial and circumferential intensities were obtained. It was shown that it is possible to obtain good quantitative agreement between predicted and measured complex intensity, provided a very simple problem is under consideration, which in this case was the use of plane waves in the 150 mm diameter pipe at the frequency of 1000 Hz. A good agreement was observed both at the end of the open ended pipe and within the pipe itself. The mean error between the measured and predicted data as in general less than 5%. It was higher for times between 0 and 2 ms, where the system response was transient, resulting in the mean error about 20%. However, at a frequency of 1800 Hz, which was beyond the first cut-on frequency for this pipe, obtaining a good match between the measurements became more challenging. The best agreement was achieved in the case of active and reactive radial intensities. It may have been caused by the fact that the influence of the supporting frame and the probe body on the radial intensity was smaller than on the remaining two intensity components. In the case of the active and reactive axial intensities, the match was good for the active component;

however, there was a shift of about 20° in the pattern of the measured intensity. The relative error between the amplitudes of the maxima in the predicted and measured active axial intensity is less than 1%, but this error increases significantly when the value of the circumferential coordinate becomes less than 120°. The mean error between the amplitudes of measured and predicted active axial intensities was less than 1%, but it became higher at low circumferential coordinates, where the amplitude of the active axial intensity was relatively small. For the circumferential intensity, a good agreement was observed for the reactive part, although there was a shift in the pattern of about 15°. The match between the measured and predicted active circumferential intensities was the weakest out of all six components. It is likely that the influence of the supporting frame is the most pronounced in the case of the circumferential component of the sound velocity, especially at high frequencies. Based on the collected measured and predicted data, it is clear that the understanding of the complex intensity vector behaviour in the vicinity of an open end of a pipe remains limited at frequencies beyond the first cut-on frequency of the pipe. Difficulties were encountered even for a simpler case, when only one mode propagated in the pipe. When more than one mode became propagating, it was possible to qualitatively assess the behaviour of the complex sound intensity in the pipe, but the agreement between measurements and predictions was insufficient for accurate quantitative analysis. It is probable that scattering from the supporting frame,probe body and imperfections in the pipe geometry have strong influence on the accuracy of the measured data.

To locate and characterise blockages in a pipe, several set of experiments in 18 m long closed pipe were conducted, and their results were compared to the model proposed by Duan et al. (2015). For this purpose, an array of four MEMS microphones was used to simulate an axial array of microphones in the pipe, by manually moving it in 40 mm steps to cover the 2 m distance. Three sets of measurements were performed: one in the empty pipe, one in front of a blockage to measure the reflection from it, and one behind the blockage to measure its transmission. A coaxial cylinder of a diameter of 110 mm

and of a length of 305 mm was used as the blockage. The measured pressure and axial velocity data were subsequently subjected to a two-dimensional Fourier transform. This led to obtaining frequency-wavenumber spectra for the three measurement conditions, which were later used to calculate reflection and transmission coefficients. The measured and predicted data were in good agreement for such simple blockage and under the plane wave conditions. The mean error was below 2% in the case of the transmission coefficient, and below 10% in the case of the reflection coefficient. This signifies that the proposed method of employing the frequency-wavenumber spectra for calculating the blockage transmission and reflection coefficients can be successfully used for locating and characterising blockages in pipes. This method can be developed further to include the transmission and reflection of higher-order modes; however, it was chosen to limit it to the plane wave conditions. Considering the effect of more than one mode would have made the theoretical model significantly more complicated and would have required much more complex measured data analysis. Confining the method to only one mode made it more attractive for practical execution.

A novel method was proposed to characterise large porous material samples in an impedance tube (Prisutova et al., 2014). This method does not require using special experimental facilities such as an anechoic chamber, is time-efficient and prone to microphone mismatch issues. It relies on simulating an axial array of microphones along the axis of the tube, by moving a single microphone with the help of a robotic arm. The obtained position-dependent data were transformed into a wavenumber space. Then a minimisation procedure was carried out, which enabled the recovery of incident and reflected amplitudes and phases for each propagating mode. These data were combined together to obtain the modal reflection and total absorption coefficients. The method was tested in three impedance tubes of different cross-sectional shape and width, and on several porous material samples of different absorbing properties. It was found to accurately measure modal reflection coefficients at normal and oblique incidence, and successfully employ sound intensity measurements to calculate total absorption coeffi-

cients. The mean error for modal reflection coefficients for such well-absorbing materials as melamine foam and wood fibre did not exceed 10% for the former and 15% for the latter, for all considered modes, measured in the 300 mm wide square tube. This error was slightly higher for Armasound foam (below 20%), which was likely due to its heterogeneous nature and inability to precisely predict its absorptive behaviour. For the thin foam the error was the highest (35% and below), which may signify that the method works worse for low-absorbing materials. These errors were higher in the 150 mm square tube, where only Armasound foam was tested. This was attributed to the higher residual absorption of the pipe walls, as well as inhomogeneities in the material structure. To calculate the total absorption coefficient, two approaches were adopted. One used the amplitudes of incident and reflected waves, and the other used the sound intensity data. Although the former approach exhibited smaller error, it was due to the used assumptions, which either did not reflect the real picture of the sound field distribution in the pipe, or were different for measurements and predictions. Because of that, the intensity method was preferred for the total absorption coefficient calculation. The mean error was within 20% for Armasound and thin foam, and within 3% for melamine foam and wood fibre. For the 150 mm circular pipe, where only a melamine foam sample was tested, the mean errors were below 20% in the case of modal reflection coefficients, and below 6% in the case of the total absorption coefficients. In general, the suggested method was proven to work successfully for characterisation of large porous material samples in an impedance tube. It allows the recovery of both frequency and angular dependent complex reflection coefficient data for a porous layer, which makes possible the laboratory measurements of the acoustical properties of a large porous specimen at a range of the angles of incidence and in a relatively wide frequency band. Furthermore, it extended the frequency range, suggested by ISO 10534-2 (1998), by at least a factor of three. Finally, it is easy to run and does not ask for special equipment or large material samples.

Subsequently, this method was used to characterise sound absorption by living plants.

Several plants specimen were chosen and bought from a local gardening centre. These plants had different leaf number, sizes and shapes, as well as height and greenery volume. It allowed to deduce which morphological parameters of plants were key to good sound-absorbing abilities. These morphological parameters were carefully quantified. A set of twenty-five leaves was selected from each plant, which was used for evaluation of the leaf area and thickness. Additionally, an average height of each plant, an average number of leaves on each plants and an average angle of leaf orientation were estimated. These parameters were subsequently substituted into a model (Horoshenkov, 2013) which related morphological parameters of plants to their acoustical behaviour, which was calculated using the Miki model (1990). A good agreement was observed between the measured and predicted reflection and absorption coefficients values, which confirmed that plants can be successfully characterised as porous media. The mean error between measurements and predictions in the case of the modal reflection coefficients was below 10% for the 300 mm square tube. This error was higher in the case of the total absorption coefficient (below 30%). This happened due to the fact that the agreement between the measurements and predictions beyond the first cut-on frequency notably decreased. It was likely caused by the theoretical model not taking into account the scattering and leaf vibration phenomena, which became more pronounced at higher frequencies. It could also be due to the method assuming no modal cross-talk, which might have been present when the plants caused too much scattering, introducing the phase error. The errors were higher in the case of the 150 mm square tube, which was likely due to the residual absorption and wall vibration of the pipe. However, it was confirmed that the morphology of the plants had influence on their sound-absorbing capabilities. Such morphological parameters of living plants as the leaf area per unit volume and the dominant angle of leaf orientation were singled out as being key to influence the sound absorption of a plant. Additionally, it was proven that living plants can be successfully characterised as porous media. They contribute noticeably to sound absorption and can be used to aid the traditional man-made means of noise abatement.

Overall, the aim of this research of studying and understanding the complex intensity behaviour in waveguides and its application to real-life problems has been achieved. Capturing the distribution of the components of the complex intensity vector has been found to be a challenging problem, however, it was shown that it is possible to resolve at least four of the six complex intensity vector components under the harmonic excitation conditions in a multimodal field. Furthermore, its application to such cases as blockage characterisation and porous media absorption measurements yielded valuable results.

## 8.2 Limitations

Several limitations were noticed in the course of this research. Firstly, it was found that obtaining a good agreement between measured and predicted complex intensity is challenging even for such well-defined problem as an open end of a pipe. This may be due to the fact that current measurement techniques, such as the tri-axial intensity probe, are not precise enough to address the assessment of all six complex intensity components simultaneously. In addition, the inaccuracies in measured data may arise from imperfections of pipe geometry or scattering off a probe supporting frame. Only four out of six complex intensity components presented a good match, with the agreement between the measured and predicted axial reactive and circumferential active intensities being insufficient.

Secondly, the blockage characterisation technique is currently limited to simple blockages and plane wave regime. However, this limitation is due to the fact that the employed theoretical model did not account for more complex geometries and modal sound field.

The discrepancies between the measured and predicted reflection and absorption coefficients of porous materials and living plants specimens were higher than expected in

some cases. The reason for this may be the sensitivity of the method to such experimental setup imperfections as residual absorption of a pipe or pipe wall vibrations. Furthermore, it was discovered that the agreement is worse in the case of thin materials, ie. when the sound-absorbing abilities of a material are lower. In addition, in the case of the living plants, the agreement between the measurements and predictions becomes weaker with increasing frequency. This happens due to not taking into account such phenomena as leaf vibration and scattering, which become pronounced at higher frequencies.

## 8.3 Future work

Although the objectives of this work were successfully fulfilled, there are several recommendations for the future work. It would be of interest to develop both the theoretical model and the measured data analysis technique for characterisation of blockages in pipes to allow for a wider variety of blockage shapes, as well as for recovering the transmission and reflection coefficients above the first cut-on frequency of a pipe. In the case of porous material absorption measurements, the wall absorption and vibration could be taken into account when analysing the measured data, to see if this improves the match with the predictions. Moreover, it is necessary to include the leaf vibration and scattering in the theoretical model for living plants absorption, thus representing the actual plants absorption at higher frequencies with higher accuracy. Finally, it would be interesting to perform living plants absorption measurements with soil, as opposed to stems and foliage only, as described in this thesis. This would require manufacturing a plant holder, which can hold the soil vertically and the size of which is small enough in order to have a negligible influence on the measurements.

# Bibliography

Acoustic Sensing (2015) *Acoustic Sensing Technology*. [Online] Available from: http://www.acousticsensing.co.uk [accessed 2 January 2015].

Akoum, M., Ville, J.-M. (1998) Measurement of the reflection matrix of a discontinuity in a duct. *Journal of the Acoustical Society of America* 103(5) 2463-2468.

Allard, J.-F., Attala, N. (2009) *Propagation of Sound in Porous Media: Modelling Sound Absorbing Materials*. Chichester: Wiley. Chap. 3.

Amir, N., Shimony, U., Rosenhouse, G. (1995) A discrete model for tubular acoustic systems with varying cross section - The direct and inverse problems. Parts 1 and 2: Theory and experiment. *Acustica* 81(5) 450-474.

Antonopoulos-Domis, M. (1980) Frequency dependence of acoustic resonances on blockage position in a fast reactor subassembly wrapper. *Journal of Sound and Vibration* 72 443-450.

Armacell (2014) *ArmaSound RD 240*. [Online] Available from: http://www.armacell.co.uk [accessed 10 October 2014].

Aylor, D. (1972) Noise reduction by vegetation and ground, leaf width, and breadth of canopy. *Journal of the Acoustical Society of America* 51 197-205.

Aylor, D. (1972) Sound transmission through vegetation in relation to leaf area density, leaf width, and breadth of canopy. *Journal of the Acoustical Society of America* 51 411-414.

Biot, M. A. (1956) Theory of Propagation of Elastic Waves in a Fluid Saturated Porous Solid. I. Low Frequency Range. *Journal of the Acoustical Society of America* 28 168-178.

Biot, M. A. (1956) Theory of Propagation of Elastic Waves in a Fluid Saturated Porous Solid. II. Higher Frequency Range. *Journal of the Acoustical Society of America* 28 179-191.

De Bree, H.-E. (2007) *The Microflown E-book* [online]. Arnhem: Microflown Technologies. Available at: http://microflown.com/library/books/the-microflown-e-book.htm [accessed 5 December 2012].

Burns, S. H. (1979) The absorption of sound by pine trees. *Journal of the Acoustical Society of America* 65 658-661.

Champoux, Y., Allard, J.-F. (1991) Dynamic tortuosity and bulk modulus in air-saturated porous media. *Journal of Applied Physics* 70(4) 1975-1978.

Coulon, J.-M., Chevillotte, F., Bécot, F.-X., Jaouen, L. (2012) Broadband acoustical characterisation in a horn shaped impedance tube. In: CD-ROM Proceedings of Acoustics 2012. *Acoustics 2012*, Nantes, France, 2012.

De Salis, M. H. F., Oldham, D.J. (1999) Determination of the blockage area function of a finite duct from a single pressure response measurement. *Journal of Sound and Vibration* 221 180-186.

De Salis, M. H. F., Oldham, D.J. (2001) The development of a rapid single spectrum method for determining the blockage characteristics of a finite length duct. *Journal of Sound and Vibration* 243 625-640.

Delany, M. E., Bazley, E. N. (1970) Acoustical properties of fibrous absorbent materials. *Applied Acoustics* 3 105-116.

Duan, W., Kirby, R. (2012) A hybrid finite element approach to modeling sound radiation from circular and rectangular ducts. *Journal of the Acoustical Society of America* 131(5) 3638-3649.

Duan, W., Kirby, R., Prisutova, J., Horoshenkov, K. (2013) The Measurement and Prediction of Complex Acoustic Intensity in an Acoustic Waveguide. *Journal of the Acoustical Society of America* 134(5) 3674-3685.

Duan, W., Kirby, R., Prisutova, J., Horoshenkov, K. (2015) On the use of power reflection ratio and phase change to determine the geometry of a blockage in a pipe. *Applied Acoustics* 87 190-197.

Embleton, T. F. W. (1963) Sound propagation in homogeneous deciduous and evergreen woods. *Journal of the Acoustical Society of America* 35 1119-1125.

Fahy, F. J. (1995) *Sound Intensity.* $2^{nd}$ edition. London: Elsevier.

Felsen, L. B., Yee, H. Y. (1968) Ray method for sound-wave reflection in an open-ended circular pipe. *Journal of the Acoustical Society of America* 44(4) 1028-1039.

Gade, S. (1982) *Sound Intensity (Theory)*. Brüel & Kjær Technical Review 1982-1983.

Heyser, R. C. (1986) *Instantaneous intensity*. 81st Convention. Los Angeles, California: Audio Engineering Society.

Horoshenkov, K., Attenborough, K., Chandler-Wilde, S.N. (1998) Pade approximants for the acoustical properties of rigid frame porous media with pore size distribution. *Journal of the Acoustical Society of America* 104 1198-1209.

Horoshenkov, K., Swift, M. J., Rushforth, I. (2004) Acoustic properties of granular materials with complex pore size distribution. In: CD-ROM Proceedings of the 18th International Congress of Acoustics 2004. *ICA 2004*, Kyoto, Japan, 2004.

Horoshenkov, K., Khan, A., Bécot, F.-X., Jaouen, L., Sgard, F., Renault, A., Amirouche, N., Pompoli, F., Prodi, N., Bonfiglio, P., Pispola, G., Asdrubali, F., Hbelt, J., Atalla,

N., Amédin, C. K., Lauriks, W., Boeckx, L. (2007) Reproducibility experiments on measuring acoustical properties of rigid-frame porous media (round-robin test). *Journal of the Acoustical Society of America* 122(1) 345-353.

Horoshenkov, K. (2013) Acoustic properties of low growing plants. *Journal of the Acoustical Society of America* 133(5) 2554-2565.

ISO 10534-2:1998 (1998) Determination of sound absorption coefficient and impedance in impedance tubes, Part 2: Transfer-function method. International Organization for Standardization, Geneva, Switzerland.

ISO 354:2003 (2003) Measurement of sound absorption in a reverberation room. International Organization for Standardization, Geneva, Switzerland.

Jacobsen, F. (1988) Active and reactive, coherent and incoherent sound fields. *Journal of Sound and Vibration* 130(3) 493-507.

Jacobsen, F. (1991) A note on instantaneous and time-averaged active and reactive sound intensity. *Journal of Sound and Vibration* 147(3) 489-496.

Jacobsen, F. (2005) Measurement of sound intensity: p-u probes versus p-p probes. In: Proceedings of Noise and Vibration Emerging Methods. *International Conference on Noise and Vibration Engineering (ISMA2006)*, St. Raphal, France, 2005.

Jacobsen, F. (2007) Sound intensity. In: *Springer Handbook of Acoustics*. New York: Springer Verlag. 1053-1075.

Jacobsen, F. (2010) *Propagation of sound waves in ducts*. Acoustic Technology, Department of Electrical Engineering, Technical University of Denmark.

Johnson, D. L., Koplik, J., Dashen, R. (1987) Theory of dynamic permeability and tortuosity in fluid-saturated porous media. *Journal of Fluid Mechanics* 176 379-402.

Kirby, R. (2008) Modeling sound propagation in acoustic waveguides using a hybrid numerical method. *Journal of the Acoustical Society of America* 124(4) 1930-1940.

Kutt, H. R. (1975) *Quadrature formulae for finite part integrals*. Report WISK 178. Pretoria: The National Institute for Mathematical Sciences.

Lafarge, D., Lemarinier, P., Allard, J.-F., Tarnow, V. (1997) Dynamic compressibility of air in porous structures at audible frequencies. *Journal of the Acoustical Society of America* 102(4) 1995-2006.

Leclaire, P., Swift, M., Horoshenkov, K. (1998) Specific area from water-suction porosimetry in application to porous acoustic materials. *Journal of Applied Physics* 84(12) 6886-6890.

Levine, H., Schwinger, J. (1948) On the radiation of sound from an unflanged circular pipe. *Physical Review* 73(4) 383-406.

Martens, M. J. M. (1980) Foliage as a low pass filter: Experiments with model forests in an anechoic chamber. *Journal of the Acoustical Society of America* 67(1), 66-72.

Martens, M. J. M. (1981) Absorption of acoustic energy by plant leaves. *Journal of the Acoustical Society of America* 69(1), 303-306.

Matelys (2014) *Acoustical Porous Material Recipes*. [Online] Available from: http://apmr.matelys.com [accessed 10 October 2014].

Microflown (2014) *Microflown Technologies*. [Online] Available from: http://microflown.com [accessed 26 September 2014].

Miki, Y. (1990) Acoustical properties of porous materials - modifications of Delany-Bazley models. *Journal of Acoustical Society of Japan* 11(1) 19-24.

Minten, M., Cops, A., Lauriks, W. (1988) Absorption characteristics of an acoustic material at oblique incidence measured with the two-microphone technique. *Journal of Sound and Vibration* 120(3) 499-510.

Morse, P. (1949) *Vibration and Sound*. Acoustical Society of America, New York: McGraw Hill.

Nomura, V., Yamamura, I., Inawashiro, S. (1960) On the acoustic radiation from a flanged circular pipe. *Journal of the Physical Society of Japan* 15 510-517.

Norris, A. N., Sheng, I. C. (1989) Acoustic radiation from a circular pipe with an infinite flange. *Journal of Sound and Vibration* 134(1) 85-93.

Pride, S. R., Morgan, F. D., Gangi A. F. (1993) Drag forces of porous-medium acoustics. *Physical Review* 47 4964-4978.

Prisutova, J., Horoshenkov, K. (2010) A method to calculate the acoustic intensity near an open end of a flanged round pipe. Proceedings of 20th International Congress on Acoustics 2010. *ICA 2010*, Sydney, Australia, 2010.

Prisutova, J. (2012) *Acoustic intensity in waveguides*. MPhil to PhD transfer report, University of Bradford.

Prisutova, J., Horoshenkov, K., Groby, J.-P., Brouard, B. (2014) A method to determine the acoustic reflection and absorption coefficients of porous media by using modal dispersion in a waveguide. *Journal of the Acoustical Society of America* 136(6) 2947-2958.

Rayleigh, Baron J. W. Strutt (1894) *The theory of sound*, Vol. 1. Macmillan.

Rayleigh, Baron J. W. Strutt (1896) *The theory of sound*, Vol. 2. Macmillan.

Schiffrer, G., Stanzial, D. (1994) Energetic properties of acoustic fields. *Journal of the Acoustical Society of America* 96(6) 3645-3653.

Schultz, T., Cattafesta III, L. N., Sheplak, M. (2006) Modal decomposition method for acoustic impedance testing in square ducts. *Journal of the Acoustical Society of America* 120(6) 3750-3757.

Sharp, D. B., Campbell, D. M. (1997) Leak detection in pipes using acoustic pulse reflectometry. *Acta Acustica united with Acustica* 83 560-566.

Shenderov, E. L. (1975) *Wave Problems of Hydroacoustics*. Moscow: Sudostroenie (in Russian).

Silva, F., Guillemain, Ph., Kergomard, J., Mallaroni, B., Norris, A. N. (2009) Approximation formulae for the acoustic radiation impedance of a cylindrical pipe. *Journal of Sound and Vibration* 322(1-2) 255-263.

Smirnov, V. I. (1967) *A Course in Higher Mathematics*. Vol.2. Moscow: Nauka (in Russian).

Smith, R. (1988) Its all in the bore!. *International Trumpet Guild Journal* vol. 12.

Stanzial, D., Prodi, N., Schiffrer, D. (1996) Reactive acoustic intensity for general fields and energy polarization. *Journal of the Acoustical Society of America* 99(4), 1868-1876.

Stanzial, D., Prodi, N. (1997) Measurements of newly defined intensimetric quantities and their physical interpretation. *Journal of the Acoustical Society of America* 102(4), 2033-2039.

Stanzial, D., Sacchi, G., Schiffrer, G. (2011) Calibration of pressure-velocity probes using a progressive plane wave reference field and comparison with nominal calibration filters. *Journal of the Acoustical Society of America* 129(6), 3745-3755.

Tamura, M. (1990) Spatial Fourier transform method of measuring reflection coefficients at oblique incidence. I:Theory and numerical examples. *Journal of the Acoustical Society of America* 88(5) 2259-2264.

Tamura, M., Allard, J.-F., Lafarge, D. (1995) Spatial Fourier transform method of measuring reflection coefficients at oblique incidence. II. Experimental results. *Journal of the Acoustical Society of America* 97(4) 2255-2262.

Telles, J. C. F. (1987) A self-adaptive co-ordinate transformation for efficient numerical

evaluation of general boundary element integrals. *International Journal for Numerical Methods in Engineering* 24, pp. 959-973.

Vinogradov, M. S., Gavrilov, A. N. (1987) Cross-correlation of normal modes in a shallow sea. *Soviet Physics - Acoustics* 33 241-243.

Ware, J. A., and Aki, K. (1969) Continuous and discrete inverse scattering problems in a stratified elastic medium. I: Planes at normal incidence. *Journal of the Acoustical Society of America* 45(4) 911-921.

Watson, A. and Bowsher, J. (1987) Recent progress in time domain work on brass instruments. Proceedings of the Institute of Acoustics. *IOA* 9 103-109.

Watson, A. and Bowsher, J. (1988) Impulse measurements on brass musical instruments. *Acustica* 66(3) 170-174.

Watson, A. (1989) Impulse measurements on tubular acoustic systems. PhD thesis, University of Surrey, 1989.

Wong, N. H., Tan, A. Y. K., Tan, P. Y., Chiang, K., Wong, N. C. (2010) Acoustics evaluation of vertical greenery systems for building walls. *Building and Environment* 45(2), 411-420.

Wu, Q. L., Fricke, F. (1990) Determination of blocking locations and cross-sectional area in a duct by eigenfrequency shifts. *Journal of the Acoustical Society of America* 87 67-75.

Zorumski, W. E. (1973) Generalised radiation impedances and reflection coefficients of circular and annular ducts. *Journal of the Acoustical Society of America* 54 1667-1673.

Zwikker, C., Kosten, C. W. (1949) *Sound Absorbing Materials.* New York: Elsevier.

# Appendix A

# Frequency-wavenumber spectra

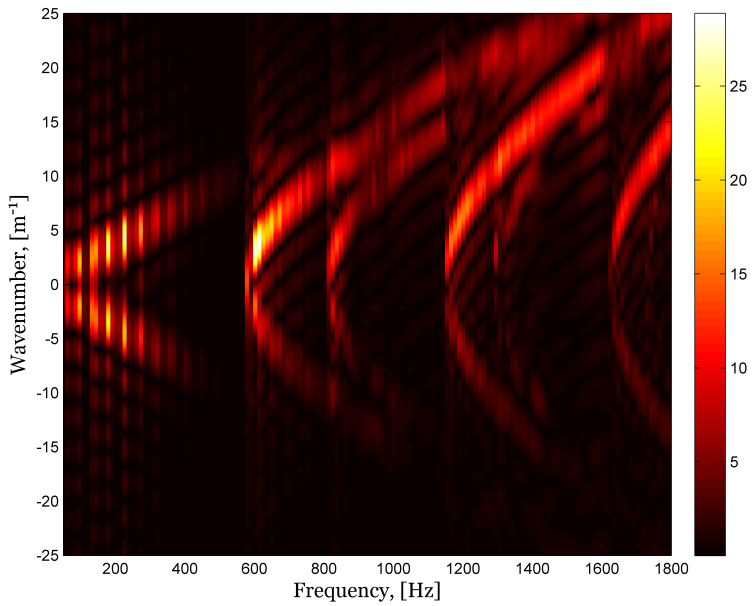


Figure A.1: The frequency-wavenumber spectrum for the layer of melamine foam measured in 300 mm wide square tube, with the microphone placed in the corner of the tube cross-section.

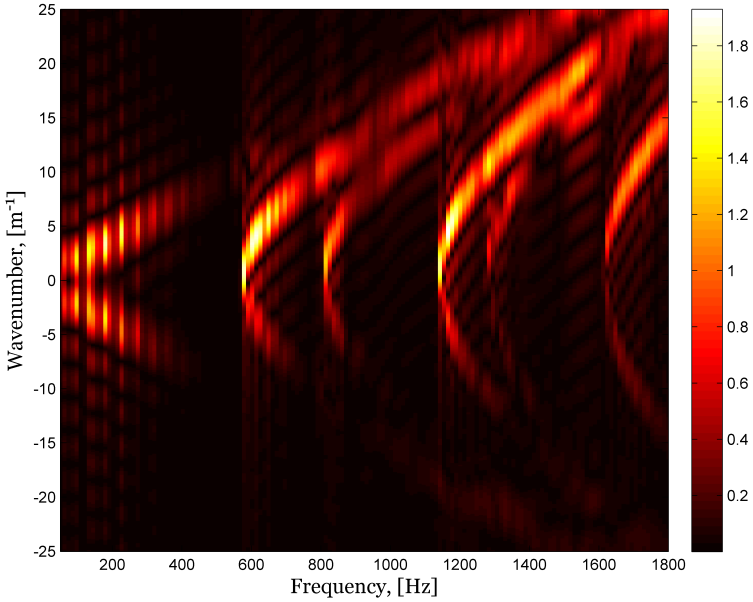


Figure A.2: The frequency-wavenumber spectrum for the layer of wood fibre measured in 300 mm wide square tube, with the microphone placed in the corner of the tube cross-section.

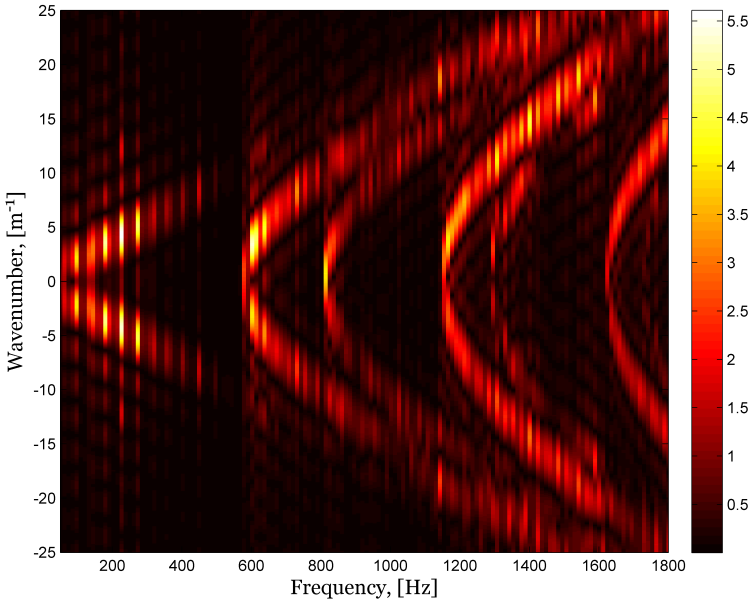


Figure A.3: The frequency-wavenumber spectrum for the layer of thin foam measured in 300 mm wide square tube, with the microphone placed in the corner of the tube cross-section.

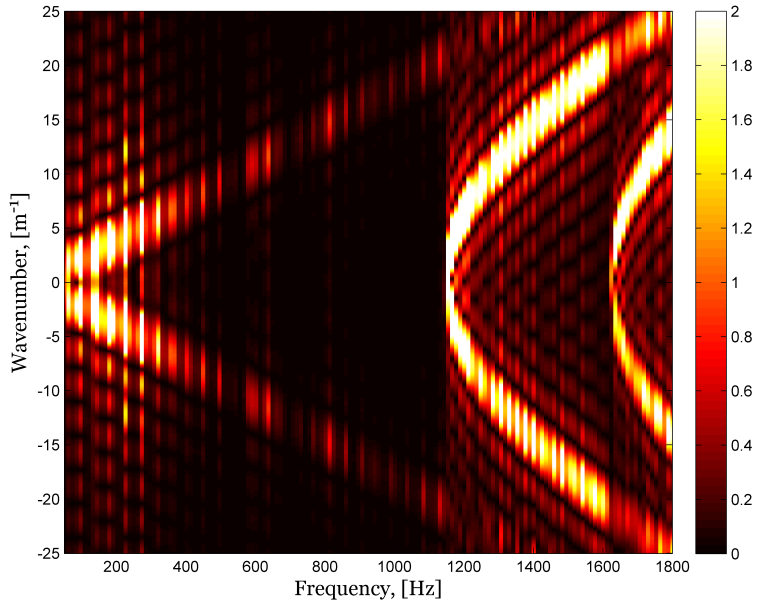


Figure A.4: The frequency-wavenumber spectrum for the layer of thin foam measured in 300 mm wide square tube, with the microphone placed in the middle of the tube cross-section.

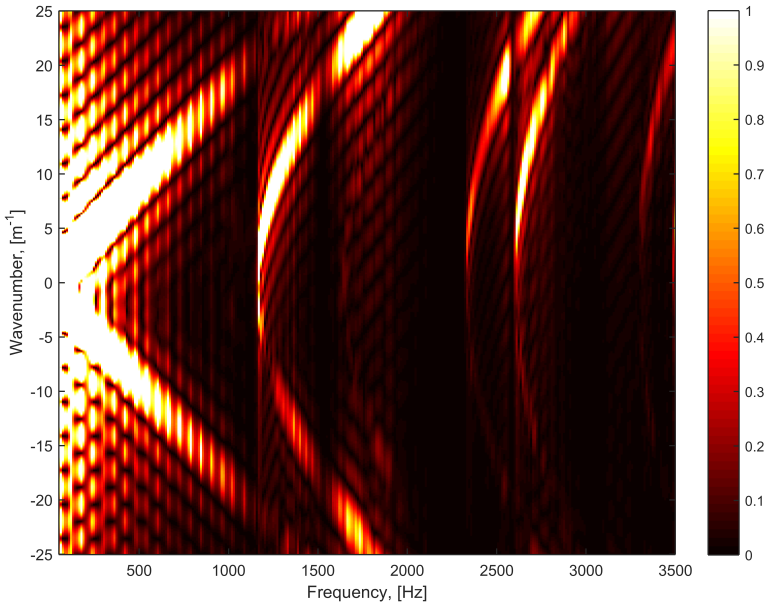


Figure A.5: The frequency-wavenumber spectrum for the layer of Armasound foam with 100 mm air gap measured in 150 mm wide square tube, with the microphone placed in the corner of the tube cross-section.

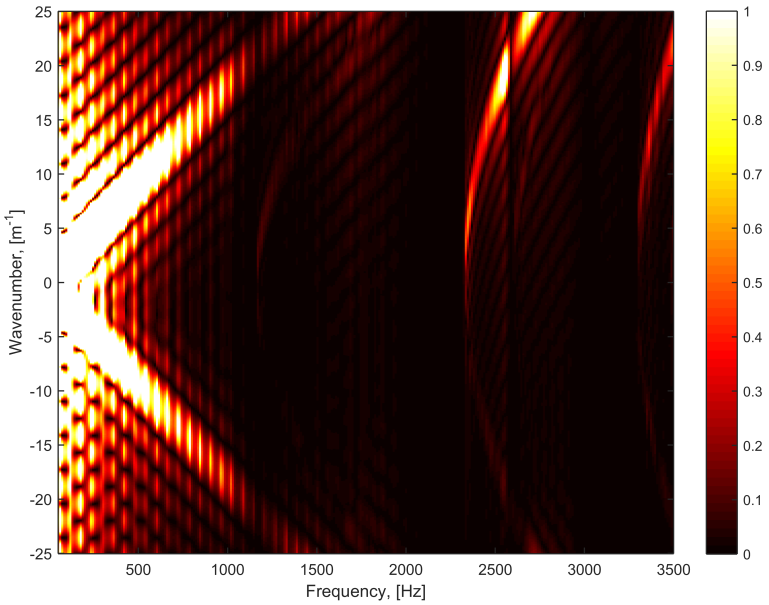


Figure A.6: The frequency-wavenumber spectrum for the layer of Armasound foam with 100 mm air gap measured in 150 mm wide square tube, with the microphone placed in the middle of the tube cross-section.

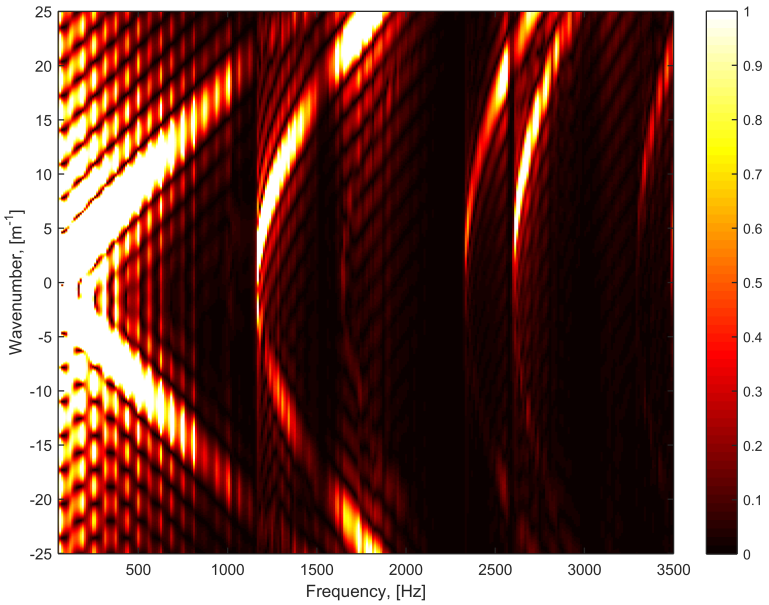


Figure A.7: The frequency-wavenumber spectrum for the layer of Armasound foam with 200 mm air gap measured in 150 mm wide square tube, with the microphone placed in the corner of the tube cross-section.

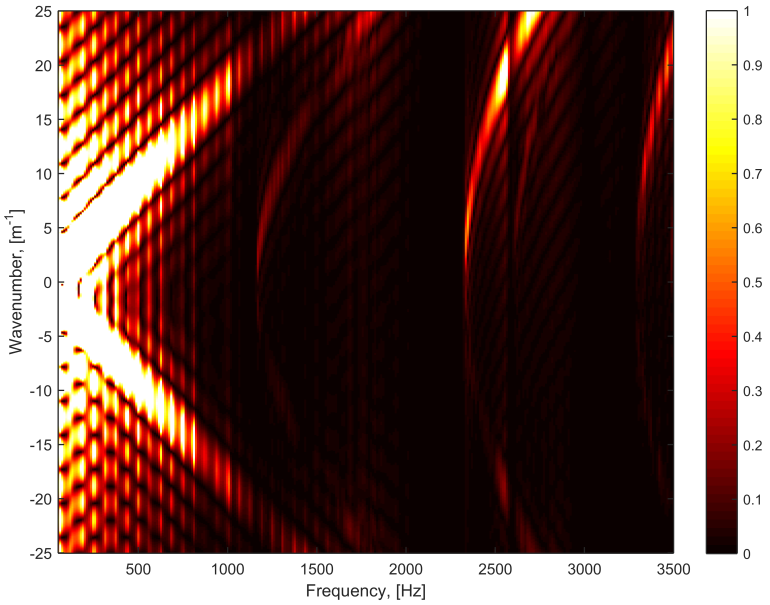


Figure A.8: The frequency-wavenumber spectrum for the layer of Armasound foam with 200 mm air gap measured in 150 mm wide square tube, with the microphone placed in the middle of the tube cross-section.

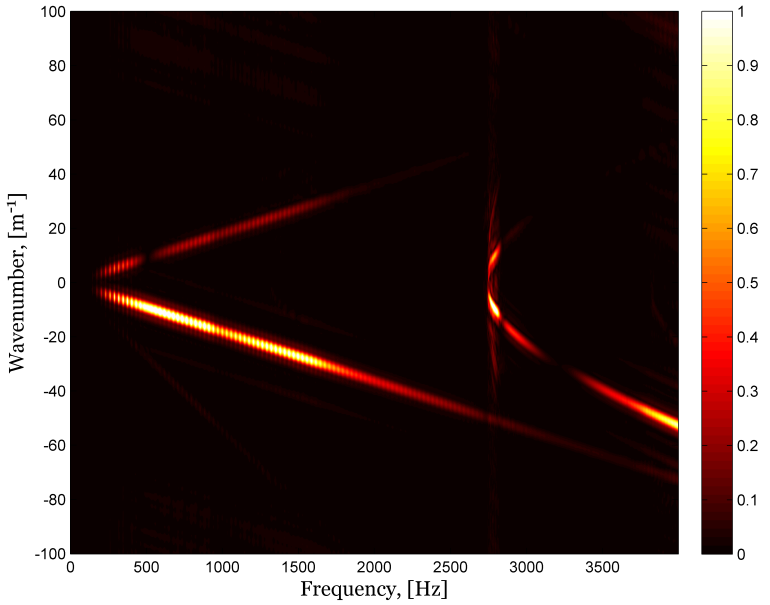


Figure A.9: The frequency-wavenumber spectrum for the layer of melamine foam measured in 150 mm circular tube, with the microphone placed near the wall of the tube cross-section.

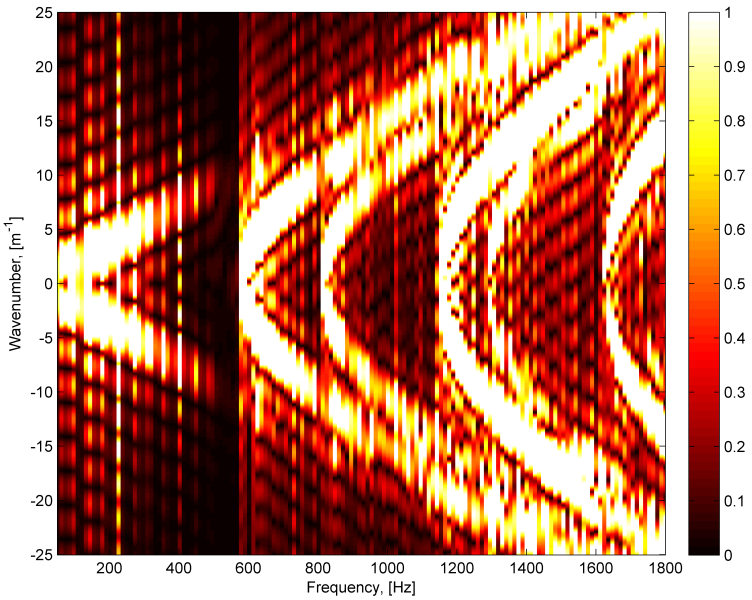


Figure A.10: The frequency-wavenumber spectrum for begonia plants measured in 300 mm wide square tube, with the microphone placed in the corner of the tube cross-section.

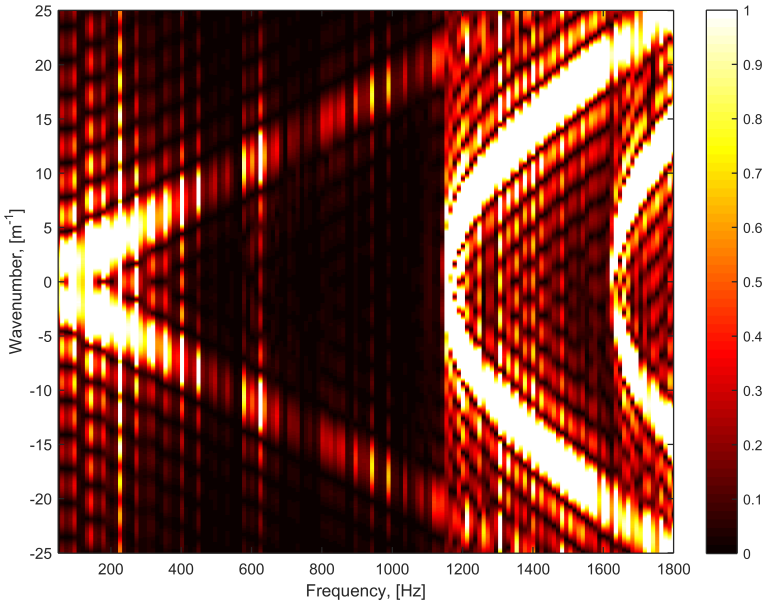


Figure A.11: The frequency-wavenumber spectrum for begonia plants measured in 300 mm wide square tube, with the microphone placed in the middle of the tube cross-section.

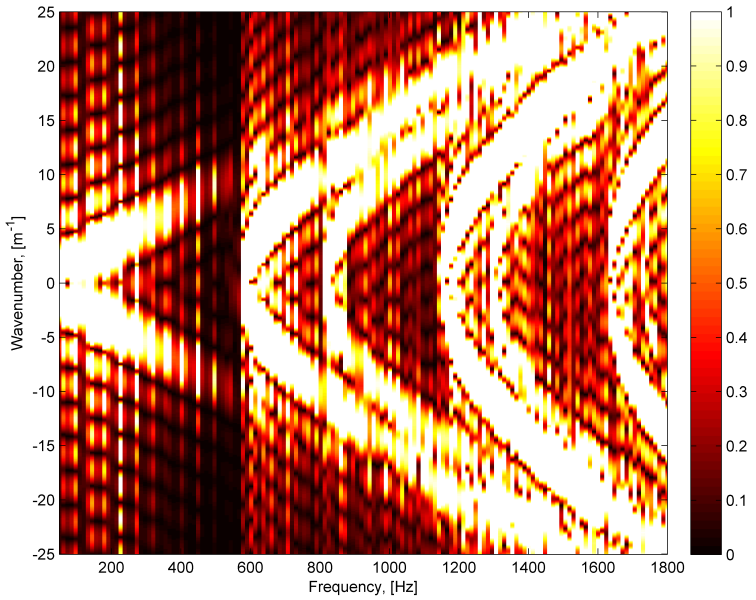


Figure A.12: The frequency-wavenumber spectrum for ivy plants measured in 300 mm wide square tube, with the microphone placed in the corner of the tube cross-section.

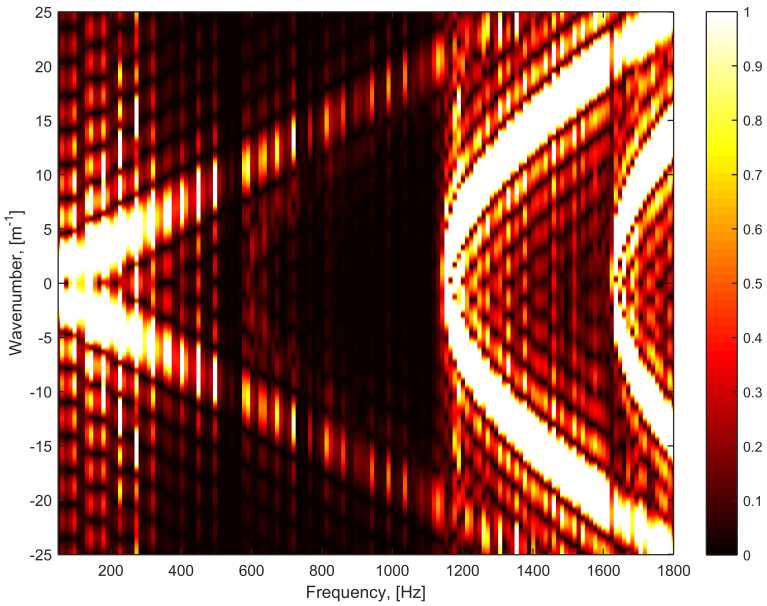


Figure A.13: The frequency-wavenumber spectrum for ivy plants measured in 300 mm wide square tube, with the microphone placed in the middle of the tube cross-section.

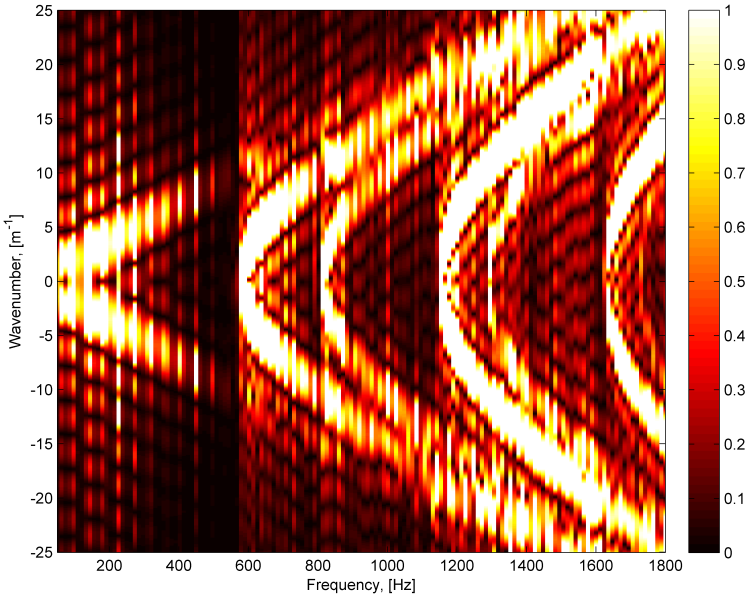


Figure A.14: The frequency-wavenumber spectrum for rudbeckia plants measured in 300 mm wide square tube, with the microphone placed in the corner of the tube cross-section.

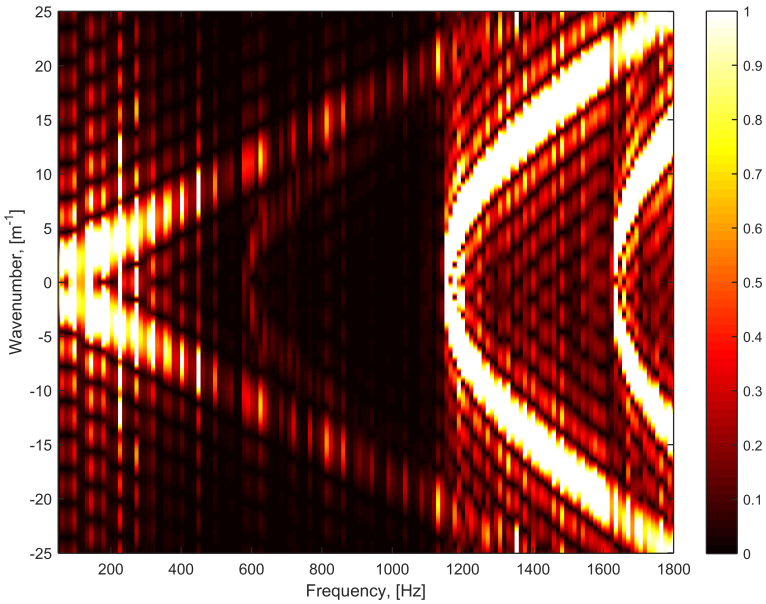


Figure A.15: The frequency-wavenumber spectrum for rudbeckia plants measured in 300 mm wide square tube, with the microphone placed in the middle of the tube cross-section.

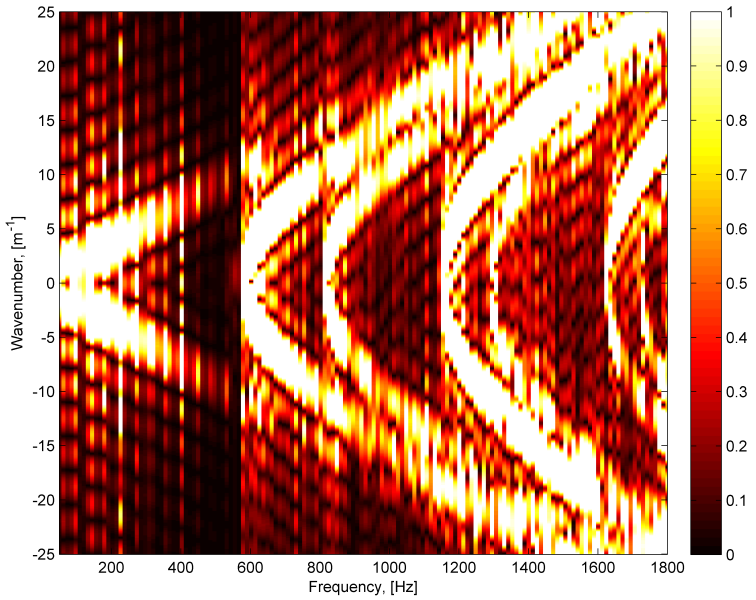


Figure A.16: The frequency-wavenumber spectrum for kalanchoe plants measured in 300 mm wide square tube, with the microphone placed in the corner of the tube cross-section.

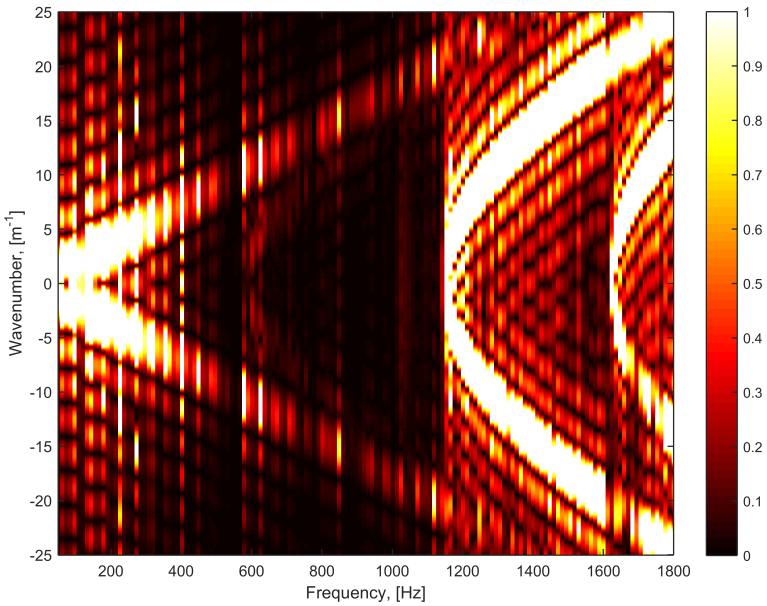


Figure A.17: The frequency-wavenumber spectrum for kalanchoe plants measured in 300 mm wide square tube, with the microphone placed in the middle of the tube cross-section.

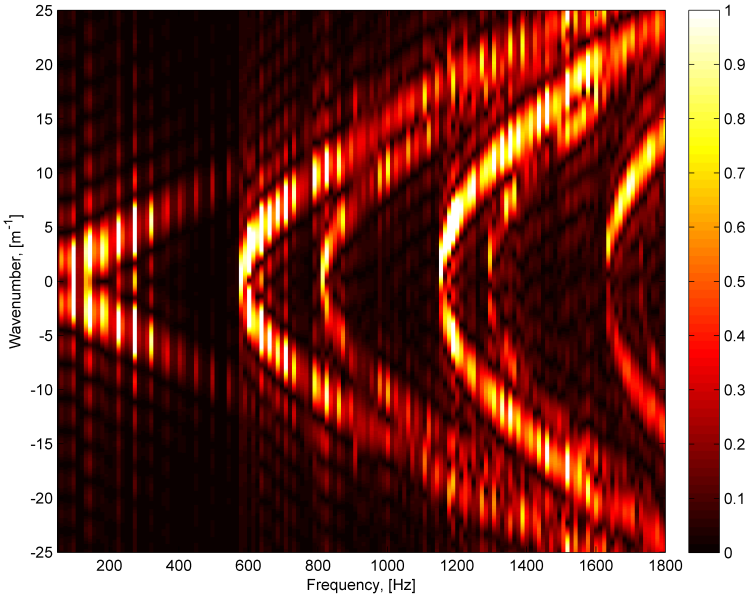


Figure A.18: The frequency-wavenumber spectrum for ficus plants measured in 300 mm wide square tube, with the microphone placed in the corner of the tube cross-section.

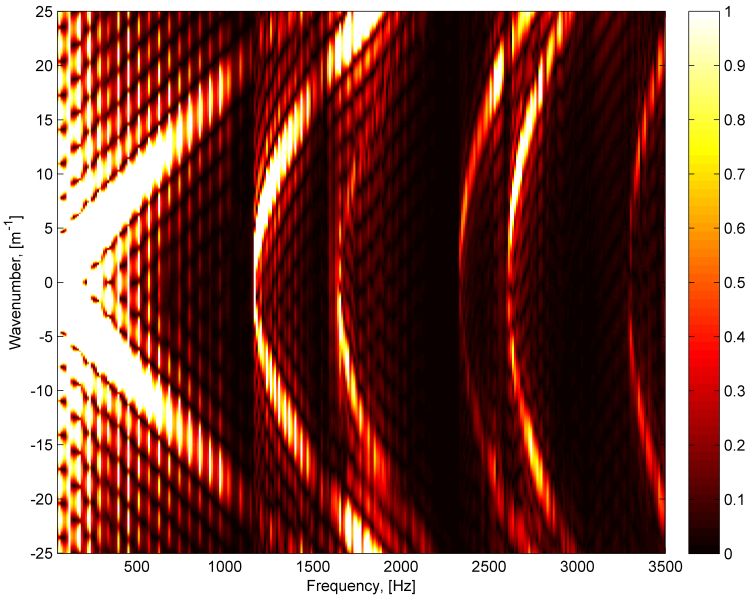


Figure A.19: The frequency-wavenumber spectrum for begonia plants measured in 150 mm wide square tube, with the microphone placed in the corner of the tube cross-section.

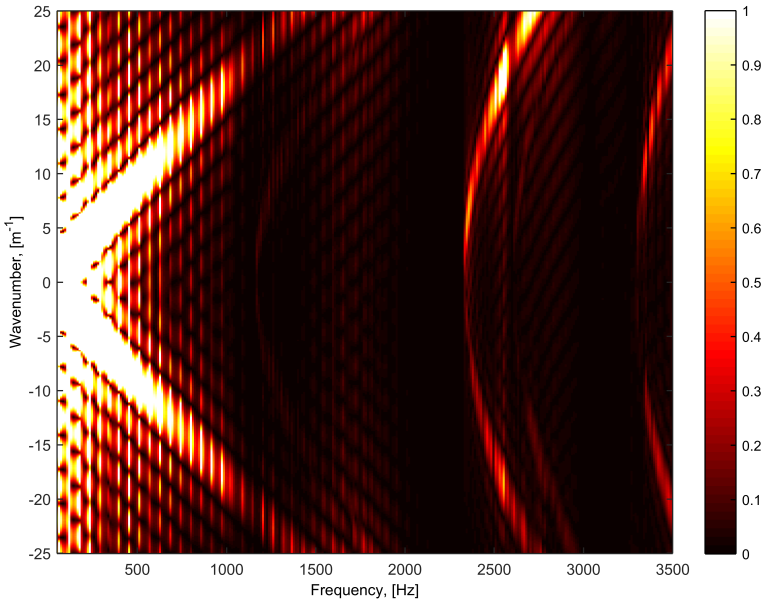


Figure A.20: The frequency-wavenumber spectrum for begonia plants measured in 150 mm wide square tube, with the microphone placed in the middle of the tube cross-section.

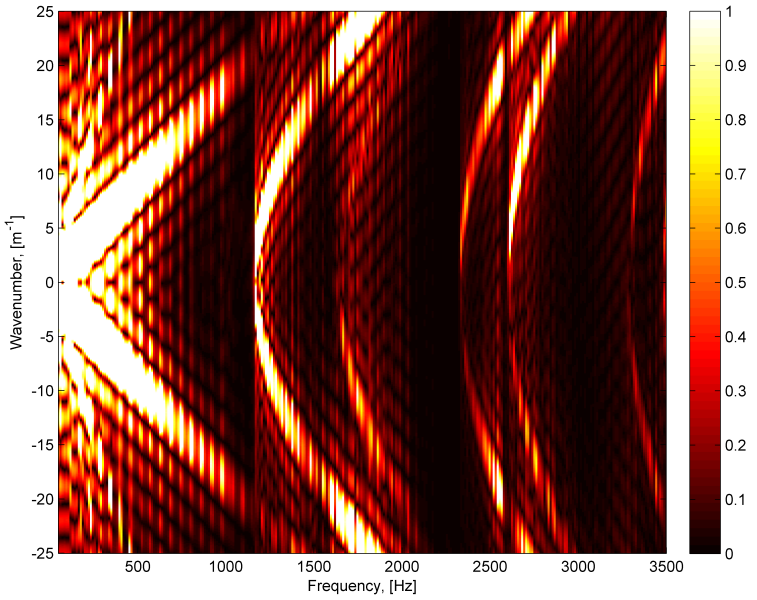


Figure A.21: The frequency-wavenumber spectrum for ivy plants measured in 150 mm wide square tube, with the microphone placed in the corner of the tube cross-section.

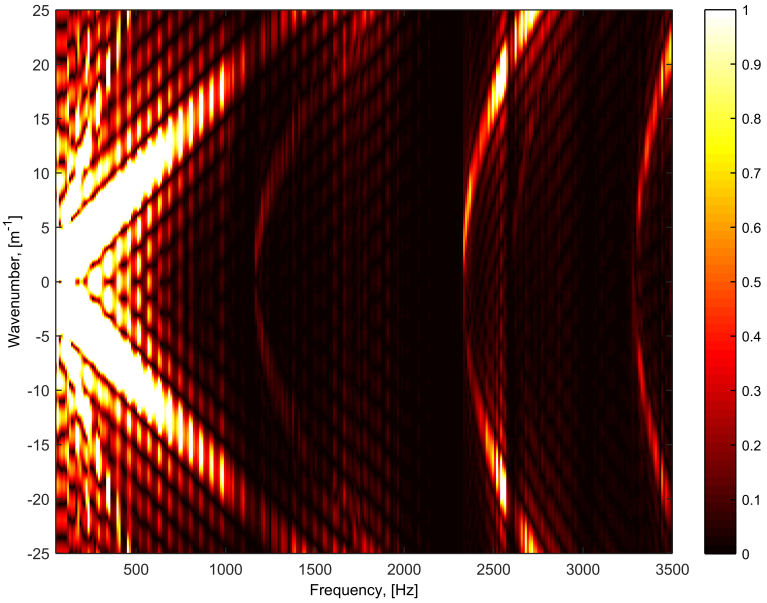


Figure A.22: The frequency-wavenumber spectrum for ivy plants measured in 150 mm wide square tube, with the microphone placed in the middle of the tube cross-section.

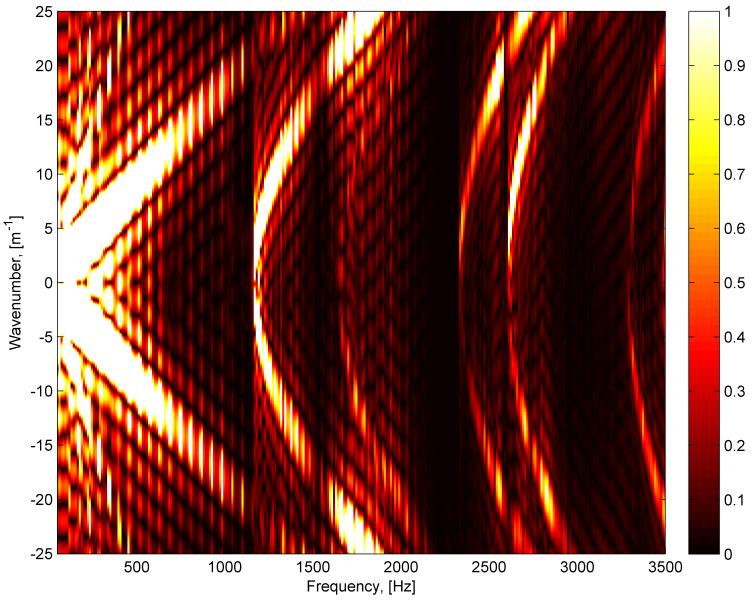


Figure A.23: The frequency-wavenumber spectrum for rudbeckia plants measured in 150 mm wide square tube, with the microphone placed in the corner of the tube cross-section.

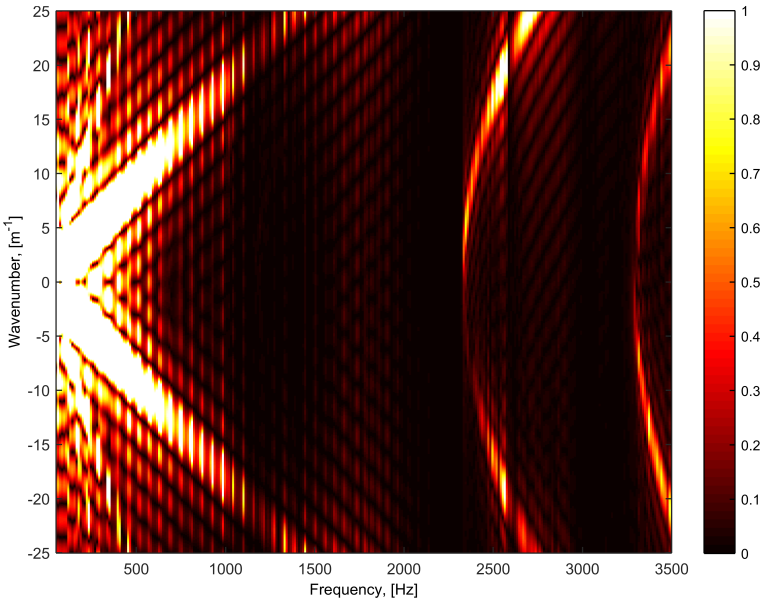


Figure A.24: The frequency-wavenumber spectrum for rudbeckia plants measured in 150 mm wide square tube, with the microphone placed in the middle of the tube cross-section.

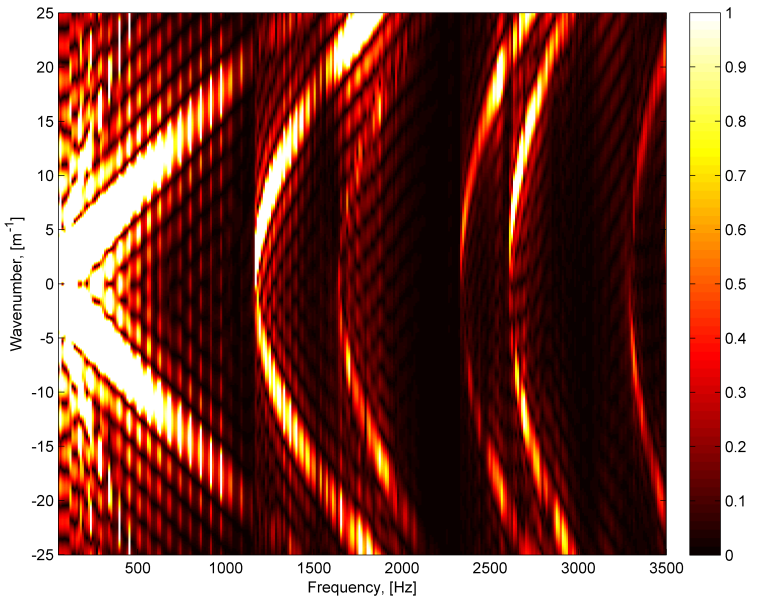


Figure A.25: The frequency-wavenumber spectrum for kalanchoe plants measured in 150 mm wide square tube, with the microphone placed in the corner of the tube cross-section.

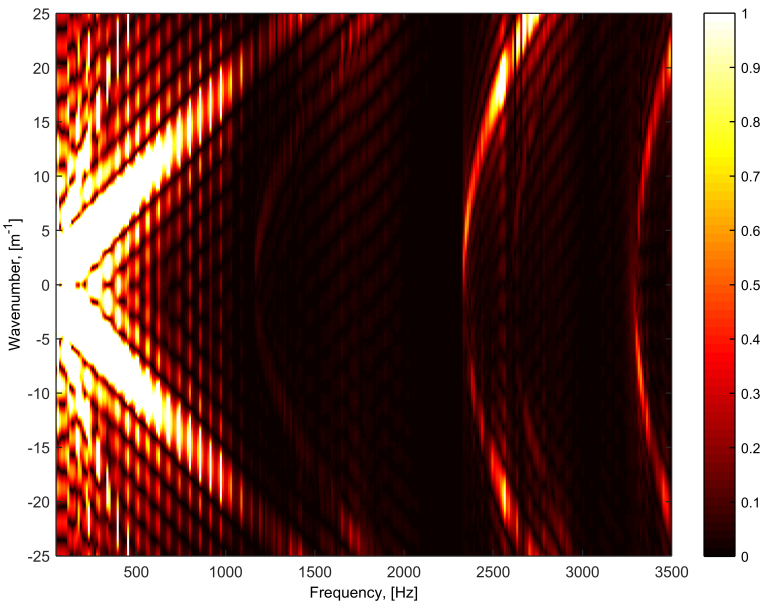


Figure A.26: The frequency-wavenumber spectrum for kalanchoe plants measured in 150 mm wide square tube, with the microphone placed in the middle of the tube cross-section.

# Appendix B

# Matlab code

The details of main Matlab subroutines used to calculate the results presented in this thesis are presented in Table B.1. All subroutines are available upon request.

| File name | Path | Description |
|---|---|---|
| Intensity_OpenPipe.m | ..\SoundIntensity | Complex measured sound intensity calculations using Eqs. (2.2.9) and (2.2.10). |
| KOmega_Refl.m | ..\IntensityApp | Applies a window designed for reflected temporal pressure signal, calculates temporal velocity and complex intensity and takes Fourier transform of these quantities. |

| | | |
|---|---|---|
| KOmega_Transm.m | ..\IntensityApp | Applies a window designed for transmitted temporal pressure signal, calculates temporal velocity and complex intensity and takes Fourier transform of these quantities. |
| TotalKOmega_Coeff.m | ..\IntensityApp | Calculates a total frequency-wavenumber spectrum for all adopted frequencies and evaluates pressure and complex intensity reflection and transmission coefficients. |
| K_Omega_Calculation_BT.m | ..\MaterialChar \BT | Converts frequency- and position-dependent amplitude and phase data measured in the 300 mm square tube into sound pressure, calculates a frequency-wavenumber spectrum. |
| R_mn_Calculation_BT_c.m | ..\MaterialChar \BT | Calculates modal reflection coefficients measured in the corner of the 300 mm square tube based on the frequency-wavenumber spectrum. |

| | | |
|---|---|---|
| TotalAlpha_BT_c.m | ..\MaterialChar \BT | Calculates total absorption coefficients measured in the corner of the 300 mm square tube using amplitude and intensity methods. |
| R_mn_Calculation_BT_m.m | ..\MaterialChar \BT | Calculates modal reflection coefficients measured in the middle of the 300 mm square tube based on the frequency-wavenumber spectrum. |
| TotalAlpha_BT_m.m | ..\MaterialChar \BT | Calculates total absorption coefficients measured in the middle of the 300 mm square tube using amplitude and intensity methods. |
| K_Omega_Calculation_MT.m | ..\MaterialChar \MT | Converts frequency- and position-dependent amplitude and phase data measured in the 150 mm square tube into sound pressure, calculates a frequency-wavenumber spectrum. |
| R_mn_Calculation_MT_c.m | ..\MaterialChar \MT | Calculates modal reflection coefficients measured in the corner of the 150 mm square tube based on the frequency-wavenumber spectrum. |

| | | |
|---|---|---|
| TotalAlpha_MT_c.m | ..\MaterialChar \MT | Calculates total absorption coefficients measured in the corner of the 150 mm square tube using amplitude and intensity methods. |
| R_mn_Calculation_MT_m.m | ..\MaterialChar \MT | Calculates modal reflection coefficients measured in the middle of the 150 mm square tube based on the frequency-wavenumber spectrum. |
| TotalAlpha_MT_m.m | ..\MaterialChar \MT | Calculates total absorption coefficients measured in the middle of the 150 mm square tube using amplitude and intensity methods. |
| FFT_CT.m | ..\MaterialChar \CT | Windows time- and position-dependent pressure data measured in the 150 mm circular tube and applies Fourier transform. |
| KOmega_CT.m | ..\MaterialChar \CT | Calculates a frequency-wavenumber spectrum of the time- and position-dependent pressure data measured in the 150 mm circular tube. |

| | | |
|---|---|---|
| R_mn_Calculation_CT_c.m | ..\MaterialChar \CT | Calculates modal reflection coefficients measured near the wall of the 150 mm circular tube based on the frequency-wavenumber spectrum. |
| R_mn_Calculation_CT_m.m | ..\MaterialChar \CT | Calculates modal reflection coefficients measured in the middle of the 150 mm circular tube based on the frequency-wavenumber spectrum. |
| BegoniaH_BT_c.m | ..\Plants \BT | Calculates measured and predicted modal reflection coefficients and total absorption coefficients using amplitude and intensity methods for begonia plants data collected in the corner of the 300 mm square tube. |
| FicusH_BT_c.m | ..\Plants \BT | Calculates measured and predicted modal reflection coefficients and total absorption coefficients using amplitude and intensity methods for ficus plants data collected in the corner of the 300 mm square tube. |

| | | |
|---|---|---|
| GeraniumH_BT_c.m | ..\Plants \BT | Calculates measured and predicted modal reflection coefficients and total absorption coefficients using amplitude and intensity methods for geranium plants data collected in the corner of the 300 mm square tube. |
| IvyH_BT_c.m | ..\Plants \BT | Calculates measured and predicted modal reflection coefficients and total absorption coefficients using amplitude and intensity methods for ivy plants data collected in the corner of the 300 mm square tube. |
| KalanchoeH_BT_c.m | ..\Plants \BT | Calculates measured and predicted modal reflection coefficients and total absorption coefficients using amplitude and intensity methods for kalanchoe plants data collected in the corner of the 300 mm square tube. |

| | | |
|---|---|---|
| RudbeckiaH_BT_c.m | ..\Plants \BT | Calculates measured and predicted modal reflection coefficients and total absorption coefficients using amplitude and intensity methods for rudbeckia plants data collected in the corner of the 300 mm square tube. |
| BegoniaH_BT_m.m | ..\Plants \BT | Calculates measured and predicted modal reflection coefficients and total absorption coefficients using amplitude and intensity methods for begonia plants data collected in the middle of the 300 mm square tube. |
| GeraniumH_BT_m.m | ..\Plants \BT | Calculates measured and predicted modal reflection coefficients and total absorption coefficients using amplitude and intensity methods for geranium plants data collected in the middle of the 300 mm square tube. |

| | | |
|---|---|---|
| IvyH_BT_m.m | ..\Plants \BT | Calculates measured and predicted modal reflection coefficients and total absorption coefficients using amplitude and intensity methods for ivy plants data collected in the middle of the 300 mm square tube. |
| KalanchoeH_BT_m.m | ..\Plants \BT | Calculates measured and predicted modal reflection coefficients and total absorption coefficients using amplitude and intensity methods for kalanchoe plants data collected in the middle of the 300 mm square tube. |
| RudbeckiaH_BT_m.m | ..\Plants \BT | Calculates measured and predicted modal reflection coefficients and total absorption coefficients using amplitude and intensity methods for rudbeckia plants data collected in the middle of the 300 mm square tube. |

| | | |
|---|---|---|
| BegoniaH_MT_c.m | ..\Plants \MT | Calculates measured and predicted modal reflection coefficients and total absorption coefficients using amplitude and intensity methods for begonia plants data collected in the corner of the 150 mm square tube. |
| GeraniumH_MT_c.m | ..\Plants \MT | Calculates measured and predicted modal reflection coefficients and total absorption coefficients using amplitude and intensity methods for geranium plants data collected in the corner of the 150 mm square tube. |
| IvyH_MT_c.m | ..\Plants \MT | Calculates measured and predicted modal reflection coefficients and total absorption coefficients using amplitude and intensity methods for ivy plants data collected in the corner of the 150 mm square tube. |

| | | |
|---|---|---|
| KalanchoeH_MT_c.m | ..\Plants \MT | Calculates measured and predicted modal reflection coefficients and total absorption coefficients using amplitude and intensity methods for kalanchoe plants data collected in the corner of the 150 mm square tube. |
| RudbeckiaH_MT_c.m | ..\Plants \MT | Calculates measured and predicted modal reflection coefficients and total absorption coefficients using amplitude and intensity methods for rudbeckia plants data collected in the corner of the 150 mm square tube. |
| BegoniaH_MT_m.m | ..\Plants \MT | Calculates measured and predicted modal reflection coefficients and total absorption coefficients using amplitude and intensity methods for begonia plants data collected in the middle of the 150 mm square tube. |

| | | |
|---|---|---|
| GeraniumH_MT_m.m | ..\Plants \MT | Calculates measured and predicted modal reflection coefficients and total absorption coefficients using amplitude and intensity methods for geranium plants data collected in the middle of the 150 mm square tube. |
| IvyH_MT_m.m | ..\Plants \MT | Calculates measured and predicted modal reflection coefficients and total absorption coefficients using amplitude and intensity methods for ivy plants data collected in the middle of the 150 mm square tube. |
| KalanchoeH_MT_m.m | ..\Plants \MT | Calculates measured and predicted modal reflection coefficients and total absorption coefficients using amplitude and intensity methods for kalanchoe plants data collected in the middle of the 150 mm square tube. |

| | | |
|---|---|---|
| RudbeckiaH_MT_m.m | ..\Plants \MT | Calculates measured and predicted modal reflection coefficients and total absorption coefficients using amplitude and intensity methods for rudbeckia plants data collected in the middle of the 150 mm square tube. |